Fraunhofer ISE

FRAUNHOFER INSTITUTE FOR SOLAR ENERGY SYSTEMS ISE

SOLAR ENERGY AND SYSTEMS RESEARCH

Bernd Steinhauser

PASSIVATING DOPANT SOURCES FOR HIGH-EFFICIENCY N-TYPE SILICON SOLAR CELLS

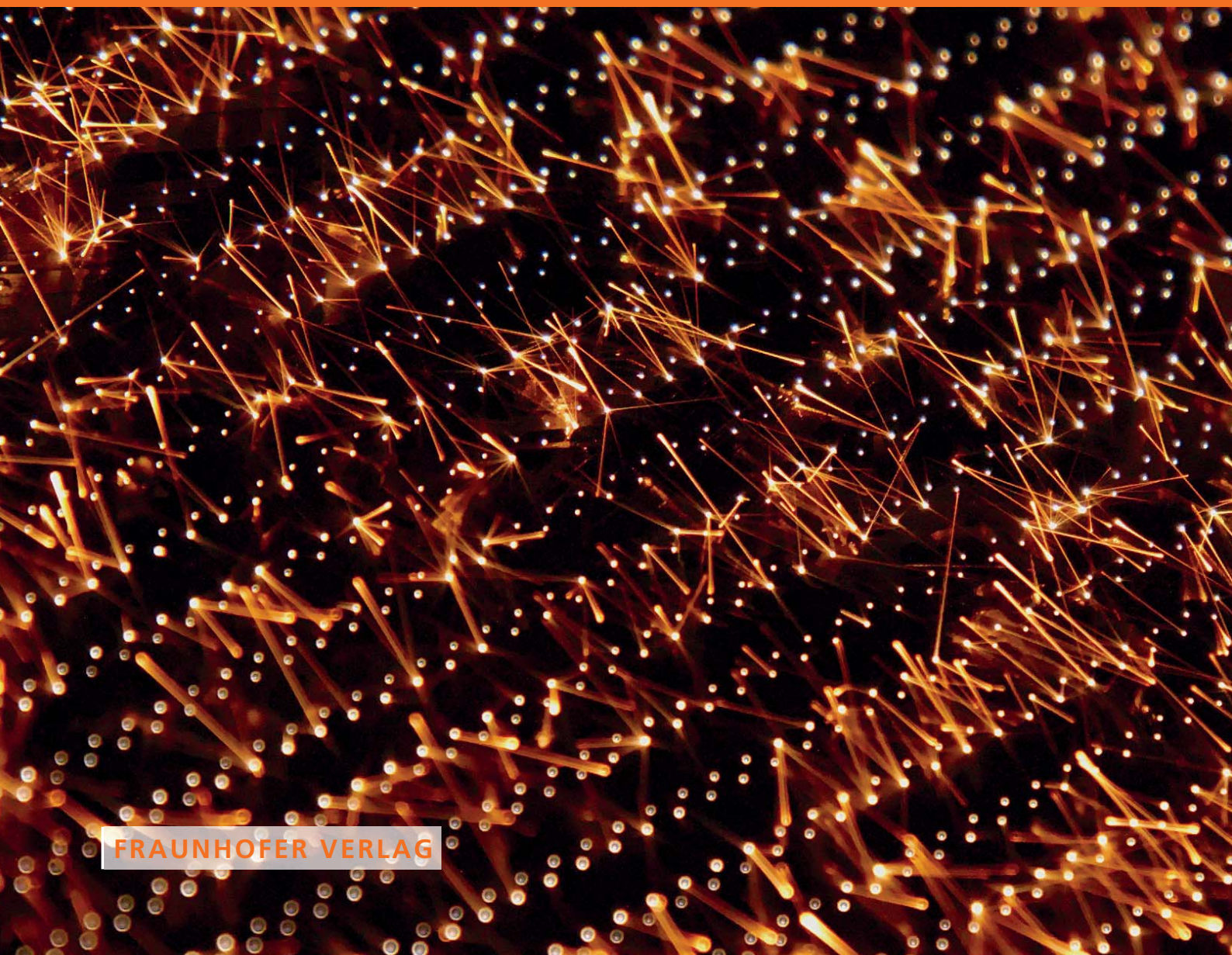

FRAUNHOFER VERLAG

Fraunhofer Institute for Solar Energy Systems ISE

SOLARE ENERGIE- UND SYSTEMFORSCHUNG /
SOLAR ENERGY AND SYSTEMS RESEARCH

Passivating Dopant Sources for High-Efficiency n-type Silicon Solar Cells

Bernd Steinhauser

FRAUNHOFER VERLAG

Contact:
Fraunhofer Institute for Solar Energy Systems ISE
Heidenhofstrasse 2
79110 Freiburg
Phone +49 761/4588-5150
Fax +49 761/4588-9342
E-Mail info@ise.fraunhofer.de
URL www.ise.fraunhofer.de

Bibliographic information published by Die Deutsche Bibliothek

Die Deutsche Bibliothek lists this publication in the Deutsche Nationalbibliografie; detailed bibliografic data is available in the Internet at <http://dnb.d-nb.de>.

D 352

Zugl.: Konstanz, Univ., Diss., 2017

Book Series: »Solare Energie- und Systemforschung / Solar Energy and Systems Research«

Printing and Bindery:
Mediendienstleistungen des
Fraunhofer-Informationszentrum Raum und Bau IRB, Stuttgart

Printed on acid-free and chlorine-free bleached paper.

Regional Planning and Building Construction IRB
P.O. Box 80 04 69, D-70504 Stuttgart
Nobelstrasse 12, D-70569 Stuttgart
Phone +49 (0) 7 11/9 70-25 00
Fax +49 (0) 7 11/9 70-25 07
E-Mail: verlag@fraunhofer.de
URL www.verlag.fraunhofer.de

Passivating Dopant Sources for High-Efficiency n-type Silicon Solar Cells

Dissertation

zur Erlangung des akademischen Grades
eines Doktors der Naturwissenschaften
(Dr. rer. nat.)

vorgelegt von

Bernd Steinhauser

Referenten:
Prof. Dr. G. Willeke
Prof. Dr. E. Scheer

Tag der mündlichen Prüfung:
03.02.2017

an der
Universität Konstanz, Fachbereich Physik, 2016
angefertigt am
Fraunhofer-Institut für Solare Energiesysteme

Contents

»I think the problem, to be quite honest with you, is that you've never actually known what the question is. So once you do know what the question actually is, you'll know what the answer means.«

(›Deep Thought‹ in Douglas Adams' Hitchhiker's Guide to the Galaxy)

1 Introduction

While the first silicon solar cells were fabricated using *n*-type silicon ([1], doped by arsenic) it was the *p*-type cell that conquered the world of energy production on a GW scale. This was mainly due to the great simplicity of the Al-BSF cell which allows for a very short and cost-effective process sequence both on mono- as well as multicrystalline material. However, not only the efficiency record of 25.6 % for silicon solar cells (under standard testing conditions, one sun irradiation) was achieved on *n*-type silicon, but today highest efficiency solar cells are almost exclusively fabricated on phosphorus-doped material [2].

There are mainly two advantages for using *n*-type crystalline silicon. The first is that *n*-type silicon is less prone to increased recombination by some impurities like iron [3]. The second is that mono-crystalline, uncompensated *n*-type silicon does not suffer from Light Induced Degradation (LID), as is known for *p*-type Cz material due to the formation of boron-oxygen related defects under illumination [4, 5]. While a permanent regeneration mechanism was found [6], it remains to be shown if such a regeneration can be implemented in the cell production, thus preventing degradation of the cell performance.

The common approaches on *n*-type silicon can be divided into two basic categories. Those keeping a short and possibly cost-effective process sequence and which are in direct competition with *p*-type Al-BSF or Passivated Emitter and Rear Cell (PERC). The second category is that of the (ultra) high-efficiency solar cells, often featuring selective/passivated contacts (and possibly even an Interdigitated Back-Contact (IBC) structure), like is the case for HIT [7, 8], Sunpowers IBC cells [9] or *TOPCon* [10]. The processing of such cell, especially for IBC structures, might however be complex and thus only be feasible for niche markets.

In case of the cell concepts aiming for low- to mid-range performance, thus competing with Al-BSF and PERC, a »quasi-standard« was established for *n*-type cells based on the Passivated Emitter and Rear Totally Diffused (PERT) layout (*n*-type PERT (nPERT)) as an equivalent to the Al-BSF cell on *p*-type.

The cells feature full-area highly doped front and rear, although the ways to create these dopings may vary, e.g. by (co-)diffusion [11, 12], implantation [13], or spin-on coating [14]. To reduce the complexity of the process (e.g. omitting single-sided texture), the cells are often fabricated with almost symmetric front and rear in a bifacial layout where it is possible to achieve almost identical performance if measured illuminating from either side and thus a gain in dedicated application [15].

While efficiencies similar to those of *p*-type PERC in the range of 21 % were demonstrated for such concepts, the concept is inherently limited by the compromises that have to be made for the homogeneous doping at the surfaces. Therefore exceeding 22 % might require using selective structures, e.g. for the Back-Surface-Field (BSF), to reduce recombination but retain a low contact resistance, resulting in increased complexity. As PERC solar cells already reached efficiencies in the range of 22 % [16], the gain by using *n*-type material with the nPERT concept might already be abundant, even if considering the possible degradation of the PERC cells.

This means that to compete with *p*-type PERC, other concepts might be required. Especially a contact selectivity like it is achieved with PERC should be implemented. Laser doping, laser diffusion or laser melting can be utilized to achieve such a selective doping and contact structure without increasing the number of process steps significantly, while at the same time retaining the capability of achieving high efficiencies. While the idea of laser doping was already developed in 1968 by Fairfield and Schwuttke [17], in case of solar cells it was not until the Laser Fired Contacts (LFC) process in 2001 [18] that its beauty was fully revealed. The LFC process makes use of the fact that aluminum can be used both as a rear side metallization (e.g. evaporated or screen-printed) as well as to form an acceptor state in crystalline silicon. By using an appropriate laser process the dopant source (the aluminum) does not have to be removed after laser doping (to create a Local Back Surface Field (LBSF)), but instead forms an integrated part of the final cell structure as the rear side metallization. In 2010, Suwito *et al.* presented the *PassDop* approach which—similar to LFC—assigns multiple functions to a specific part of the device, in this case the rear side passivation layer, the »*PassDop* layer«. This layer does not only have to provide a good passivation of the solar cells' rear, but contain dopants that in a laser doping process can be driven into the silicon creating a LBSF while at the same time opening the passivation layer locally to prepare the device for the rear side metallization. Suwito *et al.* showed that with this approach efficiencies beyond 22 % [19] can be achieved. In this concept, the *PassDop* layer is the crucial part as it has to provide both an excellent passivation as well as to contain dopants that can

be utilized during the laser doping process for LBSF formation, e.g. in case of *n*-type silicon phosphorus as a possible donor.

The present thesis is dedicated to these *PassDop* layers and the related processes for *n*-type silicon. The focus is not only on the development of such layers, but also on understanding the implications of using such a laser process, e.g. of impurities like nitrogen driven into the LBSF.

Outline of the Thesis

Chapter 2 gives an introduction to the recombination processes relevant to crystalline silicon. First the general recombination mechanisms are described, then more specific topics like the recombination at local contact structures is discussed. The recombination factor J_0 is introduced as well as its specific components that can be attributed to the specific recombination regions of the device.

In **Chapter 3** the basic characteristics of silicon solar cell devices are discussed. In addition, *Quokka* as a device simulator is introduced, as it was used to simulate these characteristics in Chapter 8.

Chapter 4 gives a short introduction into the technology that was used to deposit the *PassDop* layers: Plasma-Enhanced Chemical Vapor Deposition (PECVD). The main plasma techniques that were used are described in brief as well as the PECVD reactors.

In **Chapter 5**, a short review on the technology components of *PassDop* is given, namely passivation of crystalline silicon by a-SiC_x or a-SiN_x as well as laser doping. While each of these technologies is not new on its own, in case of *PassDop* they are combined creating a new concept of structuring the rear side selectively. The sequence necessary for the *PassDop* approach is described as well as the requirements for the PECVD layer. Finally a brief overview over the *PassDop* layers is given, those developed by Suwito [19] as well as within or aside of this thesis.

In **Chapter 6**, the *PassDop* layers that were developed and characterized throughout this work are described. In the first step, improvements to the original *PassDop* layer based on SiC_x are described. Here, the main focus is on improving the thermal stability of the stack as well as enhanced doping efficiency. In a second step, an alternative based on SiN_x:P was developed with the focus on low-temperature ($< 450\,℃$) cell processing is presented.

For this layer it is evaluated if a single layer can be used to achieve the electrical requirements (high LBSF doping and good surface passivation) for *PassDop*. In addition, two-layer stacks are investigated as well, with a dedicated a-Si:P doping layer being placed on top of the SiN_x:P layer. Finally the influence of dopants close to the c-Si/SiN_x interface is studied by removing the dopants from parts of the layer stack. In the last section of this chapter, the development of the firing-stable *PassDop* (*fPassDop*) process is outlined. This *PassDop* layer is based on SiN_x:P as well, but in this case the passivation should deliver a good performance after a corresponding firing process at around 750 °C. Similar to the low-temperature approach, both a single layer as well as double layer stacks are studied, for the latter in different variants.

Chapter 7 is dedicated to the *PassDop* LBSF. The first part in this chapter is mainly about profile characterization, where both micro- as well as macroscopic methods will be investigated. Not only dopant concentration and (in case of microscopic methods) distribution/uniformity were studied, but the inclusion of impurities originating form the *PassDop* layer as well. The focus here was on nitrogen and more specifically the *fPassDop* process. The influence of the impurities on the laser process as well as the doping profile measurement is discussed. In addition, improper ablation as well as formation of (possibly unwanted) by-products of the laser process are investigated. The second part is about the recombination in the LBSF. Based on the theory outlined in Chapter 2, S_{met} for the *PassDop* layers is determined and the influence of annealing processes on the recombination is investigated.

Finally, in **Chapter 8**, the performance of the developed *PassDop* layers at the device level is investigated. Both small-area cells are presented as well large area cells. In case of *fPassDop*, cells featuring screen-printed front side contacts are presented, in case of the low-temperature approach, cells with Ni- and Cu-plated front contacts. For comparison of the characterization samples to the devices, *Quokka* simulations are performed selectively leading to a loss analysis and a better judgment of the potential of the respective approaches.

2 Recombination in Crystalline Silicon

Recombination of charge carriers is defined as the opposite of generation. While generation is a dynamic process leading to an increase in the electron/hole states being occupied in the conduction/valence bands, respectively, recombination leads to a decrease of those.
For a solar cell device, it is essential that the carriers generated by light irradiation can be extracted to provide electric energy to the external circuit. If recombination occurs, carriers are »lost« and thus a reduction of this energy will be the result as they cannot contribute to the current extracted from the device anymore. Thus, for an efficient solar cell device, it is important to reduce recombination as much as possible and therefore to be able to quantify the respective contributions.
It should be pointed out, that while precisely understanding generation is equally important, it will not be described here. A detailed description can e.g. be found in [20].
The recombination processes can be divided into two categories: i) intrinsic recombination, which is fundamental to the semiconductor device and ii) extrinsic recombination, which is not present in a »perfect« semiconductor, but present in actual devices, i.e. due to material defects. In this section, the basic recombination processes are described and the models used throughout the thesis are given.

2.1 General Aspects

If the semiconductor is in thermal equilibrium

$$n_0 \cdot p_0 = n_{\mathrm{i,eff}}^2. \tag{2.1}$$

Where n_0 and p_0 are the respective electron and hole concentrations at equilibrium [21]. $n_{\mathrm{i,eff}}$ is the effective intrinsic carrier concentration. Since the

semiconductor is in thermal equilibrium, the rate of generation (G_0) and recombination (R_0) must be equal, thus $G_0 - R_0 = 0$.

Light excitation with an appropriate light source will lead to absorption of light and therefore generation of carriers at a rate ΔG, thus

$$n = n_0 + \Delta n \tag{2.2}$$

$$p = p_0 + \Delta p, \tag{2.3}$$

with Δn and Δp the excess carrier densities for electrons and holes, respectively. Since only pairs of electrons and holes can be generated, it follows that $\Delta n = \Delta p$ and therefore in the following only Δn will be used as a notation. As soon as the semiconductor is not in thermal equilibrium anymore, the excess carriers will lead to an increase in recombination at a rate R leading to the continuum equation

$$\frac{\partial n_0 + \Delta n}{\partial t} = (G_0 + \Delta G) - (R_0 + R) \tag{2.4}$$

and since n_0 is a constant and $G_0 - R_0 = 0$

$$\frac{\partial \Delta n}{\partial t} = \Delta G - R. \tag{2.5}$$

2.2 Minority Carrier Lifetime

It can be shown, that the decrease in Δn follows an exponential decay [21]. The time constant of this decay is called the »minority carrier lifetime« τ, or short »lifetime«:

$$\tau = \frac{\Delta n}{R} \tag{2.6}$$

The lifetime can also be expressed in relation to the diffusion length of the minority carriers [21]

$$L = \sqrt{D\tau}. \tag{2.7}$$

τ can be used to describe how fast carriers in the semiconductor will recombine after generation. Since the recombination rates in different areas of the device (e.g. emitter and base) will differ, it makes sense to differentiate between several recombination mechanisms and rates. They will be discussed

individually in the next sections. The recombination rates of the different mechanisms can be added up

$$R = \sum_i R_i \tag{2.8}$$

and thus the respective lifetimes τ_i will add up reciprocally

$$\frac{1}{\tau} = \sum_i \frac{1}{\tau_i}. \tag{2.9}$$

2.2.1 Radiative Recombination

The reverse recombination process of the carrier generation by photons is called radiative recombination. Thus an electron and a hole »recombine«, meaning that the electron is transferred to the valence band, occupying the place of the hole. After recombination, the electron and hole no longer contribute to the conductivity of the device. The energy gained by this exchange is emitted as a photon with an energy above the energy of the bandgap. The rate at which electrons and holes recombine is described by the recombination rate R_{rad} and is dependent on the product np of the carrier densities

$$R_{\mathrm{rad}} = B_{\mathrm{rad}}(np - n_{\mathrm{i,eff}}^2), \tag{2.10}$$

with B_{rad} being the recombination probability for the radiative recombination process.

In case of an indirect semiconductor like c-Si, the excess momentum has to be absorbed by a phonon and therefore B_{rad} is relatively low, meaning that most likely other recombination processes are dominant. In a more precise theory, the coulomb attraction of electron and holes has to be taken into account [22] as well as—at higher excess carrier densities—the coulomb screening of carriers [23]. As the emitted photons have $E_\lambda > E_{\mathrm{g}}$, they can be reabsorbed by the semiconductor and thus generate carriers again. Due to the above, in an indirect semiconductor, this only plays a role in case of (optically) thick semiconductor material.

Today, the radiative recombination is usually incorporated into the model describing the Auger recombination, as given in the next section.

2.2.2 Auger Recombination

In the radiative recombination, the excess energy is transferred to a photon being emitted. However, it is possible to transfer the energy to a different particle, namely an electron or a hole, which is then excited into a higher state within the band and may subsequently drop into a lower state by submitting the energy to the crystal via inelastic impacts [24]. This process is named »Auger« recombination after Pierre Auger who observed it for X-ray excitation of matter [25].

As described above, Auger recombination is a three particle process. As the excess energy can be transmitted to an electron or a hole, two Auger processes can be defined, »eeh« and »ehh« Auger recombination, respectively. The respective recombination rates are

$$R_{\mathrm{eeh}} = C_{\mathrm{n}} n^2 p \tag{2.11}$$

$$R_{\mathrm{ehh}} = C_{\mathrm{p}} n p^2 \tag{2.12}$$

with C_{n} and C_{p} the Auger coefficients for the respective processes. Over the years, a number of models describing Auger recombination have been presented, e.g. [26–34]. The reasons for the newer models are twofold: the first is that the coulomb attraction of the carriers was introduced by Hangleiter *et al.* defining »Coulomb-enhanced« Auger recombination. The second is that improved passivation processes led to the conclusion, that previous parameterizations overestimated the Auger recombination rate and thus lifetimes exceeding the limit predicted for crystalline silicon at the given dopant concentrations were determined.

Therefore in this work, only the parameterization for the bulk recombination proposed by Richter *et al.* was used [34], with the intrinsic bulk lifetime

$$\tau_{\text{intr}} = \frac{\Delta n}{R_{\text{Auger}}} = \frac{\Delta n}{R_{\text{eeh}} + R_{\text{ehh}}} \tag{2.13}$$

$$= \frac{\Delta n}{\left(np - n_{\text{i,eff}}^2\right)\left(2.5 \times 10^{-13} g_{\text{eeh}} n_0 + 8.5 \times 10^{-32} g_{\text{ehh}} p_0 + 3 \times 10^{-29} \Delta n^{0.92} + B_{\text{rel}} B_{\text{low}}\right)} \tag{2.14}$$

with n and p the carrier densities, n_0 and p_0 the carrier densities at equilibrium, Δn the excess carrier density and $n_{\text{i,eff}}$ the effective intrinsic carrier density. The above parameterization includes the Coulomb enhancement factors g_{eeh} and g_{ehh}, which are defined as

$$g_{\text{eeh}}(n_0) = 1 + 13\left(1 - \tanh\left[\left(\frac{n_0}{N_{0,\text{eeh}}}\right)^{0.66}\right]\right) \tag{2.15}$$

$$g_{\text{ehh}}(p_0) = 1 + 7.5\left(1 - \tanh\left[\left(\frac{p_0}{N_{0,\text{ehh}}}\right)^{0.63}\right]\right) \tag{2.16}$$

using the constants $N_{0,\text{eeh}} = 3.3 \times 10^{17}\,\text{cm}^{-3}$ and $N_{0,\text{ehh}} = 7.0 \times 10^{17}\,\text{cm}^{-3}$.

Equation (2.14) includes radiative recombination described by the parameters B_{rel} and B_{low}. The latter is the recombination coefficient describing the radiative recombination in low injection density and for lowly doped silicon, for which commonly the value $B_{\mathrm{low}} = 4.73 \times 10^{-15}\,\mathrm{cm^3\,s^{-1}}$ determined by Trupke *et al.* [35] is used. The former, B_{rel}, was introduced by Altermatt *et al.* to describe the Coulomb screening mentioned above [23]. As in c-Si, radiative recombination is low compared to Auger recombination, especially for highly doped or highly injected material, it is usually safe to assume $B_{\mathrm{rel}} = 1$ [34].

2.2.3 SRH Recombination

Intrinsic (radiative and Auger) recombination would be enough to describe the recombination in a perfect crystal. Real crystals however are not perfect and material defects are present. These defects can provide a defect/trap state (E_{t}) within the bandgap which carriers could utilize for indirect band-to-band interaction. If such a defect state can capture both an electron and a hole carrier recombination occurs usually without the emission of a photon, although this process would be possible as well, but with $E_\lambda < E_{\mathrm{g}}$ due to the two-step process [36]. Normally the energy is absorbed either by the crystal or another carrier. While the focus is usually on recombination, i.e. an electron is captured from the conduction band and emitted to the valence band while capturing a hole, re-mission to the same band is possible as well, which can be visible in dynamic measurements [37, 38].

Shockley, Read [39] and Hall [40] (SRH) found that the recombination at such defect states can be described using statistic methods. Hence the model is commonly call Shockley-Read-Hall (SRH) recombination. For a single, discrete defect state they determined the recombination rate

$$R_{\mathrm{SRH}} = \frac{(np - n_{\mathrm{i,eff}}^2)\nu_{\mathrm{th}} N_{\mathrm{t}}}{\sigma_{\mathrm{p}}^{-1}(n + n_1) + \sigma_{\mathrm{n}}^{-1}(p + p_1)} \tag{2.17}$$

with σ_{n} and σ_{p} the capture cross sections for electrons and holes, respectively, ν_{th} the average thermal velocity of the carriers and N_{t} the density of the defect states. The parameters n_1 and p_1 are defined as

$$n_1 = N_{\mathrm{c}} \exp\left(\frac{E_{\mathrm{t}} - E_{\mathrm{c}}}{k_{\mathrm{B}} T}\right) \tag{2.18}$$

$$p_1 = N_{\mathrm{v}} \exp\left(\frac{E_{\mathrm{v}} - E_{\mathrm{t}}}{k_{\mathrm{B}} T}\right) \tag{2.19}$$

with E_c and E_v the energy levels of the conduction and valence band, respectively. N_c and N_v denote the respective densities of states in the bands. This leads to the SRH lifetime

$$\tau_{SRH} = \tau_{p0} \frac{n_0 + n_1 + \Delta n}{n_0 + p_0 + \Delta n} + \tau_{n0} \frac{p_0 + p_1 + \Delta n}{n_0 + p_0 + \Delta n} \tag{2.20}$$

where the decay constants τ_{p0} and τ_{n0} are characteristic for the defect. These are defined as

$$\tau_{n0} = \frac{1}{\sigma_n \nu_{th} N_t} \tag{2.21}$$

$$\tau_{p0} = \frac{1}{\sigma_p \nu_{th} N_t} \tag{2.22}$$

From Equation (2.20), some observations can be made. The first is that τ_{SRH} is—via τ_{n0} and τ_{p0}—inverse proportional to the defect density. This means that more defects will lead to a reduction in the lifetime. The second observation is that doping will lead to one of n_1 and p_1 being negligible, in case of p-type silicon, this is n_1 as $N_v \gg N_c$. Therefore τ_{n0} is much more important than τ_{p0} as is the capture cross section for electrons. Thus, if the defect has a low capture cross section for electrons, the defect will reveal low recombination activity in p-type silicon. It might however, depending on σ_p, have a high recombination activity in n-type silicon.

2.2.4 Surface Recombination

In a real device, the crystal eventually has to end, thus exhibits a surface. At this surface neighbouring atoms are no longer available and thus atoms can exhibit either »dangling« bonds or impurity atoms are adsorbed. This can lead to a high density of defects with energy levels within the bandgap thus leading to recombination.

To describe the recombination at this surface, the SRH formalism was adapted. In earlier forms by Shockley [21], Fitzgerald and Grove [41, 42], as well as Gunn [43] and in it's commonly currently used form by Girisch *et al.* [44], which was extended by Aberle *et al.* [45]. The basic idea is to assume not a single defect state, but instead a continuum of defect states over the bandgap.

The recombination rate R_s is then achieved by integration over these states

$$R_s = (n_s p_s - n_{i,eff}^2) \cdot \int_{E_v}^{E_c} \frac{\nu_{th} \cdot D_{it}(E_t)}{\sigma_p^{-1}(E_t) \cdot [n_s + n_1(E_t)] + \sigma_n^{-1}(E_t) \cdot [p_s + p_1(E_t)]} dE_t. \tag{2.23}$$

with n_s and p_s the respective carrier densities at the surface.

Some authors (e.g. [46, 47]) use the definitions $S_n = D_{it} \cdot \sigma_n \cdot \nu_{th}$ and $S_p = D_{it} \cdot \sigma_p \cdot \nu_{th}$ to represent R_s. These parameters have the form of a velocity (usually given in cm/s), which highlights one of the features of the SRH formalism for surfaces: The recombination can be limited by the supply of carriers represented by the influence of the thermal velocity of the charge carriers ν_{th}, which—at 298 K—has a value of approx. 1×10^7 cm/s.

Thus, it is common to define the »surface recombination velocity«

$$S = \frac{R_s}{\Delta n} \tag{2.24}$$

which is a measure of the velocity at which carriers recombine. However, the surface passivation (or surface doping) may induce inhomogeneities in Δn close to the surface, e.g. due to band bending or fixed charges. Therefore one usually refers to Δn further within the bulk where Δn can be considered homogeneous. The depth at which Δn is taken is defined by the depth x_{scr} of the space charge region induced by the band bending/fixed charges. This leads to the definition of »effective« values, which refer to $\Delta n @ x_{scr}$ rather than to the surface Δn. Thus, the effective surface recombination velocity S_{eff} is

$$S_{eff} = \left. \frac{R_s}{\Delta n} \right|_{x_{scr}}. \tag{2.25}$$

Usually, S_{eff} cannot be measured directly, but instead the lifetime is measured. Due to the limit by ν_{th} as mentioned above, the maximum for S_{eff} is usually assumed to be $S_{eff} = \nu_{th} \approx 1 \times 10^7$ cm/s$@T = 298$ K.

Similarly to S and S_{eff}, if taking the effect of a surface (τ_{s}) into account, the effective minority carrier lifetime τ_{eff} is used instead of τ_{s}. The relation between τ_{s} and S_{eff} is given by

$$\frac{1}{\tau_{\text{s}}} = \alpha_0^2 D, \tag{2.26}$$

$$\tan(\alpha_0 W) = \frac{S_1 + S_2}{\alpha_0 D - \frac{S_1 S_2}{\alpha_0 D}} \tag{2.27}$$

where S_1 and S_2 denote the respective effective surface recombination velocities of the two wafer surfaces and α_0 is the smallest eigenvalue solution of the second equation [48]. Larger eigenvalues correspond to higher modes, but usually only the fundamental mode is considered. In this case, the effective lifetime is given by

$$\frac{1}{\tau_{\text{eff}}} = \frac{1}{\tau_{\text{b}}} + \frac{1}{\tau_{\text{s}}}. \tag{2.28}$$

Shockley [21] already gave an approximate expression for $\alpha_0^2 D$ resulting in

$$\frac{1}{\tau_{\text{eff}}} = \frac{1}{\tau_{\text{b}}} + \frac{1}{\tau_{\text{s}}} = \frac{1}{\tau_{\text{b}}} + \frac{2S_{\text{eff}}}{W}, \tag{2.29}$$

where W is the wafer thickness. Sproul [48] further analyzed the relation of τ_{eff} and S_{eff} showing that the above expression is valid for symmetrical samples with an accuracy of 4 %, if $S_{\text{eff}} W/D < 0.25$. In case of a wafer thickness of 200 µm and a base resistivity of 1 Ω cm, this would mean that $S_{\text{eff}} < 140$ cm/s. This is the expression, that is most widely used in the photovoltaic research community as these requirements are normally well fulfilled when investigating passivation performance.

It should be noted, that in section 7.2, samples will be analyzed for which this limit will be exceeded (SiN *PassDop* before annealing). Sproul gave a approximation for τ_{s} in such a case

$$\tau_{\text{s}} = \frac{W}{2S_{\text{eff}}} + \frac{1}{D}\left(\frac{W}{\pi}\right)^2, \tag{2.30}$$

which holds over the complete range of S_{eff} with an accuracy of 5 %. A comparison of the two terms showed that Equation (2.29) without the additional term will lead to an under-estimated S_{eff}. This will lead to a systematic error in S_{met} (see the next sections) of approx. 10 %. However, as S_{met} in those

cases is too high anyway (in the range of 4000 to 5000 cm/s, accuracy was not of importance and thus the higher error in favor of a simpler evaluation was preferred. While the above is valid for a symmetrical sample structure, it is not valid if the sample structure is asymmetric, like it was used in Section 7.2. Here, we have the situation of $S_1 \lesssim 5\,\mathrm{cm/s}$ while S_2 can be in the range of 5 to 300 cm/s. Sproul did calculate an approximate solution for the case where S_1 is close to zero and while this would be a good assumption if S_2 reached its maximum, it would be wrong in case of a lower S_2. Instead, calculations using Equation (2.27) showed that

$$\frac{1}{\tau_\mathrm{s}} = \frac{S_1 + S_2}{W} \tag{2.31}$$

can be used, but with an increased systematic error in case of $S_1 \ll S_2$. This expression was already used by Rauer as well [49, 50]. For $S_1 = S_2$, it is identical to the previous approximation in Equation (2.29) and therefore the same limits apply. If $S_1 \neq S_2$ the error will increase with increasing difference of the two and therefore it has to be considered, that a lower L_p will lead to a larger systematic error in the determined S_eff. For the most extreme situation in Section 7.2, with $S_1 \approx 5\,\mathrm{cm/s}$ and $S_2 \approx 300\,\mathrm{cm/s}$ the error was in the range of 9 %, which is acceptable. Similar to the argument above, for these specific samples, the S_met was too high anyway (thus the high S_eff) and therefore the precise knowledge of S_eff was not as important. Thus for these samples, Equation (2.31) was used despite the larger error.

2.2.5 Fischer Model for S_met

For the evaluation of a localized contact structure, the recombination is a key element in the characterization procedure. Some attempts were made to describe the recombination at such inhomogeneous structures, i.e. by Sterk, based on device simulations [51].
While the most recent description for such a model was provided by Saint-Cast et al. *[52], it was the model of Fischer which was adopted in the photovoltaic research community, e.g. in [53–55]. Thus it was used within this work for comparisons and therefore is described here, based on [56]. For a more detailed description, the reader is referred to the cited work. This evaluation assumes, that the device is in the dark.*

As the description of a localized structure will depend strongly on the distance of the contacts, the spreading resistance will be a key parameter as this

describes the carrier transport for such a situation. The spreading resistance R_{spr} for point contacts as determined empirically by Cox and Strack [57] was used in this work:

$$\sigma R_{spr} = \frac{1}{2\pi r_{cont}} \arctan\left(\frac{2W}{r_{cont}}\right) \tag{2.32}$$

Here σ describes the conductivity of the wafer, W the wafer thickness and r_{cont} the contact radius.

For the definition of the series resistance R_S, two limits are interesting

$$R_S = R_{spr} L_p^2 \qquad \text{for } L_p \gg W \tag{2.33}$$

$$R_S = \rho_b W \qquad \text{for } L_p \ll W \tag{2.34}$$

where L_p is the distance between two contacts (»pitch«) and ρ_b the wafer resistivity.
In the first case $L_p \gg W$ each contact can be viewed individually as interaction of the contact is negligible and thus R_S is mainly defined by the area the contact occupies. In the second case, the current flow will be almost parallel and thus R_S is limited by the series resistance of the wafer. While the sum of the two components already is a good approximation, Fischer introduced a correction term $-\rho_b W \exp(-W/L_p)$ to prevent a larger error for large L_p. This leads to the series resistance R_S

$$\sigma R_S = \sigma R_{spr} L_p^2 + W\left[1 - \exp\left(-W/L_p\right)\right] \tag{2.35}$$

with the conductivity $\sigma = 1/\rho_b$. According to Fischer, this expression for R_S holds over a wide range of metallization fractions as well as L_p (in comparison to W).

R_S can be used to calculate the diffusion resistance and thus the current flows from and to the contacts. This results in an expression for S_{cont}

$$S_{cont}^{-1} = \sigma R_S D - \frac{W}{D} + \frac{1}{f_{met} S_{met}} \tag{2.36}$$

with S_{met} the surface recombination velocity at the metallized surface and f_{met} the metallization fraction. For a detailed derivation of this relation, see [56]. Equation (2.36) holds true both for point contacts as well as line contacts as no assumptions concerning the contact geometry had to be made.

Using this equation, the effective surface recombination velocity S_{eff} for the complete surface including the passivated area (S_{pass}) can be described as

$$S_{\mathrm{eff}} = S_{\mathrm{cont}} + \frac{S_{\mathrm{pass}}}{1 - f_{\mathrm{met}}} \tag{2.37}$$

which holds true for small metallization fractions. Using Equation (2.36) this yields for S_{eff}:

$$S_{\mathrm{eff}} = \frac{1}{\sigma R_{\mathrm{S}} D - \frac{W}{D} + \frac{1}{f_{\mathrm{met}} S_{\mathrm{met}}}} + \frac{S_{\mathrm{pass}}}{1 - f_{\mathrm{met}}} \tag{2.38}$$

By resolving this equation to S_{met} and by using Equation (2.35) and (2.32) an expression for S_{met} can be achieved for round point contacts:

$$S_{\mathrm{met}} = \frac{D}{W f_{\mathrm{met}} \left[\frac{1}{\frac{W}{D}\left(S_{\mathrm{eff}} - \frac{S_{\mathrm{pass}}}{1 - f_{\mathrm{met}}}\right)} - \frac{L_{\mathrm{p}}}{2W\sqrt{\pi f_{\mathrm{met}}}} \arctan\left(\frac{2W}{L_{\mathrm{p}}}\sqrt{\frac{\pi}{f_{\mathrm{met}}}}\right) + \exp\left(-\frac{W}{L_{\mathrm{p}}}\right) \right]} \tag{2.39}$$

Thus S_{met} mainly depends on L_{p} and r_{cont} and can be calculated if these parameters as well as W, ρ_{b} (und therefore D), S_{eff} and S_{pass} are known. Alternatively, a fit of S_{eff} in dependence of L_{p} can be performed as shown in Figure 7.17a on page 173 for SiN *PassDop* Gen1. It should be emphasized, that this evaluation is only possible for low metallization fractions and that the influence of r_{cont} on S_{met} is relatively high. As in many cases r_{cont} cannot be measured reliably (e.g. due to process fluctuations within the wafer or elliptic spots), this means that S_{met} in many cases can only be determined with a high uncertainty.

2.2.6 pLPA Model for S_{met}

If one wants to use the model for S_{eff} of a locally structured surface as proposed by Fischer [56] (»Fischer model«) described in the previous section, the knowledge of the contact boundaries (e.g. r_{cont}) becomes a requirement, thus assuming a homogeneously varying surface. However, e.g. due to fluctuation in the laser power, the contact size might vary over the surface. This can be problematic, since in the Fischer model, a small variation in r_{cont} can lead to a large variation in the required S_{met} to describe S_{eff}.
The goal of the new model by Saint-Cast et al. *was therefore to define a set of parameters describing the recombination of the Locally Processed Area (LPA) but without a dependence on the contact boundaries or at least with a dependence that is reasonably low [58].*
The description of the model outlined here is closely bound to the work presented by Saint-Cast et al. *[58]. For n-type silicon, the description in the referenced article is incomplete and for lines, corrections were necessary. Thus—with the help of Saint-Cast [59]—an extended version is presented and the analysis for a selection of n-type samples is shown exemplarily.*
The term LPA is used extensively in this section and always refers to a local recombination inhomogeneity in an otherwise well passivated silicon surface, thus $S_{met} \gg S_{pass}$.

The pLPA Model

The central parameter used by the model is the point or line recombination of the LPA: p_{LPA}, which is defined by the surface integral

$$p_{\text{LPA}} n_{\text{LPA}} = \int_{\text{LPA}} S(x, y) \Delta n(x, y) \, ds \tag{2.40}$$

with n_{LPA} being the average excess carrier density on the LPA, $\Delta n(x, y)$ the local excess carrier density and $S(x, y)$ the local surface recombination velocity. Instead of evaluating Δn and S locally, a macroscopic view on the problem is established to be able to determine p_{LPA} by non-localized methods like Quasi-Steady-State Photoconductance (QSSPC). If the surface contains many LPA, then the recombination current density on the LPA is

$$j_{\text{LPA}} = q N_{\text{LPA}} p_{\text{LPA}} n_{\text{LPA}} \tag{2.41}$$

where N_{LPA} is the LPA surface density. As usually $S_{\mathrm{met}} \gg S_{\mathrm{pass}}$, the carrier density at the LPA will be lower than at the passivated area:

$$n_{\mathrm{pass}} > n_{\mathrm{eff}} > n_{\mathrm{LPA}}. \tag{2.42}$$

n_{pass} and n_{eff} are the average carrier densities at the passivated surface and the effective value for the complete surface, respectively. In addition, due to the higher S_{met}, the area fraction f_{met} is usually kept low, thus:

$$f_{\mathrm{met}} = \frac{A_{\mathrm{LPA}}}{A_{\mathrm{pass}}} \ll 1. \tag{2.43}$$

The definition of the effective surface recombination velocity S_{eff} by Saint-Cast *et al.* relates the effective recombination current density to S_{eff} [52]:

$$j_{\mathrm{eff}} = qS_{\mathrm{eff}}\left[n_{\mathrm{pass}}(1 - f_{\mathrm{met}}) + n_{\mathrm{LPA}} f_{\mathrm{met}}\right] \tag{2.44}$$

Using equation (2.43) and relation (2.42):

$$j_{\mathrm{eff}} \approx qS_{\mathrm{eff}} n_{\mathrm{pass}} \tag{2.45}$$

The definition of j_{pass} [52] is:

$$j_{\mathrm{pass}} = qS_{\mathrm{pass}} n_{\mathrm{pass}} \tag{2.46}$$

j_{eff} is also the sum of the respective contributions j_{pass} and j_{LPA}:

$$j_{\mathrm{eff}} = (1 - f_{\mathrm{met}}) j_{\mathrm{pass}} + j_{\mathrm{LPA}} \tag{2.47}$$

Using the definitions of j_{pass} and j_{LPA} (Equation (2.41)):

$$j_{\mathrm{eff}} = q(1 - f_{\mathrm{met}}) S_{\mathrm{pass}} n_{\mathrm{pass}} + qN_{\mathrm{LPA}} p_{\mathrm{LPA}} n_{\mathrm{LPA}} \tag{2.48}$$

$$\approx qS_{\mathrm{pass}} n_{\mathrm{pass}} + qN_{\mathrm{LPA}} p_{\mathrm{LPA}} n_{\mathrm{LPA}} \tag{2.49}$$

Combining Equation (2.47) and (2.49) results in a relation of S_{eff} to p_{LPA}:

$$S_{\mathrm{eff}} \approx N_{\mathrm{LPA}} p_{\mathrm{LPA}} \frac{n_{\mathrm{LPA}}}{n_{\mathrm{pass}}} + S_{\mathrm{pass}} \tag{2.50}$$

This seems already close to the desired result, but for an evaluation, the relation of the average excess carrier densities n_{LPA} and n_{pass} is required. Since j_{eff} represents a recombination current density that does not directly correspond to local inhomogeneities, a fraction of the LPA recombination current will have to be transferred onto the passivated surface for the non-local

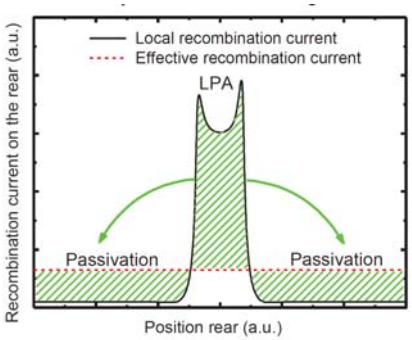

Figure 2.1: Schematic of the recombination current profiles showing the actual recombination currents (j_{pass} and j_{LPA}) as well as the effective j_{eff}. Taken from [58].

representation as illustrated in Figure 2.1. This transfer of excess carriers is specified by diffusion properties and thus given by the diffusion resistance R_{diff}

$$\begin{aligned} n_{\text{pass}} - n_{\text{LPA}} &= R_{\text{diff}} \left[j_{\text{eff}}(1 - f_{\text{met}}) - j_{\text{pass}}(1 - f_{\text{met}}) \right] \\ &\approx q R_{\text{diff}} \left(S_{\text{eff}} - S_{\text{pass}} \right) n_{\text{pass}}, \end{aligned} \tag{2.51}$$

considering, that $f_{\text{met}} \ll 1$ and using the Equations (2.45) and (2.46). This leads to an approximation of the relation of the average excess carrier densities

$$\frac{n_{\text{LPA}}}{n_{\text{pass}}} \approx 1 - q R_{\text{diff}} \left(S_{\text{eff}} - S_{\text{pass}} \right) \tag{2.52}$$

and therefore to (using Equation (2.50))

$$S_{\text{eff}} = \frac{N_{\text{LPA}} p_{\text{LPA}}}{1 + q R_{\text{diff}} N_{\text{LPA}} p_{\text{LPA}}} + S_{\text{pass}} \tag{2.53}$$

This means, that the difference $S_{\text{eff}} - S_{\text{pass}}$ depends on the LPA recombination p_{LPA}, the LPA density N_{LPA} and the diffusion resistance R_{diff}. While N_{LPA} is easy to determine (usually by measuring the distance between two LPA), calculating the diffusion resistance R_{diff} is more difficult.

Influence of the Diffusion Resistance

Saint-Cast performed some calculations for R_{diff}, which will not be repeated here [59]. If assuming either a surface opposing the LPA with a perfect emitter (negligible R_{Sheet}) or no junction, with a homogeneous carrier density, as well as a homogeneous recombination current density on the LPA

and on the passivated area, R_{diff} can be calculated in approximation. The result is shown in Figure 2.2. In the graphical representation, the normalized diffusion resistance r_{diff} is used. This is defined as

$$\text{For Points: } r_{\mathrm{diff}} = qR_{\mathrm{diff}}N_{\mathrm{LPA}}r_{\mathrm{cont}} \tag{2.54}$$

$$\text{For Lines: } r_{\mathrm{diff}} = qR_{\mathrm{diff}}N_{\mathrm{LPA}} \tag{2.55}$$

where the second equation was missing from [58]. As Fig. 2.2 shows, $r_{\mathrm{diff}} \times D$

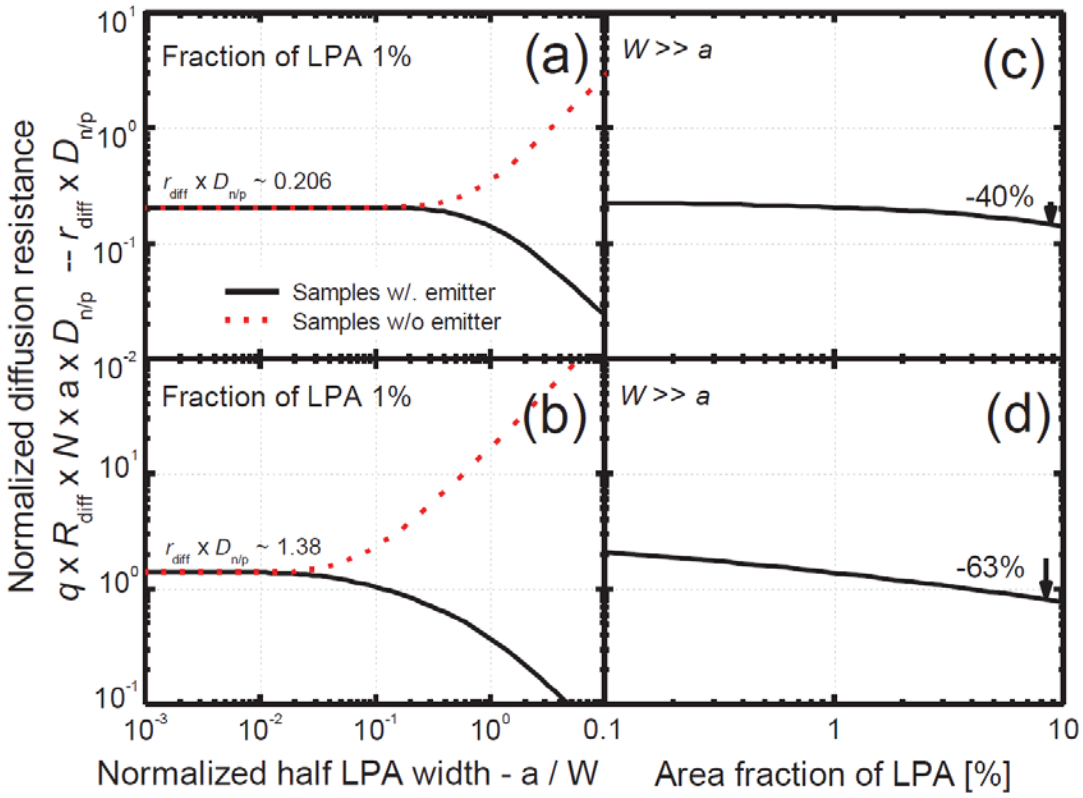

Figure 2.2: Normalized diffusion resistance as a function of the normalized contact width for point (a) and line (b) contacts. Normalized diffusion resistance as a function of the LPA fraction for point (c) and line (d) contacts, if $W \gg r_{\mathrm{cont}}$. r_{cont} in the graph is denoted as a. For line contacts, the description on the ordinate is wrong and the definition as of Equation (2.55) should be considered. The figure was taken from [58].

(D being the diffusivity) tends towards a constant value if $W \gg r_{\mathrm{cont}}$. This is the case for both point as well as line contacts. Given a common contact geometry of $r_{\mathrm{cont}} = 25\,\mu\mathrm{m}$ for point contacts, r_{diff} can therefore be assumed constant, as long as $W > 120\,\mu\mathrm{m}$, which is the case for all wafers used throughout this work. For line contacts, r_{diff} is more critical. For a typical half width of $r_{\mathrm{cont}} = 15\,\mu\mathrm{m}$, a wafer thickness of $W > 700\,\mu\mathrm{m}$ would be required

to reach the range of a constant r_{diff}. For a more realistic wafer thickness of $W = 200\,\mu\mathrm{m}$, the influence of r_{cont} on r_{diff} becomes significant.

The right half of the graph shows the dependency of r_{diff} on the LPA area fraction. While the dependency is only slight, it can still be significant, if a high area fraction is used. Thus, if an area fraction in the range of 5 to 10 % and assuming a constant r_{diff}, one has to consider, that r_{diff} will be overestimated. This is especially the case for line contacts, where an area fraction of 2 % or above is common.

Effective Point Recombination

If the influence of N_{LPA} is low, r_{diff} can be considered constant. Thus in Equation (2.53)

$$\text{For Points: } S_{\mathrm{eff}} = \frac{N_{\mathrm{LPA}} p_{\mathrm{LPA}}}{1 + \frac{r_{\mathrm{diff}}}{r_{\mathrm{cont}}} p_{\mathrm{LPA}}} + S_{\mathrm{pass}} \tag{2.56}$$

$$\text{For Lines: } S_{\mathrm{eff}} = \frac{N_{\mathrm{LPA}} p_{\mathrm{LPA}}}{1 + r_{\mathrm{diff}} p_{\mathrm{LPA}}} + S_{\mathrm{pass}} \tag{2.57}$$

the denominator will only weakly depend on the LPA density and an evaluation in the form of

$$S_{\mathrm{eff}} = p_{\mathrm{eff}} N_{\mathrm{LPA}} + S_{\mathrm{pass}} \tag{2.58}$$

can be made with p_{eff} assumed constant for a given LPA. p_{eff} is called the effective point recombination and describes the recombination of the surface including both the passivated area and the LPA independent from the LPA density. Thus, it can be used to perform an evaluation and comparison of different LPA without the knowledge of r_{cont} but just using a linear regression as will be shown exemplarily for SiN *PassDop* Gen1 in Section 7.2 (see Figure 7.17b on page 174). Although the range of area fractions used here (Minimum: 0.6 %, Maximum: 10.8 %) is quite large and a decrease in r_{diff} of approx. 30 % would be expected, the linear regression still can be used to estimate p_{eff} and variations in the *PassDop* performance for the respective area fractions are much larger than the systematic error made by overestimating r_{diff} for a high N_{LPA}.

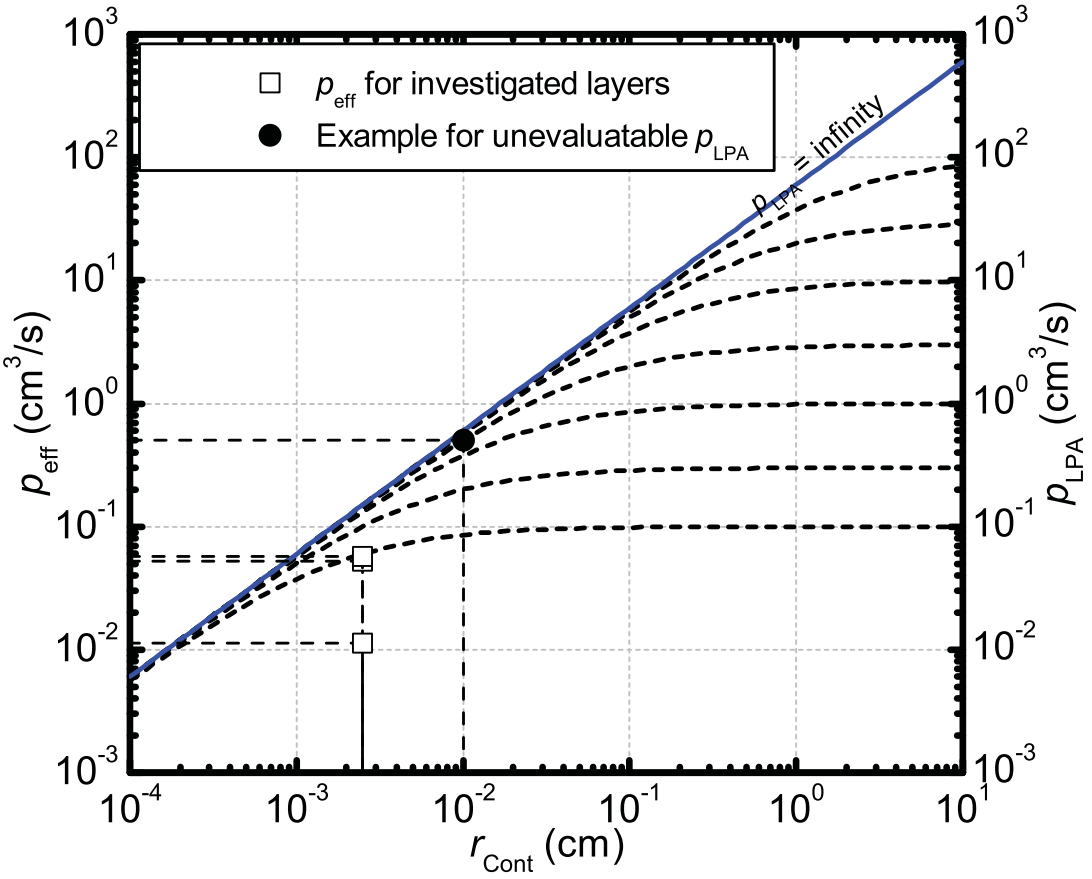

Figure 2.3: p_{eff} and p_{LPA} in relation to r_{cont} for point contacts as of Equation (2.59) on 1 Ω cm *n*-type c-Si. The solid blue asymptote indicates infinite p_{LPA}. To properly evaluate p_{LPA}, the determined values should be well below this asymptote. The open squares show the values that were determined for the *PassDop* layers (see Section 7.2). In addition an exemplary point for an unevaluable p_{LPA} was included as well. This graphic is based on [58], where an equivalent for *p*-type material is shown.

A comparison of Equation (2.53) and (2.58) yields a relation between p_{eff} and p_{LPA}:

$$\text{For Points: } \frac{1}{p_{eff}} = \frac{1}{p_{LPA}} + \frac{r_{diff}}{r_{cont}} \tag{2.59}$$

$$\text{For Lines: } \frac{1}{p_{eff}} = \frac{1}{p_{LPA}} + r_{diff} \tag{2.60}$$

However, before just calculating p_{LPA}, one should consider the case where p_{LPA} is very high, thus $p_{\mathrm{LPA}}^{-1} \ll r_{\mathrm{diff}}/r_{\mathrm{cont}}$ (for point contacts). This means that

$$\text{For Points: } \frac{1}{p_{\mathrm{eff}}} \approx \frac{r_{\mathrm{diff}}}{r_{\mathrm{cont}}} \tag{2.61}$$

$$\text{For Lines: } \frac{1}{p_{\mathrm{eff}}} \approx r_{\mathrm{diff}} \tag{2.62}$$

and therefore a precise evaluation of p_{LPA} is not possible and the errors in determining r_{cont} and r_{diff} will dominate. What this means is that the balancing of the recombination currents is limited by diffusion and therefore a variation in p_{LPA} does not result in a significant change in p_{eff} anymore. The effect is illustrated in Figure 2.3 for point contacts on n-type 1 Ω cm material. The point marking the respective r_{cont} and p_{eff} should be well below the asymptote that represents the case of $p_{\mathrm{LPA}} \to \infty$. This also leads to the observation that the lower the p_{LPA}, the better the evaluation will work and the lower the (relative) error will be, as the errors of r_{cont} and r_{diff} will have a smaller influence on the result. In addition, the calculation of S_{eff} will be more precise as was shown in Section 2.2.4, which further decreases the systematic errors during the evaluation.

Calculation of S_{met}

While p_{eff} and p_{LPA} offer good service for comparing different processes, they are not much use for simulations, at least with the usual implementations. For that an S_{met} or a $J_{0\mathrm{b,met}}$ is required. The former can be calculated from p_{LPA} by

$$S_{\mathrm{met}} = \frac{p_{\mathrm{LPA}}}{A_{\mathrm{LPA}}} \tag{2.63}$$

where A_{LPA} is the area of the LPA, or in case of lines, the width. It's important to note here, that A_{LPA} does not necessarily have to match the geometry of the LPA (but in most cases it should), but rather the geometry defined in the simulation. The S_{met} defined here then corresponds to an S_{met} that has to be assumed for the given geometry in the simulation to match the experimentally determined p_{LPA}.

Error Calculation

For each parameter there are a set of parameters that have been identified to have the strongest influence on the result. The calculation here was only performed for point contacts.

- p_{eff}: Deviation of processes
- p_{LPA}: r_{diff} and r_{cont}
- S_{met}: r_{cont}, (weakly: r_{diff})

p_{eff}

In case of p_{eff}, the uncertainty from the linear regression was used.

p_{LPA}

For the propagation of uncertainties the partial derivate method was used. This yields the following relation

$$sp_{\mathrm{LPA}} = \sqrt{\frac{r_{\mathrm{cont}}^4 sp_{\mathrm{eff}}^4 + p_{\mathrm{eff}}^4 r_{\mathrm{diff}}^2 sr_{\mathrm{cont}}^2 + p_{\mathrm{eff}}^4 r_{\mathrm{cont}}^2 sr_{\mathrm{diff}}^2}{\left(r_{\mathrm{cont}} - p_{\mathrm{eff}} r_{\mathrm{diff}}\right)^4}} \tag{2.64}$$

for the uncertainty sp_{LPA} of p_{LPA}, with sr_{cont}, sr_{diff} and sp_{eff} being the uncertainties of the respective parameters.

It should be noted, that while during the evaluation of p_{eff} a systematic error for r_{diff} was made—which could be interpreted as a larger uncertainty sr_{diff}—this would only influence sp_{eff} and not sr_{diff} in this calculation. The reason for this is that the calculation of p_{LPA} will be performed with a certain N_{LPA} density in mind, as used in the solar cell. Within this range, r_{diff} is well known, although the calculation of p_{LPA} (and hence sp_{LPA}) might have to be redone if a different LPA density is selected.

S_{met}

Similar to p_{LPA}, the partial derivate method was used for S_{met} as well. Thus

$$sS_{\mathrm{met}} = \frac{\sqrt{\frac{r_{\mathrm{cont}}^2 sp_{\mathrm{LPA}}^2 + 4p_{\mathrm{LPA}}^2 sr_{\mathrm{cont}}^2}{r_{\mathrm{cont}}^6}}}{\pi} \tag{2.65}$$

describes the uncertainty of S_{met} for circular point contacts.

Due to the additional quadratic influence of r_{cont} in Equation (2.63), the influence of the uncertainty of r_{cont} on S_{met} is quite high. Assuming a relative uncertainty of 10 %, commonly a relative uncertainty of 35 % was calculated for S_{met}. This again emphasizes the value of p_{eff} and p_{LPA}, for which the influence of r_{cont} (and its uncertainty) is much lower.

It should however be noted that the above calculated sS_{met} is only relevant if comparing different methods or processes, thus if a comparable value is required. In case of a device simulation, the area is well defined (thus $sr_{\mathrm{cont}}/r_{\mathrm{cont}} = 0$) and the relative uncertainty of S_{met} is the same as that of p_{LPA}. Thus the input value for the device simulation can be determined at significantly better precision.

2.3 Recombination Factor J_0

The definition of J_0 was originally derived from the 1-diode equation (see Section 3.1).

$$J(V) = J_0 \left[\exp\left(\frac{qV}{k_{\mathrm{B}}T} \right) - 1 \right] - J_{\mathrm{sc}} \tag{2.66}$$

Shockley called it »saturation reverse current density« [21]. Under reverse bias at the diode (*pn*-junction), one would not expect any current to flow, due to the formation of a depletion region. There will however be a small current consisting of carriers (electrons in the *p*- and holes in the *n*-type zone) that are generated within a diffusion length of the *pn*-junction which can cross the junction. Thus, for J_0 it can be found that

$$J_0 = qG_0(L_{\mathrm{n}} + L_{\mathrm{p}}), \tag{2.67}$$

with L_{n} and L_{p} the diffusion lengths of the minority carriers in the respective zones [60]. As $G_0 = R_0$ at thermal equilibrium (no external generation of carriers), J_0 can therefore be viewed both as a recombination as well as a generation current, depending on the interpretation (»saturation« due to being limited by thermal generation). For c-Si, J_0 will usually be below 1 pA/cm^2 and therefore it cannot be directly measured although theoretically, this would be possible. And even if one would be able to measure it, the precision of the measurement would likely not be good enough, as for a good solar cell the target is rather $J_0 < 100\,\mathrm{fA/cm^2}$. Instead other methods are being used to determine J_0, e.g. from lifetime measurements, as was shown in the previous section. Therefore Cuevas proposed the name »recombination factor« for J_0 to underline its role in the characterization of solar cells [61].

It should be noted that J_0 is considered constant and independent of V. This however is only true if the device strictly follows the relationship outlined in Equation (2.66), thus behaves like an »ideal« diode. In some cases this does

not hold, many of which have been discussed e.g. by Glunz [62] and McIntosh [63]. Instead of making J_0 injection-dependent (thus dependent on Δn and hence V) an ideality factor n is introduced, which for an ideal diode would be $n = 1$. Depending on the dominant recombination mechanisms of the solar cell, the ideality can range from 2/3 (Auger-limited) to 2 (SRH-limited) [20]. The second method to account for injection-dependent effects is commonly the introduction of a second diode. This method is not described here, the reader is referred to the literature, e.g. [20].

Since minority carriers can be generated in either of the doped regions, J_0 can be split into two components

$$J_0 = J_{0e} + J_{0b}, \tag{2.68}$$

where J_{0e} and J_{0b} refer to the respective contributions of the emitter and the base. These components and their sub-components will be discussed in the next sections.

2.3.1 Emitter Recombination Factor J_{0e}

Usually, the emitter recombination factor J_{0e} is determined using the method of Kane and Swanson [64]. This method assumes that the emitter is in low-injection (due to the high doping, this is usually the case) and the base is high-injected ($\Delta n \geq 10 \cdot N_D$). In addition, it is assumed, that Δn is homogeneously distributed. Then J_{0e} can be determined from S_{eff} by

$$J_{0e} = S_{eff} \frac{q n_{i,eff}^2}{N_D + \Delta n}. \tag{2.69}$$

Reichel *et al.* showed that Equation (2.69) can be used in low-injection of the base as well [65]. In this case however, the base recombination (see Equation (2.29)) must be well known, e.g. by the use of Floatzone (FZ) material with well known wafer thickness and base doping.

If the metallization fraction f_{met} is low enough ($f_{met} \ll 1$), J_0 can be further splitted into area-weighted components for the passivated ($J_{0e,pass}$) and the metallized ($J_{0e,met}$) fractions of the emitter

$$J_{0e} = J_{0e,pass} \cdot (1 - f_{met}) + J_{0e,met} \cdot f_{met}. \tag{2.70}$$

2.3.2 Base Recombination Factor J_{0b}

For the base recombination factor J_{0b}, McKelvey derived an expression, assuming a low-injected base [66]

$$J_{0b} = \frac{qn_{i,eff}^2 D}{N_D L}\left[\frac{\frac{S_{eff}L}{D} + \tanh\frac{W}{L}}{1 + \frac{S_{eff}L}{D}\tanh\frac{W}{L}}\right]. \tag{2.71}$$

Here, D is the diffusity and L the diffusion length of the minority carriers in the base. W is the base thickness. This expression was further analyzed by Godlewski who derived some expressions for special cases [67].

Similar to J_{0e}, J_{0b} can be split into components.

$$J_{0b} = J_{0b}\big|_{S_{eff}=0} + J_{0s}, \tag{2.72}$$

where J_{0s} parameterizes the recombination due to the surface solely and $J_{0b}\big|_{S_{eff}=0}$ is the recombination in the base excluding the surface

$$J_{0b}\big|_{S_{eff}=0} = \frac{qn_{i,eff}^2 D}{N_D L}\left[\frac{\frac{0\cdot L}{D} + \tanh\frac{W}{L}}{1 + \frac{0\cdot L}{D}\tanh\frac{W}{L}}\right] = \frac{qn_{i,eff}^2 D}{N_D L}\tanh\frac{W}{L}. \tag{2.73}$$

This however only makes sense if $L \gg W$, which is usually a safe assumption if defect recombination in the base is low, as common wafer thicknesses are below 500 µm.

J_{0s} can be calculated from Equation (2.71)

$$J_{0s} = J_{0b} - J_{0b}\big|_{S_{eff}=0} \tag{2.74}$$

$$= \frac{qn_{i,eff}^2 D}{N_D L}\left[\frac{\frac{S_{eff}L}{D} + \tanh\frac{W}{L}}{1 + \frac{S_{eff}L}{D}\tanh\frac{W}{L}}\right] - \frac{qn_{i,eff}^2 D}{N_D L}\tanh\frac{W}{L}. \tag{2.75}$$

Since $L \gg W$

$$\frac{L}{D}\tanh\frac{W}{L} < 0.002, \qquad \text{for } n\text{-type c-Si} \tag{2.76}$$

$$\frac{L}{D}\tanh\frac{W}{L} < 0.0007, \qquad \text{for } p\text{-type c-Si} \tag{2.77}$$

and therefore for a reasonably low S_{eff} (e.g. <50 cm/s, depending on the required precision)

$$J_{0s} \approx S_{\text{eff}} \frac{q n_{\text{i,eff}}^2}{N_{\text{D}}}, \tag{2.78}$$

which does look familiar, as it is the same as Equation (2.69) (Kane & Swanson) if assuming low-injection ($\Delta n \ll N_{\text{D}}$), which is a good approximation. e.g. for n-type silicon, the error is below 3 % if $S_{\text{eff}} < 10$ cm/s on 1 to 100 Ω cm.

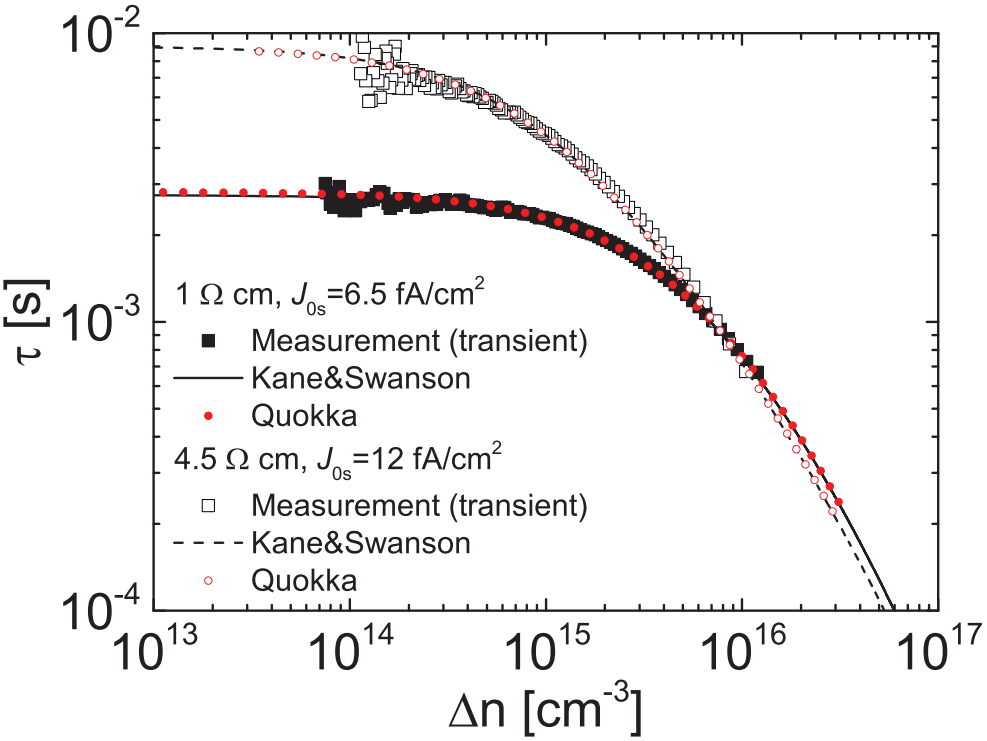

Figure 2.4: Transient QSSPC measurements for 1 and 4.5 Ω cm material passivated by SiN *PassDop* Gen1 in comparison to the predicted lifetime based on Equation (2.14) and (2.79) as well as simulations using Quokka for the same J_0.

In fact the relationship between J_{0s} for undiffused surfaces and Equation (2.69) goes even further. If the surface passivation contains fixed charges, an *accumulation* or *inversion* layer due to band bending will be the result and therefore a similar situation to that of a surface diffusion. Thus similar assumptions can be made and the same as Equation (2.69) would be the result for J_{0s}

$$J_{0s} = S_{\text{eff}} \frac{q n_{\text{i,eff}}^2}{N_{\text{D}} + \Delta n}, \tag{2.79}$$

which was used to determine J_{0s} throughout this thesis, although commonly in low-injection (at $\Delta n = 0.1 \cdot N_D$). Figure 2.4 shows the comparison of this model for J_{0s} fitted to the lifetime measurement of SiN *PassDop* Gen1 on 1 and 4.5 Ω cm. In addition, the graphs show the injection-dependent lifetime results determined by Quokka using exactly the same values for J_{0s}. As can be seen from the graph, all of the three are in good agreement. The remaining differences can be attributed to an imperfect injection-dependency of the surface passivation as well an uncertainty in the base doping of the substrate.

Thus it can be concluded, that Equation (2.79) can be used throughout the investigated injection range despite the lack of a surface diffusion. However, if the injection-dependency of the surface passivation gets too strong, a more complex model might be required, e.g. [32].

2.3.3 J_0 for PERL cells

For a Passivated Emitter and Rear Locally Diffused (PERL) cell, the rear side is not fully passivated, but instead locally removed or damaged, to allow for a localized contact formation. Thus both S_{eff} and $J_{0\mathrm{s}}$ will not be homogeneously distributed. If the metal fraction f_{met} is low, $J_{0\mathrm{s}}$ can be splitted into the area-weighted contributions [51]

$$J_{0\mathrm{s}} = J_{0\mathrm{b,pass}} \cdot (1 - f_{\mathrm{met}}) + J_{0\mathrm{b,met}} \cdot f_{\mathrm{met}}, \tag{2.80}$$

where $J_{0\mathrm{b,pass}}$ and $J_{0\mathrm{b,met}}$ are the J_0 contributions for the passivated and metallized areas, respectively. While $J_{0\mathrm{b,pass}}$ should be determined using Equation (2.79) on unmetallized structures, $J_{0\mathrm{b,met}}$ can be calculated from S_{met} using Equation (2.69)

$$J_{0\mathrm{b,met}} = S_{\mathrm{met}} q \frac{n_{\mathrm{i,eff}}^2}{N_{\mathrm{D}} + \Delta n}, \tag{2.81}$$

as the assumptions made by Kane and Swanson can be applied both to *pn*- as well as to high-low-junctions.

In case the metal fraction f_{met} is high, splitting $J_{0\mathrm{s}}$ as given does not make sense and instead an S_{eff} for the complete surface should be determined [51]. Due to the commonly high recombination at the metal contacts, this is normally not the case as the metal fraction is reduced to an acceptable minimum.

Therefore, for a PERL cell, the total J_0 can be written as

$$J_0 = J_{0\mathrm{e,pass}} \cdot (1 - f_{\mathrm{met,FS}}) + J_{0\mathrm{e,met}} \cdot f_{\mathrm{met,FS}} + J_{0\mathrm{b}}\big|_{S_{\mathrm{eff}}=0} \tag{2.82}$$

$$+ J_{0\mathrm{b,pass}} \cdot (1 - f_{\mathrm{met,RS}}) + J_{0\mathrm{b,met}} \cdot f_{\mathrm{met,RS}} \tag{2.83}$$

2.4 Lifetime Measurement by Quasi-Steady-State Photoconductance

There are many measurement techniques to determine the minority carrier lifetime, e.g. QSSPC [68] or modulated Photoluminescence (modPL) [69]. Within this work, only QSSPC was used. The original method was proposed by Sinton and Cuevas [68] and extended to its currently used form by Nagel *et al.* [70]. As the method has been described in detail in the referenced papers, only a brief introduction to the method will be given.

The main feature of the QSSPC setup (in this case a Sinton WCT-120 lifetime tester) is a calibrated coil within the measurement chuck on which the sample is placed. This coil is used to determine the conductivity of the wafer. A flash lamp is placed above the wafer to generate a light impulse. The intensity and flash decay can be tracked by a calibrated reference cell next to which the sample is placed.

2.4.1 Measurement of the Effective Lifetime

If a light impulse is ignited excess carriers within the wafer will be generated at a generation rate $\Delta G(t)$ as long as light is available. This will lead to an excess carrier density $\Delta n(t)$ leading to an excess conductivity $\Delta\sigma(t)$, which can be detected by the coil.

Assuming uniform generation of carriers the effective lifetime can be extracted by

$$\tau_{\text{eff}}(\Delta n) = \frac{\Delta n(t)}{\Delta G(t) - \frac{\partial \Delta n(t)}{\partial t}}. \tag{2.84}$$

The uniformity of the generation is achieved by placing a long pass filter between the flash lamp and the sample. $\Delta G(t)$ is tracked by the reference cell.

From Equation (2.84), two special cases can be extracted. The first is if the decay in generation is low, so that $\partial \Delta n(t)/\partial t \approx 0$. This case is called »quasi-static« (hence the name of the tool). The second is if only lifetime data is evaluated when there is no (or insignificant) generation (anymore), thus $\Delta G(t) \approx 0$. This is called »transient« evaluation or »photo conductance decay«. If the measurement is performed assuming neither of these special cases, the »generalized« method is being used.

The advantage of the transient method is that the generation rate is not required for the evaluation. Instead, it requires a short light pulse to be used to ensure that generation is insignificant during the evaluation. However, for a lower τ_{eff}, the decay will be rapid and the signal will be low leading to a higher uncertainty of the determined τ_{eff}. At $\tau_{\text{eff}} \leq 160\,\mu\text{s}$ an uncertainty $\geq 10\,\%$ will be expected [70]. Therefore the method should be used if the expected τ_{eff} is above that limit.

The advantage of the quasi-static approach is that lower effective minority carrier lifetimes can be measured (down to a few µs). However, the generation has to be well known and thus the mismatch between the specimen and the reference cell. This mismatch is called the »optical constant« and can be either determined by comparing the lifetime measurement to a reference (e.g. transient if possible) or by calculation based on the optical properties of the specimen. In addition, it was found that the generalized and quasi-static methods are prone to paper sheets or foils placed between the chuck and the specimen (to avoid contamination), which is not the case for the transient method (or the effect is negligible in this case).

If investigating passivation layers—as done within this work—a lifetime of below 200 µs on 1 Ω cm *n*-type base material would be considered too low. Thus the transient evaluation method was used almost exclusively. If the lifetime determined by the transient method was at around 100 µs or below, its precise knowledge is not of much interest and thus the high uncertainty was acceptable. Only in case of the samples measured to determine the Local Back Surface Field (LBSF) recombination in Section 7.2 were measured using the generalized method if the lifetime was below the limit. In this case, the optical constant was determined prior to the laser process and the samples were measured with the passivated (not lasered) site facing the flash lamp.

2.4.2 Implied V_{oc}

As the carrier densities n and p follow the relation

$$n = N_{\text{c}} \exp\left(-\frac{E_{\text{fc}} - E_{\text{f}}}{k_{\text{B}}T}\right) \tag{2.85}$$

$$p = N_{\text{v}} \exp\left(-\frac{E_{\text{f}} - E_{\text{fv}}}{k_{\text{B}}T}\right) \tag{2.86}$$

their product can be written as

$$(n_0 + \Delta n)(p_0 + \Delta n) = n_{\mathrm{i,eff}}^2 \exp\left(\frac{E_{\mathrm{fc}} - E_{\mathrm{fv}}}{k_{\mathrm{B}} T}\right), \tag{2.87}$$

where E_{fc} and E_{fv} are the quasi-Fermi levels. Since $\Delta n \gg p_0$ (n-type material) or $\Delta n \gg n_0$ (p-type material) and with the definition $V = q \cdot (E_{\mathrm{fc}} - E_{\mathrm{fv}})$ a relationship between V and Δn can be extracted

$$V(\Delta n) = U_{\mathrm{T}} \ln\left(\frac{(N_{\mathrm{D}} + \Delta n) \cdot \Delta n}{n_{\mathrm{i,eff}}^2}\right), \tag{2.88}$$

where N_{D} is the doping of the wafer (thus either n_0 or p_0). This voltage is called »implied« voltage, the voltage that a certain Δn would imply.

From the data of the external reference cell, each aquired data point can be linked to an intensity. Thus, the Δn at 1 sun can be determined, where the level Δn that is linked to 1 sun is determined by the effective lifetime of the sample. The implied voltage at this Δn is called »implied V_{oc}« and gives the V_{oc} that would be achieved if a device could be fabricated that would correspond to this level of recombination. Therefore, for devices that feature passivated contacts like the HIT solar cells, the implied V_{oc} corresponds to the V_{oc} that would actually be measured in the final cell. An excellent passivation can achieve an implied V_{oc} of above 730 mV. The value is especially of interest as it is (for a good passivation) independent of the doping of the wafer.

While the evaluation can be performed when using the transient method as well, since the evaluation requires data from the reference cell, knowledge of the optical constant is again important to get the correct implied V_{oc}. In addition, due to the evaluation after generation, it can happen that 1 sun intensity is not achieved during the measurement.

2.4.3 Implied *FF*

Similar to the method outlined for *PFF* in Section 3.2.1, using the intensity data from the reference cell and the implied V, a pseudo JV curve can be obtained. Thus, similar to *PFF*, an »implied *FF*« can be determined.

The implied *FF* can be seen as a measure for the injection dependency of the passivation. For a good passivation (thus τ_{eff} close to the Auger lifetime limit) values in the range of 86 to 87 % can be achieved (note that in this case

the ideality factor is 2/3 [20]). Therefore, the implied *FF* was more widely used in the research community to judge if the injection dependency of the passivation could limit the *PFF* of the device.

Such a limit applies in the case of the implied V_{oc}, where the V_{oc} of the final device cannot be above the implied V_{oc} of the passivation. In case of *PFF*, this does only apply if the device features passivated contacts and thus the recombination in the device is similar to that of the passivation test structure. Most solar cell devices however do not feature passivated contacts and the high recombination at the contacts will lead to an overall lower effective lifetime in the device. This can especially lead to the situation where the limitation at V_{oc} is stronger than at Maximum Power Point (mpp) leading to a possibly higher real *PFF* than the implied one. Thus, the implied *FF* should only be evaluated for devices featuring passivated/selective contacts.

3 Characterization and Simulation of Crystalline Silicon Solar Cells

The purpose of a solar cell is to deliver electrical power to an external circuit. It is therefore essential to understand the electrical behavior the device will expose in this circuit. Furthermore these characteristics can be used to analyze limitations and possible improvements to be made in the fabrication process.
While the general electrical characteristics are not specific to photovoltaic devices, in case of solar cells some parameters like V_{oc} or FF will be introduced which are mainly used in context of photovoltaic devices. In addition to the general characteristics, the Suns-V_{oc} method is introduced as the PFF (and its relation to FF) was used to determine the series resistance of the cell.
As a final method to characterize, predict and analyze the device performance the simulation tool Quokka is introduced.

3.1 JV Characteristics of *pn* Junctions in Semiconductors

For the characterization of a device that was built to convert light into electrical energy, the knowledge of its JV characteristics is important. Under the assumption of no or weak excitation, Shockley showed that the JV characteristics of a semiconductor *pn* junction can be described by an exponential relation [21]. A more detailed derivation can be found in the cited paper, or in [60] or [71].

$$J(V) = J_0 \left[\exp\left(\frac{qV}{k_B T} \right) - 1 \right] - J_{sc} \tag{3.1}$$

Here J and V denote the terminal current density and the terminal voltage of the device. q is the elementary charge, T the temperature and k_B the Boltzmann constant. J_{sc} is called the »Short-Circuit current density« and gives the current density that can be extracted from the device if it is in short-circuit, thus $V = 0$. J_0 is commonly called »dark saturation current density« and is discussed in more detail in section 2.3.

The voltage that is achieved under open circuit conditions, thus $J(V) = 0$, is called V_{oc}. From Equation (3.1) it follows that

$$V_{oc} = U_T \ln\left(\frac{J_{sc}}{J_0} + 1\right) \tag{3.2}$$

with the »thermal Voltage« $U_T = k_B T/q \approx 25.7\,\mathrm{mV} @ T = 298\,\mathrm{K}$.

J_{sc} is mostly influenced by the optical properties of the device, e.g. shading or light trapping. In a good solar cell $J_{sc} \approx J_{gen}$, which is the »generated current density« defined by the electron pairs generated by a flux of absorbed photons in the device. Only if recombination is high, it will be observed that J_{sc} differs significantly from J_{gen} and $J_{sc} < J_{gen} < J_{inc}$ will be found, where J_{inc} similar to J_{gen} is the external »incident« photon flux irradiating the semiconductor, including photons that will not be absorbed by the device. Under AM1.5 conditions, this is $J_{inc} \approx 46.2\,\mathrm{mA/cm^2}$, determined by integration of the AM1.5 spectrum.

As shown above, V_{oc} depends on both J_{sc} and J_0, but if the illumination is not changed significantly, the biggest influence will be J_0. Thus, like J_0, V_{oc} will be a measure for the recombination of the device.

3.1.1 Fill Factor

The power density of the device is defined as $P = V \cdot J(V)$ and will achieve a maximum P_{mpp} at a terminal voltage V_{mpp}. The corresponding current density is called J_{mpp}=$J(V_{mpp})$. In addition to J_{sc} and V_{oc}, a third parameter is often used for solar cell characterization at Maximum Power Point (mpp), the »fill factor« FF, which is defined as

$$FF = \frac{J_{mpp} V_{mpp}}{J_{sc} V_{oc}}. \tag{3.3}$$

Many effects can influence the FF, like the series resistance contributions or injection-dependent effects. An overview can be found in [62].

An upper limit (commonly called FF_0) for FF was calculated by Green [20]

$$FF_0 = \frac{v_{oc} - \ln(v_{oc} + 0.72)}{v_{oc} + 1} \tag{3.4}$$

with $v_{oc} = V_{oc}/U_T$.

3.1.2 Efficiency

The efficiency of the device is defined as the relation of the extractable (P_{mpp}) to the incident (P_{inc}) power density irradiated onto the device. Thus

$$\eta = \frac{P_{mpp}}{P_{inc}} \tag{3.5}$$

Under AM1.5 conditions $P_{inc} = 100\,\mathrm{mW/cm^2} = 1000\,\mathrm{W/m^2}$. Using Equation (3.3), η can also be described as

$$\eta = FF \cdot J_{sc} \cdot V_{oc}. \tag{3.6}$$

Shockley and Queisser calculated the limit of η for single *pn*-junction solar cells [72] without taking material-specific properties into account, resulting in a limit of approx. 32 %. In a more precise way for silicon-based solar cells, Richter *et al.* calculated the limit to be at 29.4 % [73], with the most limiting factor being Auger recombination (see Section 2.2.2). The current world record for silicon solar cells was achieved by Panasonic with an efficiency of 25.6 % [8].

3.2 *Suns-V_{oc}* Characterization

The »quasi-steady-state open-circuit voltage« (qssV_{oc}, but nowadays and in the following called »*Suns-V_{oc}*«) method was developed by Sinton and Cuevas [74]. In this measurement setup, the solar cell is wired to a voltmeter which should have a high inner resistance. The sample is then being illuminated by a flash lamp such that quasi-steady-state conditions are achieved. The variation in the voltage is tracked by the voltmeter during the decay, the light intensity by a calibrated reference cell next to the device being tested. This leads to pairs of intensity and V_{oc}, which can be plotted as shown in Figure

3.1a as intensity (»suns«) over V_{oc}, hence the name of the method. In contrast to the J_{sc}-V_{oc} method, J_{sc} is provided as an input-parameter. For best accuracy of the results, J_{sc} should be determined prior to the measurement [75], but the influence of the parameter is low, so a good guess will normally be sufficient. In addition, the wafer thickness has to be known well. The main parameters that can be determined by *Suns-V_{oc}* directly are V_{oc} (at

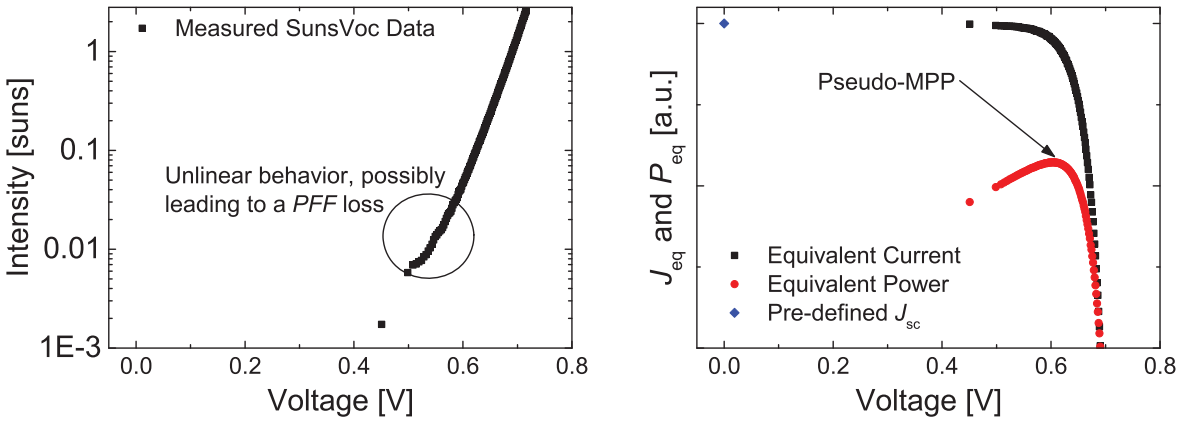

(a) »Suns-Voc« **(b)** Pseudo-JV Curve

Figure 3.1: Measured *Suns-V_{oc}* data for an exemplary cell. (a) shows the data plotted in the intensity vs. voltage method (»*Suns-V_{oc}*«) (b) shows the same data plotted as a pseudo-JV and pseudo-power curve.

one sun, but also injection-dependent), *PFF*, a Pseudo-η, the ideality at several injection levels and double diode parameters being fitted to the data. Of these—within this work—only the *PFF* was of much interest, thus it will be described here in more detail.

3.2.1 Pseudo Fill Factor

With the J_{sc} provided as input and the suns/V_{oc}(suns) pairs, a pseudo-JV curve can be generated

$$J = J_{sc} \cdot (1 - suns) \tag{3.7}$$

$$V = V_{oc}(suns) \tag{3.8}$$

The product of the two, the »Pseudo-Power« will have a maximum and thus a Pseudo-J_{mpp} and a Pseudo-V_{mpp} can be determined leading to *PFF* according to Equation (3.3). This is graphically illustrated in Figure 3.1b.

The *PFF* can be viewed as a reference for the *FF* without resistance losses (as the device is operated under Open Circuit (OC) conditions) and is thus an

important parameter to judge the device quality. Commonly Pseudo-V_{mpp} will correspond to a light intensity of approx. 0.05 suns and thus be at significantly lower injection than V_{oc} leading to the conclusion that injection dependent effects are strongly visible in *PFF*. Hence *PFF* will be reduced if J_{02} is high. It will be influenced by shunts (R_{P}) and edge recombination. In case of an injection-dependency of the passivation, this can lead to a decrease in *PFF* as well, although the effect is commonly similar to an increase in J_{02} [32]. For a solar cell that has no such issues, *PFF* is expected to be very close to FF_0. As an example the pseudo-JV curve depicted in Figure 3.1b resulted in a *PFF* of about 82.5 % and therefore in a *FF* loss of around 1.5 %.

In case of small area cells like presented in Section 8.2, it was found that a shadow mask should be used to avoid illumination of the area outside of the device. While the influence on V_{oc} was determined to be low (increase of 1 to 2 mV), the influence on *PFF* can be strong leading to values that can be above FF_0.

3.2.2 Determination of Series Resistance

As during *Suns-V_{oc}* the device is operated under OC conditions, the measurement is free of any series resistance losses. Thus a comparison of *FF* and *PFF* can be made to determine R_{S} [74], leading to the definition of

$$\Delta FF = FF - PFF. \tag{3.9}$$

Note that the definition of ΔFF was chosen such that it yields negative values indicating a *FF* loss due to the series resistance. Pysch *et al.* further analyzed ΔFF and showed that it is proportional to R_{S} with the following relation [75]

$$FF = FF_0 - mR_{\mathrm{S}}, \tag{3.10}$$

where $m \approx -5\,\%/\Omega\,\mathrm{cm}^2$. Therefore a ΔFF of 5 % will correspond to a R_{S} of approx. $1\,\Omega\,\mathrm{cm}^2$.

3.3 Cell Simulation Using Quokka

All the parameters that can be determined on test samples are not of much use if they cannot be compared to the parameters that can be determined at the device level. While some parameters can be directly measured (e.g. the total J_0 if the device shows roughly ideal behavior), the complexity of a solar cell can make it hard to judge the origin of problems that were found during the basic characterization. A large number of specific characterization methods is available for a more detailed analysis leading to a better understanding of the problem at hand. Another approach to problem analysis and performance prediction is the use of device simulation.
This can be helpful to

- *predict device performance based on cell layout / input parameters*
- *analyze the influence of specific parameters*
- *perform a loss analysis to find bottlenecks in the device performance*

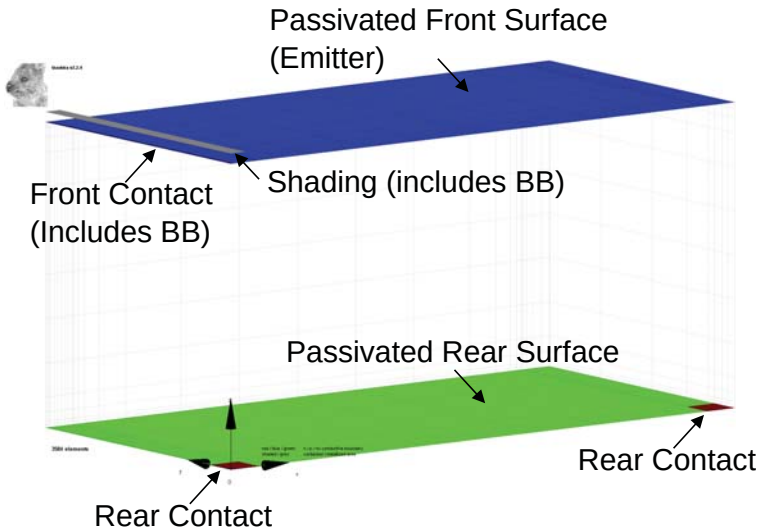

Figure 3.2: Unit cell for a PERL cell as output by *Quokka* with added annotations.

3.3.1 The Simulation Model

In this work, *Quokka* (version 2.2.4) was used for »3D« device simulations. A detailed introduction on the basic approach of *Quokka* can be found in [76].

Here just a small overview will be given. In contrast to simulation programs like *Sentaurus Device*, *Quokka* makes one basic simplification: The assumption of having conductive boundaries on the front and rear. Local differences in the doping (e.g. (selective) emitter, (local) Back-Surface-Field (BSF)) are not specified by a doping profile, but just by their "effective" parameters defining the recombinative and resistive properties. This leads to a significant reduction of the elements in the unit cell allowing for a more detailed specification of the cell structure while keeping the simulation fast even when calculating states for a detailed 3D unit cell with 15000 elements.

Based on the results that were determined for the cells, a simulation model was developed to match the cell results. The unit cell (*Quokka* output) for an exemplary *PassDop* cell is shown with annotations in Figure 3.2.

Rear Contact

The rear contact was modeled as a square (length of 44 µm) with an equivalent area to a circle with a diameter of 50 µm. While modeling circular contacts is not problematic in *Quokka*, for comparison to previous simulations using *Sentaurus Device* the rectangular shape was chosen. Comparisons showed that the difference is negligible.

Optics

The optical properties of the solar cell are included in *Quokka* within the calculated generation profile. Here, the possibility of Quokka to calculate the generation based on front side transmission and rear side path length enhancement Z were used as this allows for the calculation of a spectral response to compare the External Quantum Efficiency (EQE) of the measured and simulated cells. The front side transmission was calculated from the measured reflectance of the cell. As the measurement includes light that entered and passed the cell (possibly multiple times) and left the cell again (infrared "escape") as well as light that was reflected by the metal shading, corrections had to be made. For the metal fingers, a reflectance of 1 was assumed, which should be a good assumption for plated silver, unless the fingers exhibit a high roughness. Thus, the minimum in the reflectance curve defines the amount of metal shading and a correction can be made by subtracting the metal shading uniformly. To differentiate between surface reflection and the infrared escape, a linear fit was performed ranging from the minimum in the reflectance (usually around 600 nm) to 900 nm and subsequently extrapolating the values beyond. Finally it was assumed, that no parasitic absorption

is present within the front side Anti-Reflective Coating (ARC), which led to small errors within the range of 300 to 400 nm.

To determine Z, no direct measurements could be used. Thus, a ray tracer provided by PV Lighthouse was used to simulate the influence of the layers [77]. As the optical properties for the used layers were not available within the database of PV Lighthouse, layers with similar optical properties were used.

Shading due to metal contacts is incorporated in *Quokka* by the specification of the metal finger width. For the shading due to the metal, either the measured value from the reflectance measurement was taken (if available) or the metal shading was calculated based on the geometry of the fingers and the bus bars. From the determined amount of shading (usually in the range of 2 to 6 percent), the shading width was calculated in relation to the finger pitch. This means that the shading width was larger than the actual finger width due to the bus bars (which are not part of the unit cell). Therefore, in the unit cell, there is no excess carrier generation due to incident light in some parts where there is in the real cell. However, as the bus bars account for approx. 2 % of shading at most, only a few microns are affected. Since this is usually much lower than the diffusion length the error due to this effect is negligible.

Series Resistance

For the front side contact resistivity, values measured by the Transfer-Length Measurement (TLM) method were used. For the rear, no exact values could be determined. It was tried to determine ρ_c for the rear by fitting R_S as proposed by Fischer [56], but the uncertainty of the fit was too high for the results to be usable. The measurement suggested though that the contact resistivity was expected within a certain range and thus conservative values within that range were chosen. Nevertheless, the unavailability of exact values for this parameters is thought to be one of the biggest uncertainties within the performed simulations. As the resistive losses within the emitter and the base respectively are calculated by *Quokka* itself, this leaves the contributions from the front and rear metallization. For the front grid, an analytical model to determine the grid resistivity was used and applied within the simulation as an external series resistance [78]. The rear side metallization was done by Physical Vapour Deposition (PVD) aluminum, which was fully contacted by the measurement chuck during the measurements, the contribution of the resistivity within the rear side metal is negligible compared to all other contributions.

Recombination

The most important aspect when defining the simulation model is the specification of the recombination parameters. Here the following contributions are important for the *PassDop* cells:

1. Front passivated surface recombination (e.g. Emitter), declared as »Pass (FS)«
2. Front contact recombination, declared as »Cont (FS)«
3. Bulk recombination (usually radiative or Auger recombination), declared as »bulk«
4. Rear passivated surface recombination (*PassDop* passivation), declared as »Pass (RS)«
5. Rear contact recombination (*PassDop* Local Back Surface Field (LBSF)), declared as »Cont (RS)«

Extrinsic bulk recombination was assumed to be insignificant. For 1. and 4. the respective J_0 contributions determined on symmetrical lifetime samples were used to specify the parameters. For 2., the front contact recombination, the values were determined by calculations using *EDNA* assuming a bulk temperature of 300 K. In case of a front texture, the increased area was taken into account by multiplying $J_{0e,met}$ with a factor of 1.7, which was determined to be a good approximation for random pyramids. As the cell simulations were performed at 298.15 K, J_0 had to be corrected for the lower $n_{i,eff}$ by a factor of 0.72. For 5., the rear contact recombination, the values determined in Section 7.2 were used for the simulations.

3.3.2 Free-Energy Loss Analysis

By default, *Quokka* will not only return the basic parameters for the simulated solar cell, but also a set of results for a Free Energy Loss Analysis (FELA) [79]. This allows for a fast and comprehensive loss analysis of solar cell concepts, which can be used to understand the effects of modifications to the cell layout and to classify loss mechanisms for efficiency improvements. However, when comparing multiple cell simulations with different parameter sets or a cell parameter variation, these results should be taken with caution. If one loss mechanism is reduced, the cell efficiency and power output will increase and therefore the parameters at mpp will be different. Especially a higher Δn is expected if recombination is reduced, leading to a higher V_{mpp}.

As the example in Fig. 3.3 shows the FELA of the »FRC_basic« example cell which is delivered together with *Quokka* as well as the FELA for the same cell, but with the rear contact recombination reduced from 400 to 10 fA/cm^2. This reduction in recombination led not only to a significant increase in the simulated device efficiency, but also to an increase in the recombinative losses for the other loss paths.

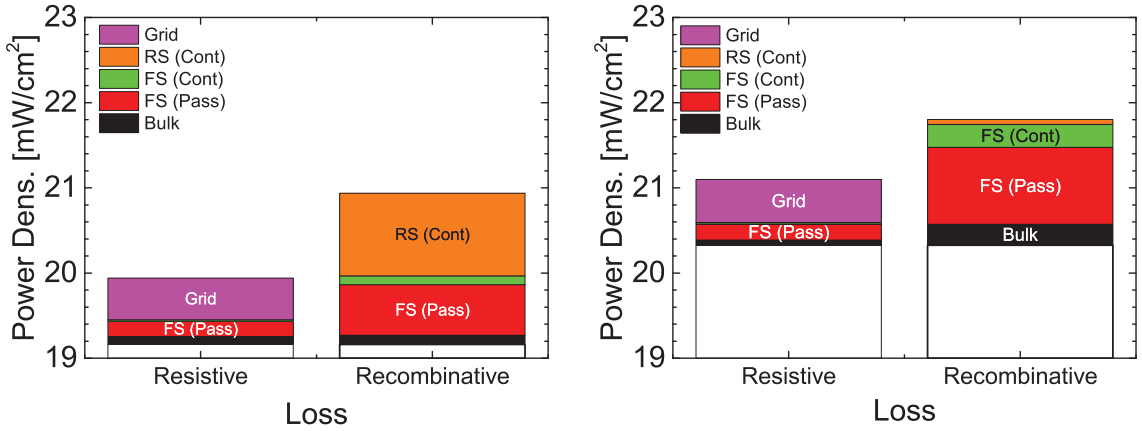

(a) $J_{0s} = 400\,\mathrm{fA/cm^2}$ **(b)** $J_{0s} = 10\,\mathrm{fA/cm^2}$

Figure 3.3: FELA of the »FRC_basic« example cell definition as delivered with *Quokka* once with default settings ($J_{0s} = 400\,\mathrm{fA/cm^2}$) and once with reduced rear side recombination ($J_{0s} = 10\,\mathrm{fA/cm^2}$). The improved recombination does not only result in an increased overall level, but the other loss contributions increase as well. Only electrical losses as determined by *Quokka* are displayed.

This can be nicely explained in the so called "leaky bucket" metaphor [80]. A bucket (the silicon) is filled with water (the carriers) at a constant flow (the generation) and has multiple holes through which water can leak out of the bucket (the recombination mechanisms). If one hole is removed or reduced, the water level will increase but so will the pressure leading to a higher flow through all other holes. In similar fashion, a higher Δn (and therefore a higher V_{mpp}) at mpp due to reduced recombination for one mechanism will lead to higher recombination currents and therefore to a higher power loss caused by other recombination paths. In addition, since optical losses are normed to V_{mpp} to calculate a power loss, a higher V_{mpp} will lead to increased power loss contributions by these power loss paths as well. This leads to an important observation regarding these kind of power loss analysis: a FELA power loss analysis will not tell exactly by how much one can improve a cell's power output when improving a certain aspect. It only gives the result for how much of the power got lost for a certain aspect for this exact device simulation. Thus such a loss analysis is most useful to classify loss contributions and define the importance for technological improvements.

Brendel *et al.* presented an approach based on this taking the »synergy effects« into account [81]. This however requires multiple simulations to determine the influence of each parameter and its influence on the synergy effects. Such an approach allows for a more complete analysis of the parameter influence, but due to the multiplication of the required simulation work was not used in the analysis presented in this work.

In the above example, another effect can be observed. The gain in the device efficiency ($\approx 1.16\,\%_{\mathrm{abs}}$) is in fact higher than the reduction of the recombinative loss at the rear ($\approx 0.91\,\%_{\mathrm{abs}}$). Part of this is a synergy effect, due to the higher possible FF_0 and therefore FF, but another contribution is that at mpp the cell is moved towards a higher Δn (or V_{mpp}) which can lead to positive or negative effects if encountering injection dependent influences like Shockley-Read-Hall (SRH) recombination. This points out another reason why the FELA of two different device simulations should only carefully be compared.

While Figure 3.3 only shows the resistive and recombinative loss contributions, the graphs in Chapter 8 will show optical losses as well. These were determined by calculating current density losses for the respective loss paths from optical simulations [77, 78] and converting them into a power density by multiplication with V_{mpp}. Similar to the recombinative losses, these therefore will increase with increasing V_{mpp}. It should be added as well, that these contributions are usually not discussed despite being dominant loss paths. e.g. the loss contribution by »Refl. Escape« (see Figure 8.9 on page 208) is larger than all of the recombinative losses combined. However, in case of the absorption in the rear metal or the light escaping the cell after passing through the wafer (»reflection escape«), not too much can be done about this, at least not for the discussed cell structures. A diffuse reflector could result in an improvement in the range of 0.5 to 1.0 $\mathrm{mA/cm^2}$, but it is not straight to implement this, at least not without sacrificing other properties.

4 Plasma-enhanced chemical vapor deposition

This chapter gives a brief overview over the Plasma-Enhanced Chemical Vapor Deposition (PECVD) technique. The two main techniques used for plasma excitation (radio frequency and microwave) are presented and their implications are being discussed.
In addition, the chapter gives an introduction to the tools that were used for the deposition.

4.1 Plasma Excitation

A plasma is defined as a collection of free charged particles moving in random directions [82]. In case of PECVD, a composition of gases is used which on their own would not start chemical reactions, e.g. SiH_4 and H_2. To achieve the state of a plasma, external excitation is required. This excitation can result in ionization of atoms and molecules and therefore radicals and free electrons. By inelastic collision, these electrons can ionize or dissociate further atoms and molecules, thus generating further radicals. As radicals may react (e.g. to their former unionized or molecule state, or to a new molecule), the ionization of the plasma may change until an equilibrium is achieved. To avoid requiring large power densities, the plasma is usually generated in a vacuum with a pressure in the range of 0.1 to 100 Pa. If the plasma is in contact with a surface (e.g. a silicon wafer), the radicals can react with the surface. The main processes in this case are shown in Figure 4.1. In case radicals are adsorpted by the surface, a new layer will be »deposited« onto it. The composition of this layer will depend on the components of the plasma, thus the precursor gases that are being used. e.g. for the deposition of SiN_x, SiH_4 can be used in combination with NH_3 or with N_2, although the former is more common.

In case of PECVD, mainly to methods to generate a plasma are being used today. These are described in the next sections.

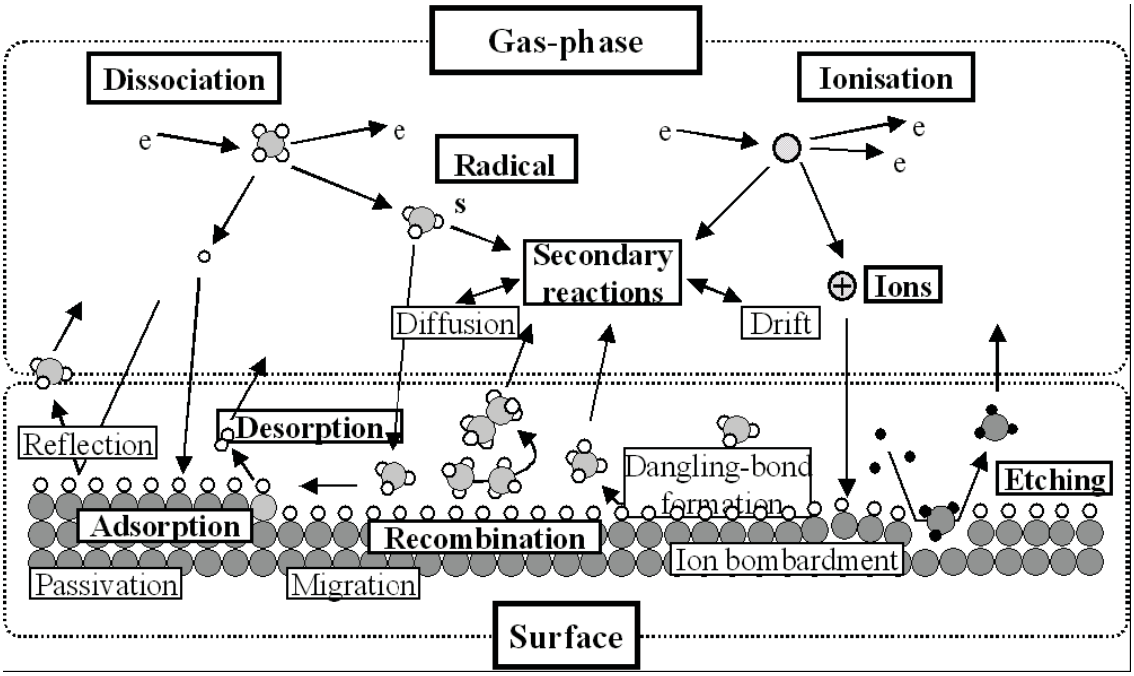

Figure 4.1: Overview over the processes that can happen in the plasma and by interaction of the plasma with the surface. Taken from [83].

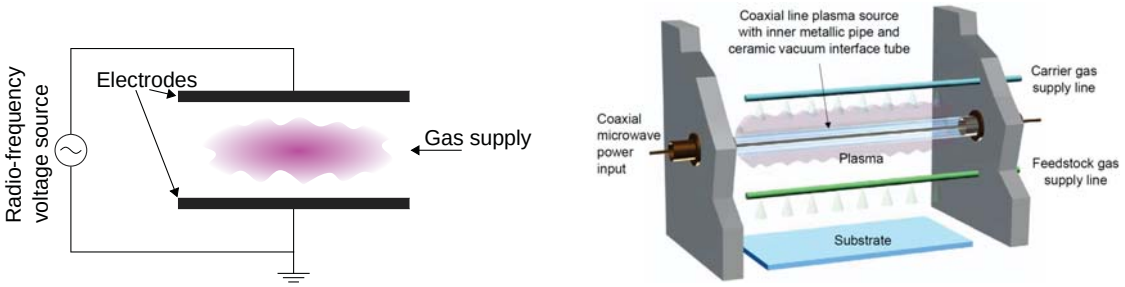

(a) Radio Frequency (RF) **(b)** Microwave (MW)

Figure 4.2: Layout of a RF and a MW plasma source. The MW picture was taken from [84].

4.1.1 Radio-frequency Plasma

The basic hardware layout for a RF plasma reactor is that of a capacitor, as shown in Fig. 4.2a. A good description of the principles of an RF plasma can be found in [82]. One of the electrodes is »active«, the other one is usually grounded. The active electrode is powered by a high frequency voltage source, usually within radio frequency range. Common frequencies range from 40 kHz to about 50 MHz.

The alternating voltage leads to an excitation of electrons and, if the provided energy is high enough, to ionization, thus to free electrons and positively charged ions. Due to their higher inert mass, the ions can not follow the alternating voltage while the free electrons will oscillate. This leads to inelastic

collisions of electrons and molecules or ions and thus to more free electrons, until a plasma state is achieved.

As noted above, the plasma is generated by two electrodes, one of which is powered. Commonly at least the active electrode will be placed relatively close to the plasma. This leads to electrons being absorbed by the surface of the electrode and thus to a »loss« of electrons in the plasma. Therefore, while normally a plasma would be expected to be quasi-neutral, in this case the plasma in relation to the electrode(s) will be on positive potential. This loss will be biggest close to the electrode, which leads to the formation of so-called »sheaths« [82], the areas close to the electrode with the highest potential. The sheaths will act as a driving force for electrons re-emitted or reflected from the electrode into the plasma and for a barrier for ions from the inner plasma. If however ions pass this barrier, they are accelerated towards the surface. This kinetic energy the ions carry can lead to bombardment of the surface and potentially damage layers present on the surface (e.g. see [85]). On the other hand, the bombardment can be utilized to remove lose bound particles from the surface and thus leads to denser layers. Therefore, for some processes controlling the potential difference between plasma and electrode can be critical and the plasma parameters have to be adjusted accordingly.

Measuring the potential difference between plasma and electrode is tricky as a probe inserted into the plasma would get negatively charged as well, thus strongly influencing the measurement. Instead commonly the »bias« voltage is measured, which however gives the effective potential difference between the two electrodes. This bias voltage is also influenced by the geometry of the electrodes, e.g. if one of the two is significantly bigger than the other. Still for two processes with different bias, the one that has the higher bias is expected to have the higher potential difference between plasma and electrode as well.

4.1.2 Microwave Plasma

The layout of a MW plasma source is very different from that of an RF source in that it does not consist of two plates as electrodes. Instead—as shown in Fig. 4.2b—a MW commonly consists of a quartz tube which holds an antenna in the middle. Between the two a dielectric might be placed, e.g. air. The antenna is coupled to a MW generator operating at 2.45 GHz. A detailed description of the principle and its implications can e.g. be found in [86].

The use of MW for Anti-Reflective Coating (ARC) and passivation deposition of SiN_x was demonstrated by Lauinger *et al.* and has since been used extensively for photovoltaic applications [87].

In common the MW plasma source is placed at a good distance from the substrate. Thus, as pointed out by Lauinger *et al.*, it can be considered a »remote« or »quasi-remote« plasma. The potential difference between plasma and substrate in this case will be low and a damage of surface layers due to bombardment will be negligible. This can be both an advantage (as in the investigations by Lauinger *et al.*) resulting in an improved passivation performance but can as well be a disadvantage as the resulting layer will be less dense and therefore can contain more defects (voids etc.), which can e.g. be important if the layer is to be used as an etch or diffusion barrier.

The second advantage of the MW technique is that no electric coupling—be it active or grounded—of the substrate holder is required. This makes it easier to develop deposition tools that can be used in-line as opposed to a stationary setup as it is almost always chosen for the RF technique.

As the power density will be the highest close to the plasma source, it is likely (depending on the parameters) that there will be a good amount of deposition on the quartz tubes, which can lead to the issue of particles being pealed off during the deposition. Therefore today the plasma source is sometimes placed underneath the substrate holder, so the deposition is performed from below.

4.1.3 Ionization and Dissociation

For creation of a stable plasma, the energy coupled into the plasma must be high enough to create excited species. To achieve a deposition, e.g. SiN_x, it is also a requirement to create the corresponding reactive species.

Table 4.1 gives an overview over the dissociation and ionization energies of interest for the deposition of SiN_x and SiC_x. The important point to note here is that the dissociation energies for CH_4 and N_2 are higher than that for SiH_4. Thus they might require a higher source power coupled into the plasma if direct decomposition is aimed for. In addition, due to the low dissociation energy for SiH_4, the deposition rate will mostly be defined by the amount of available SiH_4.

In case of SiN_x, as a precursor for nitrogen, both N_2 as well as NH_3 can be used. A comparison can be found in [93].

Table 4.1: Overview over the threshold dissociation and ionization energies for various species. For higher excitation states or stronger dissociation, higher energies will be required as can be found in the literature. All values are given in eV. Sources are CH_4: [88, 89], SiH_4: [90], H_2: [91], N_2: [92].

Precursor	Ionization	Dissociation
SiH_4	–	8.0
CH_4	12.6	14.3
N_2	15.6	9.8
H_2	15.4	8.8

4.2 Roth&Rau AK400M PECVD Reactor

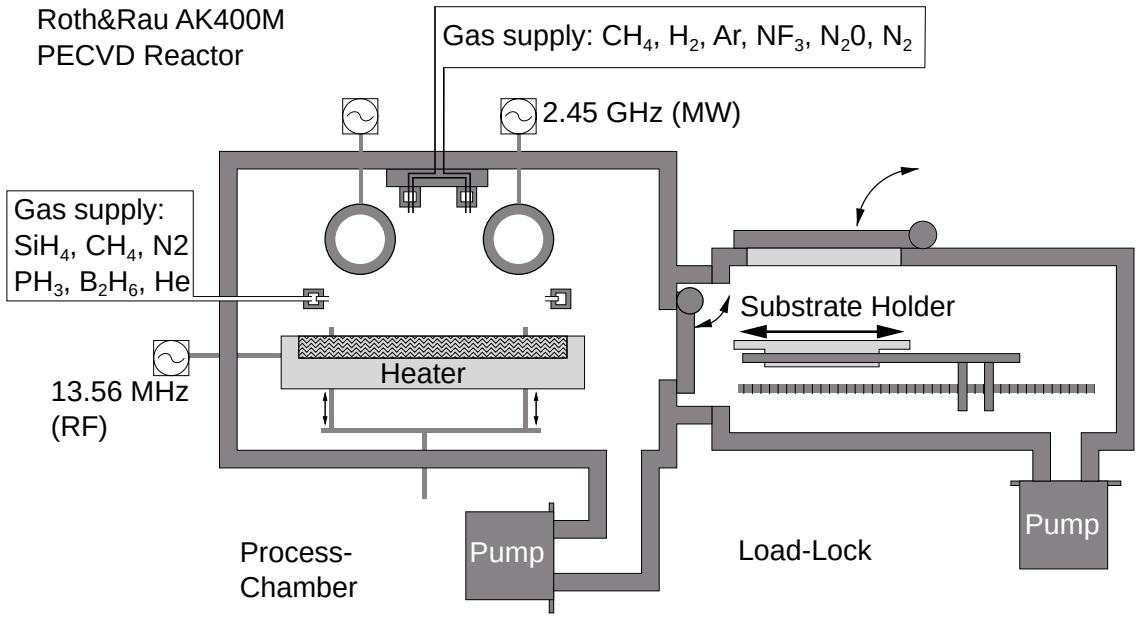

Figure 4.3: Schematic of the reactor layout of the Roth&Rau AK400M PECVD reactor. Source: internal artwork, updated to current state.

The Roth&Rau AK400M PECVD reactor was used to deposit SiC_x layers, such as SiC *PassDop*. The basic layout of the reactor is shown in Figure 4.3. The reactor consists of two chambers, the process chamber and a loading chamber (»Load-Lock«). Each chamber can be vented and evacuated separately, allowing for loading/unloading (via a tilting door and a transport mechanism) of the substrate holder while retaining the vacuum in the process chamber. Underneath the substrate holder (if loaded into the process chamber) there is a heater which allows for (substrate) temperatures in the range of 25 to 600 °C.

The substrate holder itself is made out of graphite and has a usable size of 20 cm × 30 cm. It can hold four round wafers of 100 mm diameter, two 125 mm or one 156 mm sized wafer (both square and pseudo-square). The RF generator operates at the standard ISM frequency 13.56 MHz powering the substrate holder which acts as the active electrode. The second (grounded) electrode is the process chamber, hence the reactor features an asymmetric setup. Above the substrate holder (approx. 10 cm) two MW quartz tubes are available as a second method for plasma excitation. The copper antennas inside the quartz tubes are connected to pulsed MW plasma generators operating at a frequency of 2.45 GHz. Hereby the MW generator connect from opposing sites to *both* tubes. Both plasma sources may be used in combination.

Two gas supplies are available. One is placed as a gas ring around the substrate holder (approx. 1.5 cm above). This gas supply is mainly used for reactive gases like SiH_4, CH_4, PH_3 and B_2H_6. The second gas shower is placed at the top of the chamber and is mainly for stabilizing and diluting gases, like H_2 and Ar, but as well for etching gases (e.g. chamber cleaning processes).

While the MW plasma source is available, it is not commonly used in current processes. Except for the *PassDop Optical* layer, for which the high power density of the MW sources is required. This layer makes use of both sources, to achieve a low-refractive index, but yet fairly dense layer. All other deposition processes currently in use only utilize the RF plasma source.

4.3 Roth&Rau AK800 PECVD Reactor

The Roth&Rau AK800 PECVD reactor is very similar to the AK400M as shown in Figure 4.4, but increased in size. It was used to deposit the SiN_x layers described in Chapter 6.

The substrate holder can now hold twelve 100 mm, nine 125 mm or four 156 mm wafers. Due to the increased size, the temperature range is more limited to 25 to 300 °C (actual substrate temperature).

Similar to the AK400M, the substrate holder is contacted by a 13.56 MHz RF plasma source. This plasma source however is currently not in use, all depositions are made utilizing only the 2.45 GHz MW sources, of which 4 are placed approx. 15 cm above the substrates. Each of the 4 MW generators is connected to two of the tubes (e.g. generator 1 connects to tube 1 and 2 from one side, generator 3 connects to tube 3 and 4 from the same side etc.).

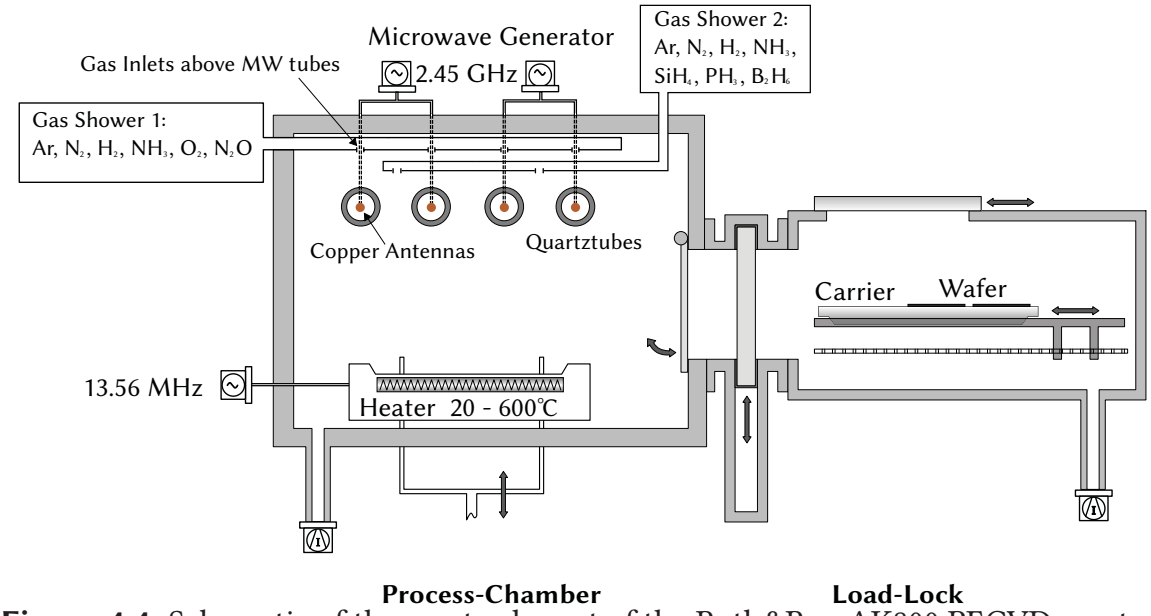

Figure 4.4: Schematic of the reactor layout of the Roth&Rau AK800 PECVD reactor. Source: [50], slightly updated.

In contrast to the AK400M, both gas showers are placed at the top of the chambers and the only difference between the two being that for reactive gases (like SiH_4) inlets in-between the tubes, while for other gases (like Ar) inlets directly above them are used.

For the deposition of SiN_x, commonly SiH_4 and NH_3 are being used. As the latter was not available when this work was started, N_2 was being used as a replacement. In the meantime a lecture bottle of NH_3 was added to the reactor and experiments comparing the two approaches were started (not within this work). Similar to the AK400M, both doping gases are connected, but only PH_3 is currently in use.

5 The *PassDop* Process

For high-efficiency silicon solar cells it is a requirement to keep recombination at the surfaces as low as possible. Passivated Emitter and Rear Locally Diffused (PERL) silicon solar cells utilize a local high-low junction underneath the rear side contacts, a Local Back Surface Field (LBSF) to minimize the recombination at the c-Si/metal interface and therefore were able to achieve highest efficiencies on both p- as well as n-type material [94, 95]. However, defining such a localized structure can require complex and expensive processes, such as (photo-)lithography.
The PassDop approach allows for defining such a localized contact structure in a short and elegant process sequence. To achieve this, the PassDop layer has to serve multiple functions, especially it has to be able to deliver a good passivation and at the same time expose compatibility with laser doping.
Each of these technologies is not new on its own, but was applied and research by others before. Thus in addition to the basic description of the PassDop approach an overview over these technologies is given.

5.1 Passivation of Silicon Surfaces

From Equation 2.71 it is evident, that the surface passivation will have a stronger influence the lower the ration W/L is, while the influence of the material properties decrease. This is especially the case for high-efficiency cells, where the total J_0 should be kept well below 100 fA/cm^2.

The methods to reduce surface recombination can be extracted from Equation 2.23 as a lower R_s will result in a lower S_{eff} and hence a lower $J_{0b,pass}$. The important parameters here are $D_{it}(E_t)$ and the carrier densities n_s and p_s.

$D_{it}(E_t)$ describes the defect state density at the surface. Such defects are usually caused by incorporation of impurities (e.g. nitrogen or oxygen from the ambient) or unsaturated bonds, so-called »*dangling bonds*«. Impurities might be removed from the surface by cleaning steps, commonly a wet-cleaning like

RCA, HCl or HNO_3+HF. This however will leave even more dangling bonds, so the cleaning can only be used to prepare the surface but does not necessarily serve passivation purposes. Instead it should be a goal to saturate the *dangling bonds* such that only a minimum of active defect states remain, hence D_{it} is reduced to a minimum and thus R_s will decrease. A common way to achieve this is by providing a large amount of hydrogen as the Si-H bond is not recombination active. Thus HF can actually result in a good surface passivation, an effect that is sometimes used for characterization purposes [96], but this passivation is inherently unstable e.g. if the surface is exhibited to mechanical stress (i.e. handling). For solar cell passivation this mechanism still is important and one goal for every passivation layer should be to provide hydrogen to passivate dangling bonds. This mechanism is also called »chemical« passivation.

The second possibility to reduce R_s is to reduce the product $n_s p_s$ by depleting one carrier type at the surface. In case the minority carriers are driven away from the surface the state is called »*accumulation*«, in case of the majority carries »*inversion*«. Such a state can be achieved by either introducing fixed charges at the surface that drive away one carrier type (while being mostly immobile themselves) or by band bending due to a band mismatch. This also leads to the possibility of using a larger bandgap semiconductor as a surface passivation [60]. Similarly, a diffused surface (be it a *pn* or a high-low junction) is expected to passivate the surface as well due to depleting one carrier type in this region. Depending on the doping profile, an additional surface passivation might be necessary for best performance.

For lowest recombination properties it is best to combine both of these possibilities to reduce surface recombination. This is achieved by almost all common passivation layers except for SiO_2, which almost exclusively relies on chemical passivation and therefore a low D_{it} (down to 1×10^9 cm^2/eV [97]).

5.1.1 Amorphous Silicon Nitride

Silicon Nitride is used in semiconductor technology for multiple purposes. Its hard and dense structure make it a good encapsulant or diffusion barrier (e.g. [98, 99]). The layers can be prepared by Chemical Vapour Deposition (CVD) by decomposition of SiH_4 (or $SiCl_4$) and NH_3, either thermally or in vaccum. It can also be prepared by reactive sputtering, glow-discharge or by Plasma-Enhanced Chemical Vapor Deposition (PECVD) using Si/SiH_4 and NH_3 or N_2 as precursors.

For application on silicon solar cells Hezel and Schörner performed early experiments by using SiN_x to create an inversion layer junction on *p*-type silicon [100], but the SiN_x did not yet serve as a passivation layer as this functionality was served by a tunnel-SiO_2. Hezel and Jäger used (in comparison to Al_2O_3) SiN_x as a passivation [101], a concept which was later on adapted by Leguijt *et al.* [102] and Aberle *et al.* [103]. However only after the development of the remote- or quasi-remote-plasma deposition of SiN_x by Lauinger *et al.* [87, 104] SiN_x developed into a standard passivation technique for the front side (emitter) passivation of silicon solar cells, as a good passivation level could be achieved after firing while retaining a high wafer throughput. Later on, the direct plasma technique was further developed and therefore today both techniques a commonly used. While it was shown that sputtered SiN_x can be used as a surface passivation as well [105, 106] PECVD remained as the standard.

It was investigated if SiN_x can be used as a rear side passivation for Passivated Emitter and Rear Cell (PERC) but inversion layer shunting was found to degrade the solar cell performance due to the positive fixed charges in the layer (see below), if used without an intermediate SiO_2 layer [107]. Nevertheless, it was investigated by various groups as a (bulk Si) passivation for PERC solar cells, either directly [108, 109] or in stacks [110–113], but was finally superseded by Al_2O_3 [114]. However, the positive fixed charges make SiN_x a good candidate for surface passivation on *n*-type surfaces (see e.g. [115]), which was since investigated by various groups [87, 109, 115, 116].

The electronic structure of Si_3N_4 and SiN_x were analyzed by Deal *et al.* [117], Ren and Ching [118] as well as Robertson [119] and in more detail [120]. Apart from sputtered SiN_x, the films usually contain a significant amount of hydrogen and is therefore denoted as SiN_x:H.[1] The x in SiN_x is defined as the ratio of the Si-N bonds to the total number of bonds

$$\frac{[\text{Si—N}]}{[\text{Si—Si}] + [\text{Si—N}]} = \frac{3}{4}x. \tag{5.1}$$

N—N bonds are not expected in SiN_x due to the low stability of N—N single bonds compared to the triple bond as in molecular nitrogen [120]. Dauwe [109] showed that an empirical description of x and the refractive index can be defined for hydrogenated SiN_x

$$x = \frac{0.74}{n - 1.35}. \tag{5.2}$$

[1] In this work all investigated layers contain hydrogen and the :H is omitted. It is however being used to distinguish between doped (SiN_x:P) and undoped (SiN_x:H) films, although both of them contain hydrogen and likely a similar amount.

Depending on the amount of incorporated hydrogen the relation between x and n might vary, though [120]. For this, Mäckel and Lüdemann determined relations taking the hydrogen content (or rather that of the Si-H and N-H bonds) into account [121]. Either relation shows that the optical properties of SiN_x are strongly influenced by the composition of the deposited material. Therefore, the bandgap of SiN_x can range from approx. 1.7 eV (Si-rich layers) up to 5.3 eV (for quasi-stoichiometric SiN_x).

Robertson noted that SiN_x can contain up to 40 % hydrogen, more than a-Si:H ($\approx$ 10 %) [122]. The hydrogen content tends to increase slightly with increasing nitrogen content according to [120]. However, these observations are made for NH_3 precursors and might not hold in case of N_2 as used in this work, since Robertson also noted that N—H groups are »strongly favoured« compared to Si—H groups, while in our material no N—H groups could be detected by Fourier-Transformed Infrared Spectroscopy (FT-IR). In-depth stud-

Table 5.1: FT-IR peak positions and calibration factors as determined by Bustarret *et al.* [123].

Bond	Position cm^{-1}	Mode	K $1 \times 10^{19}\,cm^{-2}$
SiN	845 – 870	asym. stretch	2.07
NH/NH_2	1175	wag-rock	2.07
NH_2	3445	stretch	50
$HSiN_2Si/H_2SiNSi$	2140	stretch	11
H_2SiN_2	2175	stretch	40
$HSiN_3$	2220	stretch	20

ies of the FT-IR properties of SiN_x were performed by Bustarret *et al.*, the respective peak positions are given in Table 5.1. Studies on the hydrogen content before and after firing were performed by Gatz *et al.* [112] and Cuevas *et al.* [124]. The former analyzed the peak position of the S—H bond at around 2100 cm^{-1}, which moves slightly depending on back-bonding of the S—H groups. They found that for N-rich layers, the S—H bond is back-bonded at a higher degree to nitrogen, which they attributed to the thermal stability of the surface passivation due to a larger bonding strength of hydrogen. Cuevas *et al.* analysed the Si—N bond density and found that it increased by approx. 5 to 10 % after firing depending on the Si/N ratio. They analyzed the hydrogen bond densities as well, finding that the density of of both Si—H and N—H bonds decreased significantly during firing, especially for high-n layers. e.g. for a Si/N ratio of $\approx$ 1.3 the overall (bonded) hydrogen concentration de-

creased from 20 % to 5 %. Similar to Gatz *et al.* they observed a shift towards higher wave numbers of the Si—H peak(s) during firing. A discussion of both FT-IR and *Raman* on SiN_x can be found in [125], *Raman* spectra for Si_3N_4 can be found in [126].

Defects play an important role in SiN_x:H. For Si-rich SiN_x, this defect structure is comparable to that of a-Si [122], although it is normally not a semiconductor. The transition from an insulator to a semiconductor happens in the range of 2 % nitrogen content [127]. In N-richer SiN_x, especially the K^+ centers, which represent th NH_4^+ state, are of interest, as these create a fixed positive charge density [122]. This fixed positive charge density can be in the range 1×10^{11} to $2 \times 10^{12}\,\mathrm{cm}^{-2}$, thus good prerequisites for *n*-type passivation [115]. Under certain conditions SiN_x might be forced (by corona charging) into a state featuring a negative fixed charge density, if isolated from the silicon bulk [110]. While there were studies suggesting that the charge density might be depend on light irradiation [128, 129], Dauwe *et al.* showed that the charge density of SiN_x does not depend on the injection level [130].

For an excellent passivation, not only a high fixed charge density is desirable but a low D_{it} as well. For SiN_x, the defect density is expected to increase with increasing nitrogen content which can lead to a higher D_{it} as well, although with x higher than 1.1 the defect density can decrease [122]. Thus the values given for D_{it} in the literature can range from values as low as 1×10^{11} to $1 \times 10^{13}\,\mathrm{cm}^{-2}\mathrm{eV}^{-1}$ [115]. For both Q_{f} as well as D_{it} the deposition conditions (e.g. temperature) as well as the thermal treatment afterwards (annealing temperature, firing process) can have a huge influence. Therefore—depending on the process requirements like thermal stability—adaptions to the PECVD process might be necessary as investigated in Chapter 6. As Q_{f} and D_{it} could not be measured for the deposited layers, their influence was investigated indirectly by measuring the effective minority carrier lifetime.

5.1.2 Amorphous Silicon Carbide

SiC and a-SiC_x can be used for a wide range of purposes [131]. In photovoltaics, it can for example be used as a barrier or substrate [132].

For classical, wafer based solar cells, SiC_x was commonly investigated as a surface passivation as introduced by Martín *et al.* [133, 134]. This topic was since investigated by various groups for passivation of silicon bulk [133–137]

as well as n^+ and p^+ emitter passivation [138–141]. While some investigations were made [135, 138] for the passivation after a firing step (e.g. the results by Glunz *et al.* would result in a $J_{0b,pass}$ in the range of 41 fA/cm^2), the best results were obtained for a low temperature approach (post-deposition treatment below 500 °C, $J_{0b,pass}$ below 10 fA/cm^2). It was found that the properties of passivating SiC_x are similar to those of a-Si:H [142], but with a higher deposition temperature being required [133] and with a higher annealing temperature being allowed [143]. It was determined that a small (either positive or negative) Q_f can be present [133] but mostly the passivation performance relies on a low D_{it}. All initial experiments were performed on Radio Frequency (RF) plasma reactors, but a transfer to Microwave (MW) technique was demonstrated [144]. A more detailed analysis of the properties of passivating SiC_x can be found in [143].

The similarity of a-Si:H and SiC_x:H led not only to excellent passivation performance, but also to hetero structures based on SiC_x [145]. However these could not achieve the same performance as corresponding a-Si:H layers due to a reduction in *FF* and V_{oc}, which can be attributed to the lower doping efficiency of the layers. Nevertheless the approach was further pursued both utilizing intrinsic as well as doped SiC_x layers due to the higher bandgap of the SiC_x layers [146], resulting in less absorption if applied to the solar cell front side. Another approach featuring selective contacts is *TOPCon*. In this case a SiC_x layer is used in combination with a tunnel oxide to form a selective contact on *n*-type [10, 147] as well as *p*-type [148]. In comparison to PERL, this concept has the advantage of featuring a 1D transport on the rear [149], thus reducing the influence of the wafer resistance to a minimum and overcoming the compromise between *FF* and V_{oc} that is necessary for PERL cells.

In addition to passivation purposes, SiC_x was investigated for the single purpose of a Anti-Reflective Coating (ARC) [141, 150–153] and can be an alternative to SiN_x, if the passivating properties are not important (e.g. in combination with a dedicated passivation layer like Al_2O_3).

5.2 Laser Doping

5.2.1 History of Laser Doping

The following section was adapted from the publication [154].

The first occurance of laser doping or laser diffusion for silicon devices was in 1968 by Fairfield and Schwuttke [17]. They used a ruby laser to generate a phosphorus-doped region on *p*-type silicon. Prior to laser irradiation the dopant was deposited onto the surface by a paint-on technique. The idea was soon adapted by Harper and Cohen in 1969 who deposited aluminum by Physical Vapour Deposition (PVD) on *n*-type silicon. The junction was then formed by pulsed laser irradiation by a Nd:YAG laser [155].

Due to the short process time (common pulse length was usually in the range of micro seconds) defect analysis was an important topic for early investigations, e.g. [156–161].

Not only intrinsic effects were studied, but the effect of impurity inclusion as well. For dopands, Stuck *et al.* performed a broad investigation on the solubility of dopants in silicon after laser doping for which they found concentrations exceeding the equilibrium solubility limit [162]. Such effects were investigated in more detail by Wood *et al.* who presented a model for laser diffusion of dopants. This model predicted a segregation coefficient that was significantly higher than the equilibrium segregation coefficient [163–165]. These investigations especially showed that the equilibrium diffusion theory cannot always be applied to a dynamic, driven process like laser diffusion. For example while boron and phosphorus in equilibrium show diverting behavior during diffusion, especially showing a different segregation behavior, for laser diffusion the difference in segregation between the two is expected to be negligible [164]. Another model for laser diffusion was developed by Fogarassy *et al.* [166].

While the inclusion of dopants during the laser doping is usually a wanted effect (hence the name laser doping) depending on the dopant source and ambient the inclusion of other impurities has to be considered as well, for example oxygen [167] and nitrogen [168]. For nitrogen, Hameiri *et al.* found that laser pulse processing of a SiN_x (or SiO_x/SiN_x) coated surface can result in a high amount of nitrogen being included into the silicon surface, above the equilibrium solubility of nitrogen in crystalline silicon [168]. They suggested that the induced nitrogen can result in stress and therefore crystal defects in silicon. In addition, they proposed that remnants of the SiN_x layer as well as

the high amount of nitrogen at the surface could lead to a lower conductivity at the surface as well as reduced contact ability. Geisler *et al.* found that Continuous Wave (CW) laser doping on a SiN_x coated surface can result in voids created by nitrogen bubbles forming especially at the ablation edge [169].

After the initial experiments by Fairfield *et al.*, it did not take long, until laser doping was proposed to be used in solar cell fabrication. In the first experiments the dopant source layers were either implanted [170, 171] or evaporated [172]. While for these early applications the focus was on generating a homogeneous junction, using a laser has the advantage of enabling localized processing of silicon wafers and hence defining contact and/or selective emitter structures as well as a LBSF. In addition, as reported by Fogarassy *et al.* [172], the dopant source might require removal after the laser process. This would especially be the case for local laser processing of a non-locally deposited dopant source.

This highlights one of the advantages of the Laser Fired Contacts (LFC) concept presented by Schneiderlöchner *et al.* [18]. The LFC concept used aluminum deposited on the rear as a dopant source to create a LBSF for *p*-type silicon solar cells. As the aluminum at the same time was used as the rear side metallization it was an integral part of the final cell structure and did not require removal after the laser process. However, as aluminum in silicon forms an acceptor state such an approach cannot be used for creating donor states, i.e. as (selective) emitter on *p*-type or as a LBSF on *n*-type silicon.

LFC was proposed as an alternative to PERC solar cells which at the time did not make use of laser processing or diffusion [173]. Instead the silicon bulk was commonly contacted directly, without a LBSF. However, as proposed by Agostinelli *et al.* [174, 175] today PERC cells apply a Laser Contact Opening (LCO) process on the rear followed by screen printing of aluminum and a subsequent firing process, thus forming a very similar structure. This effectively turns PERC into PERL cells.

5.2.2 Laser Doping from Amorphous Passivation Layers

In case of a desired *n*-type doping the previously mentioned approaches utilizing aluminum cannot be used. As an alternative solution, Wenham *et al.* proposed the use of dielectric passivation layers as a dopant source to create selective emitter structures [176]. The *PassDop* approach introduced by Suwito *et al.* demonstrated an industrially feasible realization based on

SiC_x:P of such a concept with the focus on the rear side passivation of *n*-type silicon and using phosphorus as the LBSF dopant [19]. Similar to LFC, the dopant source—the rear side passivation layer—is an integrated part of the final solar cell and does not have to be removed after laser doping. This concept of using passivation layers as dopant sources for laser doping was since investigated by various groups. Laser doping from SiN_x:P and SiN_x:B was demonstrated by Paviet-Salomon *et al.* as well as Hameiri *et al.* for the application as emitter passivation/selective emitter formation or rear side passivation/LBSF formation [168, 177, 178]. Steinhauser *et al.* presented a similar approach called *fPassDop* based on SiN_x:P for the application as a rear side passivation of *n*-type silicon solar cells [179]. This is covered in more detailed in the Chapters 6 and 8.

As an alternative to LFC and PERC on *p*-type silicon, Ortega *et al.* showed laser doping of aluminum from Al_2O_3/SiC_x:H stack [180]. Laser doping of aluminum and boron for *p*-type silicon from Al_2O_3/SiC_x:B stacks was demonstrated by Steinhauser *et al.* [181].

5.3 *PassDop*

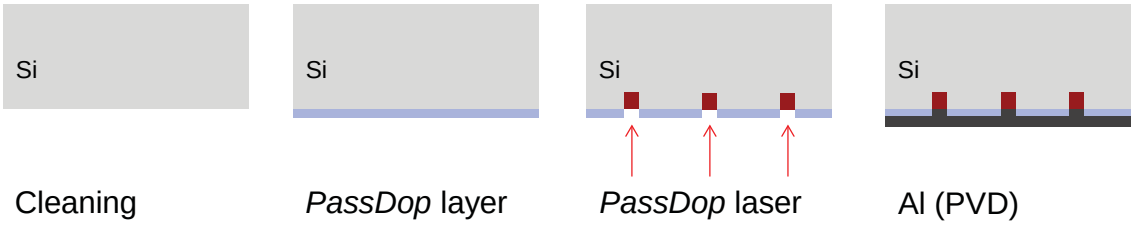

Figure 5.1: Process sequence for the *PassDop* approach. Starting with a clean surface, the rear side is coated with the *PassDop* layer, commonly by PECVD, passivating the rear side. In the next step, the *PassDop* laser process is applied, simultaneously opening the rear side and driving dopants from the *PassDop* layer into the silicon, creating a LBSF. In the last step, the rear side metallization is finished, usually by applying PVD aluminum.

The *PassDop* approach as mentioned in the previous section was originally presented by Suwito and Jäger [19, 182]. The basic process sequence is described in Figure 5.1. Three processes are required (and possibly a cleaning step prior to processing): 1. Deposition of a passivation layer, usually by PECVD. This layer must be doped. 2. Local laser processing. In this step laser doping is used to create a LBSF and at the same time the passivation layer is locally opened to allow for a metal-semiconductor contact. 3. Deposition of the rear side metal to establish a contact. Here commonly PVD is used, but other techniques like screen printing can be possible [154].

From these processes, some requirements can immediately be pointed out:

1. The layer has to provide a good passivation. The goal here was set to $J_{0b} \leq 10\,\mathrm{fA/cm^2}$.
2. The layer has to provide dopants and has to have a good doping efficiency during the laser doping. Here the goal was set to $R_{\mathrm{Sheet}} \leq 50\,\Omega/\mathrm{sq}$.
3. During the laser process, parts that did not contribute to doping should be removed, thus creating a good contact opening.
4. The layer (or stack) should result in good rear reflectance, thus improving light trapping.

In addition, it might be a requirement to reach a certain surface doping in the LBSF to achieve a good contact. The level of surface concentration depends on the metal to be used in the device, e.g. for aluminum the threshold is in the range of $1 \times 10^{19}\,\mathrm{cm^{-3}}$.

It should be noted that these requirements should not be seen as a precise limit, but instead as rough estimates for a functional *PassDop* layer. Especially the requirement »doping efficiency« is vague. One of the reasons is that while R_{Sheet} is relatively easy to determine, the better information is the doping profile, which however is rather tricky to determine properly (see Chapter 7). The other one is that the exact requirements may depend on the cell concept as in some cases the potential of the cell is limited by some other parts and compromises for the rear side might be made to allow for a simpler process.

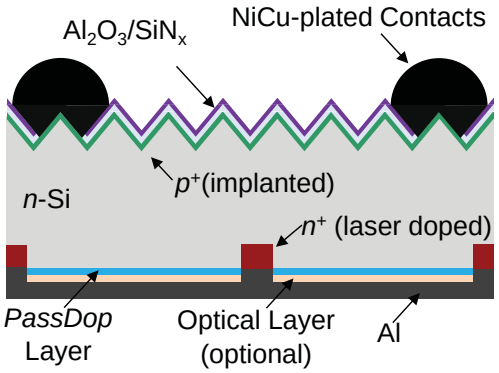

Figure 5.2: Layout of a *PassDop* PERL cell, here as an example for an *n*-type *PassDop* cell with NiCu-plated front contacts.

The basic layout for a *PassDop* cell is similar to the one shown in Figure 5.2. The cell features contacts on both side, a front emitter and both front and rear passivation. For *n*-type cells, the emitter is done by boron diffusion or implantation and is passivated by Al_2O_3. As a ARC, SiN_x is being used.

On the rear the *PassDop* process is applied. To account for the optical requirements an optional optical layer may be applied. This layer does not have to fulfill laser doping requirements other than allow for a good contact opening. As a metal contact, PVD aluminum was used throughout this work.

The front contacts can either be realized by PVD of titanium, palladium and silver, plating of nickel and copper or screen printing of aluminum/silver pastes. Which one is being used depends on the cell concept.

5.3.1 Status Quo

The original *PassDop* approach featured a multifunctional stack based upon SiC_x [19, 143, 182, 183]. In the stack, three layers were used: 1. 30 nm SiC_x:H *Passivation* layer, C-content: $\approx 3\,\%$ 2. 30 nm SiC_x:P *Doping* layer, C-content:

≈ 3 % 3. 30 nm SiC_x:P *Optical* layer, C-content: ≈ 60 %. For this stack a $S_{pass} < 5$ cm/s was given resulting in a V_{oc} of 701 mV at the device level while retaining a high *FF* of 80.1 % and an efficiency of 22.4 %. The recombination at the contacts was given by a determined value of $S_{met} \approx 3600$ cm/s.

For the laser process, a Rofin StarCut Disc 100 ICQ disk laser operating at a wavelength of 1030 nm was used with a pulse width of 1 µs. Both the profile depth and the R_{Sheet} were determined in dependence on the laser fluence.

5.3.2 Overview over the *PassDop* Approaches

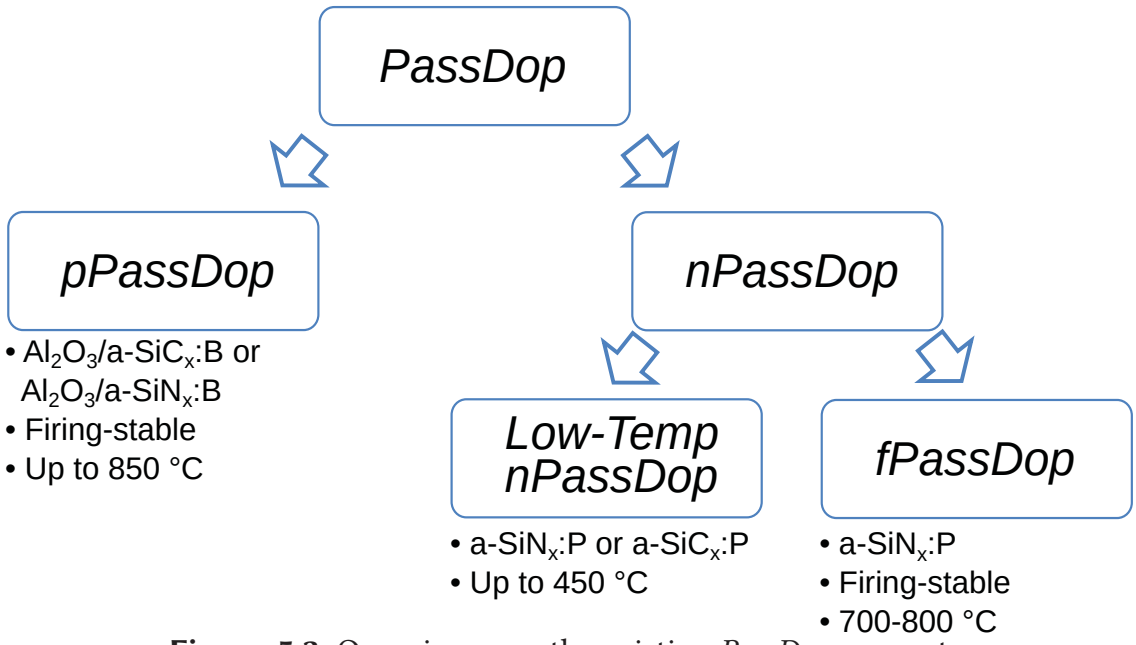

Figure 5.3: Overview over the existing *PassDop* concepts.

Figure 5.3 gives an overview over the different *PassDop* that were developed within this work as well as those that were developed besides. *PassDop* approaches for both *n*-type (*nPassDop*) as well as *p*-type (*pPassDop*) silicon rear sides do exist today. Table 5.2 lists the respective *PassDop* processes and generations including the label that was used for them throughout this thesis.

On *n*-type, the work on SiC *PassDop* was extended as presented in Section 6.2.1 (»SiC *PassDop* Gen2«). At the same time, a similar approach based on SiN_x was developed as an alternative. Both a single layer (»SiN *PassDop* Gen1«) as well as a stack (»SiN *PassDop* Gen2«) were developed. This is presented in Section 6.2.2. These approaches focus on providing a rear side concept featuring a minimum of rear side recombination (total J_{0b} below 50 fA/cm^2) with a temperature stability up to 450 °C. As these concepts

cannot be used for a metallization approach requiring high-temperature activation, an additional concept called *fPassDop* was introduced Similar to SiN *PassDop*, *fPassDop* is based on a-SiN_x:P as well, but the compositions and processes differ in detail. The properties of this concept will be discussed in Section 6.3 (»*fPassDop* Gen2« and »Gen3«). For »*fPassDop* Gen1«, see [179].

On *p*-type, the approach proposed by Suwito based on SiC_x:B [143] was not further pursued, instead an approach based on the well known and stable passivation performance of Al_2O_3 was introduced. To improve the doping efficiency either a SiC_x:B [181] (*pPassDop* Gen1) or SiN_x:B (R&D, *pPassDop* Gen2) can be used. Both solutions combine a good doping efficiency with a firing stable passivation (thus a separation like for *nPassDop* is not required).

Table 5.2: Overview over the *PassDop* layers and their label that was used throughout this work. T_{max} gives the »safe« maximum temperature for the cell process after deposition. The value is not meant as an absolute limit. It can be possible to exceed T_{max} depending on temperature and duration of the treatment. For temperatures below 500 °C T_{max} refers to a forming gas annealing. For temperatures above 500 °C this refers to a firing step with a peak duration of 3 s.

PassDop Type	Technology	Label	T_{max} [°C]	Description
nPassDop	SiC_x	SiC *PassDop* Gen1	350	[19, 182]
nPassDop	SiC_x	SiC *PassDop* Gen2	400	6.2.1
nPassDop	SiN_x	SiN *PassDop* Gen1	425	6.2.2, Single layer
nPassDop	SiN_x	SiN *PassDop* Gen2	425	R&D, Double layer
nPassDop	SiN_x	*fPassDop* Gen1	850	[179]
nPassDop	SiN_x	*fPassDop* Gen2	850	[179] and 6.3.2
nPassDop	SiN_x	*fPassDop* Gen3	800	6.3.2
pPassDop	Al_2O_3/SiC_x:B	*pPassDop* Gen1	800	[181]
pPassDop	Al_2O_3/SiN_x:B	*pPassDop* Gen2	800	R&D

6 Development and Characterization of *PassDop* layers

In this chapter, the development and characterization of PassDop layers for n-type solar cells is described.
The first part discusses the ongoing development of the original approach SiC PassDop. Here, the next generation will be presented with focus on improved doping efficiency and thermal stability.
As an alternative to SiC PassDop, a new approach based on SiN_x:P (SiN PassDop) will be presented. This approach is focused on low-temperature metallization like plating as well, but simplifies the PassDop process further by implementing a single layer.
The last approach that will be presented is the firing stable PassDop (fPassDop) based on SiN_x:P. Here, the focus is on double layer stacks for which three different variants will be discussed.

6.1 Sample Layout and Standard Parameters

In this section an overview over parameters and sample types that were commonly used throughout the development work of *PassDop* layers is given. Mainly two sample types were used: 1. *n*-type samples to determine the passivation quality 2. *p*-type samples that were used to characterize the doping capabilities in conjunction with the *PassDop* laser process. The two sample types are described in detail below. The given procedure remained identical for all discussed *PassDop* layers unless explicitely stated otherwise.

Samples for Lifetime Measurements

For the characterization of the passivation properties of *nPassDop* layers, 1 Ω cm *n*-type, Floatzone (FZ) shiny-etched wafers with a thickness of 200 µm

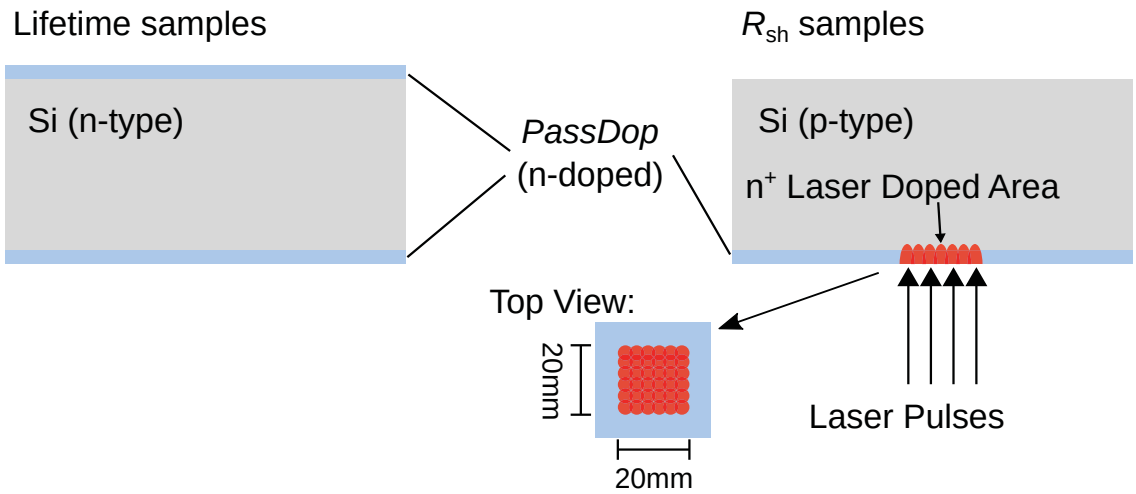

Figure 6.1: Standard sample structure as used throughout this work. The passivation samples were symmetrically passivated *n*-type wafer. The R_{Sheet} samples were *p*-type samples that were coated on one side and subsequently processed with overlapping laser points to create laser doped areas.

were used. Prior to the deposition of the layers, the samples received a cleaning in Nitric Acid (HNO_3) followed by a dip in Hydrofluoric Acid (HF). The samples were then coated with the layer on both sides as shown in Figure 6.1 on the left. Depending on the whether a firing stability was required or not, a temperature step was selected to activate the passivation. *fPassDop* samples received a high temperature step in a single wafer rapid thermal processing reactor at an actual sample temperature of 700 to 850 °C with a peak duration of 3 s. The process temperature was controlled by a pyrometer which was calibrated for the respective samples. For layers aiming for low temperature metallization and thus not requiring a firing step, a Forming Gas Anneal (FGA) at 425 °C for 25 min was used in case of SiN_x passivation layers. The lifetime was measured before and after the activation of the passivation. All lifetime measurements were done using a WCT-120 Quasi-Steady-State Photoconductance (QSSPC) lifetime tester by Sinton Instruments [68] unless stated otherwise. The lifetime was determined at $\Delta n = 5 \times 10^{14}\,\text{cm}^{-3}$.

Samples for Laser Doping

To characterize the basic doping properties and the doping efficiency of the *PassDop* layers, samples with a base doping opposite to the layer doping were used to form a *pn*-junction after applying the laser process. Thus, for *nPassDop* layers, *p*-type, FZ shiny-etched wafers with a thickness of 250 µm were used. After the deposition, the samples were processed with the laser to characterize the doping efficiency. During the laser process, a pulse distance of 25 µm with a line distance of 25 µm was used, creating seven 20 mm × 20 mm

areas of overlapping laser spots, each processed with a different laser fluence as shown in Figure 6.1 on the right. The operlapping point structure was necessary to create a macroscopic structure large enough for characterization with common tools. R_{Sheet} was measured by using a 4-point probes (4pp) measurement tool.

Samples for other Characterization Methods

10 Ωcm *p*-type, FZ shiny-etched c-Si samples with a thickness of 250 µm were used to measure Fourier-Transformed Infrared Spectroscopy (FT-IR). The samples were coated with the (single) layer of interest single sided. These samples were not only used for FT-IR measurements, but for spectral ellipsometry as well to determine the refractive index and the film thickness. If a single value is given for the refractive index, it refers to the value of n at a wavelength of 632 nm. If a single value is given for the extinction coefficient, it refers to the value of k at a wavelength of 300 nm.

Laser Parameters

Unless stated otherwise, all laser processes were done using a Jenoptik IR70 diode pumped solid state laser system operating at a repetition rate of 30 kHz and a wavelength of 1030 nm. The pulse length was set at 1300 ns, the beam waist on the substrate was $2\omega_0(1/e^2) = 68.5\,\mu\mathrm{m}$.

6.2 Layers for low-temperature Metallization for n-type Solar Cells

6.2.1 SiC *PassDop*

Motivation

Originally developed within the work of Suwito [143], the SiC_x passivation process gave a reliable and good reference point for the implementation of a *PassDop* layer, which is referred to as »SiC *PassDop* Gen1«. However, there were some areas, where there was thought to be some room for improvement, mainly the temperature stability and the doping efficiency. Thus, within this work, fine-tuning was done for this layer stack. The updated stack is referred to as »SiC *PassDop* Gen2«. A new *Capping* layer (see Figure 6.2) was introduced to retard effusion of hydrogen, which was the main degradation

mechanism with increasing temperature as pointed out by Suwito. The thickness of this layer was varied to point out the effect the *Capping* layer has on the passivation properties.

To improve the doping efficiency, adjustments were made to the thicknesses of the *Passivation* and *Doping* layers (see Figure 6.2). The thickness of the *Passivation* was reduced to a minimum (from 30 nm to approx. 3 to 5 nm). The thickness of the *Doping* layer was increased (from 30 nm to approx. 40 nm). This led to an increased fraction of doped layers (*Passivation + Doping* layer) from approx. 50 % to approx. 90 %. As it will be shown that neither the *Capping* nor the *Optical* layer contribute significantly to the laser doping process, this is the main influence on the doping efficiency.

The experiment can be divided in three parts:
Experiment 1: the influence of the changes in the stack on the basic *PassDop* properties passivation (S_{pass}) and doping efficiency (R_{Sheet}).
Experiment 2: the influence of the *Capping* layer on the temperature stability of the passivation (S_{pass}).
Experiment 3: the influence of the *Capping* and *Optical* layer on the doping efficiency(R_{Sheet}).

Experimental

For the deposition of the SiC *PassDop* stacks, a Roth & Rau AK400M batch-type Plasma-Enhanced Chemical Vapor Deposition (PECVD) was used, which is described in Section 4.2. For the *Passivation*, *Doping* and *Capping* layers, only the Radio Frequency (RF) plasma source was used for plasma excitation. For the *Optical* layer, a higher power density was required, thus both the RF as well as the Microwave (MW) plasma source were used in combination.

The annealing steps in *Experiment 2* were performed on a hotplate under ambient air atmosphere. After the initial measurement of the lifetime using QSSPC the samples were annealed at the desired temperature for a given time multiple times until a total time of 60 min was achieved. After each hotplate step, the lifetime was measured again using QSSPC. For different temperatures different samples were used to avoid influences of previous temperature steps.

Results

Experiment 1 – Comparison of Gen1 and Gen2
Figure 6.3a shows the determined S_{pass} for the SiC *PassDop* Gen1 and Gen2 stacks. For Gen1, the best values were found close to 1 cm/s, the worst at

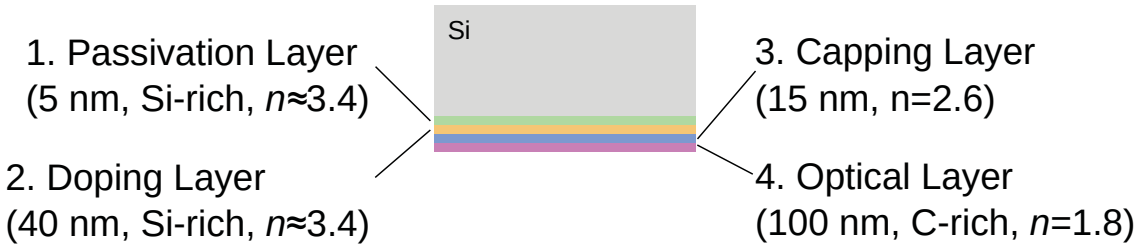

Figure 6.2: Basic layout of the SiC *PassDop* Gen2 stack, numbered in the order of the deposition process. 1. Initial passivation by an intrinsic, Si-rich ($n \approx 3.8$) *Passivation* layer, thickness approx. 3 to 5 nm. 2. The second layer is similar in composition ($n \approx 3.8$), but phosphorus-doped and therefore called *Doping* layer. This layer had a thickness of approx. 40 nm. 3. Newly introduced in Gen2: *Capping* layer of stoichiometric composition ($n \approx 2.6$), which protects the before-mentioned layers against effusion of hydrogen. 4. To improve internal reflectivity, a C-rich ($n \approx 1.8$) *Optical* layer finalizes the stack.
The SiC *PassDop* Gen1 stack is similar, but without the *Capping* layer and slightly different thicknesses for the *Passivation* layer (30 nm and *Doping* layer (30 nm).

6 cm/s with a mean value of 2.5 cm/s. For Gen2, S_{pass} was found to be generally lower, with all values being below 1 cm/s. The maximum was at 0.7 cm/s, the minimum at 0.15 cm/s. The mean was deteremined at 0.4 cm/s. Figure 6.3b shows the determined R_{Sheet} for the two stacks. R_{Sheet} for Gen1 was determined at around 20 Ω/sq for all laser fluences. For Gen2, R_{Sheet} was determined lower with a slightly increasing trend with increasing laser fluence. The values for R_{Sheet} reach from 11.5 Ω/sq to 13 Ω/sq.

Experiment 2 – Temperature Stability, Capping Layer Thickness Variation
Figure 6.4a and Figure 6.4b show S_{pass} after the temperature stability for a variation of the capping layer thickness of SiC *PassDop* Gen2 at 400 and 450 °C, respectively. Not shown are the results for a temperature of 350 °C, where no significant degradation within 60 min was found. For 400 °C (Figure 6.4a), it was found that a short treatment of 5 min does not result in a degradation but leads to a small improvement in S_{pass}. Starting at 10 min, an increase of S_{pass} with increasing annealing time was found. All *Capping* layer thicknesses showed a similar trend, but 15 and 20 nm were found to have a lower level of S_{pass} overall. After 60 min of annealing at 400 °C S_{pass} for these two *Capping* layer thicknesses was determined around $S_{\text{pass}} \approx$ 1 cm/s.

For 450 °C (Figure 6.4b), the overall trend was similar to 400 °C but stronger. A short annealing for a duration of 1 min led to a decrease in S_{pass}. Starting with 2 min annealing time, an increasing trend in S_{pass} was found. After 4 (*Capping* layer thickness of 5 nm) to 8 min (*Capping* layer thickness of 20 nm),

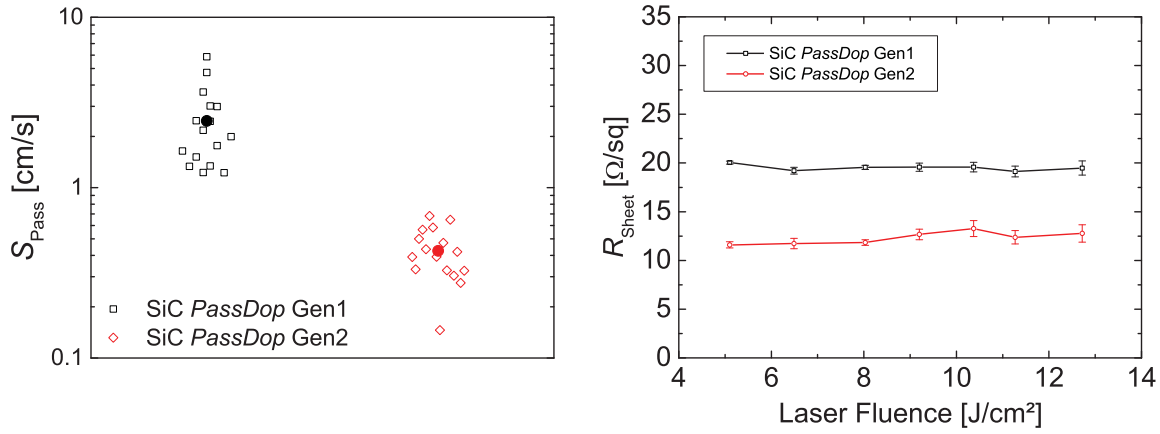

(a) S_{pass} **(b)** R_{Sheet}

Figure 6.3: Comparison of the SiC *PassDop* Gen1 and Gen2 stacks, showing the improved S_{pass} and R_{Sheet} by the performed changes in the layer stack outlined above. In (a) the solid circles give the mean of all measurements. In (b) the symbols give the mean of multiple measurements of the same laser doping area at different positions, the error bars give the standard error these measurements.

$S_{pass} = 1$ cm/s was exceeded. Similar to 400 °C the *Capping* layer thicknesses of 15 and 20 nm were found to have lower S_{pass}. With these, after annealing at 450 °C for 60 min, S_{pass} was determined around 3 to 5 cm/s. For 5 and 10 nm *Capping* layer S_{pass} after 60 min annealing was determined at around 9 and 20 cm/s, respectively.

Experiment 3 – Effect of Capping and Optical Layer on Laser Doping
Figure 6.5a shows R_{Sheet} for the (phosphorus-doped) *Capping* layer, the SiC *PassDop* Gen2 stack and the same stack, but with an undoped *Capping* layer. In all three cases, the thickness of the *Capping* layer was 10 nm. For the *Capping* layer alone, after exceeding a threshold below 6.5 J/cm^2, a R_{Sheet} of around 40 Ω/sq was determined with a tendency towards a lower R_{Sheet} with increasing fluence. For SiC *PassDop* Gen2, both with a doped and an undoped *Capping* layer, R_{Sheet} in the range of 13 to 15 Ω/sq was determined.

Figure 6.5b shows R_{Sheet} for *Doping* layer alone and for a stack consisting of only the *Doping* and *Optical* layer. After exceeding a threshold of 6.5 J/cm^2, R_{Sheet} was determined at approx. 17 Ω/sq with a nearly constant R_{Sheet}. For the stack of *Doping* and *Optical* layer, R_{Sheet} was found to be higher (around 21 Ω/sq) then for the *Doping* layer alone. No clear trend of R_{Sheet} with the laser fluence was found but the variation remained low.

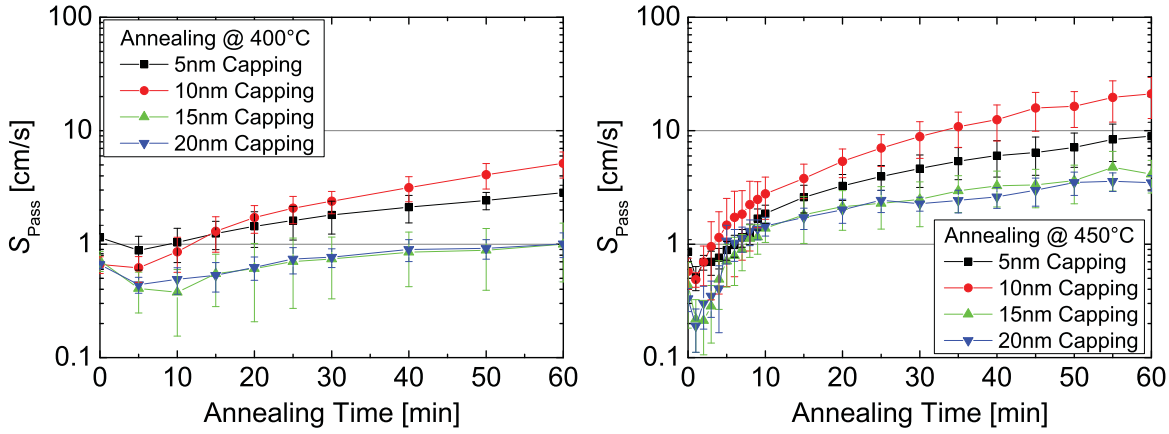

(a) Annealing at 400 °C. **(b)** Annealing at 450 °C.

Figure 6.4: Investigation of the temperature stability of the SiC *PassDop* Gen2 stack in dependence on the *Capping* layer thickness for 400 and 450 degree annealing temperature.

Discussion

As the passivation of the original SiC_x-based *PassDop* stack was already excellent, there was not much to do in regard to this. However, within previous work [141] it was found that a 5 nm thick *Passivation* layer was enough to achieve an excellent and reliable passivation. Thus, decreasing the thickness of the *Passivation* layer from 30 to 5 nm was not expected to have a a negative effect on the passivation performance. As shown in *Experiment 1* in Figure 6.3a, this was confirmed for the SiC *PassDop* Gen2 stack in comparison to Gen1, which still had the 30 nm thick *Passivation* layer. While a thinner intrinsic layer can lead to a stronger band bending and therefore an improvement in the passivation performance (due to field effect passivation), this should not be seen as the origin for the improvements in S_{pass} that can be observed in Figure 6.3a. As outlined above, the Gen2 stack features not only a change in the thicknesses of the *Passivation* and *Doping* layers, but a newly introduced *Capping* layer as well, which should prevent effusion of hydrogen during temperature steps. As the samples have to be flipped after depositing the films on one side, the passivation can degrade slightly during the deposition process of the second side. To be sure about this, samples were prepared, one with only the (30 nm thick) *Passivation* layer and one with a stack of the *Passivation* and (10 nm thick) *Capping* layer. While the former yielded a S_{pass} of 4.8 cm/s after the deposition, the latter achieved 1.7 cm/s. The remaining difference to S_{pass} of the SiC *PassDop* Gen2 stack can be explained by the absence of the doping layer and therefore band bending. Thus, the observed differences in S_{pass} between SiC *PassDop* Gen1 and Gen2 would not be expected when only performing a single sided deposition of the layers

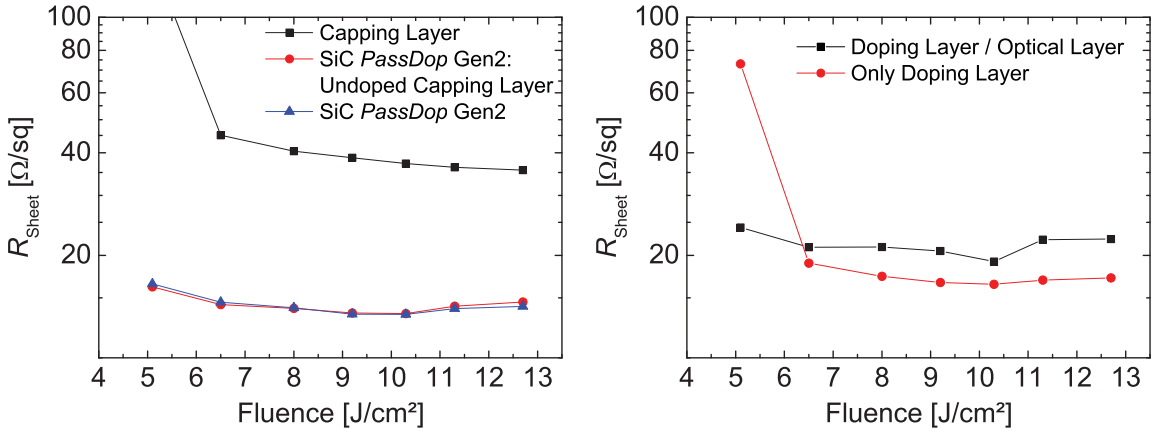

(a) Capping variation

(b) Anti-Reflective Coating (ARC) variation

Figure 6.5: R_{Sheet} results for two layer variations explaining the role of the *Doping* and *Optical* layer on the doping efficiency of the SiC *PassDop* Gen2 stack. (a) shows that the *Capping* layer itself does not contribute significantly to the doping process. (b) shows that the optical layer can have a slightly negative effect on the doping efficiency.

as done on solar cells and even if, at the given surface recombination velocities, the differences would be barely noticeable, as the increase in J_0 would amount to approx. 3 to 5 fA/cm^2.

As the passivation of the rear side is certainly not the last thermal treatment of the rear side passivation, it was important to further explore and possibly improve the thermal stability of the SiC *PassDop* stack. Suwito pointed out that for the SiC$_x$ passivation layer, the main degradation mechanism was found as being effusion of hydrogen under thermal treatment [143]. While it cannot be fully prevented, to retard this degradation mechanism a new layer was introduced, the *Capping* layer. Deposited at conditions resulting in very dense layers [184], it features near stoichiometric composition and thus a refractive index in the range of $n = 2.6$. While it was already shown in *Experiment 1* that the layer fulfilled its purpose, the effect was studied in more detail in *Experiment 2* as shown for an annealing temperature of 400 °C in Figure 6.4a and for 450 °C in Figure 6.4b. This experiment showed that the *Capping* layer can indeed reduce the degradation during annealing steps at 400 °C or above. While a 10 nm layer already did have some influence on the passivation performance (as already shown above) as the initial passivation performance was better than with a 5 nm *Capping* layer. The reason for the worse temperature stability of the stack with 10 compared to 5 nm *Capping* layer was not known, such an effect was not expected. However, it was clear that a *Capping* layer thickness of at least 15 nm was required for the best per-

formance. This allowed to keep S_{pass} at excellent level even when applying a long annealing of 60 min at 400 °C. The annealing at 450 °C (see Figure 6.4b) showed the limits of this approach. While the capping layer can retard the effects of hydrogen effusion, it cannot prevent them. If the temperature is increased, the diffusion of hydrogen was faster and therefore more electrical degradation of the passivation was the result. Still, if applying a minimum of 15 nm, the passivation was well preserved with $S_{pass} < 5$ cm/s after annealing for 60 min at 450 °C. For the SiC_x passivation layer alone (without *Doping* or *Capping* layer), such a temperature step would result in $S_{pass} \approx 30$ cm/s [143].

The second goal for the Gen2 optimization of the SiC *PassDop* stack was improving the doping efficiency. As shown in *Experiment 1* (see Figure 6.3b), this was successful as R_{Sheet} was reduced by approx. a third. Although the precise amount of phosphorus in the Local Back Surface Field (LBSF) could not be determined, this was less than expected given that the doping ratio in the *Passivation*/*Doping* layer stack was increased from 50 % to 90 %.

While it was relatively clear that the changes made to the *Passivation* and *Doping* layers would have a positive effect on R_{Sheet}, the influences of the *Capping* and the *Optical* layer were not so clear. The *Optical* layer itself can be doped, but the resulting R_{Sheet} would be in the range of of 150 Ω/sq which compared to the laser doping of the *Doping* layer would be insignificant. However *Experiment 3*, where the doping effect with and without the *Optical* layer was investigated, showed that the *Optical* layer can have a negative effect on R_{Sheet} in the stack as shown in Figure 6.5b.

As described by Jäger *et al.* [182], the c-Si is molten by the induced energy from the laser pulse. One additional result of the melting process and the heating of the c-Si is volume expansion. This expansion can lead to a burst of layers that were not (or could not be) molten. The overall higher level of R_{Sheet} in case of the *Doping*/*Optical* stack can be attributed to such an effect due to the higher thermal stability of the C-rich *Optical* layer. During the burst-off, this layer can take parts of the *Doping* layer that were not yet molten with it, hence the higher R_{Sheet}.

This leads to the possible role of the *Capping* layer in the Gen2 stack. From Figure 6.5a it can be extracted that the *Capping* layer itself can only provide a dose high enough to result in a R_{Sheet} of approx. 40 Ω/sq. Consequently, the influence on R_{Sheet} in the stack was almost non-existant, since the stack with the doped and the undoped layer yielded pretty much the same R_{Sheet}. Considering the dense and stable nature of (stoichiometric) SiC, both in crystalline as well as amorphous form, the *Capping* layer could retard the

burst of the layers under the pressure and heat of the melt and thus increase the amount of time available to transport phosphorus into the melt. This would—as a consequence—mean that the laser doping efficiency increased. The other effect the *Capping* layer could have on the laser doping process is to act as a sacrificial or buffer layer of which some parts can be peeled off without significantly affecting the doping efficiency, thus protecting the *Doping* layer.

As a last remark on the laser doping experiments, an explanation of the commonly observed trend of a slightly decreasing R_{Sheet} with increasing laser fluence is given. Such a trend can e.g. be observed in Figure 6.5a. Both the *Doping* layer (40 nm) and the *Capping* layer (15 nm) have a relatively small thickness. Hence, the laser process can be considered as doping from a finite doping source, the dose is nearly constant. With increasing laser fluence the penetration depth of the laser pulse will increase and so will the melting depth [182]. This will lead to a higher doping profile depth as well. If the dose is assumed constant a lower surface concentration will be the consequence [182]. As lower concentrations result in an increase in the carrier mobility, a decrease in R_{Sheet} is the result. At higher fluences, ablation of the doping source can influence the process and thus the assumption of a constant dose would not be correct anymore, the dose would be reduced (by the fraction of the ablated layer thickness) and therefore R_{Sheet} would increase, as observed above 10 J/cm^2.

6.2.2 SiN *PassDop*

Motivation

As shown in the previous section, the SiC *PassDop* stack provided excellent performance. However, this technology made use of the RF plasma source. Implementing high-throughput RF plasma deposition tools is certainly possible [185], but the in-line industrial standard is deposition of SiN_x (e.g. for ARC) using MW plasma excitation. As lined out in Section 5.1.1, SiN_x can serve as an excellent passivation of *n*-type silicon, it can be doped by both phosphorus and boron and it was shown that laser doping can be used to create localized doping structures.

Thus, in this section, a *PassDop* alternative to SiC_x:P based on SiN_x:P is developed. The goal is to deposit only a single layer and only to use MW plasma excitation as used in in-line industrial tools. Such a process might lead to a

higher acceptance of the *PassDop* technology as no significantly revised tools would be required.

Table 6.1: Comparison of the original process that was present when starting the work on the AK800 and the improved process that was used as a base for the development of SiN *PassDop*

	SiH_4 [sccm]	N_2 [sccm]	H_2 [sccm]	PH_3 [sccm]	p [Pa]	T_{dep} [°C]
Original	65	25	20	0	6.5	475
Improved	84	41	0	300	9.0	500

Process Basis

To establish a process for SiN *PassDop*, the process developed in the diploma thesis of Rauer [50] was used as a base. He developed a SiN_x passivation process for *p*-type bulk material on the AK800 PECVD reactor (see Section 4.3).

Prior to the *PassDop* experiments the process was significantly improved with the focus on passivation homogeneity, *n*-type passivation and temperature stability as well as doping capabilities. The pressure was increased from 6.5 Pa to 9 Pa, the hydrogen gas flow was increased to 300 sccm. Both had positive effects on the homogeneity of S_{pass}. As PH_3 diluted in H_2 was used, this also allowed to deposit doped layer under similar conditions as undoped layers. The gas flows of SiH_4 and N_2 were increased as well to 84 sccm and 33 sccm to decrease the effect of small gas flow changes on the process making the process more reproducible. To improve thermal stability, the N_2 gas flow was further increased to 41 sccm.

The relevant parameters for the original process and the improved process are listed in Table 6.1.

In contrast to SiC *PassDop*, a dedicated *Optical* layer is not used within these experiments. At the device level, a MgF_2 layer deposited by Physical Vapour Deposition (PVD) was used to improve light trapping (see Section 8.2).

Single Layer – Motivation

This experiment is used to performe a basic screening of the SiN_x:P process, both to determine the passivation quality as well as to acquire information about the doping capabilities. At the same time it is used to determine if a

single layer *PassDop* process can be found. The goal is a layer that can achieve $J_{0b,pass} < 10\,fA/cm^2$ (approx. $S_{pass} < 4.5$) as well as $R_{Sheet} < 50\,\Omega/sq$. Based on this experiment, SiN *PassDop* Gen1 was defined.

Single Layer – Experimental

All layers in this experiment were deposited using the base process. Only the nitrogen gas flow was varied from 30 sccm (highest n) to 41 sccm (lowest n). The PH_3 flow was kept constant at 300 sccm.

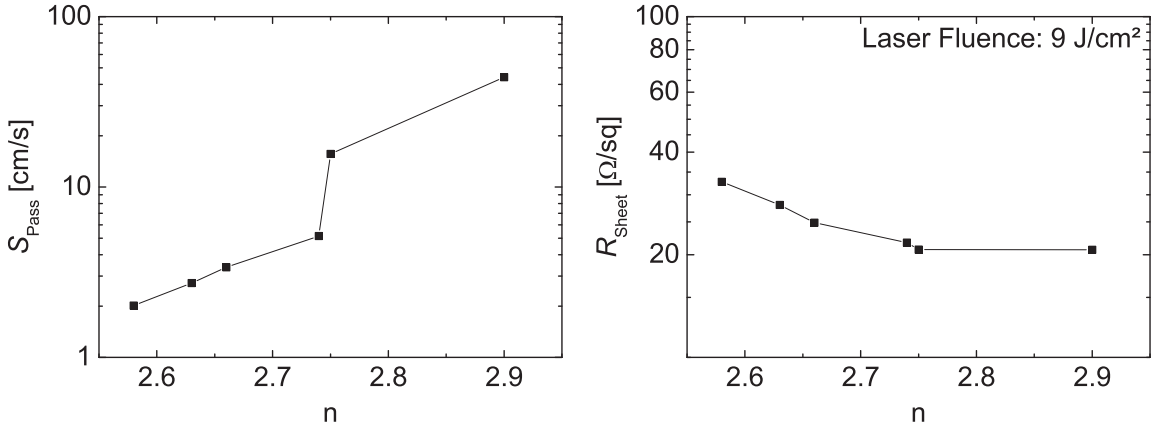

(a) S_{pass} **(b)** R_{Sheet}

Figure 6.6: S_{pass} and R_{Sheet} for the SiN *PassDop* layer in dependence on the refractive index. The process giving a refractive index of 2.58 was defined as »Gen1«. R_{Sheet} is shown for a laser fluence of $9\,J/cm^2$.

Single Layer – Results

Figure 6.6a shows S_{pass} for a single SiN_x:P layer in dependence on the composition, which is indicated by the refractive index. With increasing refractive index, an increase in S_{pass} was observed. At the lowest refractive index, $S_{pass} = 2\,cm/s$ was observed. At approx. $n = 2.75$ a large step in S_{pass} was observed from around 5 to above 10 cm/s. Figure 6.6b shows R_{Sheet} for the single layer. For the lowest refractive index R_{Sheet} of approx. $33\,\Omega/sq$ was observed. With increasing refractive index, R_{Sheet} decreased to a level of approx. $20\,\Omega/sq$. No significant changes in the layer thickness was observed within this experiment. All layer compositions were determined with a thickness in the range of 130 nm.

Single Layer – Discussion

There were two tasks for this first experiment to accomplish. The first was a general screening of the doping efficiency of the layer and the second was

to find out if a single layer *PassDop* system was possible with the SiN_x:P approach. The results determined for R_{Sheet} as shown in Figure 6.6b revealed that there was an influence of the layer composition and therefore the refractive index on the resulting R_{Sheet}, but even with the lowest investigated n of 2.58, R_{Sheet} at 35 Ω/sq was still below low the target of 50 Ω/sq.

Moving to a Si-richer layer and therefore to a higher n shows a gain in doping efficiency, but the R_{Sheet} reached for the lowest n should be sufficient. In comparison, the influence of the layer composition on S_{pass} was stronger as shown in Figure 6.6a. Therefore the final layer might be determined by the passivation performance rather than doping efficiency.

The observed trend mostly is a consequence of the temperature stability of the passivation. With increasing Si content and therefore increasing n, the layer composition is shifted towards a-Si and therefore the layer properties adapt to that. For the SiN_x deposition process, the sample temperature was determined by Rauer at 250 °C, while (pure) a-Si would require temperatures below 200 °C for a good passivation due to the decreasing hydrogen content with increasing temperature [186]. Thus for the SiN_x layers, with increasing Si content, the chosen deposition temperature was too high, explaining the increasing S_{pass}. If the effect is strong, it can be accompanied by blistering of the first deposited side lying on the carrier during the deposition of the second side. This could be compensated by reducing the deposition temperature. However, it would result in a lower temperature stability against annealing as well. One of the goals outlined in the motivation was to find a process that can withstand 425 °C to be compatible with the Al_2O_3 front side passivation of n-type solar cells with a front side boron emitter. Thus, thermal stability is an inherent requirement in the process and choosing a process closer to amorphous silicon would be the wrong direction.

However, as even for the lowest refractive index layer, R_{Sheet} was sufficiently low to act as a *PassDop* layer and as this layer showed an excellent S_{pass} potential, this layer was defined as SiN *PassDop* Gen1. This process used a SiH_4 gas flow of 84 sccm and an N_2 gas flow of 41 sccm. It was used in the following experiments as a reference.

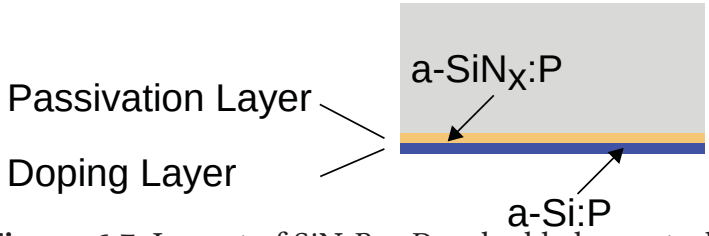

Figure 6.7: Layout of SiN *PassDop* double layer stack.

Double Layer – Motivation

The previous section showed that a single layer *PassDop* based on SiN_x:P was possible, both achieving a low S_{pass} as well as a low R_{Sheet}. However, the influence of the layer composition on S_{pass} and R_{Sheet} was strong in the used regime and therefore the process could be prone to process fluctuation. A two layer stack with each layer dedicated to a specific purpose could improve this as variations within each process would not yield such a strong influence on the overall *PassDop* properties. The layout of the stack is shown in Figure 6.7. The two layers in this section are denoted as *Passivation* layer, based on the SiN *PassDop* Gen1 single layer, and *Doping* layer based on a-Si:P. As a references the SiN *PassDop* Gen1 layer is used. Based on the experiment, SiN *PassDop* Gen2 was defined.

Double Layer – Experimental

The *Passivation* layer was based on SiN *PassDop* Gen1. The nitrogen gas flow was varied from 41 to 45 sccm to compensate a possible reduction in the S_{pass} performance. The thickness of the layer in comparison to Gen1 was slightly decreased to $\approx$ 80 nm to reduce the overall thickness of the stack. The *Doping* layer was based on SiN *PassDop* Gen1 as well, but with the nitrogen gas flow cut off, thus depositing a-Si:P. The thickness was set to $\approx$ 80 nm. Both layers were deposited without restarting the plasma, only the gas flows were changed, while pressure, temperature and plasma excitation remained constant. The Gen1 deposition was repeated as reference.

After the deposition, the layers received a thermal treatment by FGA at 425 °C for 25 min to investigate the compatibility with the front side passivation by Al_2O_3 as used in the solar cell process. The lifetime measurements by QSSPC were performed before and after FGA.

Double Layer – Results

Figure 6.8a shows S_{pass} for the double layer stacks as well as the reference Gen1. Directly after deposition for Gen1 a S_{pass} of 3.5 cm/s was determined, which is slightly higher than determined previously. For all of the double layer stacks a S_{pass} in the range of 2.5 to 3 cm/s was determined, thus lower than Gen1. No clear trend was observed after deposition when varying the nitrogen content in the *Passivation* layer. For all layers, a reduction of S_{pass} was observed after applying the anneal. With increasing nitrogen content, the effect of the annealing increased, thus S_{pass} before and after annealing showed a bigger difference.

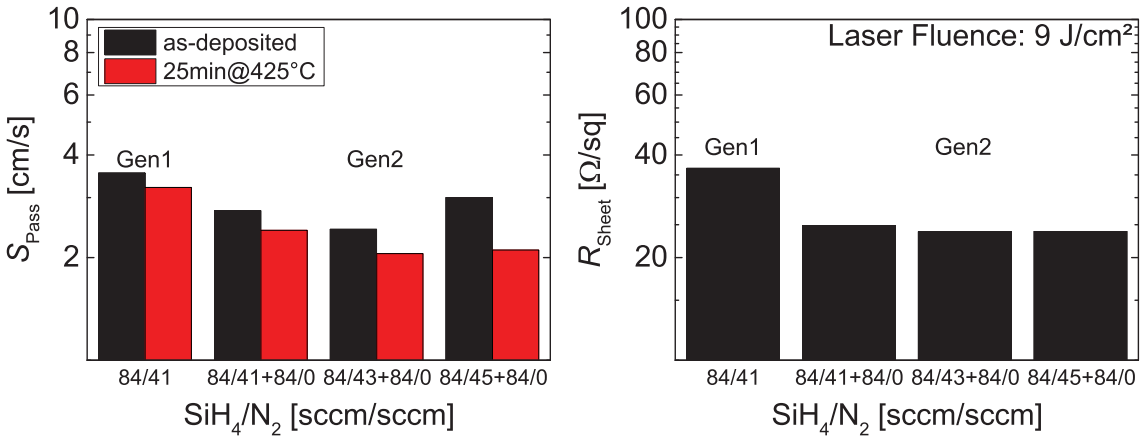

(a) S_{pass} **(b)** R_{Sheet}

Figure 6.8: S_{pass} and R_{Sheet} for a stack of an a-SiN$_x$:P passivation layer in combination with an a-Si:P doping layer in dependence on the nitrogen gas flow of the passivation layer. R_{Sheet} is shown for a laser fluence of 9 J/cm^2. The stack SiN$_x$:P/a-Si:P with 43 sccm N_2 was defined as »Gen2«.

Figure 6.8b shows R_{Sheet} for these stacks and Gen1. R_{Sheet} for Gen1 was comparable to the original result. For the double layers, R_{Sheet} was determined below 25 Ω/sq with no major variation due to the changes made to the *Passivation* layer.

Double Layer – Discussion

As the SiN *PassDop* Gen1 process was established, for this experiment the target was to improve the doping efficiency without significantly affecting the S_{pass} performance. As shown in Figure 6.8b, this was accomplished, as the double layer stacks showed a lower R_{Sheet} (in the range of 20 Ω/sq) than the reference Gen1 (around 35 Ω/sq). In addition, the N_2 gas flow variation for the *Passivation* layer had practically no influence on the determined R_{Sheet}. While the refractive index of the *Passivation* layers in the stacks could not be determined (and therefore is not given), a variation from approx. 2.6 to 2.4 in the refractive index would be expected based on previous depositions of these parameters. As the effects of such a double layer stack are expected to be more important for the firing-stable *fPassDop* process, the effects on laser doping are discussed in more detail in Section 6.3.2 and 7.1.3.

For the interpretation of S_{pass}, two effects have to be considered. First, a higher amount of nitrogen in the *Passivation* layer can lead to an increased amount of defects [120]. The second is that the formation of the (positively charged) K-centers is related to the nitrogen content as well. Thus an increase in the nitrogen content will lead to an increase in fixed positive charges. Especially this would be expected after thermal activation (i.e. FGA). This

means that an increase in the nitrogen content can lead to either an increase in S_{pass} or a decrease, as both effects influence the recombination at the interface.

While the overall differences in S_{pass} were small both for the Gen1 single layer as well as the stacks, these effects can explain the observed trends. For a given deposition temperature, it is expected that there is an »ideal« gas composition leading to a minimum in S_{pass} directly after the deposition. For Si-richer compositions, D_{it} is low, but the K-center density as well, thus leading to a higher S_{pass}. For N-richer compositions, D_{it} would be higher, but not enough K-centers were formed during the deposition to compensate the effect. To quantify this, a measurement of the surface potential (using, Corona Oxide Characterization Of Semiconductor (COCOS), see [187]) was performed, but due to leakage currents within the layer, the deposited charges were removed during the measurement invalidating the results.

Annealing had a positive effect on S_{pass}. As the effect was stronger for the N-richer compositions, this seemed to confirm the effects outlined above. The annealing results in the formation of more K-centers and therefore improved field-effect passivation. While the density of fixed charges could not be determined, it is known that the density increases with increasing nitrogen content [122].

In addition, hydrogen can diffuse during the thermal treatment and saturate dangling bonds at the surface. This especially could explain the (small) difference in the performance of Gen1 and the »84/41+84/0« double layer, as the a-Si:P layer can be seen as a hydrogen source. In case of hydrogen originating from N-H bonds in the *Passivation* layer, these do not contribute to the recombination as at these compositions the defect state lies outside of the band gap [122]. In case of S-H bonds, their contribution to recombination is insignificant if they are not close to the surface.

Overall, after annealing, the S_{pass} of the three double layer stacks in this experiment was similar. Thus, the process with a 84/43+84/0 was defined as SiN *PassDop* Gen2. As the changes in S_{pass} and R_{Sheet} with the changing *Passivation* layer composition were low, the Gen2 process is thus expected to be more prone against process fluctuation than Gen1.

The Role of Phosphorus – Motivation

The third experiment regarding SiN *PassDop* aimed at investigating the role of phosphorus in the layers. For a-Si, it is known that the presence of dopants increases the defect density and therefore recombination. The first part of

this experiment was performed to investigate the influence of phosphorus on S_{pass} by comparing the doped layers to respective undoped layers.

In the second part of the experiment parts of the *PassDop* layer or layer stack close to the c-Si/SiN_x interface were changed from SiN_x:P to SiN_x:H, thus not being doped anymore. This helps to understand the role of phosphorus close to the surface on the doping efficiency.

The Role of Phosphorus – Experimental

In the first part, only symmetrical passivation samples were created. The depositions using pure hydrogen were performed first to avoid cross-contamination by phosphorus. After the depositions using PH_3, a control deposition using pure hydrogen again was performed to test for cross-contamination. Only single SiN_x layers were deposited, stacks like Gen2 were not specifically investigated. Either the hydrogen or the phosphine gas flow were varied, thus the total gas flow changed and was not kept constant.

The second part with focus on doping efficiency was performed for Gen1 and Gen2. For Gen1, an additional SiN_x:H layer was introduced in between the SiN_x:P layer and c-Si, resulting in an SiN_x:H/SiN_x:P stack which is here called »Gen1:H«. For the SiN_x:H layer phosphine was set to 0, hydrogen to 300 sccm. All other deposition parameters were not changed. This resulted in an SiN_x layer of approx. 130 nm where the first approx. 25 nm were undoped. For Gen2, the *Passivation* SiN_x:P layer was replaced by SiN_x:H with the same parameters but phosphine changed to pure hydrogen, thus the first 80 nm of the SiN_x:H/a-Si:P stack being undoped. This stack is called »Gen2:H« here. As reference, the fully doped Gen1 and Gen2 were deposited as well. These standard layers are here called Gen1:P and Gen2:P to avoid confusion. Apart from replacing PH_3 (diluted in hydrogen) by pure hydrogen, no deposition parameters were changed compared to the Gen1 and Gen2 presented in the previous two sections.

In addition to 4pp, Electrochemical Capacitance-Voltage Profiling (ECV) measurements were performed as well. The ECV measurements were used to extract the profile depth. A significant increase in the profile depth due to the higher phosphorus concentration was not determined. As will be discussed in Section 7.1.3, the doping concentration cannot be reliably deteremined by ECV. Thus, a Gaussian profile ($N(x) = N_{\mathrm{peak}}\mathrm{Exp}(-x^2/{z_{\mathrm{F}}}^2)$) was defined using this profile depth and adjusting the surface concentration such that the R_{Sheet} determined by 4pp was matched. The profile was then used to calculate the phosphorus dose inside the silicon.

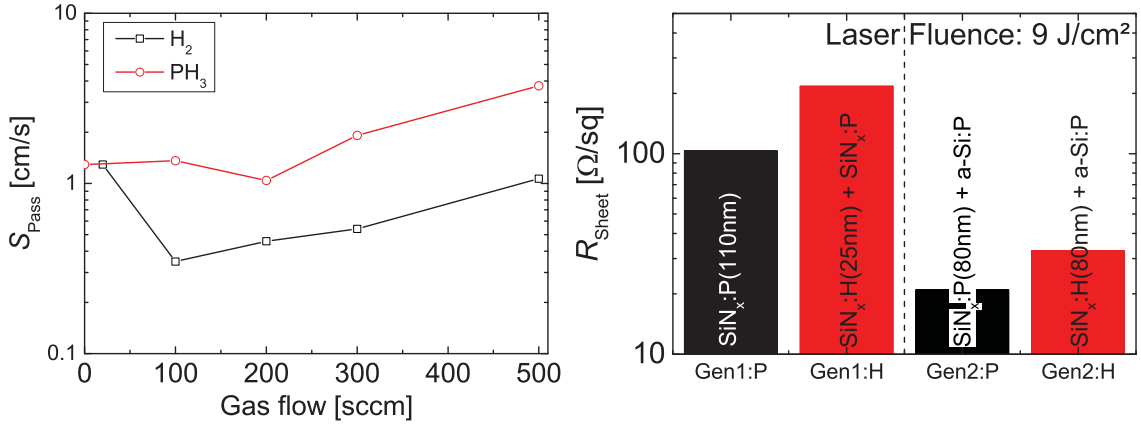

(a) S_{pass} **(b)** R_{Sheet}

Figure 6.9: (a) S_{pass} for a variation of the PH_3 doping gas flow during the deposition of SiN_x:P single layers. As a reference the layer was deposited without phosphorus doping, thus with a variation of the hydrogen gas flow. (b) shows R_{Sheet} for the stacks, where part of the stack was replaced by an undoped layer. The basis are SiN *PassDop* Gen1 and Gen2 (here denoted as Gen1:P and Gen2:P). For Gen1:H, the first 25 nm of the layer were undoped. For Gen2:H, the SiN_x *Passivation* layer was undoped and dopants were only provided by the a-Si:P *Doping* layer.

The Role of Phosphorus – Results

Figure 6.9a shows S_{pass} for a gas flow variation of hydrogen and phosphine for the SiN_x *Passivation* layer. Overall an increasing trend in S_{pass} with increasing gas flow was observed for pure H_2. 20 sccm pure hydrogen significantly deviated from the overall trend, since a decrease in S_{pass} from 1.3 cm/s (20 sccm H_2) to 0.35 cm/s (100 sccm H_2) was observed. At the maximum H_2 flow of 500 sccm, S_{pass} was just above 1 cm/s.

For diluted PH_3, S_{pass} was determined generally higher than with pure H_2. The overall trend was similar to that of pure hydrogen, but less pronounced below 300 sccm. The minimum S_{pass} was found at 200 sccm with 1 cm/s, the maximum at the maximum PH_3 gas flow of 500 sccm with $S_{pass} = 3.7$ cm/s.

Figure 6.9b shows R_{Sheet} for Gen1 and Gen2. The black bars give results for the normal (completely doped) layers as defined previously. The red bars give results for Gen1:H and Gen2:H stacks with an undoped *Passivation* layer. Gen1:H and Gen2:H gave a significantly higher R_{Sheet} than Gen1:P and Gen2:P, respectively. For Gen1 a R_{Sheet} of 100 Ω/sq was determined. For Gen1:H (the variant with 25 nm SiN_x:H) R_{Sheet} increased to over 200 Ω/sq. For Gen2, the standard with a doped *Passivation* layer was determined to be 21 Ω/sq. The Gen2:H variant with an undoped *Passivation* layer was determined to be 33 Ω/sq.

Table 6.2: Calculation of the phosphorus dose by adjusting a Gaussian profile with the formula $N(x) = N_{\text{peak}}\text{Exp}(-x^2/{z_F}^2)$ such that the depth matches the determined depth from the ECV profile and the calculated R_{Sheet} matches that determined by 4pp.

	4pp	Calculated			
PassDop Layer	R_{Sheet} [Ω/sq]	R_{Sheet} [Ω/sq]	N_{peak} [cm^{-3}]	z_F [µm]	P Dose [cm^{-2}]
Gen1:P	103	101	3.5×10^{18}	1.13	3.4×10^{14}
Gen1:H	217	215	8.0×10^{17}	1.3	9.0×10^{13}
Gen2:P	20.9	20.8	3.3×10^{19}	1.05	3.0×10^{15}
Gen2:H	32.9	32.4	1.8×10^{19}	1.1	1.7×10^{15}

The depth of the profiles determined by ECV was 2.7 µm for Gen1:P and Gen1:H and 3.0 µm for Gen2:P and Gen2:H. The results for the Gaussian profile evaluation are summarized in Table 6.2. For Gen1:P, the integration of the profile yielded a dose of 3.4×10^{14} cm^{-2}, for Gen1:H the dose was determined as 9×10^{13} cm^{-2}. The doses for Gen2:P and Gen2:H were 3×10^{15} cm^{-2} and 1.7×10^{15} cm^{-2}, respectively.

The Role of Phosphorus – Discussion

For a-Si layers—as used for hetero-junction solar cells—it is well known that the addition of dopants to the layer results in an increase in the defect density [186]. Robertson *et al.* [120, 122] noted that the defect structure of SiN_x is related to a-Si:H. Thus, it could be expected that the addition of phosphorus to the layer can result in an increase in S_{pass} due to a higher defect density. As shown in Figure 6.9a, such an effect was observed for phosphorus in SiN_x. While the performance without any PH_3 was similar to a process with low hydrogen[1], when adding dopants, the curves were spreading and for PH_3 the passivation performance was significantly worse.

When comparing the curves denoted as »H_2« and »PH_3 « an almost constant offset can be observed. Here, one has to keep in mind that the used PH_3 was diluted and 99.75 % of the gas was hydrogen. Therefore at identical gas flows the amount of hydrogen in the chamber was almost identical as well. This means that the differences can be attributed to the incorporation of phosphorus in the SiN_x layer and therefore—similar to a-Si—to de-

[1] The additional 20 sccm do not make a significant difference here, the performance with 0 sccm hydrogen would be very similar, but 20 sccm was a standard for passivation at that time.

fects related to the dopants. This was further confirmed by a SiN_x:H control sample which was deposited directly after the 500 sccm PH_3 deposition and could not achieve the same performance that was observed for the previous SiN_x:H samples, due to cross-contamination with phosphorus. While the S_{pass} performance of the phosphorus-doped SiN_x layers was worse than their hydrogen-counterparts, it should be emphasized that the passivation performance was still excellent. The performance of the SiN_x:H layers here was simply outstanding. For 300 sccm PH_3, as used by SiN *PassDop* Gen1, a S_{pass} of 2 cm/s was achieved, which would result in a $J_{0b,pass}$ of only 4 fA/cm^2 and thus barely visible at the device level. Therefore, for the *PassDop* cells the slight loss in passivation performance due to the dopants is—unlike for silicon hetero-junction solar cells—acceptable.

One may wonder why S_{pass} changed with the increasing hydrogen flow in the observed way. Measurements by spectral ellipsometry showed that the refractive index increased from approx. 2.55 (0/20 sccm PH_3 or H_2) to 2.67 (500 sccm PH_3 or H_2). Since the pressure was kept constant during the deposition, the increase in hydrogen resulted in a dilution of the remaining process gases, which influenced the composition of the layers. The lower dissociation energy of SiH_4 compared to molecular nitrogen (see Table 4.1) led to a shift towards Si-richer layers. The increase in S_{pass} can therefore be attributed to decreased thermal stability and hence degradation during the process as described for Gen1 previously. For such Si-rich SiN_x layers, the deposition temperature was too high, leading to a degradation during the process.

While the passivation results suggested that an intrinsic *Passivation* layer would not be required, it was still important to investigate what effect such a change would have on the doping efficiency of the stack. Here, despite identical process parameters, process fluctuation influenced the outcome of the experiment, which resulted in a much higher R_{Sheet} than previously determined for Gen1:P, as can be observed in Figure 6.9b. Comparing the result for Gen1:P with R_{Sheet} of 100 Ω/sq to the previously determined approx. 35 Ω/sq as shown for the previous two experiments underlined the importance of a stable and reproducible process. As the process was still in a prototype state, this could not always guaranteed, at least not on different processing days and in this case, it resulted in a layer with a significantly lower refractive index of approx. 2.4. However, despite the process fluctuation, the influence of a 25 nm intrinsic thick layer as for Gen1:H was clearly visible, as R_{Sheet} increased by more than a factor of 2 from 100 to over 200 Ω/sq, which shows that the first nanometers are of major importance for laser doping from SiN_x.

For a deeper analysis, it would be desirable to not only have the R_{Sheet}, but the dopant dose as well, as this it the parameter that is changed when leaving parts of a *PassDop* stack undoped. To acquire the dose a doping profile would be necessary, but as will be shown in Section 7.1.3, ECV profiles are an unreliable reference for the doping profiles when performing laser doping from SiN_x:P layers. This was due to the incorporation of nitrogen in the LBSF. The better reference would be Secondary Ion Mass Spectrometry (SIMS) measurements, but this was not possible for this experiment. However, one parameter from ECV and SIMS that does match quite well is the profile depth (e.g. see Figure 7.7). Thus, a good approximation of the doping profile should be to adjust a Gaussian doping profile such that the depth matches that determined by ECV (including corrections if applicable) and set the surface concentration such that the R_{Sheet} for the doping profile matches that measured by 4pp. It should be made clear that this is just an approximation for the doping profile, but it can be used to illustrate the changes in the dose which will certainly exceed the error on the dose calculation as already indicated by the changes in R_{Sheet}.

The results from this approximation are summarized in Table 6.2. It was clear that the changes in the doses were very strong. For the Gen1:H stack the dose decreased by a factor of 3.8 (from 3.4×10^{14} to 9×10^{13} cm^{-2}) in comparison to the fully doped Gen1:P (R_{Sheet} increased by a factor of ≈ 2.2), thus almost 300 % more dopants were incorporated into the LBSF. Therefore, it can be concluded that the first approx. 30 to 50 nm have by far the highest contribution to the laser doping process.[2] The effect can be explained by the thermal stability of SiN_x. For Si-rich SiN_x layers like the Gen1 SiN_x:P layer that was used in this experiment, the melting point is expected to be in between that of c-Si (1400 °C [188]) and the melting/decomposition point of Si_3N_4 (1900 °C [189]) and the thermal conductivity is expected to be low. This means that at some point the pressure of the molten silicon underneath the SiN_x layer will get high enough to burst off the SiN_x layer or stack while only part of the layer was molten and contributed to the laser doping process, as will be discussed in more detail in Section 7.1.3. Thus leaving the first few nm of the layer undoped will result in a strong influence on R_{Sheet} as observed.

For Gen2, the effect was not as pronounced, but even here the change from Gen2:H (undoped SiN_x:H *Passivation* layer, 100 nm) to Gen2:P (doped SiN_x:P *Passivation* layer, 100 nm) will lead to an increase in the dose by a factor of 1.7 from 1.7 to 3.0×10^{15} cm^{-2} (decrease in R_{Sheet} by a factor of 1.6). This is

[2] A similar effect was observed for the N-richer *fPassDop* layers, which will be discussed in Section 6.3.2, e.g. Figure 6.18b.

because the a-Si:P *Doping* layer due to the lower melting point will be molten much earlier during the laser doping process and improve its contribution to the laser doping process either by supporting melting the *Passivation* layer or by diffusion through (already) broken parts of the *Passivation* layer.

6.3 Firing-stable *PassDop* based on a-SiN$_x$:P

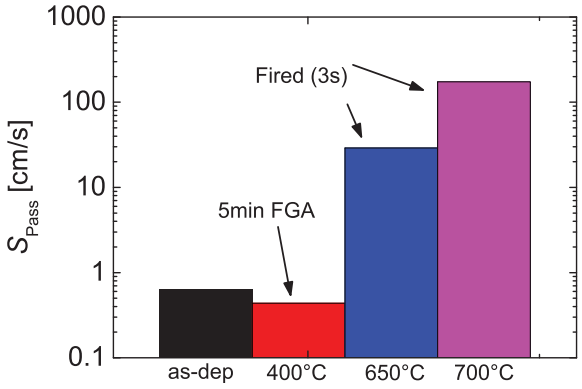

Figure 6.10: S_{pass} after applying a thermal treatment to the SiC *PassDop* Gen2 stack.

Motivation

In industrial fabrication, the most commonly used technique to create the contacts is screen printing of silver. As shown in Figure 6.10, SiC *PassDop* was not found to be compatible with a firing step at high temperatures above 650 °C, even if only applied for a short time. As described in Section 5.1.1, SiN$_x$ is a commonly used technique to create both an ARC for *p*-type silicon solar cells as well as known for a good passivation on phosphorus emitters. In Section 6.2.2, it was shown that it is possible to use SiN$_x$:P to form a *PassDop* passivation layer. This made SiN$_x$ a good candidate for a firing-stable passivation on *n*-type silicon (*fPassDop*). However, the SiN *PassDop* process aimed for a passivation directly after the deposition or after FGA at relatively low temperature and was not stable under firing conditions. Thus, modifications to the process were necessary. The development of the *fPassDop* layer was mainly done in the focus of a supervised masters thesis [190].

6.3.1 *fPassDop* Single Layer based on a-SiN$_x$:P

Motivation

As defined in Section 5, the two most basic properties for a *PassDop* layer are surface passivation as well as doping efficiency during the laser process. In Section 6.2.2 it was shown that a single layer can provide these properties for a low-temperature metallization approach. However, the SiN *PassDop* process would not withstand the temperatures required for the activation of screen printed contacts and therefore a modified surface passivation was required. Similarly to SiN *PassDop* Gen1, the first experiment was a process screening to determine if a single layer was feasible.

The experiment here is therefore a simple variation of the gas flows and leading to a variation in the composition of the SiN$_x$:P layer. R_{Sheet} is determined to get information about the doping efficiency in dependence on the composition. S_{pass} after firing is determined for a selection of firing temperatures to get information about the passivation quality. FT-IR measurements are used to differentiate the compositions helping to understand the observed results.

Experimental

The depositions were made in the Roth&Rau AK800 batch type reactor as described in Section 4.3. The deposition set temperature was 475 °C. The pressure throughout the experiment was set to 12 Pa and kept constant. The changes in the composition were achieved by varying the gas flows of SiH_4 and nitrogen while keeping the total gas flow constant. Firing was done as denoted in Section 6.1. FT-IR was performed for a selection of samples directly after the deposition. The absorption was normalized to the layer thickness and a baseline correction was made. For all investigated compositions it was tried to do the baseline correction similarly to improve comparability of the curves, which is essential for the region from 600 to 1100 cm^{-1} but not as critical at higher wave numbers.

Results

Figure 6.11 shows S_{pass} for the investigated a-SiN$_x$:P layers after firing for a temperature range of 700 to 850 °C. The first observation is that the temperature at which the minimum S_{pass} after firing was achieved shifted with the composition. For Si-rich (high refractive index) layers, this minimum was

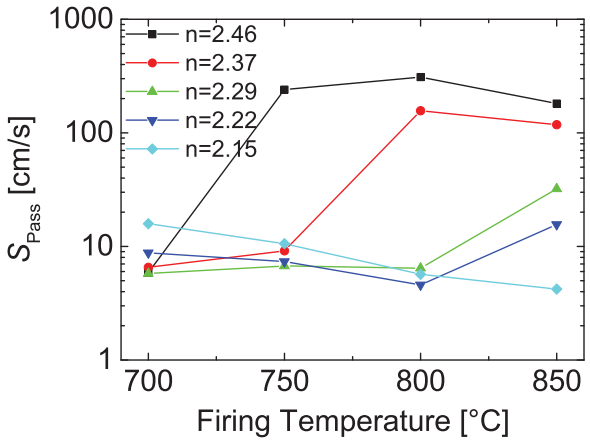

Figure 6.11: S_{pass} after firing for a-SiN$_x$:P layers with a refractive index in the range of $n = 2.15$ to $n = 2.46$.

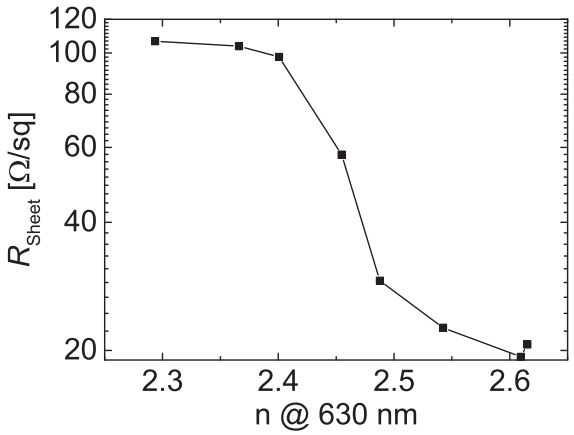

Figure 6.12: R_{Sheet} at a laser fluence of 9.3 J/cm^2 for a single layer a-SiN$_x$:P process.

determined at lower firing temperatures and with increasing nitrogen content (decreasing refractive index) the minimum shifted towards higher firing temperatures. Thus for Si-rich layers, the lowest S_{pass} was determined at 700 °C while for the layer with the highest nitrogen content, it was found at 850 °C. All investigated compositions achieved a S_{pass} below 10 cm/s, each at their individual optimum firing temperature. For all investigated compositions with $n > 2.15$ a temperature limit was found above which S_{pass} was significantly higher by at least a factor of 3. If the temperature limit was exceeded the higher S_{pass} was accompanied by a high amount of blistering.

Figure 6.13 shows the baseline-corrected FT-IR measurements performed for the investigated layers. Two signal peaks were found in the measured wave number range. At a wave number of approx. 835 cm^{-1}, a strong absorption was determined, which was attributed to asymmetric stretching of Si-N bonds [123]. With decreasing refractive index, the maximum of this peak was observed to increase. At 1175 cm^{-1}, at the lower shoulder of the large Si-N peak, a small bump was observed that could be attributed to N-H rocking [123], a clear trend with the composition was not observed. At a wave number of 2150 to 2200 cm^{-1}, a second peak was determined, which was attributed to the stretching mode of Si-H bonds [123]. With decreasing refractive index, the absorption signal of this peak decreased and the peak position shifted from 2150 to 2200 cm^{-1}. A third peak at around 3300 to 3450 cm^{-1} related to N-H bonds was expected, but was not observed.

Figure 6.12 shows the determined R_{Sheet} for a laser fluence of 9.26 J cm^{-2} in dependence on the layer composition and therefore the refractive index. For a $n < 2.4$ the measured R_{Sheet} was almost constant around 100 Ω/sq. Between 2.4 and 2.5, a strong decrease of R_{Sheet} from 100 to 30 Ω/sq was ob-

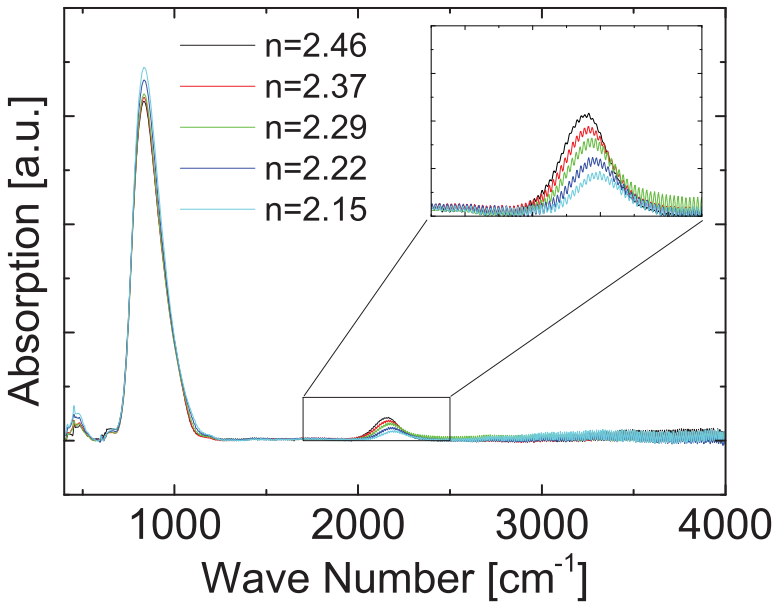

Figure 6.13: FT-IR spectra for a-SiN$_x$:P layers after deposition. For all layers, a baseline correction was made. The smaller graph shows the variation in the SiH peak in dependence on the layer composition.

served. Above 2.5, a further slight decrease in R_{Sheet} was observed reducing R_{Sheet} down to 20 Ω/sq at the maximum investigated n around 2.6.

Discussion

From the results it was clear that for a suitable firing stable layer a refractive index of 2.3 or lower was required as shown in Figure 6.11. At the same time only compositions with a refractive index of at least 2.45 seemed to result in a low R_{Sheet} (see Figure 6.12). This means that depositing a film that at the same time provides a sufficient passivation after firing in the range of 700 to 800 °C and at the same time has a high doping efficiency is a tough call. For the feasibility of a single layer it would be important to either improve the doping efficiency for N-rich layers or improve the firing stability for Si-rich layers.

For the doping efficiency it is important to understand—as will be discussed for *fPassDop* Gen2 in Section 7.1.3, but the same applies to the single layer as well—that the high R_{Sheet} is not (mainly) a consequence of an insufficient amount of dopants in the layer, but instead an incompatibility with the laser process. Ni-rich layers are expected to have a higher melting (or decomposition) point closer to that of Si_3N_4 and therefore cannot be molten as effectively by the laser as Si-rich layers. Thus, for laser doping, Si-rich layers with a lower melting point might be required.

The alternative could be to improve the firing stability of the Si-rich layers. For that, it is important to understand what limits the firing stability with Si-rich layers. Here the analysis of the FT-IR data for the SiN_x:P layers is helpful. While the first result shown from Figure 6.13 was pretty trivial—an increase in Si-N bonds with decreasing refractive index—the more interesting result was the second peak around 2200 cm^{-1} shown in the embedded graph. The shift toward a higher wave number is an indication that more of these Si-H bonds are back bonded to nitrogen [123] for increased nitrogen content. A similar effect was found by Gatz *et al.* [112]. The modified back bonding leads an increase in the binding energy of the Si-H bonds, which then leads to an increase in the thermal stability of the bonds. This clearly raises the release temperature of the bonds as observed by Gatz leading to a reduced or no blistering. Therefore, the nitrogen plays an essential role in the thermal stability of the layers and achieving a good and reliable passivation with Si-rich layers ($n > 2.4$) would be a tough task. The second effect of nitrogen in SiN_x can be observed especially for the layers with $n = 2.15$ and 2.22, where an improved S_{pass} with increasing peak temperature was observed (see Figure 6.11). A higher concentration of Si-N bonds in the material is known to result in defects, the K-centers, which are positively charged, formed during thermal treatment. This resulted in an increased $Q_f > 0$ with decreasing refractive index [122]. The higher thermal budget at higher peak temperatures is expected to lead to a higher amount of K-centers and therefore to an improved S_{pass}.

In conclusion this means that defining a single layer process that can be used as an *fPassDop* layer would be very hard. If achieved, the boundary conditions discussed in this section mean that such a process would likely be very prone to process fluctuation, mainly due to the strong slope in R_{Sheet} at intermediate n, an effect that was already observed in the previous chapter for SiN *PassDop* Gen1. Nevertheless, a single layer ($n = 2.15$) was tested at the device level, for which the results can be found in Section 8.1.1.

6.3.2 *fPassDop* Double Layer Systems based on a-SiN_x:P

Motivation

The previous section showed that for SiN_x:P, a basic trade-off for the layers between firing stable passivation (requiring N-rich layers) and doping efficiency (requiring Si-rich layers) has to be made. The logical solution to solve

this is to use a layer stack consisting of two or more layers, each with a specific purpose. In the following, these layers will be called *Passivation* and either *Doping* or *Capping* layer. For a specific declaration, see below. In this work, three posibilities to create such a stack are discussed. Schematics for these stacks can be seen in Figure 6.14.

1. Variant A: SiN$_x$:P (Si-rich, *Passivation*) + SiN$_x$:P (N-rich, *Capping*)
2. Variant B: SiN$_x$:P (N-rich, *Passivation*) + SiN$_x$:P (Si-rich, *Doping*)
3. Variant C: SiN$_x$:P (N-rich, *Passivation*) + a-Si:P (*Doping*)

The focus was on changing as few deposition parameters as possible to reduce process complexity. Thus, for the different layers of the stack it was mainly the gas ratio that was changed, while plasma excitation, pressure and temperature are kept constant. This could allow for a deposition of the layers in sequence within a single chamber when processing in-line.

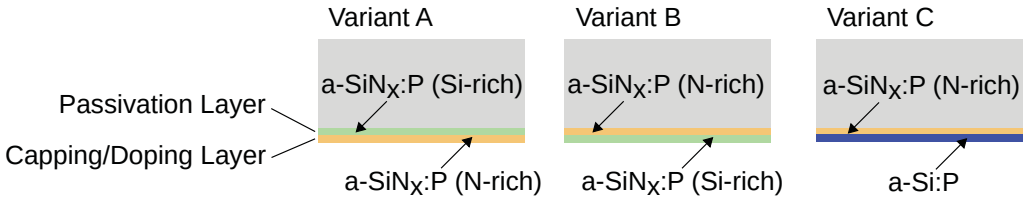

Figure 6.14: Schematics of the investigated *fPassDop* double layer systems. Variant A: Si-rich *Passivation* layer with N-rich *Capping* layer. Variant B: N-rich *Passivation* layer with Si-rich *Doping* layer. Variant C: N-rich *Passivation* layer with a-Si:P *Doping* layer.

Variant A: SiN$_x$:P (Si-rich) + SiN$_x$:P (N-rich)

Motivation

The approach to use an Si-rich *Passivation* layer and an N-rich *Capping* layer is the most straight forward one and was already investigated by multiple authors [112, 113, 191] for the combination of an a-Si or Si-rich SiN$_x$ *Passivation* layer with an N-rich SiN$_x$ *Capping* layer. In these cases undoped layers were used aiming only for a good S_{pass}, usually for application on the rear of *p*-type Passivated Emitter and Rear Cell (PERC).

The basic idea is to use an Si-rich *Passivation* layer for interface passivation benefiting from high hydrogen mobility, lower Si defect density and hence a low D_{it}. This alone could already be an advantage to an N-rich single layer passivation, as D_{it} for these layers can be a weak spot regarding passivation,

hence the investigations by before-mentioned authors upon the firing stability of such stacks. The purpose of the N-rich layer here is to act as a *Capping* layer. The »capping« functionality here is defined as to reduce out-diffusion of hydrogen, possibly even provide hydrogen during the firing process to reduce the amount of dangling bonds at the interface. However—as noted in the previous section—blistering can limit the passivation and thus the amount of hydrogen has to be controlled. The second functionality of the *Capping* layer is to improve the lifetime after firing due to the formation of the positive fixed charges.

For the design of the experiment it was important to keep in mind that only Si-rich layers with a refractive index above 2.45 were found to result in a low R_{Sheet}. At the same time experiments showed that a thick *Passivation* layer will result in blistering, thus limiting the thickness. As the dopants will almost exclusively be provided by the *Passivation* layer (for the *Capping* layer, the doping efficiency would be too low), a higher refractive index resulting in improved doping efficiency for the passivation layer is desirable. This means that for the design of the experiment a thin *Passivation* with a high refractive index should be selected, but likely as thin as possible.

Doping gases were not yet available at the time of processing and due to the results for S_{pass} the approach was not further pursued.

Experimental

All layers were deposited in the Roth&Rau AK800 batch reactor. The process was based directly on the original »Passin« process developed by Rauer (see Table 6.1, page 6.1). The pressure was 12 Pa and the temperature was 475 °C.

An Si-rich *Passivation* layer was deposited with 60 sccm silan and 25 sccm N_2. The refractive index of this layer was 2.6, the thickness was varied from 0 to 40 nm.

For the *Capping* layer, 54 sccm (SiH_4) and 27 sccm (N_2) were used. The thickness of the *Capping* layer was set to approx. 70 nm. The refractive index of the *Capping* layer was around 2.1. A firing temperature variation was not performed, all samples were fired with a peak temperature of 800 °C.

Results

Figure 6.15 shows the S_{pass} after firing in dependence on the *Passivation* layer thickness. In absence of the *Passivation* layer, a S_{pass} of just below 10 cm/s

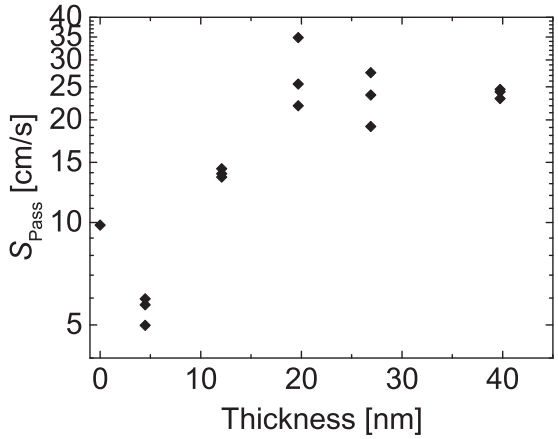

Figure 6.15: S_{pass} after firing at 800 °C for a stack of Si-rich a-SiN$_x$:P and N-rich a-SiN$_x$:P in dependence on the thickness of the Si-rich layer.

was observed. When introducing a thin *Passivation* layer of approx. 5 nm thickness, S_{pass} decreased to 5 to 7 cm/s. Increasing the thickness to 10 nm or above resulted in a significant increase in S_{pass} to values $\geq$ 15 cm/s. When exceeding a *Passivation* layer thickness of 10 nm blistering was observed. With increasing *Passivation* layer thickness the amount of blistering increased.

Discussion

While the introduction of a thin *Passivation* layer had a clear effect on the passivation performance, for thicker layers the passivation degraded, as can be observed in Figure 6.15. N-rich SiN$_x$ layers like the *Capping* layer are known to have more defects than Si-rich layers like the *Passivation* layer [122] and thus the *Passivation* layer can reduce D_{it} and therefore improve the passivation performance. However starting with 10 nm thickness, the accumulation of hydrogen in the *Passivation* layers starts to degrade the performance as blistering occurs. In addition, the fixed charges from the *Capping* layer (see the previous section) are less effective due to the thicker *Passivation* layer in between the c-Si and the *Capping* layer, although at 10 nm thickness, this would be expected to be a minor effect. At higher thicknesses, blistering gets more pronounced resulting in a further increase in S_{pass} and thus rendering higher thicknesses useless. As the S_{pass} were only promising for a *Passivation* layer thickness of 5 nm and the laser doping contribution of such a layer would not be expected to be significant (if doped), this approach was not further pursued.

Variant B: SiN_x:P (N-rich) + SiN_x:P (Si-rich)

Motivation

In this section the approach to combine an N-rich *Passivation* layer with an Si-rich *Doping* layer will be investigated. The basic idea behind this approach is to use a firing stable SiN_x:P layer as a *Passivation* layer to build upon a known and stable basis as the passivation capabilities for such a process was already investigated in Section 6.3.1. The *Passivation* layer is combined with a second, Si-rich layer acting as a doping source. This *Doping* layer is deposited on top of the *Passivation* layer. While the *Passivation* layer—if deposited as a single layer—has already proving its passivation capabilities, the passivation performance could still be influenced by the *Doping* layer. While blistering in the *Doping* layer in principle should not affect the c-Si/*Passivation* layer interface, a damage to the *Passivation* layer by this effect might still occur. In addition—if the laser doping process is done after the firing step—blistering could result in lowered doping efficiency as parts of the layer could be ablated by blistering prior to the laser.

The most critical aspect however is the doping efficiency. As shown in Section 6.3.1, SiN_x:P layers with $n < 2.4$ did result in a low R_{Sheet}, but are required for a low S_{pass}. The task of the *Doping* layer is to improve the doping efficiency and thus lower R_{Sheet}. However, as the *Doping* layer is placed on top of the *Passivation*, the question arises if this can be fulfilled, as the *Passivation* layer could possibly act as a shield and prevent doping from this layer.

Temperature Variation – Motivation

The goal of the first experiment is not only to test the feasibility of such an approach, but also to determine the influence of the deposition temperature. The temperature could be one way of controlling the amount of hydrogen incorporated into the layer. This could allow for the use of Si-richer compositions for both the *Passivation* and the *Doping* layer. Thus, this might lead to an improved trade-off regarding surface passivation after firing and doping efficiency.

Temperature Variation – Experimental

Both the *Passivation* as well as the *Doping* layer were based on the process used for the single layer in Section 6.3.1. The temperature during the deposition was varied from 475 to 575 °C. For the *Passivation* layer, the process

with $n = 2.15$ was the basis and for the *Capping* layer the process with $n = 2.4$. Due to the higher temperature (the previous single layer was deposited at 475 °C), the values for the newly deposited layers can be different as will be discussed. Both layers were deposited in sequence with constant plasma excitation. The deposition time of the *Passivation* layer was 1:30 min (around 50 nm), for the *Doping* layer 3:30 min (around 130 nm) was used. The thickness of the layers in the stack could not be determined, the given values represent estimates.

The deposition was then repeated depositing single layers for either the *Passivation* or *Doping* layer to determine the refractive index by spectral ellipsometry.

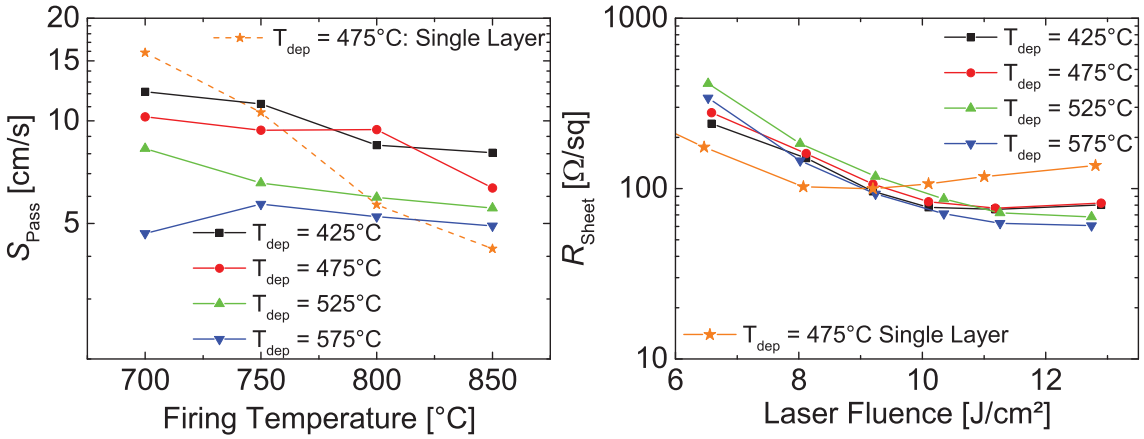

(a) S_{pass} **(b)** R_{Sheet}

Figure 6.16: S_{pass} after firing and R_{Sheet} for a stack of N-rich a-SiN$_x$:P and Si-rich a-SiN$_x$:P in dependence on set deposition temperature.

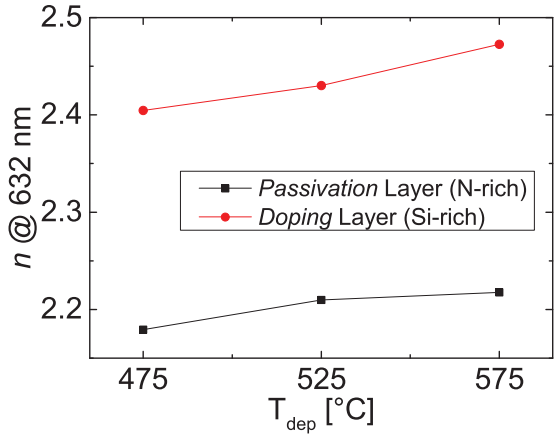

Figure 6.17: Refractive index for the two *fPassDop* layers in dependence on the set deposition temperature. Data at $T_{dep} = 425$ °C is not available as the depositions were not repeated for single layers.

Temperature Variation – Results

Figure 6.16a shows S_{pass} for the variation of the set temperature during the deposition. An overall trend toward lower S_{pass} with higher deposition temperature was observed. For the temperatures in the range of 425 to 525 °C a trend towards lower S_{pass} with higher firing temperature was observed. This trend was less pronounced for higher firing temperatures. For a firing temperature of 525 and especially for 575 °C, S_{pass} was found to be relatively constant, the latter with values in the range of 4.5 to 6 cm/s. As a reference the single layer with $n = 2.15$ from Section 6.3.1 was included. Figure 6.16b shows R_{Sheet} for the this variation. Almost no influence of the deposition temperature on R_{Sheet} was found. A common trend towards decreasing R_{Sheet} with increasing laser fluence was observed.

As a reference the values for the single layer with $n = 2.15$ from Section 6.3.1 was included. With increasing firing temperature, this layer showed a decreasing S_{pass}. For R_{Sheet}, a minimum around 8 to 9 J/cm^2 was determined with the minimum R_{Sheet} of around 100 Ω/sq.

Figure 6.17 shows n for both *Passivation* and *Doping* layer at 475, 525 and 575 °C. For both layers, an increasing n with increasing deposition temperature was observed. No blistering was observed during the experiments.

Temperature Variation – Discussion

In section 6.3.1, it was found that for SiN_x:P single layers the trade-off between doping efficiency and passivation quality seems essential. Either R_{Sheet} (N-rich layers) or S_{pass} (Si-rich layers) were found to be high and not suitable for a *PassDop* layer. Combining an N-rich *Passivation* and an Si-rich *Doping* layer it was tried to overcome this limitation and to achieve both a low S_{pass} as well as a low R_{Sheet}. This was partially successful as the experiment showed. The passivation performance of the best stack (at 575 °C deposition temperature) was on par with the single layer, but over a wider range of firing temperatures. At other deposition temperatures the performance was not far behind with only few S_{pass} values above 10 cm/s. The important aspect here was that for these samples, no blistering was observed, which was surprising, as the *Doping* layer directly deposited onto the substrate resulted in severe blistering. This means that either the deposition of the layer was slightly modified due to the different interface (SiN_x:P/SiN_x:P instead of c-Si/SiN_x:P) or the *Passivation* layer consumes some of the hydrogen during the firing process and therefore prevents blistering. Such a consume of hydrogen could also explain the modified temperature behavior compared to

the single layer, as an increased amount of hydrogen would improve S_{pass} at lower firing temperatures, as observed. Thus, the experiment showed that with an *fPassDop* double layer stack, excellent passivation performance is possible over a broad range (700 to 850 °C) of firing temperatures.

One important aspect regarding S_{pass} was the shift towards lower S_{pass} with higher deposition temperatures. To understand this, one has to take into account the composition of the layers, for which the refractive index a good indicator. As shown in Figure 6.17 it was observed that with a higher deposition temperature, the refractive index for both layers increased, thus the layers had a higher Si content. As already discussed for SiN *PassDop* in Section 6.2.2, a higher Si content results in a lower defect concentration in the *Passivation* layer. In addition, around $n \approx 2.1$ the N dangling bond becomes inactive [122]. This is not expected to be an abrupt change in D_{it}, instead a decreasing influence in D_{it} with increasing refractive index would be expected.
Karabacak *et al.* found that an increase in the deposition temperature results in a decrease in the hydrogen concentration due to outdiffusion during the deposition Karabacak et al. [93]. While their process made use of an RF plasma source, it is still likely that the investigated layers behave similar. Thus, the increase in the deposition temperature helps to keep the hydrogen content of the *Passivation* layer at a level that blistering can be prevented and together with the hydrogen consumed from the *Doping* layer a low S_{pass} can be achieved. In the AK800 reactor, the maximum set temperature is 600 °C. In a later experiment this was tested, but no significant difference to 575 °C was found. Therefore from this point on, 575 °C was used as the set temperature for all *fPassDop* processes.

The main reason to use a two-layer stack instead of a single layer was to improve the doping efficiency. Above it was mentioned that the double layer was »only« partially successful and Figure 6.16b shows why. Up to approx. 9 J/cm^2, R_{Sheet} was not significantly reduced in comparison to the single layer. Only at higher laser fluences a lower R_{Sheet} would be achieved. The influence of the increased silicon content in the layers (see Figure 6.17) was minimal.

While the lower R_{Sheet} of 60 Ω/sq at higher laser fluences means that in principle the *Doping* layer does fulfill its purpose, the higher laser fluence that was required indicates that the laser doping process was hindered and the barrier responsible for this was the *Passivation* layer. The reasons for this will be discussed in more detail in Section 7.1.3, but in short the temperature stability of the N-rich SiN$_x$ prevents an early melting of the *Passivation*

layer. This can lead to the *Passivation* layer bursting under the pressure of the molten silicon taking the *Doping* layer with it. Thus the influence of the *Doping* layer can be to either support the melting of the *Passivation* layer or contribute via already molten areas of the layer or holes (e.g. through already broken parts) in the *Passivation* layer. Thus, even though the *Doping* layer may have a much better doping efficiency (see the next section) than the *Passivation* layer and a higher Si content (thus it would melt earlier during the process), it cannot contribute as much dopants as would be necessary for a really stable process. Still, the lower R_{Sheet} in the range of 60 Ω/sq at a laser fluence of 10 J/cm^2 led to the definition of the stack deposited at 575 °C as *fPassDop* Gen2 (due to the improved S_{pass}).[3]

Influence of the Passivation Layer Thickness – Motivation

As outlined in the motivation, the main purpose of the *Doping* layer is to improve the doping efficiency In the previous experiment, it was observed that this was only partially successful and that possibly the *Passivation* layer acted as a barrier during the laser doping. Reducing the barrier thickness could be a way to reduce this influence. On the other hand, a low thickness might lead to a degradation in the surface passivation.

Therefore the goal of this experiment is to investigate the influence of the *Passivation* layer thickness on the passivation performance and the doping efficiency. In addition, the R_{Sheet} for the *Doping* layer without the intermediate *Passivation* layer is determined as well.

Influence of the Passivation Layer Thickness – Experimental

For this experiment a deposition temperature of 575 °C was used. Both layers were deposited in sequence with constant plasma excitation.

The *Passivation* layer deposition time was varied from 0 to 0:50 min. The estimated layer thickness would be in the range of 5 to 10 nm for 0:20 min and 30 nm for 0:50 min. The exact layer thickness cannot be determined by ellipsometry as the stack deposition can influence the resulting thickness, especially for thin layers. From the previous experiment, the refractive index for the *Passivation* layer would be expected to be around 2.2.

The deposition time for the *Doping* layer was kept constant at 3:30 min (corresponding to approx. 130 nm thickness). The refractive index for the *Doping* layer was determined in the previous experiment at 2.47.

[3] For *fPassDop* Gen1, see [179].

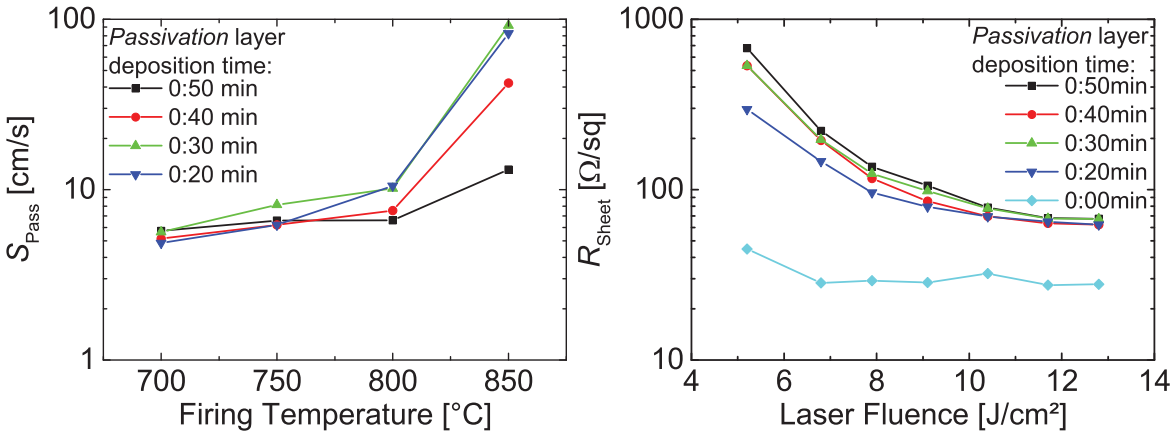

Figure 6.18: S_{pass} after firing and R_{Sheet} for a variation of the *Passivation* layer thickness in the N-rich/Si-rich stack *fPassDop* approach. 0:20 min should correspond to approx. 5 to 10 nm, 0:50 min to approx. 30 nm. The *Doping* layer thickness was kept constant throughout the experiment.

Influence of the Passivation Layer Thickness – Results

6.18a shows the dependency of S_{pass} on the N-rich *Passivation* layer deposition time ranging from 0:20 min to 0:50 min. All deposited layers show a clear trend: with increasing temperature S_{pass} increased. For a lower *Passivation* thickness, this increase in S_{pass} was stronger. While at a firing temperature of 700 and 750 °C S_{pass} was similar throughout the variation, 800 and especially 850 °C a trend towards lower S_{pass} with higher *Passivation* layer thickness was observed. Blistering was observed for thinner *Passivation* layers, especially at higher firing temperatures.

Figure 6.18b shows R_{Sheet} for the same variation. In addition 0:00 min was included, which corresponds to R_{Sheet} for the Si-rich *Doping* layer deposited directly on the substrate. For this *Doping* layer, above a laser fluence of 6 J/cm^2, R_{Sheet} was found to be in the range of 30 Ω/sq without much variation and therefore significantly lower than the stacks. For the samples with a *Passivation* layer, a clear trend was observed: decreasing R_{Sheet} with increasing laser fluence. The thickness of the *Passivation* layer was minimal and only present at lower laser fluences. Only at laser fluences below 9 J/cm^2, a trend towards lower R_{Sheet} with lower *Passivation* layer deposition time was observed, but most of the R_{Sheet} values were determined at 100 Ω/sq or above.

Influence of the Passivation Layer Thickness – Discussion

In the previous experiment it was suggested that the *Passivation* layer acted as a barrier during the laser doping process. One could expect that reducing

the thickness of the *Passivation* layer would help the laser doping process as this reduces the thickness of the barrier. As shown in Figure 6.18b, such an effect was present, as all samples which had a *Passivation* layer showed a significantly higher R_{Sheet} than the reference for the *Doping* layer. The influence of the *Passivation* layer thickness was minimal and only all present at fluences below 10 J/cm^2. Even with the thinnest *Passivation* layer (deposition time of 0:20 min), the barrier seemed to be effective. It was a surprise that even such thin layers would have such a big impact on the doping efficiency leading to an increase by a factor of 2 to 3 in R_{Sheet} in comparison to the *Doping* layer deposited onto the substrate directly. This means that this approach is fundamentally flawed and an alternative solution needs to be found, which will be discussed in the next section.

The influence of the *Passivation* layer thickness on S_{pass} was mainly present at higher temperatures as shown in Figure 6.18a. As blistering was observed for the thinner *Passivation* layers, this supports the consumption of hydrogen by the *Passivation* layer outlined in the previous experiment. For the thinner *Passivation* layers, not enough hydrogen was consumed leading to blistering, especially at higher temperatures. Thus for a stable passivation, at least a deposition time of 0:50 min should be selected.

Variant C: SiN_x:P (N-rich) + a-Si:P

Motivation

With Variant B (SiN_x:P (N-rich) + SiN_x:P (Si-rich)) of double layer *fPassDop* stacks the first functional *fPassDop* layers were introduced. These experiments led to *fPassDop* Gen1 and Gen2 being defined with which the first *fPassDop* solar cells were fabricated successfully.

As discussed in the previous section, this approach faced some fundamental issues, which will be discussed in more detail in Section 7.1.3: The limitation of the doping efficiency by the *Passivation* layer. This led to a stack that »might« work, but clearly was not a very reproducible solution in terms of doping efficiency and contact ability. Within some batches of solar cells, a large distribution in the fill factor was found, due to the variations in the LBSF doping. These variations are discussed in the sections 7.1.3 and 8.1.

To overcome these trade-offs, a new approach was developed, which made use of an N-rich *Passivation* layer similar to that of *fPassDop* Gen2, but combining it with an N-free a-Si:P *Doping* layer. The basic idea of this approach

is to decrease the melting point of the *Doping* layer as much as possible as well as to reduce the nitrogen content in the stack (see Section 7.1.3). The important questions to answer are:

1. How will the a-Si:P layer affect the passivation performance and if negatively, can the effect be compensated
2. Can a-Si:P improve the doping efficiency significantly and can this improvement be kept if adjustments have to be made to the *Passivation* layer

Throughout all experiments, *fPassDop* Gen2 will be used as a reference.

Feasibility – Motivation

The intention of this experiment is to investigate if the new a-Si:P *Doping* layer can be used as a drop-in replacement for the *fPassDop* Gen2 *Doping* layer, without performing changes to the *Passivation* layer.

Feasibility – Experimental

The *Passivation* layer used in this experiment is the same as applied in the *fPassDop* Gen2 stack. The *Passivation* layer thickness was ≈ 30 nm with gas flows of 115 sccm SiH_4 and 75 sccm N_2.

The a-Si:P process is based on the *fPassDop* Gen2 *Passivation* layer as well, but with the nitrogen flow set to 0 sccm. The resulting thickness of the layer was approx. 100 nm. For a-Si:P, modeling a 100 nm layer for spectral ellipsometry is tricky, therefore a thin layer (approx. 20 nm) was deposited. The denoted thickness was calculated by assuming a constant deposition rate. Therefore, the given values for the thickness represent approximated values. One should also take into account that the deposition of the layer on top of the *Passivation* can differ from the deposition on a silicon substrate. However, the influence on the determined thickness should be minor.

The deposition set temperature at 575 °C were the same as *fPassDop* Gen2 for all layers. The results shown for *fPassDop* Gen2 differ slightly from the results shown in the previous section as the layer was deposited again. This was done to control the process as the Gen3 experiments were done approx. 1 year after the Gen2 experiments.

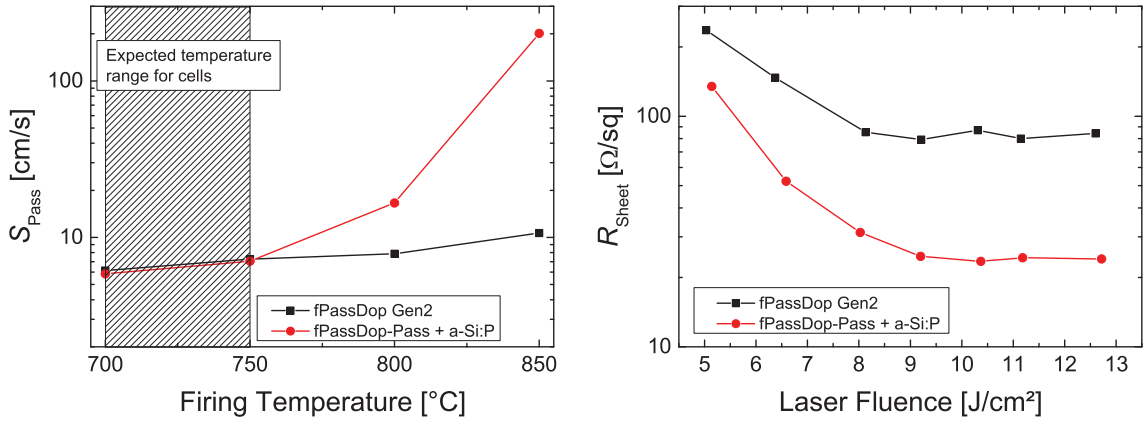

(a) S_{pass} **(b)** R_{Sheet}

Figure 6.19: Comparison of S_{pass} after firing and R_{Sheet} for *fPassDop* Gen2 (N-rich SiN_x:P + Si-rich SiN_x:P) to a stack of the *fPassDop* Gen2 *Passivation* layer (N-rich SiN_x:P) and a-Si:P as a *Doping* layer. The N-rich *Passivation* layer thickness for both approaches was approx. 30 nm with a refractive index around $n \approx 2.2$.

Feasibility – Results

In all graphs showing results for S_{pass} an area was marked indicating the firing temperature range that was determined as the optimum at the device level when using Ag-Al screen printing pastes.

Figure 6.19a and Figure 6.19b show the S_{pass} and R_{Sheet} if the a-Si:P *Doping* layer is used as a drop-in replacement for the *fPassDop* Gen2 *Doping* layer. While a clear improvement in R_{Sheet} was observed resulting in a drop from approx. 80 Ω/sq to approx. 25 Ω/sq (at laser fluences above 9 J/cm^2), this was accompanied by a significant change in the passivation properties. At firing temperatures of 700 and 750 °C, low values in the range of 6 to 7 cm/s were achieved with both stacks. At higher firing temperatures the new *Doping* layer resulted in an increase in S_{pass} up to 200 cm/s when firing at 850 °C, while showing severe blistering. The reference Gen2 stack was able to retain a low S_{pass} at the higher firing temperatures.

Feasibility – Discussion

As discussed in the previous section for the Gen2 approach, the Si-rich SiN_x:P Gen2 *Doping* layer itself would provide a good doping efficiency, but if used in a stack (as for *fPassDop* Gen2), the N-rich *Passivation* layer acts as a barrier hindering the laser doping process. The main goal of this experiment was to determine if an a-Si:P *Doping* layer would be able to support the laser doping process better than the *fPassDop* Gen2 *Doping* layer. As Figure 6.19b shows, this was definitely the case. R_{Sheet} was found to be much lower ($\approx$ 25 Ω/sq)

than for Gen2. To understand this, two effects have to be considered. The first is the overall nitrogen content of the stack. Even at a refractive index of 2.6, the SiN$_x$ contains approx. 40 % nitrogen (determined by FT-IR [190]). Reducing this amount within the doping layer to ≈ 0 resulted in a drop in the overall nitrogen content from approx. 40 % to 15 % (assuming similar densities for all layers), thus significantly reducing the effect of nitrogen on the doping within the LBSF. The other effect is due to the changed layer properties expected for the (a-Si:P) *Doping* layer. For c-Si, it is known that the melting point (approx. 1400 °C [188]) is significantly lower than for Si_3N_4 (melts or decomposes at approx. 1900 °C [189]). While amorphous layers might show diverting behavior, the tendencies are expected to be similar and the observed behavior in the sheet resistance in dependence on the laser fluence suggests that. Here, only with the a-Si:P doping layer, a sufficient doping was achieved at a low laser fluence of 6.5 J/cm^2 (resulting in a lower process temperature during the laser process).

However, a-Si is not known for being stable under firing conditions. Thus it was questionable if the stack would sustain after firing. The results shown in Figure 6.19a were promising. There was blistering at temperatures ≥ 800 °C, but at lower firing temperatures S_{pass} was similar to Gen2. Here—similar to Si-rich SiN$_x$:P layers—the hydrogen content in the *Doping* layer is causing blistering leading to the degradation in the passivation performance at temperatures ≥ 800 °C.
While firing stability within the temperature range of 700 to 750 °C as shown in Figure 6.19a might sound sufficient it should be tried to widen the temperature range that can be used for firing. First, because future generations of screen printing pastes could have different requirements and second, because process fluctuation might result in stronger degradation within the desired temperature window. Thus the next steps should aim for widening the window of usable firing temperatures when using the a-Si:P *Doping* layer, which will be investigated in the next experiment.

Influence of the Doping Layer Thickness – Motivation

In the first experiment with this *fPassDop* double layer stack the focus was on improving the doping efficiency. While this worked well, the passivation performance was influenced at higher firing temperatures. As a first step, the passivation layer thickness was increased from 30 nm to 100 nm. The nitrogen content was increased slightly as well.

The purpose of this experiment is to investigate if modifications to the *Passivation* layer reduce the effect of the a-Si:P *Doping* layer and if this improves

firing stability at firing temperatures above 800 °C. In addition, the *Doping* layer thickness is varied to prove that it is the a-Si:P layer which increases the doping efficiency.

Influence of the Doping Layer Thickness – Experimental

The *Passivation* layer thickness in this experiment was increased to 100 nm (originally 30 nm). This thickness was calculated based on the known deposition rate of the layer and was not measured separately and thus is an approximate value. The gas ratio for the *Passivation* layer was adapted to 111 sccm SiH_4 and 79 sccm N_2 (originally: 115 sccm SiH_4 and 75 sccm N_2) This should result in a refractive index around 2.15, which however was not determined specifically.

The a-Si:P *Doping* layer was the same as in the first experiment, but the thickness was varied from 50 to 100 nm.

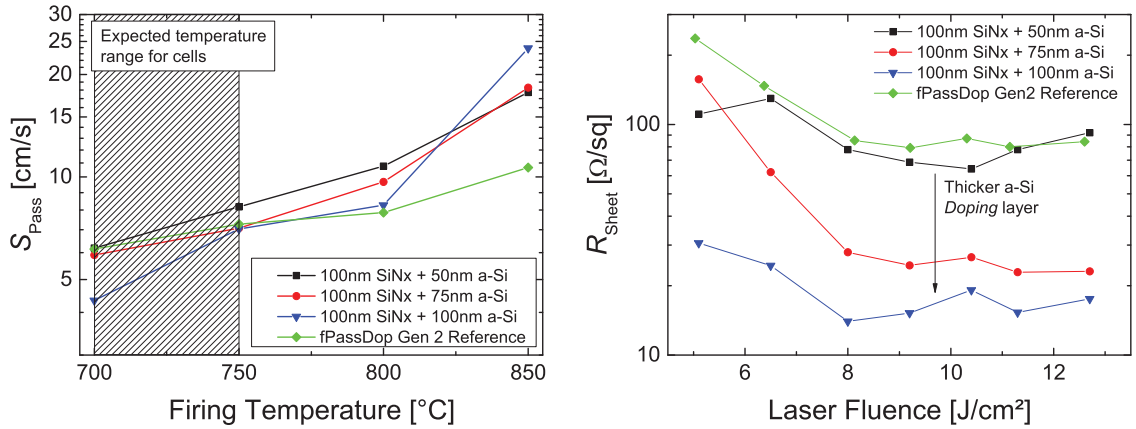

(a) S_{pass} **(b)** R_{Sheet}

Figure 6.20: Influence of the a-Si:P *Doping* layer thickness on S_{pass} after firing and R_{Sheet}. As a reference, the *fPassDop* Gen2 stack is shown.

Influence of the Doping Layer Thickness – Results

In this experiment, no blistering was observed.

Figure 6.20a shows the influence of the a-Si:P *Doping* layer thickness on S_{pass}, which was found to be minimal. Only for a *Doping* layer thickness of 100 nm a stronger increase of S_{pass} with increasing firing temperature was observed. With the increase in the *Passivation* layer thickness S_{pass} was significantly lower than before with a maximum of 25 cm/s for a *Doping* layer thickness of 100 nm.

Figure 6.20b shows the influence of the a-Si:P *Doping* layer thickness on R_{Sheet}. The influence was very strong leading to a drop in R_{Sheet} from approx. 70 Ω/sq to below 20 Ω/sq (laser fluence of 8 J/cm^2 or above) when increasing the *Doping* layer thickness from 50 to 100 nm. With 100 nm of a-Si:P *Doping* layer thickness it became possible to use laser fluences of 8 J/cm^2 or below as $R_{\mathrm{Sheet}} \leq 30\,\Omega$/sq was achieved with this stack even at a laser fluence of 5 J/cm^2.

Influence of the Doping Layer Thickness – Discussion

The first thing to note about this experiment is that—in comparison to the first experiment—S_{pass} was found to be more stable at 850 °C, which is why the scale in Figure 6.20a reaches only to 30 cm/s. Equally important was that blistering was successfully prevented. This was caused by the modifications that were already made to the *Passivation* layer, which was thicker (100 instead of 30 nm) and N-richer (now 111 SiH_4 and 79 N_2). While the influence of the firing temperature on the surface passivation was still stronger than for *fPassDop* Gen2, the modifications showed that the negative influence of the a-Si:P *Doping* layer on the passivation performance can be compensated. As the influence of the *Doping* layer thickness was found to be low, even a partial decoupling was achieved.

With regard to the doping efficiency, Figure 6.20b shows that there was a very strong influence of the a-Si:P *Doping* layer thickness on R_{Sheet} as it decreased from approx. 70 Ω/sq (for 50 nm *Doping* layer) down to below 20 Ω/sq (for 100 nm *Doping* layer). Previously one explanation for the improved doping efficiency with a-Si:P could have been that it supports the melting (i.e. by retarding the burst-off) of the *Passivation* layer, but not necessarily contributed itself. The results show that this cannot be the only explanation. Instead the a-Si:P layer contributed significantly to the doping efficiency as R_{Sheet} decreased with the *Doping* layer thickness. It should also be noted that despite the changes made to the *Passivation* layer (thicker, N-richer), similar results as in the first experiment could be achieved. Thus, the a-Si:P *Doping* layer works well with N-richer, thicker compositions.

To conclude the experiment, there is one important point to make: the a-Si:P *Doping* layer thickness is a parameter that can be used to improve the doping efficiency of the stack *without* affecting S_{pass} strongly. This means that if R_{Sheet} increases due to some changes that had to be made to the *Passivation* layer, it could be compensated by increasing the *Doping* layer thickness. At least 75 nm of *Doping* layer should be used, but 100 nm will yield slightly better R_{Sheet} results.

Influence of the Passivation Layer Composition – Motivation

In the previous experiment it was already shown that modifications to the *Passivation* layer can compensate for the loss of firing stability at higher firing temperatures. It was also shown that such modifications can be made while still achieving a low R_{Sheet}.

The goal of this experiment is to further pursue this route to see if a firing stability similar to that of *fPassDop* Gen2 can be achieved while still achieving a significant improvement in R_{Sheet}. This will be achieved by varying the gas flow ratio to use N-richer layers as *Passivation* layers.

Influence of the Passivation Layer Composition – Experimental

In this experiment, gas ratios are given in the form X:Y and always refer to SiH_4:N_2, both given in sccm.

The thickness of the *Passivation* layer was set to ≈ 80 nm calculated from the deposition rate. The gas ratio was varied from 111:79 ($n \approx 2.15$) to 107:83 ($n \approx 2.10$), the total gas flow was kept constant.

The thickness of the *Doping* layer was set to ≈ 70 nm.

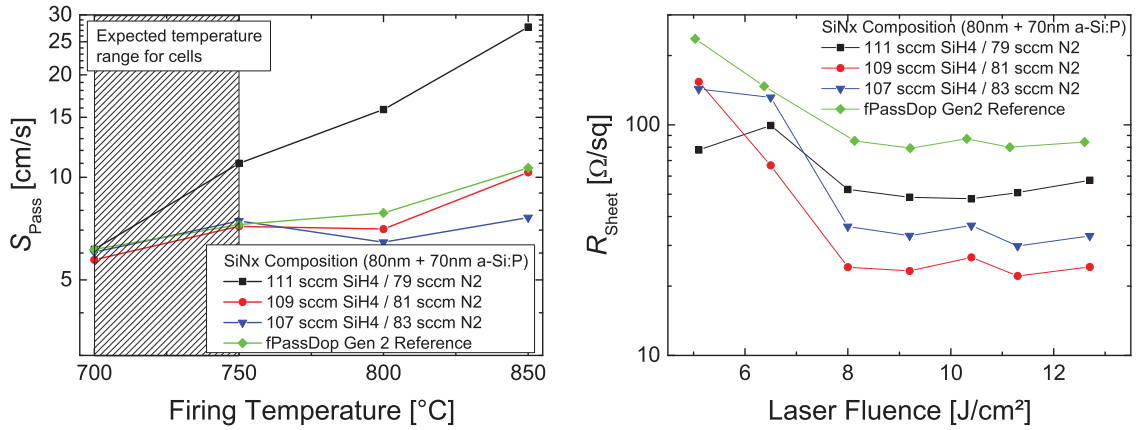

(a) S_{pass} **(b)** R_{Sheet}

Figure 6.21: Influence of the composition (SiH_4/N_2 ratio) of the SiN_x:P *Passivation* layer on S_{pass} after firing and R_{Sheet}. As a reference, the *fPassDop* Gen2 is shown.

Influence of the Passivation Layer Composition – Results

In this experiment, no blistering was observed. Figure 6.21a shows the influence of the *Passivation* layer gas composition on S_{pass} after firing. A clear trend towards lower S_{pass} at firing temperatures ≥ 750 °C with N-richer gas ratio was observed. With a gas ratio of 109:81 or richer in nitrogen, S_{pass}

equal to or lower than that of *fPassDop* Gen2 was achieved at all firing temperatures.

Figure 6.21b shows R_{Sheet} for the gas flow variation. At all gas ratios, a lower R_{Sheet} than for *fPassDop* Gen2 was achieved. A trend with increasing N-content was not observed. Instead, it was the layer with the lowest N-content (111:79) resulted in the highest R_{Sheet} at approx. 50 Ω/sq. The lowest R_{Sheet} of approx. 25 Ω/sq was determined for a gas ratio of 109:81. The highest N-content (gas ratio of 107:83) resulted in a R_{Sheet} of approx. 30 Ω/sq. For all layers, the required laser fluence was approx. 8 J/cm^2 below which R_{Sheet} was found to be significantly higher.

Influence of the Passivation Layer Composition – Discussion

The improvements in R_{Sheet} determined in the previous experiments when using an a-Si:P *Doping* layer were encouraging. However as shown in the first experiment, the a-Si:P *Doping* layer can also lead to a degradation in S_{pass} at firing temperatures above 750 °C. While this would include the firing temperature range currently used for Ag-Al screen printing pastes widening this process window of usable firing temperatures would make the process more prone to process fluctuation and therefore was investigated in this experiment. As already mentioned in the previous experiment, increasing the *Passivation* layer thickness (here from ≈ 30 to ≈ 80 nm) and adjusting the gas ratio to 111:79 already helped to lower S_{pass}. As can be observed in Figure 6.21a this trend continued with higher N content in the *Passivation* layer. The negative effect of the a-Si:P *Doping* layer on the firing stability can be fully compensated. This strong influence of the gas ratio on the firing stability can be explained by a higher density of positive fixed charges that SiN$_x$ is known for to form during thermal treatment for N-rich layers [122]. In addition, the N-rich layers can act as a hydrogen sink thus preventing blistering and achieving a good S_{pass} at firing temperatures in the range of 800 to 850 °C. The experiment showed that even with a-Si:P acting as a *Doping* layer, a firing stable *fPassDop* can be achieved with $S_{\mathrm{pass}} < 10$ cm/s in a broad range of firing temperatures of 700 to 850 °C. With a gas ratio of 109:81 or 107:83 for the *Passivation* layer, the stack out-performed *fPassDop* Gen2 at all investigated firing temperatures in regard to S_{pass}.

While the influence of an N-richer gas ratio on S_{pass} was clearly positive, the results for R_{Sheet} were not as clear. As Figure 6.21b shows the gas ratio with the highest Si content 111:79 actually resulted in the highest R_{Sheet} at around 50 Ω/sq, which was not expected and cannot be explained. However, the more important point is that even with the N-richest gas ratio 107:83 R_{Sheet}

was found to be below 40 Ω/sq and therefore still significantly lower than *fPassDop* Gen2 despite the matching or improved S_{pass} performance after firing. Thus, while the exact influence of the gas ratio and therefore the *Passivation* layer composition on R_{Sheet} cannot be fully tracked, it is sufficiently low that this parameter can be used to adjust S_{pass}, while the influence on R_{Sheet} can be compensated by adjusting the a-Si:P *Doping* layer thickness.

6.4 Summary

In this chapter the development and basic characterization of *PassDop* layers was described. Based on the original *PassDop* layer developed by Suwito *et al.* [19], a second generation for SiC *PassDop* was developed with the focus on improving the doping efficiency as well as the thermal stability. The first was achieved by increasing the ratio of the SiC_x:P layer in the SiC_x:H/SiC_x:P stack. As the intrinsic SiC_x:H layer thickness was decreased to 5 nm leading to a decrease in R_{Sheet} from 20 to 13 Ω/sq. To improve the thermal stability, a stoichiometric *Capping* layer was introduced. The main purpose of this layer was to prevent or retard outdiffusion of hydrogen during thermal treatment. If applying at least 15 nm of this layer, a S_{pass} of 1 cm/s was achieved after annealing at 400 °C for one hour. At below 5 cm/s S_{pass} was still reasonably low if annealing at 450 °C for one hour. The *Capping* layer not only influenced the thermal stability but acted as a sacrificial layer during the laser doping process. While the R_{Sheet} contribution by the layer itself was insignificant, applying this layer prevented a burst-off of the *Doping* layer, thus resulting in a higher *Doping* efficiency.

As an alternative to SiC *PassDop*, SiN *PassDop* was developed based on SiN_x:P. Similar to SiC *PassDop*, the focus was on solar cells with a low-temperature metallization approach like plating. The new SiN *PassDop* uses only MW plasma excitation allowing for a possible implementation in-line. For the first generation (SiN *PassDop* Gen1), a single SiN_x:P layer was developed. With achieving a R_{Sheet} of approx 33 Ω/sq and a S_{pass} of approx. 2 cm/s this single layer fulfilled all of the electrical requirements for a *PassDop* layer. For SiN *PassDop* Gen2, the focus was on further improving the doping efficiency to obviate reduced contact ability by process fluctuation. An additional *Doping* layer based on a-Si:P was introduced on top of the *Passivation*. Using this new *Doping* layer, a reduction in R_{Sheet} to approx. 25 Ω/sq was achieved. For this two layer stack, it was found that R_{Sheet} did not depend significantly on the composition of the *Passivation* layer anymore. Finally the influence

of phosphorus in the SiN *PassDop* stack was investigated. Similar to a-Si:P, where a degradation in the surface passivation is observed for doped layers, SiN_x:P shows similar effects. However, the results showed that that even with strongly doped layers, an excellent surface passivation as low as 2 cm/s could be achieved and that an intrinsic layer as used for HIT solar cells is not required. For the laser doping process it was shown that for SiN_x the first 30 to 50 nm are very important. If this part of the SiN_x layer is not doped by phosphorus, the phosphorus dose in the LBSF was calculated to decrease by a factor of 3.8 compared to a fully doped SiN_x:P layer. The a-Si:P *Doping* layer was able cushion this effect, but even in this case the phosphorus dose decreased by a factor of 1.7.

Both SiC *PassDop* and SiN *PassDop* do not provide a stable surface passivation under thermal treatment above 600 °C. As an alternative, based on SiN_x:P as well, the *fPassDop* process was investigated. It was shown that for the requirement of a firing stable surface passivation, the doping and passivation properties were complementary. For a good surface passivation after firing at 750 °C layers with a refractive index of below 2.4 were required, but these layers resulted in a R_{Sheet} of around 100 Ω/sq at a laser fluence of 9 J/cm^2. As an alternative three variants of double layer stacks were investigated. The first variant used an Si-rich *Passivation* layer combined with an N-rich *Capping* layer, similar to what was investigated by other authors before. For this variant, no firing stabile surface passivation with a *Passivation* layer thickness above 10 nm could be achieved, which would be required to achieve a suitable doping efficiency. The second variant was based on an N-rich *Passivation* layer and an Si-rich *Passivation* layer. Compared to the single layer, an improvement in the doping efficiency was achieved, but only at higher laser fluences $\geq$ 10 J/cm^2. The minimum in R_{Sheet} decreased to 60 Ω/sq, which led to the first »standard« *fPassDop* stacks Gen1 and Gen2 being defined.

The third variant that was tested was based on an N-rich *Passivation* layer that was similar to the *Passivation* layer used for *fPassDop* Gen2. However, The *Doping* layer was replaced by a-Si:P, similar to what was investigated for SiN *PassDop* Gen2. The a-Si:P *Doping* layer led to a significant improve in R_{Sheet} as values as low as 25 Ω/sq were determined. This improvement was mainly attributed to the lower melting point of the a-Si:P layer. While the new *Doping* layer had a negative impact on the firing stability it was shown that this can be compensated by adjusting the composition and thickness of the N-rich SiN_x *Passivation* layer. Similar to SiN *PassDop* Gen2, the influence of the *Passivation* layer composition on the doping efficiency was found to be low. In addition, it was shown that the doping efficiency can be improved by increasing the *Doping* layer thickness without affecting the firing stability

of the surface passivation significantly. This means that with the composition of the *Passivation* layer and the thickness of the *Doping* layer a set of parameters were found that can influence the surface passivation and the doping efficiency, without affecting the other significantly. Thus, a partial decoupling of surface passivation and doping efficiency was achieved. Due to these significant improvements the most current *fPassDop* Gen3 is based on this approach. With *fPassDop* Gen3 a S_{pass} of 6 to 8 cm/s can be reached after firing at 700 to 850 °C combined with a R_{Sheet} after laser doping of approx. 20 Ω/sq for laser fluences above 8 J/cm^2.

7 Properties of the *PassDop* Local Back Surface Field

In the previous chapter, a selection of PassDop layers based on SiC_x:P and SiN_x:P was established. In this chapter, a more detailed investigation in the properties of the PassDop Local Back Surface Field (LBSF) after the laser doping process is presented.
The first part is dedicated to the doping profiles. Here, several methods are investigated, both to analyze single laser spots as well as macroscopic methods like Secondary Ion Mass Spectrometry (SIMS) and Electrochemical Capacitance-Voltage Profiling (ECV). Not only dopants are in the focus, but also impurities that may be induced into the LBSF as a side-effect, like nitrogen. It will be shown that these impurities can have a significant impact on methods like ECV.
In the second part, the recombination at the LBSF is analyzed for SiC PassDop and SiN PassDop. The recombination is analyzed both directly after the laser as well as after annealing. Here, the methods by Fischer [56] and Saint-Cast [58] are being compared.

7.1 Profile Characterization

In principle, the characterization of the doping concentration for emitter or Back-Surface-Field (BSF) profiles is an established process. However, for selective laser doping like the *PassDop* process, characterization can be difficult for mainly two reasons: First, the structures generated by the laser are relatively small (below 100 µm), while most characterization methods are designed to be used with macroscopic structures in the range of mm. Second, due to the profiling of the laser pulse (both time- as well as lateral fluence profile) inhomogeneities are expected within a single spot, which most profile characterization methods cannot resolve. In addition, impurities (e.g. nitrogen) induced during laser doping could have an impact on the measurement methods, therefore multiple methods should be compared.

This section discusses the methods that were used to analyze the doping and impurity content within the *PassDop* LBSF. Both methods investigating the microscopic structure of the laser spots (e.g. Scanning Electron Microscope (SEM)) as well as macroscopic methods (e.g. ECV) were investigated.

7.1.1 Sample Design for Macroscopic Methods

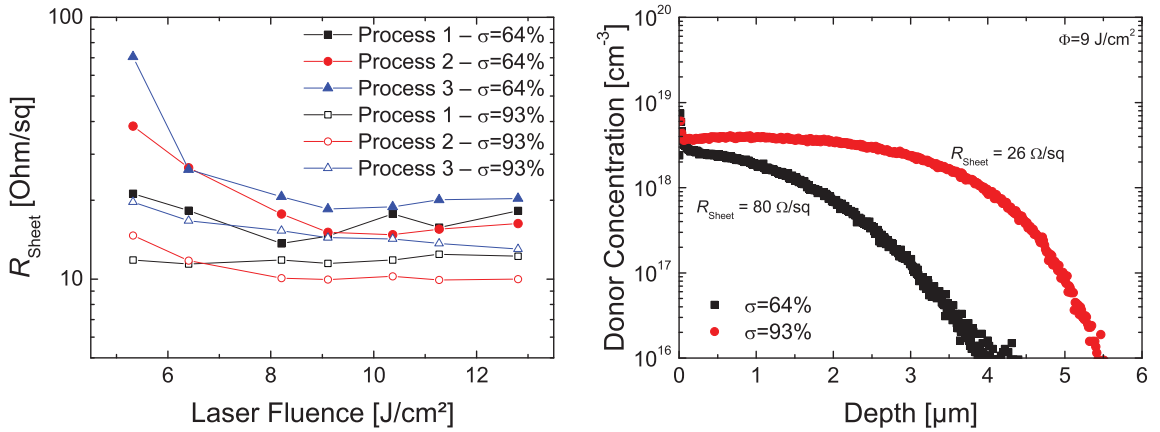

(a) R_{Sheet} for a selection of *fPassDop* processes. The legend gives the pulse to pulse distance for the laser process.

(b) SIMS profiles for *fPassDop* Gen2 at a fluence of $\phi = 9\,\text{J/cm}^2$

Figure 7.1: Variation of the pulse distance/pulse overlap for *fPassDop* processes

Motivation

Determining the doping concentration for a single laser spot is difficult due to the small dimensions ($d_{\text{cont}} \approx 50\,\mu\text{m}$). Thus a sample structure with single laser spots cannot be used to characterize the LBSF with macroscopic methods for which the measured area strongly exceeds the point size. Examples for such methods are: 4-point probes (4pp), ECV, Spreading Resistance Profiling (SRP) and SIMS

While some investigations were made for microscopic methods (see Section 7.1.2), characterization using 4pp and ECV is fast and simple. However, to be able to use these methods, a transformation from a microscopic to a macroscopic structure was required. This was solved by using overlapping laser pulses to generate areas of 20 mm × 20 mm or larger. The sketch of such a structure can be seen in Figure 6.1 (page 78) on the right.

With this kind of sample structure, one has to keep in mind that—depending on the amount of overlap—certain areas of the laser spot will be molten multiple times and not only once like it is the case for the final cell process (unless using line or dash contacts). Thus, the results determined using these

methods cannot be identical to the properties of the LBSF in the cell and were mainly used to compare different processes. Especially it has to be considered that the overlap or laser pulse distance can have a significant influence on the determined results.

Therefore, the limitations of such structures and the influence of the overlap are briefly discussed in this section. In more detail, this influence was investigated in the diploma thesis of Wenclawiak [192].

Experimental

Commonly, on *p*-type samples, an area of 20 mm × 20 mm was created with a pulse to pulse distance of 25 µm. The overlap σ is defined by the relation of the pulse distance p_d and the beam waist ω_0 [183]:

$$\sigma = 1 - \frac{p_\mathrm{d}}{2 \cdot \omega_0} \tag{7.1}$$

Usually $p_\mathrm{d} = 25\,\mu\mathrm{m} = r_\mathrm{cont}$ was used resulting in $\sigma \approx 64\,\%$. In the comparisons outlined here, a selection of *fPassDop* processes is shown which were lasered with a pulse distance of $p_\mathrm{d} = 25\,\mu\mathrm{m}(\hat{=}\sigma \approx 64\,\%)$ as well as $p_\mathrm{d} = 5\,\mu\mathrm{m}(\hat{=}\sigma \approx 93\,\%)$. For higher pulse distances than 25 µm a fully processed area cannot be guaranteed. In both cases the line distance was chosen at 25 µm.

The *fPassDop* processes used in this experiment are based on *fPassDop* Gen3, thus using a Si-rich SiN_x:P *Passivation* layer in combination with an a-Si:P *Doping* layer as described in Section 6.3.2. Within Process 1 to 3, the *Passivation* layer composition was varied as well as the thickness of the two layers. The process variations were:

1. Process 1: SiH_4: 111 sccm, N_2: 79 sccm, Thickness: 80 nm + 70 nm
2. Process 2: SiH_4: 111 sccm, N_2: 79 sccm, Thickness: 100 nm + 100 nm
3. Process 3: SiH_4: 107 sccm, N_2: 83 sccm, Thickness: 70 nm + 80 nm

The Thickness here is given as *Passivation+Doping* layer. After laser doping, the measurement of R_Sheet were performed using 4pp.

The evaluation of the pulse distance on the doping profile was performed for *fPassDop* Gen2 samples. The phosphorus concentration was determined by SIMS. In this case, the laser process was performed at a fluence of 9 J/cm^2. For the integration of the SIMS profile, complete ionization and dopant activation

was assumed as well as the carrier mobility in silicon as defined by Klassen [193, 194].

Results

Figure 7.1a shows R_{Sheet} measurements for the *fPassDop* Gen3 processes for a pulse distance of 5 as well as 25 µm. The solid symbols correspond to a pulse distance of 25 µm, the open symbols to 5 µm. For all layers, the determined R_{Sheet} was lower when using 5 µm, usually by a factor of 1.3 to 1.8. Using a higher overlap led to a slightly lower dependency of R_{Sheet} on the laser fluence.

Figure 7.1b shows the determined SIMS profiles for *fPassDop* Gen2 for a pulse distance of 5 and 25 µm. Using a pulse distance of 5 µm, the depth of the profile was found to be significantly higher, resulting in a significantly lower integrated R_{Sheet}. The surface concentration remained almost unchanged at approx. $4 \times 10^{18}\,\mathrm{cm}^{-3}$.

Discussion

The first observation to be made is that the pulse distance clearly has an influence on the resulting R_{Sheet}, as can be observed in Figure 7.1a. The fact that the measured R_{Sheet} was lower and seemed to be more constant over a wide range of laser fluences could lead to the conclusion that it might be desirable to use a higher overlap to achieve more reproducible results. However, it has to be considered that an overlap of over 90 % is even further away from the non-overlapping laser process that is used in the device process.
To explain the lower R_{Sheet}, two effects have to be considered. The first is that the dose was increased, possibly by dissolving remnants of the *PassDop* stack that the lower overlap of 64 % was not able to include in the LBSF. The second is that the subsequent laser processes resulted in a drive in of dopants and therefore a deeper profile but a lower surface concentration (at the same dose), which—due to the higher mobility of the carriers—would result in a lower R_{Sheet}.

To further evaluate these influences, the example of the doping profiles of *fPassDop* Gen2 can be used as shown in Figure 7.1b. This example was particularly interesting as a strong drop in R_{Sheet} by a factor of 3 occurred. The first conclusion that could be drawn from the observations (similar surface concentration, but deeper profile when using a higher overlap) was that the phosphorus dose ending up in the LBSF was not constant. These additional dopants were very likely leftovers from the dielectric that were not fully

molten and resided at the surface and therefore did not contribute to the laser doping process. During remelting of subsequent laser pulses, the (parts) of these leftovers can add their dopant content and increase the phosphorus dose.

While the higher overlap results in a significantly lower R_{Sheet}, the surface concentration remained low and therefore the advantages remain low (mainly a lower LBSF recombination would be expected). The contact ability of the LBSF would still be questionable at the given surface concentration.

For the doping profile test structures that were investigated in this chapter a pulse overlap of 64 % was therefore used as a standard, since the target at the device level were single laser spots. The given overlap was close to the lower limit that allowed a fully processed area but with the doping profile as close as possible to the single spots. Still, in the following sections, one should keep in mind that the overlap can have a significant influence on the doping profile. Therefore, these structures are mainly useful to compare and evaluate different processes for which the samples were processed using the same overlap.

7.1.2 Doping Concentration in a Single Laser Spot

Motivation

Most of the doping profile investigations were performed using macroscopic methods on overlapping point structures. However due to the implications described in the previous section, the overlapping point structures have certain limitations:

1. The doping profile determined (by either measurement) does not correspond exactly to the doping profile (anywhere) in a single laser spot as some areas were processed multiple times by the laser.
2. Local inhomogeneities in the LBSF doping cannot be visualized
3. Improper ablation is expected to occur at a higher rate as multiple laser processing would be expected to reduce this effect

Due to the microscopic nature of the laser spots and the fact that the doping concentration is mostly accessable by indirect measurement methods (e.g. determining the carrier concentration by ECV or *Raman*). Determining the doping profile for a single laser spot is a tough task.

Here, a selection of methods were tested on *PassDop* single laser spots. The main goal was to gather information about the dopant distributions, i.e. local inhomogeneities. As the specific measurements are not necessarily related to each other and in some cases were not even performed for the same layers, each method will be discussed individually.

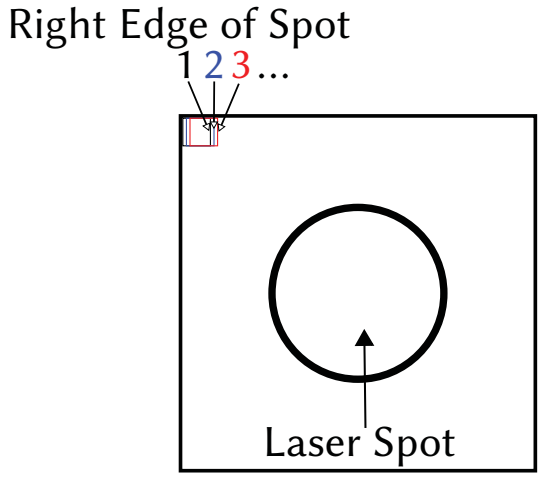

Figure 7.2: Sketch of the scanning SIMS technique, referred to as »3D«-SIMS here. A focused sputter beam is used to scan the surface. For each spot, the concentration of the desired element can be logged.

»3D« SIMS

Motivation

The advantage of the SIMS technique is that the actual concentration of an element can be measured (almost) directly. Usually it is applied on a spot with a size in the range of mm and thus of much larger scale than a *PassDop* laser spot. However, the spot size can be reduced significantly, until the measured area would fit easily into a laser spot. An estimation for a lateral distribution of dopants can be made if the technique is used in a scanning mode (see Figure 7.2). Thus, it is an interesting method to test on *PassDop* laser structures.

Experimental

For the experiment a SiC *PassDop* Gen2 sample was used. The laser spot was created at a laser fluence of $9\,\mathrm{J/cm^2}$.

The technique makes use of a small focused Cs^+ sputter beam of 8 µm width. The sputter depth for each step was approx. 37 nm. The beam was then moved by approx. 0.58 µm and another measurement sample was taken. The schematic is shown in Figure 7.2. As 256 measurements were taken per row in 256 rows, this resulted in a measurement area $150\,\mu\mathrm{m} \times 150\,\mu\mathrm{m}$. Due to the overlapping measurement spots, each spot cannot be viewed individually, but an integration of multiple spots has to be performed. Here, 4 areas were chosen, each at a size of 11×11 spots, and thus an area of approx. $34\,\mu\mathrm{m}^2$.

Results

Figure 7.3c shows a slice of the determined phosphorus concentration close to the surface by »3D« SIMS. The area with a high phosphorus concentration—the area of the LBSF— shows a high contrast to the c-Si bulk. Figure 7.3a shows the determined phosphorus counts of the fifth measurement slice. A high amount of counts was detected in the surrounding area. This influence decreased with each slice until it was only visible in the edges. Figure 7.3b shows the sixth slice, which indicates this development in the measurement data. Figure 7.3d shows the profiles that were determined for the areas indicated in Figure 7.3c. Each point corresponds to the integration over the respective area of one measurement slice. The measurement showed that in each case the surface concentration for the layer was found in the range of $1 \times 10^{20}\,\mathrm{cm^{-3}}$ or above. For the different areas the strongest influence was

found in the profile depth. For region 1 and 3, a depth of approx. 2 µm was determined, for region 2 and 4, the depth was found to be 30 µm.

Discussion

For the interpretation of the results, it is important to bear in mind the fundamentals of the method. The nature of overlapping (relatively large) measurement spots results in a collection of particles from a wider range and an influence of neighboring spots. Thus, the method indicates a localization that is not—or only partly—present. This was especially visible with the influence of the SiC_x *PassDop* layer in the edge regions. Although the regions were not chosen very close to the edge of the laser spot, an influence in the data was found within the first 500 nm of the evaluated data. This explains the peaks in the concentration that were found for the regions 1 and 3, as here, the signal was a mix between the phosphorus concentration in the SiC_x layer and that of the LBSF. As the phosphorus concentration in the SiC_x layer can be at a level of 1×10^{21} cm^{-3} or higher, it dominated the measurement until the SiC_x layer was removed. In comparison, influence of the lowly doped bulk is not expected to be as high, as the concentration is orders of magnitude below that of the LBSF. An influence was found up to a (c-Si) depth of just below 500 nm, which is significantly above the thickness of the SiC_x *PassDop* layer stack. However, the sputter rate of the SiC_x layer is not known and could be significantly below that of c-Si which was the material being assumed during the measurement. This and the inclusion of carbon (see Section 7.1.4) could affect the results significantly and therefore the results within the first 500 nm should be taken with care.

Having discussed these influences the profiles can now be discussed. Here the most important result was to see that in all regions the concentration showed a tendency towards the same level (see the range between 500 and 700 nm depth). The decrease in the laser fluence towards the edge of the ablated region mostly seemed to influence the depth of the doped region, but not the level of surface concentration. This is an important observation, since this leads to the conclusion that for the process of contacting the metal, the whole ablated spot can contribute.

Another important influence of the profile (both depth and surface concentration) would be expected on the LBSF recombination. However, for the current processes, the doping concentration was not found to be of major importance for the level of recombination in the LBSF (see Section 7.2). Still, the decreasing depth towards the ablation edge could indicate that at the edge

the profile was very shallow. This could lead to increased recombination in these areas.

In conclusion, this method has the strong advantage of the direct measurement of the phosphorus concentration, which allowed for localized profile calculation of the *PassDop* LBSF. However, the measurement method itself already limited the application of the method to structures where the concentration remains constant over at least 10 to 15 µm. Especially in regions where a rather sharp change in the concentration is expected (within a few µm), a reliable evaluation is not possible.

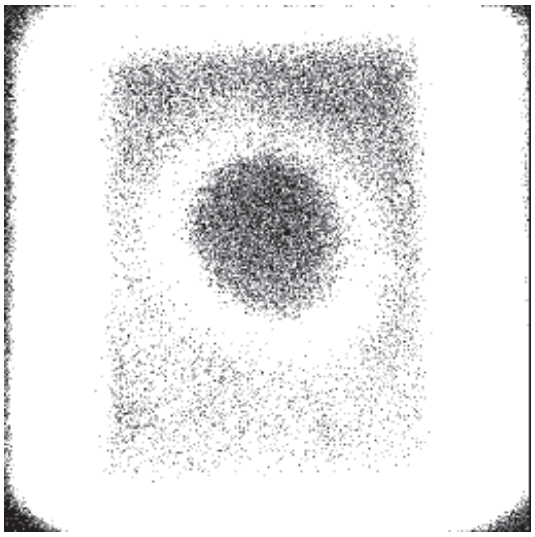

(a) P: Slice 5

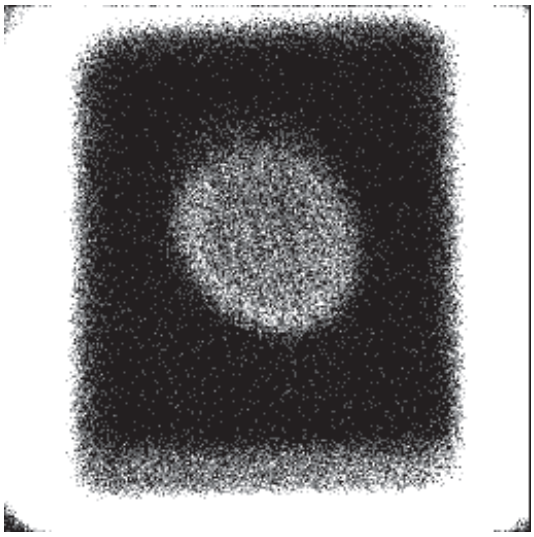

(b) P: Slice 6

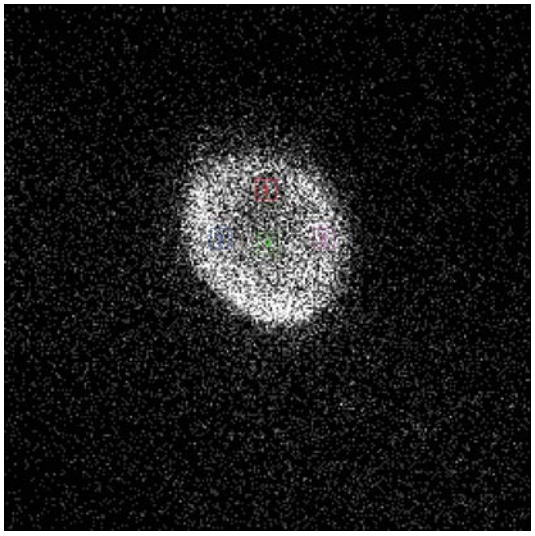

(c) Investigated areas

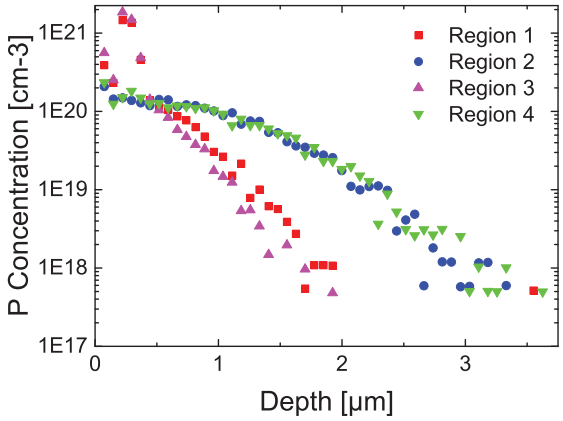

(d) P Profiles determined within the areas

Figure 7.3: Results from the »3D«-SIMS investigation. Slice 5 and 6 of the phosphorus counts are shown to illustrate the influence of the surrounding Plasma-Enhanced Chemical Vapor Deposition (PECVD) layer. The profiles were determined by integrating the counts over the indicated areas.

Micro *Raman*

Motivation

Raman spectroscopy describes the inealistic scattering of photons with matter [195]. It is one of the most important methods to gather information about the lattice vibration frequencies [196]. For incident photons of energy $h\nu_0$, the scattering leads to a frequency shift of the secondary photons $h(\nu_0 \pm \Delta\nu)$, where $\Delta\nu$ is characteristic for the investigated matter. For crystalline silicon, the width of the resulting peak can be correlated to the doping concentration [197]. As the width in this work was the only parameter of interest, it is here referred to as »*Raman* signal«. It can be used to (locally) evaluate the doping concentration for an Al BSF [197]. However, for *n*-type doping, a doping concentration above $1 \times 10^{19}\,\mathrm{cm}^{-3}$ is required to be detectable. Thus, for *n*-type doping, the method can only be applied for very high doping concentrations and is not directly useful for the processes investigated here [197]. Instead, an indirect method was applied. Here, two variants were investigated:

1. The idea of the first method is based on a paper published by Müller *et al.* [198]. They found out that a present concentration of phosphorus can block the diffusion of boron. The effectivity of the blocking depends on the doping concentration at the surface. Therefore it would be interesting to find out if the *PassDop* LBSF has a high enough concentration of phosphorus to induce such a blocking effect. Any significant amount of boron that diffused into the surface should be easily detectable by *Raman*. Thus the method could reveal inhomogeneities in the surface concentration.

2. The basic idea of the second method was that a change in the hole concentration can be detected by more precision than that of electrons due to the reason given above. To achieve such a situation with *nPassDop*, a high background *p*-type doping generated by boron diffusion and drive-in steps was used. On these surfaces, the *PassDop* layers were deposited and the *PassDop* laser process was applied. The induced phosphorus doping leads to a compensation of the background *p*-type doping and thus to a decreased net carrier concentration which should be detectable by the *Raman* signal.

In this section, the term »Micro *Raman*« is used. This always refers to *Raman* excitation and measurement through an optical microscope.

Experimental

For these experiments, the SiN *PassDop* Gen1 layer was used and is here referred to as a-SiN:P. *n*-type 1 Ωcm Floatzone (FZ) shiny-etched samples were used as base material.

Method 1: The SiN *PassDop* Gen1 layer was deposited onto the samples. The laser process was performed at a fluence of 9 J/cm^2. After the laser process, the samples received BBr_3 furnace diffusion at 990 °C followed by etching the boron glass in Hydrofluoric Acid (HF). The samples were then measured by Microscopic *Raman* (Micro-Raman) to determine the effective hole concentration. To differentiate between blocking by phosphorus and (possible) blocking by nitrogen, two reference samples were included. For the first, denoted as a-SiN:H, phosphorus was replaced with pure hydrogen, to investigate blocking by nitrogen. For the second, the nitrogen gas flow was set to 0 sccm, thus depositing an a-Si:P layer. This sample is a reference for the phosphorus blocking.

Method 2: The samples first received BBr_3 furnace diffusion at 850 °C followed by a drive-in step at 1075 °C in Ar atmosphere for 120 min and etching of the boron glass in HF. Then, the *PassDop* layer was deposited onto the surface followed by the laser process at a fluence of 9 J/cm^2. Finally, the samples were measured to determine the change in the effective hole concentration.

The boron diffusion processes differ for the two methods as they serve a different purpose. For the first method, a high diffusion temperature would be expected to highlight differences in the doping concentration (and therefore the blocking effect) in a stronger way. For the second method, a high and almost constant background concentration of boron was the goal, thus diffusion at a moderate temperature followed by a long drive-in step.

In all cases, the signal level could not yet be calibrated to a specific doping concentration, as a reliable calibration source would be required (e.g. SIMS).

Results

Method 1: Figure 7.4 shows the Micro-Raman image for the first method, where the samples received the boron diffusion after the deposition of the *PassDop* layer and the laser process. As references layers, a-Si:P and SiN_x:H

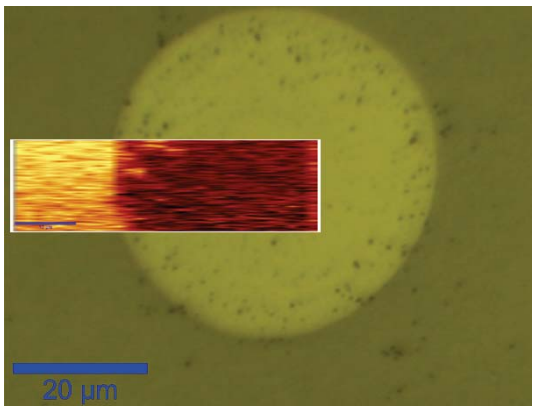

(a) Boron diffusion on a-Si:P background

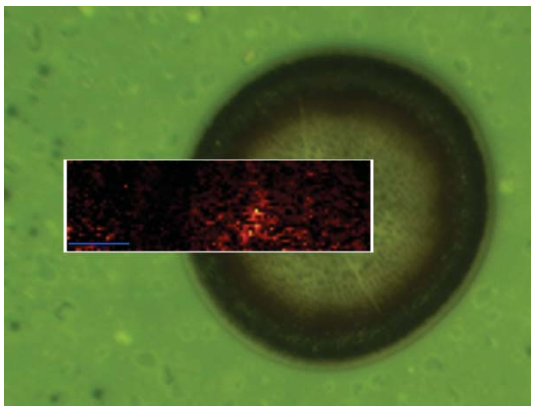

(b) Boron diffusion on a-SiN:P background

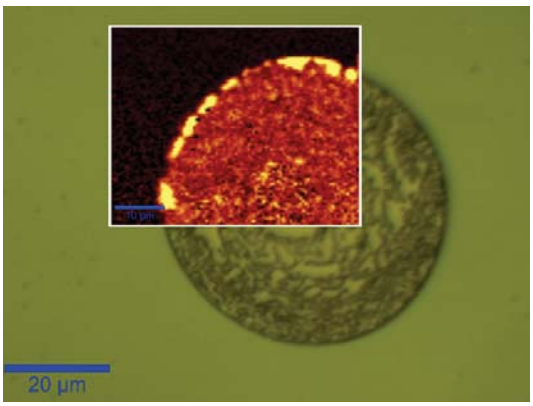

(c) Boron diffusion on a-SiN:H background

Figure 7.4: Method 1: Micro-Raman pictures of *PassDop* samples that were processed by the *PassDop* laser process and then received a tube BBr_3 furnace diffusion. The pictures were embedded in corresponding microscopy images of the same spots. The scale for all pictures is identical.

were used. The *Raman* mappings were embedded into the corresponding microscopy images. For a-Si:P (Figure 7.4a) outside of the laser spot, a high signal was found with the signal significantly decreasing within the laser spot. For a-SiN:P (Figure 7.4b) the signal was generally lower both inside and outside of the spot. Only a few spots showed a strong signal. For a-SiN:H (Figure 7.4c) the signal outside the spot was similar to a-SiN:P. A strong signal was observed at spots around the edge, while the signal inside the spot was again lower. Figure 7.6 shows the line scans that were performed for the three samples (roughly along the horizontal center line). The a-SiN:P sample showed the lowest overall line scan with a very high scattering. The a-Si:P sample showed a nearly constant signal level outside and inside the spot with the connecting areas transiting between the two levels. For a-SiN:H, the signal outside of the spot was similar to a-SiN:P, but increased to the level of a-Si:P at the edge of the spot. For this sample a higher signal was determined inside the spot than for the other two.

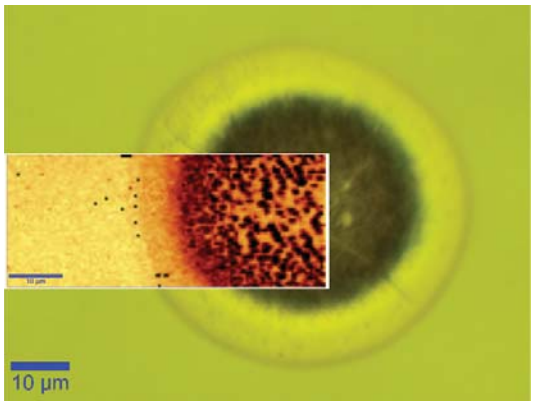

Figure 7.5: Method2: SiN_x *PassDop* sample with background boron diffusion. The sample received a BBr_3 furnace diffusion and a drive-in step to add a high-level boron background (doping approx. $9 \times 10^{19}\,cm^{-3}$). The *Raman* mapping was embedded in the corresponding microscopy image of the sample spot.

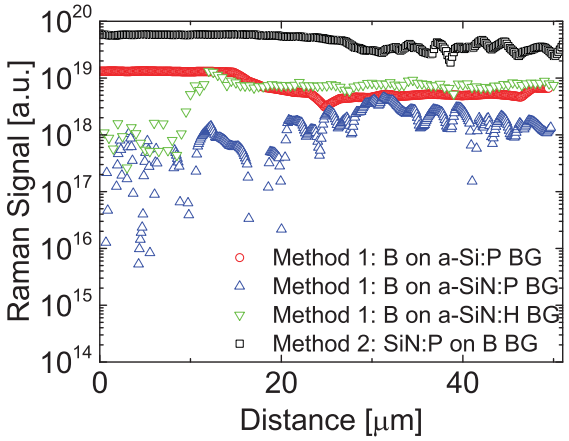

Figure 7.6: Linescans for the investigated samples.

Method 2: Figure 7.5 shows the Micro-Raman image for the second method, where the samples first received boron diffusion and drive-in to create a high boron background doping level and then were coated with the SiN_x:P layer and processed by the *PassDop* laser. The *Raman* mapping was embedded into the corresponding microscopy image. A constantly high signal was found outside of the laser spot with only a few black spots. Inside the laser spot, the signal was more splattered into dark and glowing areas. In the intermediate ring between the fully opened and the »untouched« areas, the signal was relatively constant with the level being slightly lower than in the outside. The line scan is shown in Figure 7.6. For this sample, the signal overall was significantly higher than for the other samples. The signal decreased slightly when reaching the intermediate ring structure and showed a high variation inside the laser doping spot.

Discussion

Method 1:
The results for a-Si:P (Figure 7.4a) clearly showed that the blocking of the boron diffusion by phosphorus was in place. While the thin a-Si:P layer itself would not be expected to significantly block the diffusion (but possibly still retarded it to some degree), inside of the laser spot, the *Raman* signal was

significantly lower, leading to the conclusion that phosphorus was blocking the diffusion process.

However, phosphorus is not the only element that can hinder boron diffusion. It is known that silicon nitride can block dopant diffusion [199] and this effect showed clearly outside of the laser spot for the a-SiN:P and a-SiN:H samples (see Figure 7.4b and 7.4c). Here, the boron diffusion was blocked by the respective amorphous (non-ablated) layers.

Inside the laser spot, it would be expected that the blocking of the a-Si:P layer would be improved due to its superior doping efficiency (surface concentration of the LBSF approx $8 \times 10^{19}\,\mathrm{cm}^{-3}$) compared to a-SiN:P (surface concentration approx $3 \times 10^{19}\,\mathrm{cm}^{-3}$). As the results—especially the line scans shown in Figure 7.6—showed, the a-SiN:P LBSF (signal 1 to 5×10^{18}) led to a stronger blocking than the a-Si:P LBSF (signal $\approx 5 \times 10^{18}$), which means that inside the laser spot, phosphorus cannot be the only influence on the boron diffusion. Since for a-SiN:H blocking was determined inside the laser spot as well (signal 6 to 8×10^{18}), this led to the conclusion, that nitrogen had to be present in the LBSF and hindered the boron diffusion. This means that the method cannot distinguish between blocking by phosphorus and by nitrogen in a reliable way. Hence, it cannot be used to estimate the (local) phosphorus content and distribution in the LBSF

One interesting feature for the a-SiN:H sample was the hot spots at the edge of the laser spot that can be observed in Figure 7.4c. Since the sample did not contain phosphorus, this means that in these areas the nitrogen concentration is significantly lower. One explanation would be that here the a-SiN:H layer was ablated, but the surface was not or only briefly molten, thus no nitrogen was induced into the surface. The second explanation would be that the area was molten, but the nitrogen was transported to other areas during the melting process, e.g. to the middle where the melt solidified the latest (due to the Gaussian fluence distribution). From the results, it was impossible to judge which of the two occurred.

Method 2:
For the second method, boron diffusion was performed before the laser process. For this kind of sample, there would always be expected to be a high signal level given the high boron background level. However, one has to keep in mind that the melting process could result in a redistribution of the dopants in addition to the compensation effect. Thus, while outside of the laser spot, a high constant level was observed, the doping level inside the spot was lower (see Figure 7.5 and 7.6) and reference samples without doping (and without nitrogen) are required to find out if this reduced doping

level was due to a compensation by phosphorus or redistribution of boron. Measurements of the cross-section could help in this regard as well. The most interesting feature of the measurement was the observed clustering of dark and glowing parts inside the spot (see Figure 7.5). This could be an indication of the silicon nitride clustering that was observed by X-Ray Diffraction (XRD) (see Section 7.1.3).

An additional feature was the signal in the ring structure that was observed by microscopy. The corresponding range in the linescan would reach from approx. 20 to 25 µm (Figure 7.6, black squares). As discussed in the next section, this was expected to be an improperly ablated part of the layer, where the passivation was damaged, but the silicon possibly was not molten. While the doping signal from Micro-Raman was slightly lower in this area, the decrease would be explained by the optical influence of the damaged *PassDop* layer. This contrast in behavior between the area of this ring structure and the inner part of the laser spot was a direct indication that in the ring structure, no significant doping by the laser process occurred in this ring structure and therefore no LBSF formation happened. Overall, the method showed promising results. To better judge its value at understanding the phosphorus distribution in the LBSF more test samples would be required to better understand the effect of the laser process on the boron background.

To conclude, both methods yielded interesting results. However, it can be hard to separate the influences of phosphorus and nitrogen, especially for Method 1. The prominent result from Method 2 was the direct indication that the area of laser-induced damage to the surface passivation and that of the LBSF do not have to match, giving an explanation for possibly elevated recombination within the laser spot. However, for an improved qualitative analysis and especially for a quantitative evaluation, measurements of more reference samples would be required for both Methods, especially for different *PassDop* layers as well as SIMS measurements to calibrate the signal.

7.1.3 Nitrogen as an Impurity in the *PassDop* LBSF

Motivation

During the development of the SiN_x:P-based *PassDop* layers, 4pp and ECV measurements were used for a fast and basic analysis of the doping efficiency. A significant mismatch between the R_{Sheet} determined from the 4pp measurement and the R_{Sheet} acquired by integration of the doping profile determined by ECV was found. It was suspected that nitrogen incorporated into the silicon was responsible for this mismatch. Therefore, this section is dedicated to the characterization of the effect of nitrogen in the *PassDop* LBSF for the SiN_x:P-based *PassDop* layers.

The first part in this section is an experiment that was performed to confirm the results obtained by 4pp using a separate method. In the second part, the influence of nitrogen on the profile measurements and the LBSF formation will be discussed using methods like SIMS, XRD and Energy-Dispersive X-Ray spectroscopy (EDX).

Most of this section was published in [154].

Validity of the 4pp Measurement

Experimental

For this experiment SiN *PassDop* Gen2 and *fPassDop* Gen3 were used. The laser process was performed at a laser fluence of $9\,J/cm^2$. For these measurements the lasered area was increased such that it span across half of the wafer. The other half remained untouched.

In addition to 4pp, R_{Sheet} was determined by inductively measuring the conductivity of the sample. For this measurement, the Sinton WCT-120 lifetime tester was used. The measurement is therefore referred to as »QSSPC«. As a reference for R_{Sheet} of the c-Si bulk, the same measurement was taken on the half of the wafer that was not processed by the laser. For the calculation of R_{Sheet} of the LBSF a parallel circuit of the LBSF and the base was assumed, thus: $1/R_{Sheet} = 1/R_{Sheet,meas} - 1/R_{Sheet,base}$. As base material 1 Ωcm *p*-type FZ c-Si wafers were used. The wafer thickness was 200 µm and therefore an expected R_{Sheet} in the range of 50 Ω/sq for the base.

Table 7.1: R_{Sheet} comparison for 4pp and Quasi-Steady-State Photoconductance (QSSPC). Bold characters highlight the values in each row that should be compared.

PassDop Layer	Type	4pp		QSSPC		
		Meas	Calc	Meas	Calc	Base
		R_{Sheet} [Ω/sq]				
SiN *PassDop* Gen2	*p*	**29.7**	–	19.2	**30**	52.8
fPassDop Gen3	*p*	**103.5**	–	35.5	**108**	52.8

Results

The results for a comparison of QSSPC and 4pp can be found in Table 7.1. The bold characters highlight the values that should be compared. The R_{Sheet} determined by QSSPC for the base was 52.8 Ω/sq. The R_{Sheet} results determined by both methods were at approx. 30 Ω/sq for SiN *PassDop* Gen2 and approx. 105 Ω/sq for *fPassDop* Gen3 similar.

Discussion

Before discussing the results, it should be mentioned that due to processing issues the layers exhibit a lower doping efficiency. R_{Sheet} values are not comparable to other depositions of these layers.

However, the experiment can still be used to compare the results by the two methods to determine R_{Sheet}. This comparison is shown in Table 7.1. The inductive method to determine the conductivity (and thus the R_{Sheet}) for the structure has the advantage that contacting errors (as would be possible for 4pp) can be excluded. The main uncertainty for the method is the resistivity of the base but since a reference measurement on the same wafer (but within a different area) could be performed it is well known for the respective wafers. The results—as shown in Table 7.1—for the inductive method (QSSPC) and 4pp matched very well (the difference was well below 10 %) and thus it can be concluded that 4pp for the *PassDop* layers can be used as the reference for the R_{Sheet} of the *PassDop* LBSF.

The Effect of Nitrogen in the LBSF

Experimental

Three *PassDop* layers are investigated: *fPassDop* Gen2 and Gen3 as well as SiN *PassDop* Gen1 (low-temperature metallization). The layers are described in the Sections 6.3.2 and 6.2.2.

R_{Sheet} samples were prepared for all three stacks as described in 6.1, although only the $20\,\mathrm{mm} \times 20\,\mathrm{mm}$ area that was processed with a laser fluence of $9\,\mathrm{J/cm^2}$ was further investigated here. On these samples 4pp measurements as well as ECV measurements were performed. For the ECV measurement, no cleaning prior to the measurement was performed. A dip in HF was previously found to influence the propability of electrolyte leakage but not the resulting profile. Thus if the time frame between the laser process and the ECV measurement was kept reasonably low (less than approx. two weeks), a dip in HF was not required. The area enlargement factor of the surface due to the laser process was determined to be in the range of 1.02 and thus neglected.

For comparison to ECV, SIMS was measured on the same samples. The first Gen2 sample was measured at RTG Berlin, the second Gen2 sample as well as those for Gen3 and SiN *PassDop* Gen1 were measured at the National Renewable Energy Laboratory (NREL). The second Gen2 sample was measured to verify the profile. The electron profile determined from ECV and the phosphorus profile determined from SIMS were integrated to calculate R_{Sheet} assuming the carrier mobility as defined by Klaassen [193, 194]. The nitrogen and phosphorus doses were calculated by integration of the corresponding SIMS profiles. For nitrogen, the integration was performed three times: The »Nmax Dose« refers to the integration of the profile as determined by SIMS. »Nmin Dose« refers to the integration of the nitrogen profile but with the surface peak disregarded. »N Dose« refers to the integration of the profile, but with a constant value replacing the surface peak based on the first measurement point that was taken into account. The actual nitrogen dose was expected to be above Nmin, below Nmax and close to N. From a comparison of the electron (ECV) and phosphorus (SIMS) concentrations, $\xi = N_{\mathrm{ECV}}/N_{\mathrm{SIMS}}$ and $\delta = N_{\mathrm{ECV}} - N_{\mathrm{SIMS}}$ were calculated.

For Gen2, on the areas that were processed with 8 and $10\,\mathrm{J/cm^2}$, XRD was recorded to detect Si_3N_4 as well as polycrystalline silicon. For XRD, a Philips X'Pert MRD system equipped with a Cu K-alpha 0.154 nm x-ray source was

used. The maximum signal intensity was achieved under an angle of incidence of $\omega = 0.3°$. The measurement range for 2Θ was selected from 10° to 90°. The measurement was performed such that any signal from the (<100> oriented) c-Si bulk should vanish. The depth of XRD for this setup was unknown but should exceed the LBSF depth. A quantitative analysis using XRD could not be performed.

To support the observations determined by the results on R_{Sheet} samples, single laser spots were investigated by SEM for *fPassDop* Gen2 and Gen3, where EDX mappings were performed for nitrogen. These spots were created at a laser fluence of 9 J/cm^2. Images were acquired both at an electron energy of 5 keV as well as 10 keV highlighting features at the surface and slightly beneath, respectively.

Table 7.2: R_{Sheet} determined by 4pp, ECV and SIMS. All values were determined for a laser fluence of 9 J/cm^2.

PassDop Layer	4pp [Ω/sq]	ECV [Ω/sq]	SIMS [Ω/sq]
fPassDop Gen2	79.2	51.6	77.4
fPassDop Gen3	18.5	14.1	15.8
SiN *PassDop* Gen1	32.7	18.2	25.0

Results

A comparison of R_{Sheet} as measured by 4pp and as determined by integration of ECV and SIMS is shown in Table 7.2 for all investigated *PassDop* layers. As already described in the sections 6.2.2 and 6.3.2, the *fPassDop* Gen3 approach is expected to achieve the lowest R_{Sheet} and did so with just under 19 Ω/sq (4pp). *fPassDop* Gen2 was determined significantly above that at approx. 80 Ω/sq. SiN *PassDop* Gen1 was in between the two at approx. 33 Ω/sq. The sheet resistances determined by 4pp were the highest, while ECV resulted in significantly lower values and SIMS being in between the two. It is important to point out that these trends were similar for all investigated *PassDop* processes. The absolute discrepancy was the highest for the *fPassDop* Gen2 process and the lowest for the *fPassDop* Gen3 process.

Figure 7.7a shows the profiles that were determined by ECV and SIMS for the *fPassDop* Gen2 and Gen3 layers. Figure 7.7b shows the same information for the SiN *PassDop* Gen1 layer and the second *fPassDop* Gen2 sample. For all layers, the ECV electron, SIMS phosphorus and SIMS nitrogen profiles were

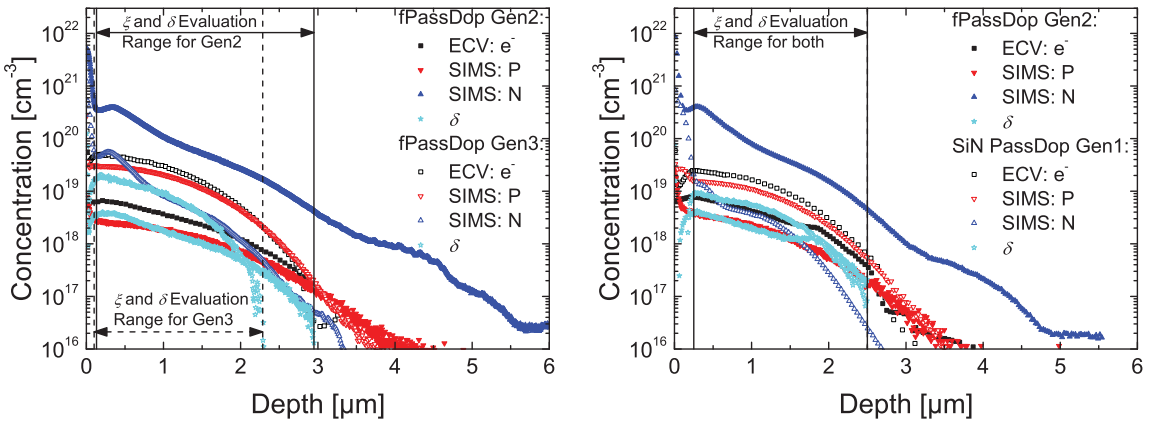

(a) *fPassDop* Gen2 and Gen3

(b) SiN *PassDop* Gen1 and a second *fPassDop* Gen2 sample

Figure 7.7: Electron profiles as determined by ECV and profiles for phosphorus and nitrogen as determined by SIMS. In addition, the δ of the electron (ECV) and phosphorus (SIMS) profiles is shown. The profiles were determined for $\phi = 9\,\mathrm{J/cm^2}$.

acquired. As additional information, the graphs show the determined δ (the difference between ECV and SIMS) in dependence of the depth as well as the limits that were used for the evaluation of δ and ξ.

For both the SIMS phosphorus as well as the ECV electron profile roughly a Gaussian profile shape was observed. For the ECV measurements a peak concentration within 200 to 300 µm from the the surface was observed with a decrease of the determined concentration at the surface. This effect was most pronounced for SiN *PassDop* Gen1 (open black squares, Figure 7.7b). The phosphorus SIMS profiles showed no such decrease but instead either followed the Gaussian shape up to the interface or showed an increase as found for SiN *PassDop* Gen1 and *fPassDop* Gen2. Except for these surface effects the ECV profile was always found to indicate a higher concentration than the respective SIMS measurement up to the interface, where uncertainties in the depth calibration can lead to a crossover point.

The differences in the doping level in between the different layers was significant. SiN *PassDop* Gen1 and *fPassDop* Gen3 both showed a phosphorus (SIMS) concentration well above $1 \times 10^{19}\,\mathrm{cm^{-3}}$, while the *fPassDop* Gen2 samples were found to be in the range of 3 to $4 \times 10^{18}\,\mathrm{cm^{-3}}$ (excluding the surface peak).

The concentration of nitrogen determined by SIMS did not follow a Gaussian shape as the phosphorus profiles did. As can be observed in Figure 7.7a and 7.7b, the Gaussian shape was superposed by an additional peak starting at a depth of around 600 to 1000 nm leading to a more pronounced increase in

Table 7.3: Nitrogen and Phosphorus doses for the SiN_x *PassDop* layers. Nitrogen doses are given in $1 \times 10^{15}\,cm^{-2}$, while the values for the phosphorus doses are given in $1 \times 10^{14}\,cm^{-2}$. For nitrogen, three values for the dose are given: Nmax, Nmin and N. Nmax refers to the integration of the profile as provided by SIMS. Nmin disregards all of the values related to the surface peak, where the SIMS measurement might have a larger error. For N, a constant value was assumed as a replacement of the original values, based on the first measurement point that was taken into account. The actual nitrogen dose was expected to be above Nmin, below Nmax and close to N.

PassDop Layer	Nmax Dose $[10^{15}cm^{-2}]$	Nmin Dose $[10^{15}cm^{-2}]$	N Dose $[10^{15}cm^{-2}]$	P Dose $[10^{14}cm^{-2}]$
fPassDop Gen2	57	30	35	3.6
fPassDop Gen3	6.2	3.0	3.6	42
SiN *PassDop* Gen1	7.6	0.76	1.3	23
fPassDop Gen2 2nd	53	25	30	5.6

the nitrogen concentration. For the *fPassDop* layers (Gen2 and Gen3), a decrease after reaching a peak concentration of approx. $6 \times 10^{19}\,cm^{-3}$ (Gen3) and $4 \times 10^{20}\,cm^{-3}$ (Gen2) was observed. SiN *PassDop* Gen1 did not reveal such an effect. Close to the surface (within the first 200 nm) a surface peak was observed for all layers, with the concentration increasing by an order of magnitude. The highest concentration of nitrogen was observed for the *fPassDop* Gen2 samples, reaching concentrations above $1 \times 10^{21}\,cm^{-3}$. Both, the profile shape and the concentration level were similar for the two *fPassDop* Gen2 samples. For these samples, the nitrogen concentration was found to be higher than that of phosphorus by approx. two orders of magnitudes and deeper by approx. 1.5 µm. For SiN *PassDop* Gen1 and *fPassDop* Gen3, the nitrogen concentration was similar to or lower than the phosphorus concentration except for surface effects.

The results for the dose of nitrogen as well as phosphorus in the LBSF for the respective layers can be found in Table 7.3. Note that the nitrogen dose is given per $1 \times 10^{15}\,cm^{-2}$, while the phosphorus dose is given in $1 \times 10^{14}\,cm^{-2}$. The values were determined from the integration of the profiles as outlined in the Experimental section. Three values are given for the nitrogen dose: Nmax (complete profile), Nmin (excluding surface peak) and N (constant concentration towards the surface). The overall trend is the same for all three: SiN *PassDop* Gen1 and *fPassDop* Gen3 had a dose of nitrogen within similar range, while the dose for *fPassDop* Gen2 was larger by a factor of ≈ 10. For SiN *PassDop* Gen1 and *fPassDop* Gen3, the nitrogen dose was lower than

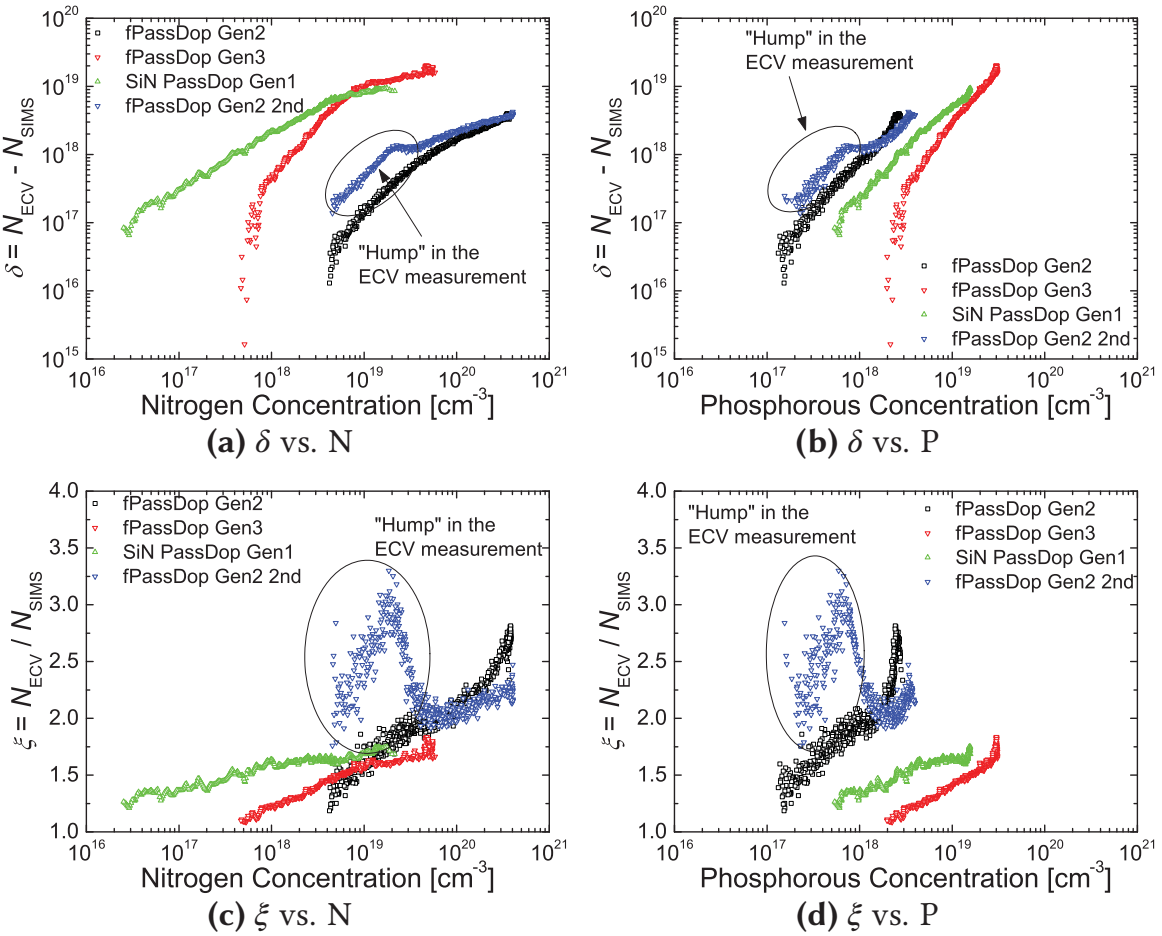

(a) δ vs. N **(b)** δ vs. P

(c) ξ vs. N **(d)** ξ vs. P

Figure 7.8: Representations of δ and ξ in dependence on the concentrations of nitrogen and phosphorus. The range for the evaluation for each layer can be extracted from Figure 7.7. For the second Gen2 and the SiN *PassDop* Gen1 sample, areas where inactive phosphorus might be as well as measurement errors during the ECV measurement where still included to show the strong effect they can have on the respective values. For the other samples, the range was adapted such that the effects do not occur.

the phosphorus dose if not taking Nmax as a reference. For *fPassDop* Gen2, the nitrogen dose was higher than that of phosphorus by an order of magnitude.

As shown in Figure 7.7, for all layers a discrepancy between the respective ECV electron profiles and the SIMS phosphorus profiles was found. To further evaluate the data, the representations of the quotient $\xi = N_{\mathrm{ECV}}/N_{\mathrm{SIMS}}$ and the difference $\delta = N_{\mathrm{ECV}} - N_{\mathrm{SIMS}}$ were calculated. In dependence on the depth, a increasing δ with decreasing depth was observed (see Figure 7.7). In all cases, the δ was within the range of the phosphorus concentration or slightly below. Figure 7.8c and Figure 7.8d show the calculated quotient ξ in dependence on the phosphorus and the nitrogen concentration respectively

for all of the investigated samples. Figure 7.8a and 7.8b show the the same for the calculated difference δ. The used limits for the investigations as well as a representation of δ in dependence on the depth are shown in the respective graphs for the ECV and SIMS profiles (see Figure 7.7a and 7.7b). The limits were chosen such that inactive phosphorus (as indicated by ECV) was not included as well as data beyond the crossover point of ECV and SIMS, thus $\xi \geq 1$.

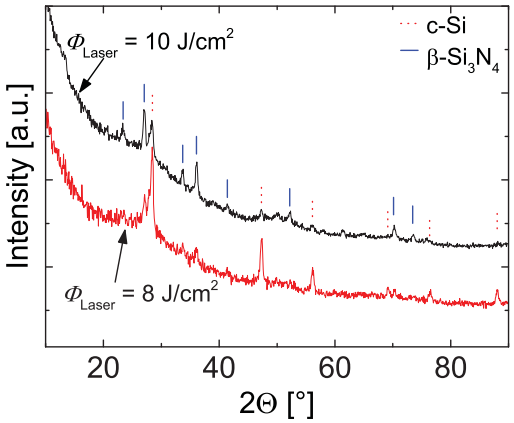

Figure 7.9: XRD measurements of *fPassDop* Gen2 samples for laser fluences of 8 and 10 J/cm^2. The red dotted vertical lines indicate peaks that were attributed to crystalline silicon, the blue solid vertical lines indicate peaks that identified β-Si_3N_4.

Both ξ and δ were found to increase with the respective concentrations of phosphorus and nitrogen. For the second *fPassDop* Gen2, the ECV measurement had a pronounced "hump" in the electron profile which showed significantly in ξ and δ and was marked in the graphs. For δ the trends for all layers in dependence on phosphorus or nitrogen was similar as δ increased with increasing concentration, but the level was different for each layer, thus the horizontal shifts in the graphs. For ξ in dependence on phosphorus, increasing trends with increasing phosphorus concentration were observed, but again the level was different for each layer. For ξ in dependence on nitrogen, a correlation could be postulated as for a similar nitrogen concentration a similar ξ was determined. This was especially the case above a nitrogen concentration of 1×10^{19} cm^{-3}.

To determine if Si_3N_4 as a product of the laser process was present, XRD measurements were performed at a laser fluences of 8 and 10 J/cm^2. This was done for *fPassDop* Gen2. The results are shown in Figure 7.9. Several peaks were found within the measured range, some of these peaks could be attributed to β-Si_3N_4, others were found to indicate c-Si. For the lower laser fluence of $\phi = 8$ J/cm^2, the signal corresponding to β-Si_3N_4 was lower, while the signal for c-Si was higher.

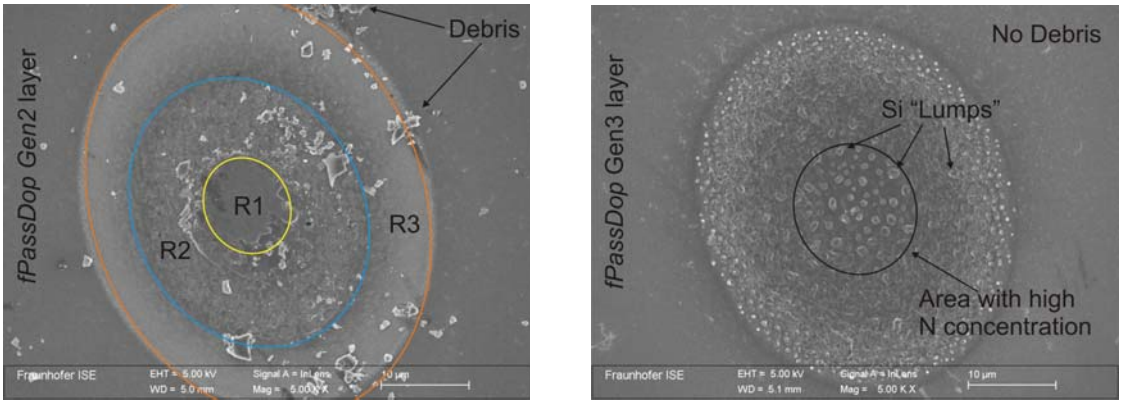

(a) *fPassDop* Gen2 **(b)** *fPassDop* Gen3

Figure 7.10: SEM images taken at 5 kV of single laser spots for the *fPassDop* Gen2 and Gen3 layers. Both layers were processed with a laser fluence of $\phi = 9\,\mathrm{J/cm^2}$. For Gen2, several ring-like structures were observed denoted as R1 to R3. Debris from the laser process was found within the spot and in the surrounding. For Gen3, no such ring structure or debris was observed, but lumps of silicon paved the spot. A circle marks the area where a high nitrogen concentration was determined by EDX.

Figure 7.10a and 7.10b show the SEM images that were gathered for *fPassDop* Gen2 and *fPassDop* Gen3 single laser spots respectively. For *fPassDop* Gen2, the spot showed multiple ring structures declared in the image as R1 (inner ring), R2 (middle ring) and R3 (outer ring) accompanied by a large amount of debris from the laser process. For the *fPassDop* Gen3 layer, the laser spot was observed to be much more like a clean cut without significant ring structures and no debris outside of the laser spot. SEM characterization at higher energy (10 keV) shown in Figure 7.11 indicated that for *fPassDop* Gen2 voids can be found in the region between R2 and R3. For *fPassDop* Gen3, no such effect was observed. Instead, a large amount of small Si »Lumps« were observed that seemed to lie on top of the c-Si surface. Increasing the electron energy didn't not reveal any voids but a smooth surface apart from the Si lumps. The image at higher energy suggested that the Si lumps were solid and not hollow.

EDX-Mapping of nitrogen within these spots shown in Figure 7.12 indicated that the behavior was significantly different for the two layers. For *fPassDop* Gen2 a high concentration up to the R1 area was observed, while for *fPassDop* Gen3, the opposite was found: the nitrogen signal was the largest in the middle. As the scale of the two images was not adapted to each other, the color intensity cannot be compared for the two layers. Oxygen mappings (not shown) showed that for *fPassDop* Gen2, the oxygen concentration was only high in the R1 area. For *fPassDop* Gen3, the surrounding of the laser

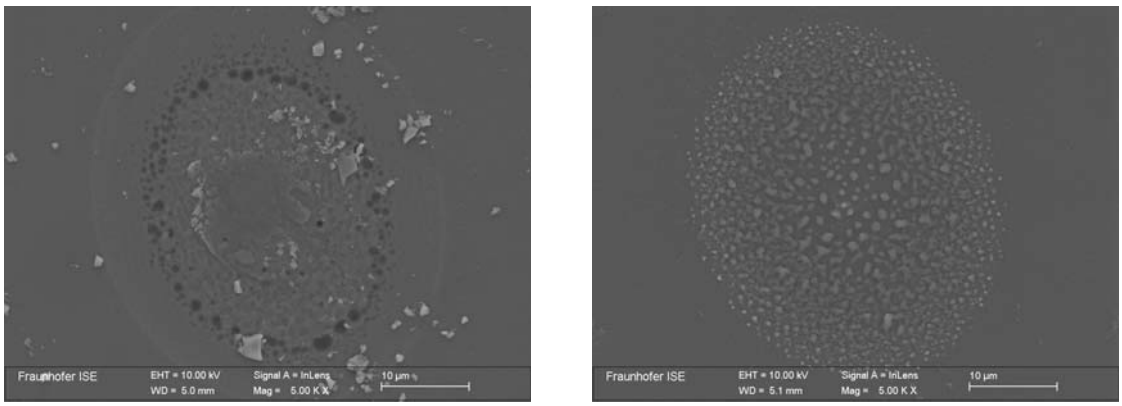

(a) *fPassDop* Gen2 **(b)** *fPassDop* Gen3

Figure 7.11: SEM images taken at 10 kV of single laser spots for the *fPassDop* Gen2 and Gen3 layers. The SEM settings were chosen similar for both layers. The higher energy resulted in a deeper penetration. Therefore the measurement shows features slightly below the intermediate surface.

spot showed a high oxygen concentration and the laser spot itself a lower one.

Discussion

The comparison of 4pp, ECV (integrated electron profile) and SIMS (integrated phosphorus profile) suggested that at least one of the methods yielded wrong results, see Table 7.2. As a first reason for this discrepancy a possible enlargement of the surface due to roughening after the laser process had to be considered. However, an investigation with a laser microscope revealed that the enlargement of the surface was in the range of 1.02 and thus can be neglected. Hence, it became imminent that alternative interpretations of these differences would be required.

Since it was established that 4pp is the best reference for the (overall) doping of the LBSF and since (e.g. for *fPassDop* Gen2) SIMS (77 Ω/sq) and 4pp (79 Ω/sq) match much better than 4pp and ECV (52 Ω/sq) it seemed very likely that the latter yielded erratic results for the doping profile. For *fPassDop* Gen3 and SiN *PassDop* Gen1 the agreement of 4pp and SIMS was not as good, but that can be attributed to inactive phosphorus being present close to the surface. The presence of inactive phosphorus is suggested by a significant »surface dip« that can be found for the ECV measurement within the first 200 nm. For SiN *PassDop* Gen1 (Figure 7.7b, open black squares) and *fPassDop* Gen3 (Figure 7.7a, open black squares), these effects were most pronounced and for these the mismatch between 4pp and SIMS was the strongest. Such a »dip« was not present for SIMS or even a surface peak was observed (as

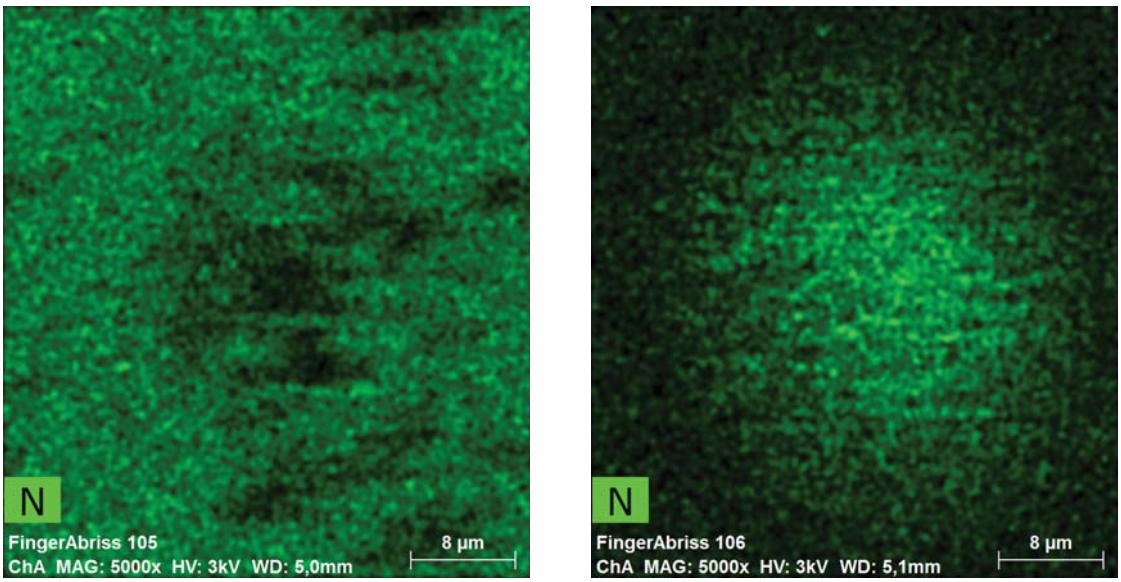

(a) *fPassDop* Gen2 **(b)** *fPassDop* Gen3

Figure 7.12: EDX mappings of single laser spots for the *fPassDop* Gen2 and Gen3 layers. The scale for both layers was not set similar, thus intensity and color cannot be compared to each other. The pictures show a relative change in the concentration of nitrogen for each sample. The laser spots were identical to the ones in Figure 7.10, thus the same annotations apply, especially the ring structures.

for SiN *PassDop* Gen1), thus the disagreement between SIMS and 4pp can be attributed to these effects.

As the (integrated) »electron concentration« determined by ECV was found to disagree with the corresponding 4pp measurement and as this concentration was higher than that for phosphorus as determined by SIMS, it is important to conclude that the amount of phosphorus cannot be the only influence on this concentration determined by the ECV measurement. One observation by SIMS was that the nitrogen concentration in the LBSF was very high, especially for *fPassDop* Gen2 (see Figure 7.7a and 7.7b). The discrepancy (compare 4pp and ECV in Table 7.2) was found to be the strongest for the *fPassDop* Gen2 samples and as shown in Table 7.3, these were the samples with the highest nitrogen dose in the range of 3 to 4×10^{15} cm^{-2}. Thus, a more deep investigation was required to determine if this influence was indeed related to the concentration of nitrogen.

If such a high amount of nitrogen can be found in the LBSF for the SiN_x-based *PassDop* layers, what happens with it? The first observation to note here is that the concentration exceeds the equilibrium solubility of nitrogen (in the range of 5×10^{15} cm^{-3}) in c-Si [200] and the segregation coefficient in the liquid phase ($k \leq 5 \times 10^{-4}$). While Wood *et al.* suggested that the segregation coefficient for rapid laser doping might be significantly higher (e.g. for phos-

phorus: equilibrium $k = 0.35$, non-equilibrium $k \approx 1$), for impurities with a very low equilibrium segregation coefficient like In ($k = 0.0004$) the non-equilibrium segregation coefficient was still given significantly lower than 1 ($k = 0.10$ to 0.20) [164].

The accumulation of nitrogen at the surface was therefore likely a segregation effect and can be explained by the low solubility of nitrogen in crystalline silicon [200]. Such an effect was observed by Hameiri *et al.* as well, for which they gave the same explanation [168]. Due to the low solubility and as indicated in the phase diagram (see [189]), the nitrogen is expected to be included in the LBSF in the form of SiN clusters or precipitates. This was proved for *fPassDop* Gen2 using XRD which—as shown in Figure 7.9—clearly indicated the presence of β-Si_3N_4. While this is the form of Si_3N_4 that is expected to be formed at higher temperatures [189], it does not exclude that crystallites of α-Si_3N_4 or amorphous structures were present as well. However, the fact that crystalline Si_3N_4 was found proves that this is a by-product of the laser process and not (non-ablated) left-overs of the previously amorphous layer. This was confirmed by an XRD control measurement of the areas that were not processed by the laser and for which no corresponding signal was detected. As shown in Figure 7.9 the results suggest that the amount of SiN was reduced with a decreased laser fluence, but this was not necessarily the case as the SiN could have been present in the amorphous state, which would not have been visible in the measurement. Also a change in the crystallite size would influence the XRD signal despite the amount of Si_3N_4 remaining similar. A higher laser fluence resulted in a higher amount of energy induced into the laser spot as well as a longer relaxation time, thus a higher thermal budget. This seemed to be at least partially used to form (more) SiN in the crystalline state or to cluster the crystallites.

As Si_3N_4 is an insulator, two effects can immediately be pointed out: i) The »dip« that was found within the ECV measurement could be explained by phosphorus dopants that were trapped within the Si_3N_4 particles and thus cannot contribute to the electron concentration. ii) Any Si_3N_4 or SiN_x layer that is still (or again) present at the surface can result in electrical shielding of these areas and therefore partly prevent contact formation and thus (in addition to the low phosphorus concentration) be an explanation for the observed contacting issues with the Gen2 layer as well as the high scattering of the *FF* observed in Section 8.1 for the Gen2 process. Such an effect was proposed by Hameiri *et al.* [168].

To analyze the observed difference between the amount of determined free carries by ECV and the actual concentration of phosphorus atoms in the LBSF

by SIMS, the representation of δ as the difference and ξ as the quotient of the two concentrations were chosen as shown in Figure 7.8. As origins for the indicated mismatch, the following were considered:

1. Modified mobility of c-Si due to the impurities (i.e. nitrogen).
2. Validity of the ECV assumptions?
3. Increased conductivity *during the ECV* measurement, e.g. due to traps. Effects in δ could suggest this.
4. Misinterpretation of valid ECV data, i.e. wrong assumptions during the evaluation. Effects in ξ would be a bias toward this.

While it has to be considered that the nitrogen clusters in the LBSF modified the mobility of the charge carriers, the match of SIMS and 4pp was so good that this seemed rather unlikely but cannot be fully excluded. SRP was tried to solve this, but while the surface roughness was not found to be critical for ECV and SIMS, it rendered the SRP measurement unusable due to the large uncertainty in the measurement probe positioning. *Hall* measurements were performed to compare with 4pp and did not indicate a change in the mobility. However, the measurements could not be performed on the same samples (but similarly processed), thus the comparability is questionable. To fully exclude a change in the mobility a dedicated comparison of a larger amount of samples would be required, especially with »stripping« *Hall* profiling, which would allow a direct comparison to SIMS. This was unfortunately not possible within this work.

The second point to be discussed is the validity of ECV, especially the assumption of having a meta-semiconductor interface and if the Mott-Schottky relation holds true. A comparison to a diffused profile at similar doping concentration to *fPassDop* Gen2 showed that all parameters during the measurement were within similar range. Especially the serial and parallel resistances were normal, the dissipation was low. The JV and CV measurement curves were shaped as expected, the $1/C^2$ curves linear around V_{fb}. Thus, from the measurement setup, it was not obvious that the ECV measurement might be invalid and did not seem to be completely “off”. While it still has to be considered that the ECV measurement was not usable, it can certainly be used for comparisons.

The third effect that was considered was an increase in the conductivity, i.e. more free carrier are available than phosphorus atoms. The increase in δ with the nitrogen concentration could lead to the assumption that nitrogen as a donor could be responsible (see Figure 7.8a). In principle, nitrogen could

form a shallow donor and therefore increase the electron concentration, but the dopant activation is expected to be orders of magnitude below the given phosphorus concentration (Kaiser *et al.* give an upper limit of $1 \times 10^{12}\,\mathrm{cm}^{-3}$ [200]). If nitrogen as a donor was not present, then it might be possible that nitrogen introduced defects (e.g. grain boundaries or substitutional defects) that could carry charge. Even if considered so, such an effect should be visible not only in the ECV measurement, but in the 4pp measurement as well. Instead a mechanism responsive only to dynamic current methods like CV was required. One possibility would be traps that in a steady-state measurement like 4pp would be filled and not contribute to the conductivity, while for CV there might be an influence, depending on the frequency of the Alternating Current (AC) source as discussed by Kimerling [201]. This was investigated by stopping the ECV etching process and repeating the measurement using multiple frequencies at this measurement point. While the uncertainty of the capacitance measurement increased due to a higher dissipation, the resulting slopes of the $1/C^2$ curves—and therefore the electron concentration—remained the same within the measurement error and the electron concentration did not decrease significantly. Unfortunately, the ECV profiler is limited to frequencies in the range of 1 to 50 kHz, which might no be broad enough to fully exclude traps but still made them less likely.

The other argument against traps is the shift in the curves shown in Figure 7.8a and 7.8b. If traps were present, a correlation to either of these impurities would be expected, as these were the ones that could induce material defects in the c-Si. For *fPassDop* Gen2, this would mean that based on a phosphorus doping level of around or below $1 \times 10^{18}\,\mathrm{cm}^{-3}$, the traps led to an increase in the conductivity by a factor of 1.5 to 2 and therefore to an active trap density within the same range as the phosphorus concentration. For *fPassDop* Gen3, where the phosphorus concentration exceeded $1 \times 10^{19}\,\mathrm{cm}^{-3}$ δ was still found to be within the same range as the phosphorus concentration, reaching up to $2 \times 10^{19}\,\mathrm{cm}^{-3}$. As can be observed, δ for SiN *PassDop* Gen1 was in between the two. However, if phosphorus solely would have been responsible for the observed increase in the conductivity (e.g. via traps), δ for all of the layers would be expected to match for similar phosphorus concentrations and thus no shift should be observed. Instead all of the investigated layers showed their own level of δ and only the two *fPassDop* Gen2 samples did match (apart from the »Hump«). Similar could be said about the dependence on nitrogen, where again different levels for the layers were observed (see Figure 7.8a). Especially, an inverted effect was observed. For Gen3—as shown in Table 7.3—the phosphorus dose was found to be *higher* by a factor of approx. 10 and the nitrogen dose *lower* by a factor of 10 compared

to Gen2. If the traps were caused by nitrogen, it would therefore require an increase in the activation ratio of the traps by two orders of magnitude and therefore a relation of the traps to nitrogen was very unlikely. Similar (but not as extreme) relations showed for SiN *PassDop* Gen1. Thus, an explanation for an increased conductivity would require a more complex mechanism that is not bound to only the nitrogen or phosphorus concentration, but rather a combination of the two. For example, the properties of phosphorus bound to nitrogen (P-N) in silicon are unknown and have to be considered as a candidate for such behavior. Here, even an influence on the SIMS measurements of phosphorus and nitrogen has to be considered, as P-N might not be detected.

The last explanation would be a misinterpretation of the ECV results in a way that wrong properties were assumed during the evaluation of the data, most of which would be expected to show in ξ. From Figure 7.8d it can be extracted that an influence of phosphorus was rather unlikely, as again different levels of ξ were observed for the layers at similar phosphorus concentrations. However, as shown in Figure 7.8c, a correlation of ξ to nitrogen could be postulated as for a similar nitrogen concentration a similar ξ was observed for all layers with nitrogen concentration in the range of 4×10^{18} to approx. $3 \times 10^{20}\,\mathrm{cm}^{-3}$.

So, if such a correlation was present, what would it affect? The carrier concentration from the ECV data was evaluated with a relation (see [202] as well) derived from Gauss's law:

$$N_{\mathrm{ECV}} = \frac{-2}{q\epsilon_0\epsilon_{\mathrm{r}} A^2 \frac{d}{dV}\left(\frac{1}{C^2}\right)} \tag{7.2}$$

Here, ϵ_0 and ϵ_{r} denote the vacuum and the relative permittivity. A gives the area of the sample that is in contact with the liquid (and therefore in electrical contact). q is the elementary charge.
Investigations using Laser Excitation Microscope (LEXT) did not show a significant increase in the surface area (factor 1.1 at most, but more likely 1.02). In addition, such an influence would not necessarily explain the observed correlation of ξ to the nitrogen concentration. On the other hand if a larger portion of the surface would be covered by SiN_x remnants, this would lead to a decreased surface area (due to inactive areas) and therefore to an underestimation of the electron concentration, thus the opposite of what was observed. A nanostructure in the surface could be an explanation, but it was unclear if such a nanostructure was present and how it would influence the measurement.

The other parameter that could be adjusted would be the relative permittivity ϵ_r as all other parameters are known and/or constant. The effective values for the relative permittivity could be determined as $\epsilon_r = \xi \cdot \epsilon_{r,Si} = \xi \cdot 11.68$. Therefore values in the range of $\epsilon_r = 20$ to $\epsilon_r = 30$ would be required for the ECV and SIMS measurements to match. However, it is unknown why the permittivity of c-Si would increase this much by incorporation of nitrogen or Si_3N_4. The permittivity of the latter would actually be expected in the range of 6 to 7 and therefore lower than that of silicon. For some mixtures (e.g. paraffin wax in titanium-oxide by Ghosh [203]) calculations and measurements were reported and in those cases, the effective permittivity was found to be in between the values of the host and the embedded material. Thus—especially at the present concentrations—the effect of the lower permittivity of Si_3N_4 on the effective permittivity of the LBSF would be expected to be low and of reducing nature (not increasing as observed).
In addition, a relation of the mobility and permittivity would be expected, although this relation is not currently expressed in the commonly used models. While the relation (both form and strength) is not known at this time, such a large change in the permittivity would likely be visible in the mobility due to modified scattering of the charge carriers.
Still, the results show that such effects have to be considered when discussing and comparing ECV and SIMS measurements on impure laser doped materials. To fully understand and explain the origin of these effects dedicated measurements of both ECV and SIMS as well as other comparing methods would be required, more than was possible within this work. Therefore, while the discrepancy could not be fully explained, the results showed that an evaluation of ECV profile data for such laser spots has to be taken and interpreted carefully. Relative comparisons of ECV profiles for different layers should still be possible, but the effect of nitrogen has to be taken into account, i.e. if a different amount of nitrogen has to be expected in the LBSF, an influence on the ECV profile (of increasing nature) is expected. Thus even the use for relative comparisons of *PassDop* SiN_x layers is limited.

For the profiles for Gen2 determined by SIMS (see Figure 7.7) a substantial difference was found in the profile depth of phosphorus and nitrogen. It should be pointed out that this was the case for both *fPassDop* Gen2 samples even though they were measured by two independent institutions. The origin of this difference in depth was not completely clear but thought to be caused by the high nitrogen dose (higher than phosphorus by a factor of approx. 100), especially since the solubility of nitrogen in liquid silicon is relatively low (in the range of $1 \times 10^{19}\,cm^{-3}$ [200]). Such an influence of the dose was observed by Young *et al.* for laser doping of implanted boron [204].

The further evaluation will focus on SIMS. As measurements by Wenclawiak showed, the phosphorus content in the *fPassDop* SiN_x:P layers does not depend significantly on the composition [192]. However, as can be extracted from the phosphorus profiles in Figure 7.7a, the resulting phosphorus doping in the LBSF was found to be much higher for the *fPassDop* Gen3 process. As discussed in Section 6.3.2, the layer stack from *fPassDop* Gen2 to Gen3 was changed to include an a-Si:P *Doping* layer instead of Si-rich SiN_x:P on top of the *Passivation* layer. This raised the question after the effect causing the higher phosphorus doping profile in the LBSF. Was this a result of an increased dopent content or just a change in the doping efficiency during the laser doping process. While it should still be considered, that the a-Si:P *Doping* layer contained more dopants an increase in the dopant concentration by a factor of 10 compared to the previous *Doping* layer was not realistic. Instead additional effects reducing the doping efficiency for *fPassDop* Gen2 have to be considered.

Figure 7.10a and 7.10b show SEM images of single laser spots for *fPassDop* Gen2 and *fPassDop* Gen3, respectively. As can be observed from the images the structures defined by the laser process were significantly different. For *fPassDop* Gen2, the ring structures R1 to R3 suggested that only the R1 was properly ablated. In R2 and R3, the passivation is thought to be damaged, but the layer was at least partially still present, thus possibly hindering contact formation. This was accompanied by a large amount of debris, which indicated some kind of explosion behavior and therefore high pressures and temperatures. For Gen3, no such ring structures were found. The laser spot looked like a clean cut in the passivation with no debris as found for Gen2. Instead, a large amount of small lumps were found that indicated a completely different melting behavior.

To understand this, one has to take into account that both Si_3N_4 as well as SiN_x are rather stable at high temperatures, as the material melts or decomposes above 1900 °C [189]. In the nitrogen-rich *fPassDop* Gen2 concept, this led to a high laser fluence and therefore a high thermal budget being required to increase the temperature of the molten silicon in such a way that at least some parts of the SiN_x:P layers were induced into the melt. Due to the high temperature requirement at this point the pressure from the molten silicon beneath is already high, possibly leading to a burst of the not yet molten parts of the *fPassDop* Gen2 stack and therefore to the debris found in the SEM image (see Figure 7.10a). Thus, the thermal stability of the layers led to a decreased doping efficiency as only parts of the *PassDop* stack could be used for laser doping. And it leads to the conclusion, that the laser fluence has a significant influence on the doping efficiency. This is indicated in the

SEM image (Figure 7.10a), where only in the R1 area »proper« laser doping and ablation is expected. In the R2 area laser doping happened, but due to the reduced laser fluence (due to the Gaussian laser profile) it was incomplete, hence leaving SiN_x remnants at the surface. Such an effect of the dependency of the laser doping process on the laser fluence was also regularly observed for R_{Sheet} samples, e.g. see Figure 6.16b in Section 6.3.2. In the R3 area, the fluence was too low to achieve significant laser doping, but the influence of the laser process still led to a damage of the passivation, which can be observed optically. An indication of the edge of the molten area can be found in Figure 7.11a, where the dark holes indicate voids in the crystalline silicon created by the laser process. Such voids were already observed by Geisler *et al.* and Hameiri *et al.* [168, 169]. According to Geisler *et al.* these voids were caused by nitrogen bubbles forming during the laser process at the edge of the molten silicon.

As described in Section 6.3.2, the main difference between *fPassDop* Gen2 and Gen3 was the change of the *Doping* layer to a-Si:P. This a-Si:P layer is also expected to have a much lower melting point than the SiN_x:P layers and much closer to that of c-Si (around 1400 °C [188]). Hence, the melting of the doping layer can start earlier during the laser process and both support melting the passivation layer as well as improve contribution to the doping process itself. A strong indication toward such an effect are the Si lumps that were observed in the SEM image. These were found to be of low nitrogen content and are thought to be leftovers of the a-Si:P layer, which would mean that the melting of the a-Si:P layer started separately from that of the c-Si bulk, very much in contrast to the behavior of the SiN_x layer. The lumps are thought to be parts of the a-Si:P layer that recrystallized prior to the c-Si, thus cannot contribute anymore to the laser doping process. Hence with an adapted laser process (i.e. lower fluence, longer pulse duration or multiple pulses) the doping efficiency of the layer might be further improved.

As shown in the EDX images (see Figure 7.12), the nitrogen distribution was found to be significantly different for the two layers. This is already noticeable for the passivation layer itself for which the signal for *fPassDop* Gen2 was found to be higher, for *fPassDop* Gen3 lower than within the laser spot. While the scale was different for the images and therefore the signals from the layers cannot be compared, it allows for certain conclusions. First, for *fPassDop* Gen2—as already mentioned above—only the R1 area is thought to be properly ablated, for the rest, at least some parts of the SiN_x layer might still present. In the EDX image (Figure 7.12a), this is visible in a nitrogen concentration that remained high until the R1 area, where a few black spots (meaning low nitrogen concentration) were found).

For *fPassDop* Gen3, the surrounding a-Si:P layer resulted in a low nitrogen concentration indicated by EDX with an increase toward the middle of the laser spot. As expected for a-Si:P, in this area the oxygen concentration was high as well due to native oxidation of the a-Si:P layer, an effect that is not as strong for SiN_x:P. The highest nitrogen concentration was found in the middle as this was the area with the highest laser fluence and therefore the highest thermal budget recrystallizing the latest. Due to the segregation effects of nitrogen in silicon outlined above it was expected that nitrogen enriched in the melt and therefore concentrated in the middle as observed. In fact, a similar behavior would be expected for *fPassDop* Gen2 as well, but the high surface concentration (i.e. due to non-ablated SiN_x) might hide this effect. Due to the significantly higher concentration of nitrogen that was detected by SIMS for *fPassDop* Gen2, it would be expected that even in the R1 area, the nitrogen concentration would be higher than for *fPassDop* Gen3. This leads to an important conclusion, regarding the contact ability of the *fPassDop* Gen2 approach. Not only is the afore-mentioned reduction of the contact area expected to have as significant influence on the contact resistivity, but as the R1 area is expected to retain the highest concentration of nitrogen *within* the LBSF, even for the properly ablated areas a high specific contact resistivity is expected in case of *fPassDop* Gen2. This again emphasizes the importance of reducing the nitrogen concentration in the *PassDop* LBSF.

In contrast to *fPassDop* Gen2, for *fPassDop* Gen3 no voids were found at the edge of the molten area (see Figure 7.11b), instead the spot looks more like a »clean« cut. This and the lower dependency of *fPassDop* Gen3 on the laser fluence (e.g. see Figure 6.20b) was expected to lead to a much more homogeneous laser doping.

One additional feature that was observed within the XRD measurement was the presence of c-Si peaks. This was not expected, as the measurement setup was chosen as such that the bulk signal vanished. Therefore, the presence of c-Si signal indicated that c-Si having a crystal orientation other than that of the bulk (<100>) existed within the measured area. In a »perfect« laser process, this would not happen, as the silicon would recrystallize in the orientation defined by the bulk. Thus the presence of these peaks could indicate that parts of the molten silicon crystallized in a polycrystalline structure, possibly influenced by (e.g. nitrogen-related) defects. These defects could be similar to those observed by Hameiri *et al.* when applying a Yang etch [205] after laser doping from SiN_x stacks [168]. These peaks were reduced as the laser fluence was increased due to the higher relaxation time and therefore possibly reducing the amount of polycrystalline Si in the LBSF, which would be another indication that longer laser pulses might be rewarding. As the ni-

trogen is most likely expected to be incorporated into the silicon as clusters of Si_3N_4, such polycrystalline structures could very well be a result of the incorporation of these clusters, as the lattice constants and atom distances of the two crystals differ. Such a polycrystalline structure is a good candidate when discussing increased recombination often found when analyzing the recombination properties of laser doped spots.

7.1.4 Carbon as an Impurity in the *PassDop* LBSF

Motivation

As shown in the previous section, nitrogen can have a significant influence on the laser doping process. Both on determining the doping profile as well as on the doping efficiency. Similarly, carbon would be expected to have an influence as well. However, in this case it has to be considered that silicon carbide itself is a semiconductor as well and thus the influence might be significantly different.

Therefore, the goal of this section is to determine if an influence of carbon on the characterization methods was present and if it was similar to nitrogen.

Experimental

Results for two variants of SiC *PassDop* Gen2 are presented: The first »Sample 1« is SiC *PassDop* Gen2 as described in Section 6.2.1. The second »Sample 2« is (SiC *PassDop* Gen2+), for which the thickness of the *Capping* layer was increased to 70 nm (standard: 15 nm). This sample featured a MgF_2 *Optical* layer instead of SiC_x.

Both Sample 1 and 2 were processed at a laser fluence of 9 J/cm^2. Sample 1 was used for the »3D« SIMS measurements discussed in Section 7.1.2. This sample featured both single laser spots (used for »3D« SIMS) as well as overlapping structures (used for the other methods). The results for Region 2 of that measurement is repeated here for comparison. To determine the profiles for phosphorus and carbon, SIMS measurements were performed by NREL. To calculate R_{Sheet} from the profiles determined by ECV and SIMS, the mobility model of Klaassen [193, 194] was assumed.

For SiC *PassDop* Gen2, XRD was measured. This area was processed at a laser fluence of 10 J/cm^2.

To further investigate the influence of carbon on the ECV profiling, 4 samples were prepared based on the SiC *PassDop Doping* layer where the gas flow of CH_4 during the deposition was varied from 0 to 60 sccm (standard: 30 sccm). The thickness of the layers was approx. 40 nm. The given carbon concentrations correspond to the values determined by Suwito [143].

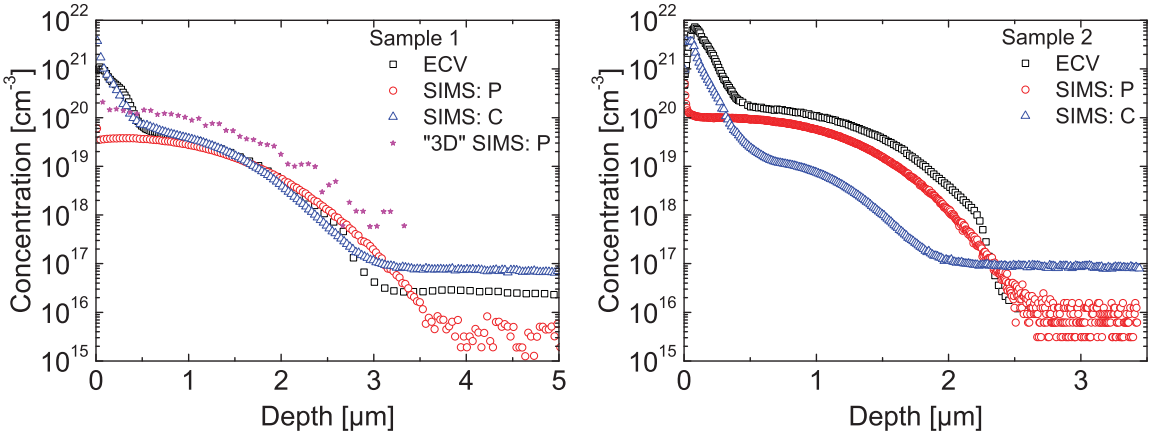

(a) Sample 1 **(b)** Sample 2 with MgF_2

Figure 7.13: ECV and SIMS measurements for two SiC_x *PassDop* samples.

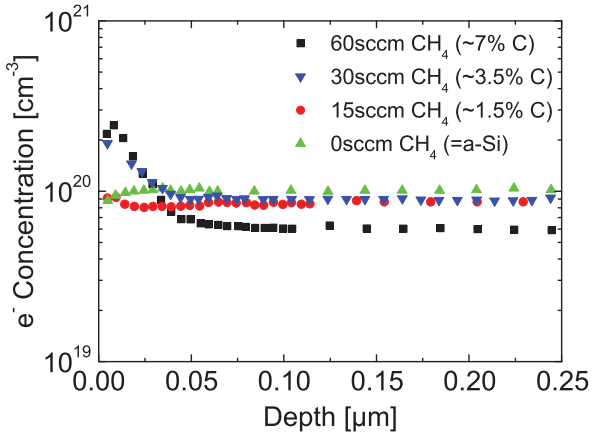

Figure 7.14: ECV measurements for the *Doping* layer with varying carbon content.

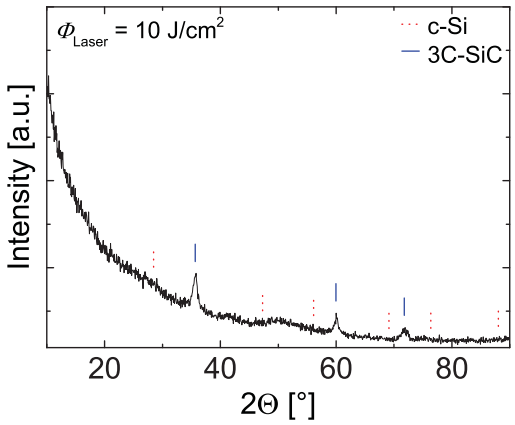

Figure 7.15: XRD measurement for SiC_x *PassDop* Gen2. The red dotted lines indicate peaks expected for c-Si, the blue lines indicate peaks expected for 3C-SiC.

Results

The values determined by integration for electrons (ECV) and phosphorus (SIMS) as well as the values determined by 4pp can be found in Table 7.4. R_{Sheet} values for Sample 2 at around 7 Ω/sq were generally lower. For Sample 1, a R_{Sheet} of 14 Ω/sq was determined by 4pp. In both cases 4pp values were the highest, SIMS close to 4pp and ECV was significantly lower.

Figure 7.13a shows the determined ECV and SIMS profiles for Sample 1 (SiC *PassDop* Gen2). The phosphorus concentration determined by SIMS followed a nearly perfect Gaussian shape, with a surface concentration in the range of 4×10^{19} cm^{-3} and a depth of approx. 3.5 µm. The (electron) concentration determined by ECV showed a similar shape in the range of 600 nm to 3 µm.

Table 7.4: R_{Sheet} determined by 4pp, ECV and SIMS for the SiC *PassDop* samples as well one *pPassDop* sample. All values were determined for a laser fluence of 9 J/cm^2.

PassDop Layer	4pp [Ω/sq]	ECV [Ω/sq]	SIMS [Ω/sq]
Sample 1 (Gen2)	14.0	5.7	12.9
Sample 2 (Gen2+/MgF_2)	7.2	2.5	7.1

Below 600 nm a strong increase of the concentration was found reaching a concentration of 1×10^{21} cm^{-3}. Above 3 µm the decrease in the concentration was faster than determined by SIMS leading to a profile depth in the range of 3 µm. The carbon concentration determined by SIMS showed a very similar shape to the ECV profile with the surface peak starting at a similar depth. The »3D SIMS« profile discussed in Section 7.1.2 indicated a higher concentration compared to the other profiles, the profile shape followed that of the SIMS phosphorus profile.

Figure 7.13b shows the profiles determined for Sample 2 (SiC *PassDop* Gen2+). Most of the general observations outlined for Sample 1 hold for Sample 2 as well. The phosphorus concentration determined by SIMS indicated a higher doping level with a surface concentration of approx. 1×10^{20} cm^{-3} and a depth of 2.5 µm. The concentrations for carbon (SIMS) and electrons (ECV) were significantly different for this sample, but both showed a surface peak starting at a similar depth of approx. 500 nm. Compared to the phosphorus (SIMS) profile, the ECV profile indicated a higher doping level over the whole range, even at higher depth than the surface peak. The maximum concentration indicated by ECV in this case was 7×10^{21} cm^{-3}.

Figure 7.14 shows ECV profiles for a variation of the carbon content of the *Doping* layer. Only the first 250 nm of the profiles are shown, the depth for all profiles was similar, with a slightly higher depth with higher carbon content. For a carbon content of 0 % (a-Si:P), the profile shape close to the surface was flat with a decreasing tendency towards the surface. At 1.5 % concentration of carbon in the layer the profile was still flat, but now with an increasing tendency towards the surface. For a carbon concentration of 3.5 and 7 % a significant increase of the ECV concentration towards the surface was observed with the effect being more pronounced for 7 % carbon.

Figure 7.15 shows the XRD measurement performed for SiC *PassDop* Gen2 processed at a laser fluence of 10 J/cm^2. Three peaks were detected in the

measured range. All of these peaks could be attributed to 3C-SiC. No peaks related to crystalline silicon were detected.

Discussion

As was the case for nitrogen, significant differences between the R_{Sheet} determined by 4pp and that determined by integration of the ECV profile were observed as shown in Table 7.4. ECV yielded a significantly lower R_{Sheet} than 4pp. However, the comparison of the profiles shown in Figure 7.13 suggested, the effect was very different to that of nitrogen. While ECV indicated a significantly higher concentration than the phosphorus profile determined by SIMS, the more pronounced effect was the presence of a surface peak (below a depth of 500 to 600 nm) in the ECV concentration, which was not present in the phosphorus profile determined by SIMS. As a similar surface peak was determined by SIMS for carbon (thus for a different element), this suggested, that the surface peak was caused by carbon.

To further investigate this an experiment was performed utilizing only the *Doping* layer, for which the (well known) carbon content was varied. As shown in Figure 7.14, a direct correlation between the formation of the surface peak and the increase in the carbon content could be found, since at 3.5 % the surface peak formed and was more pronounced at 7 % carbon. Thus, it can be concluded, that the surface peak was indeed caused by carbon and—similar to nitrogen again—questionable results were determined by ECV. This was supported by the fact that again the agreement between 4pp and (integrated) SIMS was good.

For the complete SiC *PassDop* Gen2 stack, the carbon content was significantly higher, especially due to the high content in the *Capping* layer (approx. 50 %) and *Optical* layer (approx. 63 %). While the profiles suggest something different, the carbon dose for Sample 1 and 2 was actually within similar range (3 to $4 \times 10^{16}\,\mathrm{cm}^{-2}$). However, as the optical properties of the two stacks were slightly different due to the adapted *Capping* and *Optical* layer, the effective laser fluence changed and the profiles cannot be compared directly.

The *carbon* concentration at which the surface peak started to appear was at approx. 6×10^{19} and $3 \times 10^{19}\,\mathrm{cm}^{-3}$ for Sample 1 and 2, respectively. Thus it might be possible that an accumulation effect of carbon in silicon was the trigger at this concentration or higher. Such a concentration would already exceed the equilibrium solubility of carbon in c-Si ($3 \times 10^{17}\,\mathrm{cm}^{-3}$ close to

the melting point of silicon [206]). Newmann [206] pointed out that oxygen can result in a higher amount of carbon incorporated into the silicon, by building a carbon-oxygen complex. He noted that with an oxygen concentration of about $1 \times 10^{18}\,\mathrm{cm}^{-3}$ it was »easy« to introduce substitutional carbon up to $2 \times 10^{18}\,\mathrm{cm}^{-3}$ into the crystal. As the oxygen concentration in case of the *PassDop* LBSF was likely within the same range (see 7.1.5), such an effect might be possible. Together with the increase in the segregation coefficient as proposed by Wood for dopants for non-equilibrium rapid laser processes [164], this could explain the high concentrations of carbon that were observed.

The high concentration of carbon alone however does not explain the effects that were observed and why the ECV measurement yielded incorrect results for the electron concentration. The XRD measurements depicted in Figure 7.15 showed that crystalline SiC was found within the LBSF area. As the *PassDop* layer was amorphous this cannot be the result of improperly ablated passivation layer parts, but instead the c-SiC was a product of the laser process. Thus the energy induced by the laser processed seemed to have been partially used to form 3C-SiC. Given the high concentrations of carbon, this was expected. Si and C are known to build no mix phases other than SiC at a concentration of 50 %, so similar to Si_3N_4, it would be expected that exceeding the solubility would result in the formation of SiC crystallites embedded into the c-Si matrix. While other polytypes of SiC do exist, it might be possible that in c-Si, the 3C variant might be preferred due to the same cubic crystal system. However, as the crystal geometrics do not match completely, crystal defects might be the result, which could be the origin of increased recombination (in comparison to the respective Auger limit) as discussed in Section 7.2.

Regarding the ECV measurements this does not yet explain the observed behavior. Similar to SiN_x, a frequency dependence on the CV measurement was investigated within the frequency range allowed by the ECV profile, but similar to SiN_x, no significant influence was found other than the capacitance measurement error increasing. Therefore traps as the origin were again rather unlikely. The observed SiC crystals however are a very good candidate due to the good correlation to the carbon concentration, as SiC itself is a semiconductor and thus an influence on the CV measurement would be expected. To predict this influence too many variables are unknown, e.g. the size of the crystallites.

Aside of the measurement via ECV, carbon can be thought to be much less critical as an impurity in the *PassDop* LBSF as the doping efficiency remains

high even if a large amount of carbon was incorporated as shown in Figure 7.13b. For an estimation of the doping profile, ECV can be used if the surface peak is removed by extrapolation, i.e. by assuming a Gaussian profile.

7.1.5 Other Impurities

Motivation

As it was shown that nitrogen and carbon are induced into the LBSF during the laser process if the respective layers contain them, other impurities have to be considered to affect the LBSF formation as well, if provided within the layer stack at the time of the laser process. Here, especially magnesium and fluorine are of interest, as MgF_2 was extensively used as an optical layer to enhance light trapping within the solar cells. However, not only the elements within the *PassDop* layer have to be considered, but also impurities like oxygen and nitrogen as the laser process was performed under air ambient or carbon due to organic contamination during wafer handling.

Therefore in this section, the concentration of carbon, fluorine, magnesium, nitrogen and oxygen after the laser doping process is investigated. However, the investigations presented here were not within the explicit focus of this work, thus only brief results and discussion are presented.

Experimental

All of the investigations outlined here were done on R_{Sheet} type samples with the point and line distances set to 25 µm. The measurements were done using SIMS. Five different samples were investigated:

1. SiC *PassDop* Gen2 (SiC1): C and N
2. SiC *PassDop* Gen2+ (SiC2): C, F, Mg, N and O
3. *fPassDop* Gen2 (SiN1): C, F, Mg, N and O
4. *fPassDop* Gen3 (SiN2): C and N
5. SiN *PassDop* Gen1 *PassDop* (SiN3): C and N

The carbon results for the SiC-samples as well as the nitrogen results for the SiN-samples were already presented in the previous sections and are only shown for comparability. In addition, for the samples SiC2 and SiN1, SIMS measurements of fluorine and magnesium were performed. For two samples, the oxygen concentration was tracked as well.

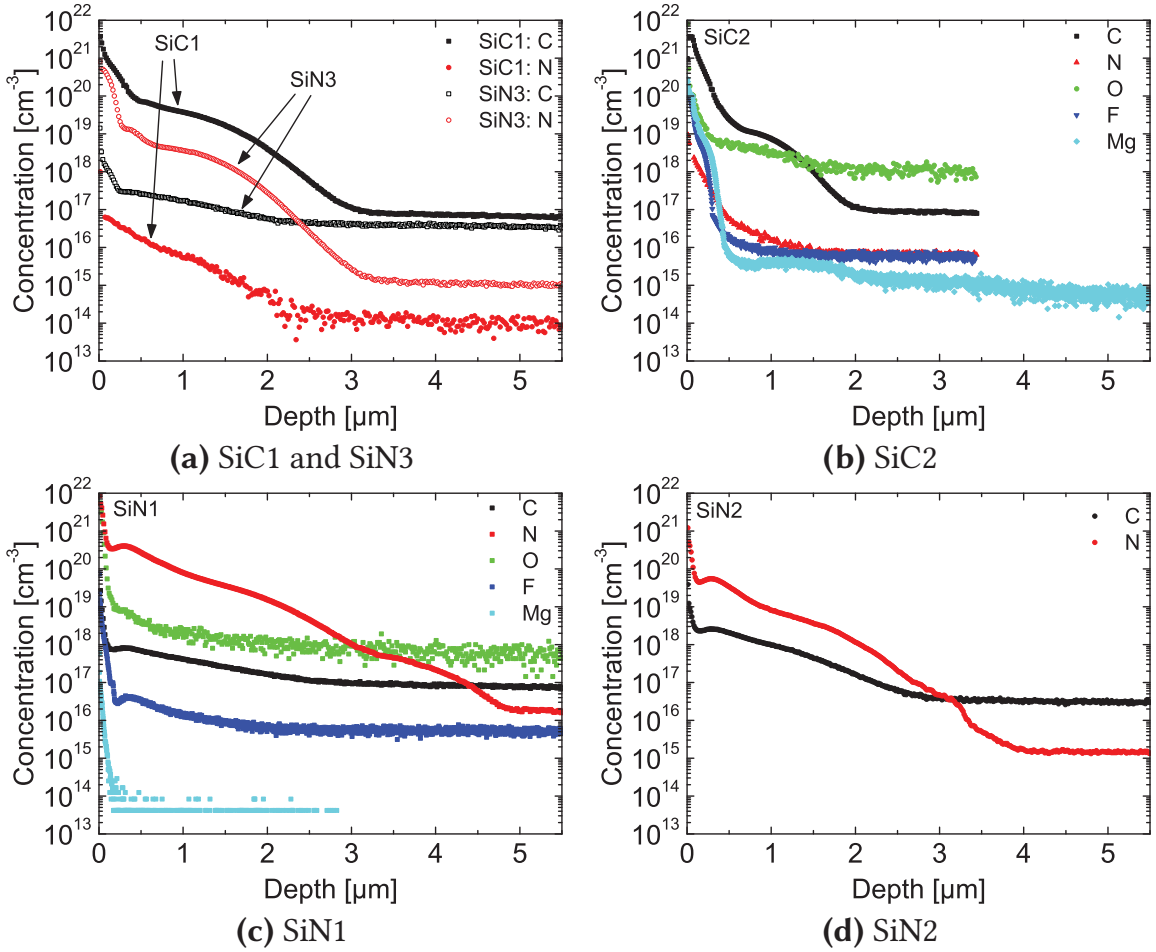

Figure 7.16: SIMS results for two SiC_x and three SiN_x *PassDop* samples. For all samples C and N were detected. For the SiC2 and SiN1 samples, O, F and Mg were detected as well. Only the SiC2 sample had a MgF_2 layer.

Results

Figure 7.16a to 7.16d show the results of the SIMS measurements for the respective samples. Note that the same scale was applied to all graphs for comparability.

The measurements of carbon showed that carbon can be found in all of the samples, even if the layers themseleves did not be contain carbon. The limit that was detected was in the range of 7 to $8 \times 10^{16}\,\mathrm{cm}^{-3}$ for three of the samples, while for two of the samples it was found in the range of 3 to $4 \times 10^{16}\,\mathrm{cm}^{-3}$. The two SiC samples showed a pronounced carbon peak with a surface concentration of more than $1 \times 10^{20}\,\mathrm{cm}^{-3}$. The three SiN samples showed a significant increase in the carbon concentration towards the surface from the background concentration up to a peak concentration of $1 \times 10^{18}\,\mathrm{cm}^{-3}$, 2 to $3\,\mathrm{cm}^{-3}$ and $3 \times 10^{17}\,\mathrm{cm}^{-3}$ for SiN1, 2 and 3, respectively. At the surface a steep increase towards even higher concentrations was found.

For nitrogen, the picture looked different. A strongly varying background signal was observed. The background level for the respective samples was in between $1 \times 10^{14}\,\mathrm{cm}^{-3}$ and $2 \times 10^{16}\,\mathrm{cm}^{-3}$. Nitrogen as a background element was found to be detectable up to 2 µm depth. The SiN samples showed a high concentration of nitrogen. The SiC samples showed an increase of the concentration from background level of $1 \times 10^{16}\,\mathrm{cm}^{-3}$ up to $7 \times 10^{16}\,\mathrm{cm}^{-3}$ (SiC1) and $2 \times 10^{18}\,\mathrm{cm}^{-3}$ (SiC2) close to the surface.

For both the SiC2 and the SiN1 sample, oxygen was detected. The determined oxygen concentration was almost identical for the two samples. From the background level of approx. $1 \times 10^{18}\,\mathrm{cm}^{-3}$ an increase in the concentration towards the surface up to just below $1 \times 10^{19}\,\mathrm{cm}^{-3}$ was found with a steep increase in the concentration directly at the surface.

Fluorine was measured on the SiC2 and the SiN1 sample, only the SiC2 sample had the additional MgF_2 source. The measured concentrations for the two samples were significantly different. At around $5 \times 10^{15}\,\mathrm{cm}^{-3}$, the background level was similar for the two samples. The SiC2 sample (with MgF_2) showed an increase from the background level starting at a depth of around 1.5 µm towards the surface. At a depth of approx. 500 nm, the increase was stronger with a peak in the concentration of over $1 \times 10^{20}\,\mathrm{cm}^{-3}$. The SiN1 sample (no MgF_2) showed an increase starting at around 1.5 µm in the fluorine concentration as well. At 400 µm a plateau in the concentration was observed with a strong increase up to $1 \times 10^{19}\,\mathrm{cm}^{-3}$ close to the surface.

Magnesium was measured on the SiC2 and SiN1 as well. For the SiC2 sample (with MgF_2), the constant concentration at around $1 \times 10^{14}\,\mathrm{cm}^{-3}$ was detected at depths higher than 2 µm. At a depth of around 2 µm, an increase in the concentration was found resulting in a plateau at a concentration of 3 to $4\,\mathrm{cm}^{-3}$. At around 600 nm a strong increase in the concentration towards the surface was observed with a peak concentration of over $1 \times 10^{20}\,\mathrm{cm}^{-3}$. For the SiN1 sample, no magnesium was expected. The background level was very low at below $1 \times 10^{14}\,\mathrm{cm}^{-3}$. Only close to the surface a steep increase in the concentration was determined. The peak concentration was approx. $1 \times 10^{17}\,\mathrm{cm}^{-3}$.

Discussion

The most important aspect to note regarding these measurements is that all of them were taken with one dominating impurity, carbon for the SiC samples and nitrogen for the SiN samples. This aspect is import as one has to consider an influence of this dominant impurity, both on the laser process

and therefore the diffusion of the investigated impurities as well as the measurement itself, as the calibration standards were done for crystalline silicon. In addition, it has to be noted that the background level for the measurements depends on the amount of time that was invested to evacuate the SIMS measurement chamber, thus the observed differences in the background signal for carbon [207].

As an example for such an influence on the calibration the sample SiN1 (see Figure 7.16c) is of interest, for which the shape of the nitrogen concentration was found again in the fluorine concentration and an influence on the other investigated impurities seemed to be present as well. As noted above the sample was not coated with a MgF_2 layer and since magnesium and fluorine are not expected to be common impurities during the laser process no deviation from the background signal would be expected. A cross-contamination with a MgF_2-coated sample can be excluded as well as the SiC2 and other such samples were not processed at the *PassDop* laser at the same time. This means that for the SiN1 sample, within the first approx. 200 nm, the SIMS calibration was not correct. Therefore, the concentrations that were determined for all of the elements in this range cannot be trusted and should be disregarded. While it is not clear what concentration of nitrogen is tolerable, concentrations above $1 \times 10^{20}\,\mathrm{cm}^{-3}$ have to be seen critical, especially as an influence on the measurement of nitrogen itself has to be considered as well.

Similarly, carbon seemed to have an influence on the measurement as well. Especially for fluorine, carbon and magnesium, correlations of the profiles with carbon were found. However, as in this case a MgF_2 layer was actually present at the surface, it has to be considered that at least to some degree the measurements correspond to actual concentrations in the LBSF, especially as MgF_2 at 1251 to 1263 °C [208] is expected to have a melting point below that of crystalline silicon. For fluorine, Jeng et al. [209] noted that it tends to diffuse to the surface. At the surface it can build $SiOF_2$ which then exaporates from the surface. However, Robinson [210] found that while pure fluorine in silicon shows that exact behavior, boron as an additional element can modify the diffusion mechanisms when both are implanted subsequently or simultaneously. As the carbon-fluorine bond is expected to be rather strong, such an effect has to be considered for carbon as well and hinder the out-diffusion of fluorine. However, from the results due to the high carbon concentration, it cannot be said definitely that fluorine was still present in the sample. Since the concentration of fluorine in the SiC2 sample (with the MgF_2 layer) was found to be well above that of the SiN1 sample (without the MgF_2 layer), it

has to be considered, but if so, it was bound closely to the surface, within the first 500 nm.

Similar to fluorine, magnesium was found to tend to diffuse to the surface by Francois-Saint-Cyr et al. [211]. Even after deep implantation of magnesium (up to 0.8 µm shown) a high temperature treatment 900 °C or above resulted in migration of the element to the surface, with some Mg remaining in the bulk. For our samples the differences in the concentration of the two samples indicated that magnesium was present at some level even in the deeper parts of the LBSF. A slight deviation from the background signal in the range of 1 to 2 µm indicated this effect although the absolute concentration would be an order of magnitude below the one observed by Francois-Saint-Cyr et al. In addition, it is not clear if the signal they showed corresponded to the background or was meant as actual concentration of magnesium. However, the strongest signal for magnesium was detected at the very surface. While this might have been influenced by the carbon concentration (a correlation to the strong increase in that concentration below 500 nm seems to be present), such an increase would be in good agreement with the observations by Francois-Saint-Cyr et al.

Assuming that magnesium was present in the LBSF, what would it affect? Additional recombination in the LBSF due to the magnesium was briefly investigated on samples similar to the ones discussed in Section 7.2, but no effect was found ($J_{0b,met}$ identical to the values note in that section before and after annealing). Chen et al. [212] noted that magnesium occupies an interstitial lattice site and has two donor energy levels. This was confirmed by Arutyunyan et al. who determined an *n*-type doping for magnesium [213] for laser-annealed implanted magnesium for concentrations in the range of $5 \times 10^{14}\,\mathrm{cm}^{-3}$ to $1 \times 10^{16}\,\mathrm{cm}^{-3}$. However, as the doping in the LBSF by phosphorus is significantly higher, no impact by this would be expected. Thus, the MgF_2 layer is not expected to have a significant impact on the performance of the *PassDop* LBSF, neither regarding the doping nor regarding recombination. While an influence cannot be completely ruled out, at the current level of recombination other effects were found to be dominant.

This leaves the »contamination« impurities carbon, nitrogen and oxygen. While oxygen and nitrogen are provided as ambient gases during the process, the amount of carbon would be expected to be dependent on the handling and storage for the SiN layers, explaining the differences in the concentrations determined for the three samples. While an influence of nitrogen on the SIMS measurement has to be considered, it can be ruled out as the origin for the differences, as the sample with the lowest amount of nitrogen showed

the highest concentration of carbon, while the lowest influence would be expected. Only within the first 300 nm, a decrease in the concentration can be attributed to nitrogen. As the concentration of carbon is well above the solubility, it is unclear what effect would be expected from this. More SIMS measurements with dedicated »clean« samples would be required. As noted in Section 7.1.4, carbon would be expected to form SiC crystals, which could lead to changes in recombination (increase/decrease?) or material properties. In addition, it has to be considered that organic impurities at the surface during the laser process can transport other severe impurities into the c-Si.

For nitrogen, the picture was different. Again, it was the sample with a lower amount of carbon that was found to exhibit the higher amount of nitrogen. However, this was the sample with a lower effective melting depth (see the carbon profiles), which means that the effective laser fluence changed, possibly influenced by the replacement of the optical layer (MgF_2 instead of SiC). Due to the low solubility in the solid phase, a strong increase in nitrogen towards the surface is the result similar as observed for the SiN layers, just at a lower level. However, at this level, the nitrogen is not expected to have a significant impact on the performance of the LBSF.

The last element that was investigated was oxygen. While the background level was high, an increase close to the surface indicated that oxygen was incorporated into the LBSF. The concentration was at a similar level for both SiN1 and SiC2 and thus an influence of the major impuritiy—nitrogen and carbon, respectively—is unlikely. In addition, very similar concentrations were observed for *pPassDop* samples. Therefore, the observed concentration should correspond to the actual oxygen concentration. The effects that could be thought of would be i) formation of SiO_2 close to the surface ii) oxygen-related defects reducing recombination and iii) thermal donors due to oxygen. While i) would be expected in any case if a c-Si surface is exhibited to air ambient, the oxide could increase in thickness due to the additional oxygen provided resulting in a formation of a dielectric layer hindering contact formation if metal is applied and thus reducing the contact resistivity. The formation of such an oxide was suggested by the EDX measurements that were shown in Section 7.1.3, where oxygen formation happened mostly if the nitrogen concentration was relatively low. An influence of the contact resistivity and therefore on the fill factor was mostly found to rather correlate with the nitrogen content of the layer, whereas *PassDop* LBSF with low nitrogen concentration were not found to exhibit fill factor issues. Therefore this effect is thought to be minimal. ii) was briefly investigated on a *pPassDop* sample, for which the lifetime was measured after several annealing steps. First, the samples were annealed at 400 °C, which could lead to degradation

due to the boron-oxygen defect. Afterwards, the samples were annealed at 200 °C, which should reverse this mechanism. No difference in the lifetimes after these annealing steps were found. Therefore, boron-oxygen defects are not thought to significantly influence recombination. For *nPassDop*, oxygen is not thought to strongly add to recombination, therefore the observed concentration is thought to be uncritical. iii) was not investigated, but might be a an interesting topic.

7.2 Recombination

In a Passivated Emitter and Rear Locally Diffused (PERL) solar cell, the recombination at the passivated surface and at the contacts is very different, as at the contact the passivation has to be locally removed. While it is easy to determine the S_{pass} of the passivated surface, determining S_{met} at the contacts and therefore $J_{0b,met}$ is more difficult. Here two methods based on the work by Fischer ([56] and Section 2.2.5, referred to as »Fischer-Model«) and Saint-Cast ([58] and Section 2.2.6, referred to as »p_{LPA}-Model«) are presented and their implications, advantages and disadvantages are discussed.

Experimental

The LBSF recombination was investigated for three layers: SiC *PassDop* Gen2 (see Section 6.2.1), SiN *PassDop* Gen1 (single layer SiN_x:P) and SiN *PassDop* Gen2 (SiN_x:P/a-Si:P double layer, both see Section 6.2.2).

The layers were deposited onto both sides of 1 Ωcm FZ shiny-etched *n*-type wafers. After the passivation the samples were processed single-sided with the *PassDop* laser at a laser fluence of 9 J/cm^2. L_p was varied from 140 µm up to 600 µm such that the $1/{L_p}^2$ values were roughly equidistant. Subsequently, the samples received a Forming Gas Anneal (FGA) anneal at 425 °C for 25 min in case of SiN *PassDop* and at 400 °C for 5 min for SiC *PassDop*. After each step, QSSPC measurements were performed in the transient mode to determine the passivation performance. The lifetime and thus all following parameters were determined in low-injection at $\Delta n = 5 \times 10^{14}$ cm^{-3}.

From the lifetime data p_{eff} was extracted as described in Section 2.2.6. The point diameter was determined using LEXT but only used as a reference as the »real« recombination diameter cannot be determined optically. Thus for the calculations, a point diameter of 50 µm was assumed, which is well within 10 % of the optically determined diameter (48 to 52 µm). Using the point diameter, p_{LPA} was determined after checking that it was evaluable (see Section 2.2.6 and especially Figure 2.3). From p_{LPA}, both S_{met} and $J_{0b,met}$ were calculated as values comparable to those extracted using the Fischer-Model.

For the point diameter, an uncertainty of 10 % was found to describe both measurement errors as well as variations in the laser process well. For r_{diff}, an uncertainty of 1 % was assumed for the calculation of p_{LPA}. The uncertainty of p_{eff} was determined from the linear regression. The propagation of

uncertainties was taken into account by calculating the partial derivatives of the respective relations under the assumption that the variables do not correlate (which should hold) and applying the variance formula as shown in Section 2.2.6. To evaluate the Fischer-Model, S_{met} was fitted to S_{eff} versus L_{p} according to equation (2.38) for each L_{p}. Calculating the uncertainty for the Fischer-Model is not as easy, as the Formula is rather complex and simplifications are not straight forward. To estimate the uncertainty, S_{met} was calculated for both the minimum (45 µm) and maximum (55 µm) value of d_{cont}. Thus, minimum, maximum and mean value of S_{met} is given which indicates the range in which S_{met} would be expected. Note that in this case the min/max subscript refers to the min/max value of d_{cont} and not S_{met}, thus $S_{\mathrm{met,max}}$ will yield the lowest result.

To further evaluate the annealing, samples were fabricated with the SiN *PassDop* Gen1 process to which the laser process was applied with a point distance of 140 µm on each side, leading to a contact fraction of approx. 10 %. Thus the recombination in the LBSF should be the strongly limiting factor in the determined lifetime and S_{eff}. The lifetime was determined by QSSPC before and after the annealing in the generalized evaluation mode.
In addition, for a selected sample, Microscopic Photoluminescence (Micro-PL) was measured before and after annealing on a single laser spot. It was ensured that the same spot was measured in both states. This allowed for analyzing the areas that improved due to the annealing process.

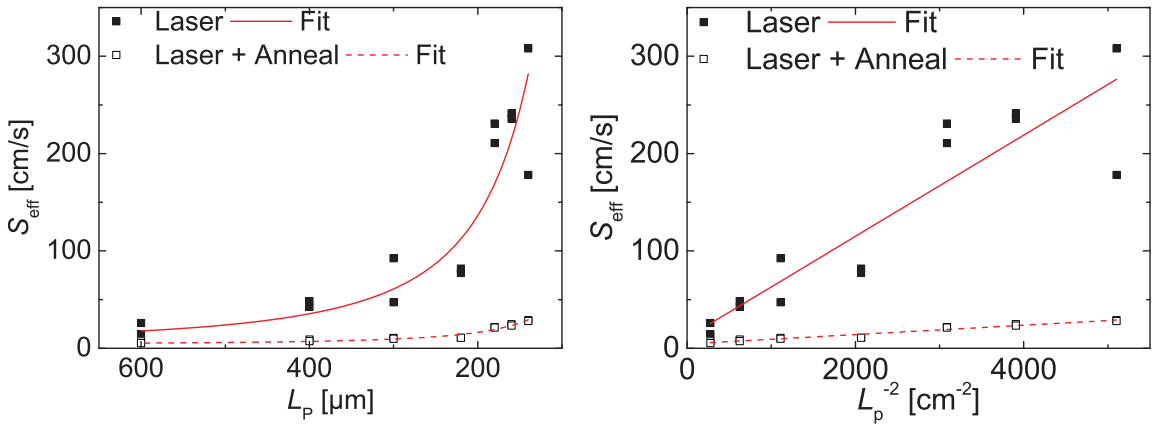

(a) Fischer-Model **(b)** p_{LPA}-Model

Figure 7.17: The Fischer- and p_{LPA}-Model applied to the SiN_x-*PassDop* Gen1 sample. The solid symbols and lines correspond to values determined directly after the laser process, the open symbols and dashed lines correspond to values after annealing.

Table 7.5: Results for S_{met} when fitting the Fischer-Model to the measured data. The $S_{met,min}$ values were determined at $d_{cont} = 45\,\mu m$, S_{met} at 50 µm and $S_{met,max}$ at 55 µm.

Sample	After Laser			After Laser + Annealing		
	$S_{met,min}$ [cm/s]	S_{met} [cm/s]	$S_{met,max}$ [cm/s]	$S_{met,min}$ [cm/s]	S_{met} [cm/s]	$S_{met,max}$ [cm/s]
SiC *PassDop*	680 ± 30	540 ± 30	513 ± 13	590 ± 20	474 ± 18	387 ± 15
SiN *PassDop* Gen1	5700 ± 700	4200 ± 500	3300 ± 300	319 ± 12	256 ± 10	210 ± 08
SiN *PassDop* Gen2	6200 ± 500	4500 ± 300	3500 ± 200	310 ± 30	248 ± 20	203 ± 18

Table 7.6: Results for S_{met} when using the p_{LPA}-Model to the measured data. p_{LPA} and S_{met} were calculated by assuming $d_{cont} = 50\,\mu m$

Sample	After Laser			After Laser + Annealing		
	p_{eff} [10^{-4}cm^3/s]	p_{LPA} [10^{-4}cm^3/s]	S_{met} [cm/s]	p_{eff} [10^{-4}cm^3/s]	p_{LPA} [10^{-4}cm^3/s]	S_{met} [cm/s]
SiC *PassDop*	113 ± 5	122 ± 6	624 ± 128	85 ± 5	90 ± 5	459 ± 96
SiN *PassDop* Gen1	520 ± 70	820 ± 180	4200 ± 1200	48 ± 3	50 ± 3	250 ± 50
SiN *PassDop* Gen2	570 ± 50	970 ± 150	5000 ± 1200	48 ± 7	50 ± 8	260 ± 70

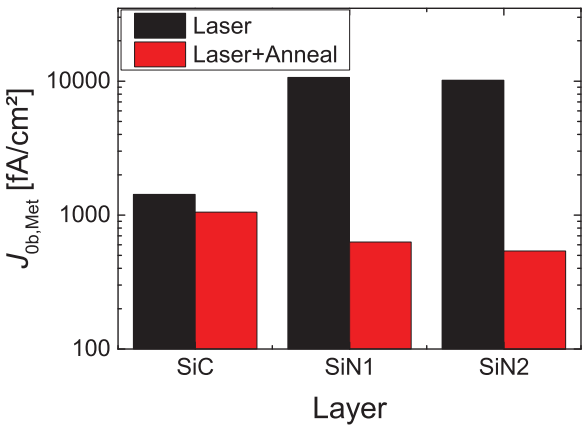

Figure 7.18: $J_{0b,met}$ before and after the annealing step. The values were calculated from p_{eff} under the assumption of having a contact diameter of $d_{cont} = 50\,\mu m$.

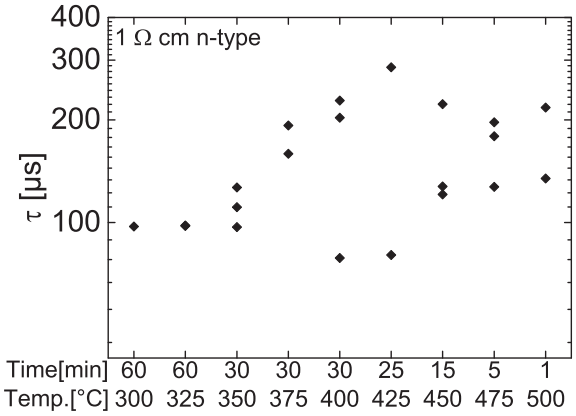

Figure 7.19: Lifetime after annealing for a selection of annealing steps. The lifetime before the annealing step was determined at approx. 30 µs.

Results

Figure 7.17a and 7.17b show exemplary the fit of the corresponding models to the measurement data for the SiN *PassDop* Gen1 samples. In each graph, the solid and open symbols represent the values determined directly after the laser process and after annealing, respectively. The red solid and dashed lines correspond to the model fits to the respective data sets. Scattering was found to be high, but the trend did roughly correspond to that predicted by the models. Table 7.5 and 7.6 show the results for p_{eff}, p_{LPA} and S_{met} for the Fischer- and p_{LPA}-Method, respectively. Directly after the laser process, the values determined for the SiN *PassDop* layers were significantly higher, by a factor of 5 to 8, depending on the parameter that is compared. After annealing, these showed a strong benefit resulting in significantly lower p_{eff}, p_{LPA} and S_{met}. In case of SiC *PassDop*, a low S_{met} in the range of around 600 cm/s could be determined directly after the laser process, but the benefit of the anneal was lower. Thus, after the annealing, the recombination was found to be lower for SiN *PassDop* than for SiC *PassDop*. The S_{met} values determined from the Fischer-Model and from the p_{LPA}-Model at $d_{cont} = 50\,\mu m$ were similar and usually within the uncertainty to each other.

Figure 7.18 shows the $J_{0b,met}$ that was calculated from p_{eff} under the assumption of having contacts with a diameter of $d_{cont} = 50\,\mu m$. The graph illustrates the strong improvement in recombination observed for the SiN *PassDop* layers after annealing. Prior to the annealing step, the $J_{0b,met}$ values were in the range of 10 000 fA/cm^2, after the annealing they decreased to values slightly above 500 fA/cm^2. For SiC *PassDop*, the effect was slightly

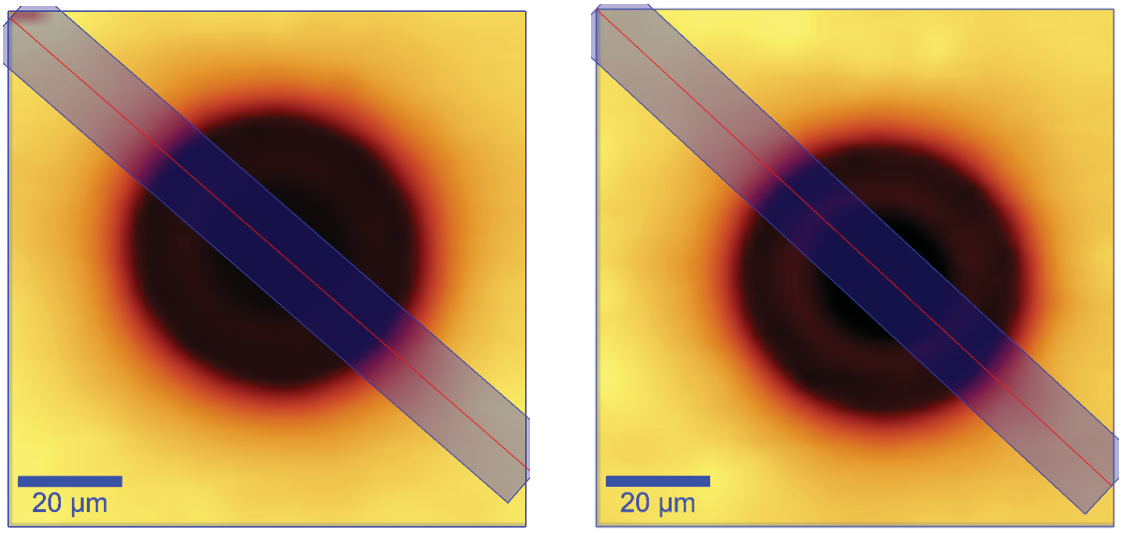

(a) Before Annealing **(b)** After Annealing

Figure 7.20: Photoluminescence (PL) signal of a single laser spot measured by Micro-PL before and after the annealing step. The spot was chosen such that after the annealing step it could be ensured that the same spot was selected again. The red lines and blue shaded areas indicate the orientation and position of the shown line scans.

lower. Starting with $J_{0b,met}$ around 1400 fA/cm^2 the gain was small with a resulting $J_{0b,met}$ after anneal of approx. 1000 fA/cm^2.

Figure 7.19 shows the lifetime after the annealing process for a selection of temperatures and durations. The lifetime level for all of the samples before the annealing step was in the range of 25 to 35 µs with only one sample being measured at slightly higher 44 µs. After the annealing step, a trend toward higher lifetimes was observed, possibly with a peak at a temperature around 425 °C.

Figure 7.20 shows the PL signal determined by Micro-PL for a single laser spot before and after the annealing. It was ensured that the same spot was reused, for improved comparability. The dark part in the middle roughly corresponded to the area up to the outer ring of the *PassDop* laser spot ($d_{cont} \approx$ 50 µm) shown in Figure 7.21a. Both before and after the anneal, there was a strong contrast between the laser-damaged part of the spot and the outer area where the passivation would be expected to be intact. Figure 7.21b shows the line scans of the luminescence signal before and after annealing. The position and orientation of the line scan is indicated by the redlines and blue shaded area in Figure 7.20. The translation was corrected (−7.5 µm). The line scan confirmed that the PL signal within the dark area increased after the anneal. The elevation factor was in the range of 2.5 to 4. The flanks showed a slight

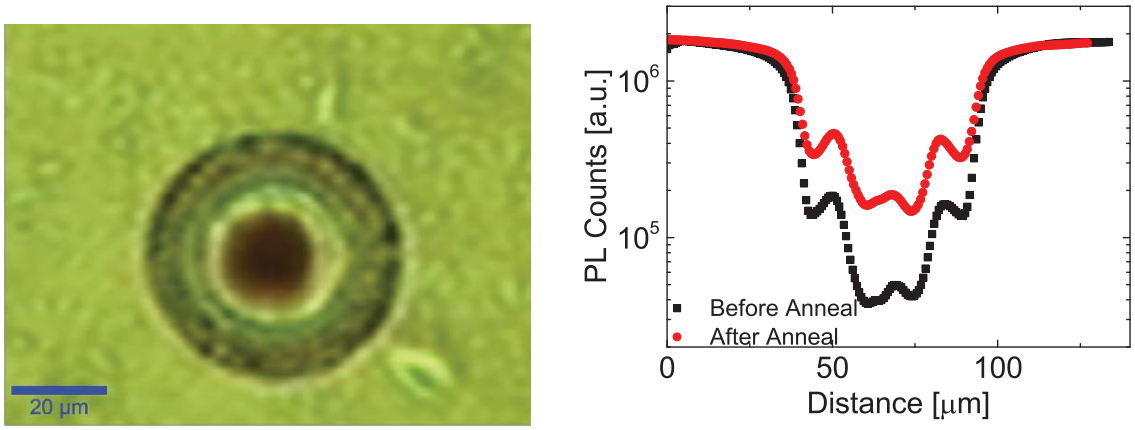

(a) Microscope image of the laser spot. **(b)** Line scans of the Micro-PL signal.

Figure 7.21: Microscope image and PL line scans for the investigated laser spot. For the line scans, the translation was corrected for better matching curves.

improvement as well with the surrounding of the spot having pretty much the same PL as before.

Discussion

Before further evaluating the p_{eff} data, it is necessary to check if the recombination was limited by the diffusion resistance as noted in Section 2.2.6, which was not the case. This evaluation is shown in Figure 2.3. In essence for the highest p_{eff} of 570×10^{-4} cm^3/s, the minimum d_{cont} the point may have would be in the range of 20 µm. Experimentally a d_{cont} of around 50 µm was observed, a factor of 2.5 higher than required. Thus $p_{\mathrm{LPA}} \to \infty$ does not have to be assumed and further evaluation can be performed.

The first conclusion to be drawn from the results is that both models can be used to describe the recombination of point contacts and, if given the comparable input, lead to similar results. However, the p_{LPA}-Model has one advantage here: Some parts of the evaluation are possible even without specifying critical parameters like d_{cont}. As the min/max calculations for the Fischer-Model show, this is a parameter that has a very strong influence on the result and unfortunately, this is the one parameter with the highest uncertainty. As a first reason for an uncertainty, a variation in the laser focus and fluence has to be considered that could lead to small variations in the point size. Local inhomogeneities in the layer can add their portion to these variations. The second reason is that despite the microscopic pictures, one cannot always be certain about what diameter to define as the contact opening. For the recombination properties the area where the passivation was removed or damaged is certainly the most relevant, but this does not always have to correlate the same way with the observed contact opening by microscopy.

With the p_{LPA} Model, the recombination is almost fully characterized by p_{eff} and the rest of the calculations can mainly be performed to achieve values comparable to other models or to be used with simulation programs. The latter was the main reason for the given procedure of using a constant $d_{\mathrm{cont}} = 50\,\mu\mathrm{m}$ as variations in the contact diameter only play a minor role in the simulations as long as the matching $d_{\mathrm{cont}}/J_{0\mathrm{b,met}}$ pair was selected. For a specific d_{cont} selected, the calculated $J_{0\mathrm{b,met}}$ would be required to parameterize the recombination according to the determined p_{eff}. The second »new« parameter from the model is the name giver: p_{LPA}. The influence of d_{cont} on S_{met} is basically that of the area, thus quadratic. In case of p_{LPA}, the influence is linear and therefore p_{LPA}—as shown in Table 7.6 can be determined at significantly lower uncertainty than S_{met}. It should also be noted that while a large uncertainty is given in S_{met} (in the range of 20 to 30 % relative), in case of an input parameter for device simulations as performed in Chapter 8, the precision of S_{met} is actually that of p_{LPA}. In this case, the area of recombination is well defined in the simulated unit cell and p_{LPA} has to be evaluated such that this area is matched. Here, the uncertainty for S_{met} is mainly given to allow for a comparison to the Fischer model.

Applying the models did show that both can be used to describe the data. While the large scattering especially directly after the laser indicated that process fluctuations (e.g. by the PECVD process or the *PassDop* laser) did limit the precision at which the data could be evaluated with either model, the overall trend did correspond to the prediction in both cases. In case of the p_{LPA} model (Figure 7.17b)—as noted in Section 2.2.4 and 2.2.6—two main errors are being made during this evaluation. At a LPA density of $5000\,\mathrm{cm}^{-2}$, which corresponds to an area fraction of 9-10 %, the r_{diff} is underestimated (see Figure 2.2). If taken properly into account, this would show in a deviation from the simple linear model that is being used here. While the linear regression was far from being perfect, the uncertainty in the regression was much stronger influenced by the scattering of the data rather than a trend. For a very reproducible local processing, such an influence might be detectable though. In addition, it should be mentioned that the Fischer model is affected as well. This is the case as Equation (2.37) is only a valid approximation for a small f_{met}, which at approx. 10 % is an ambitious assumption. The second effect that has to be kept in mind—for both models equally—is the error being made in the calculation of S_{eff} for high S_{eff} values. As outlined in Section 2.2.4, in this case S_{eff} was being underestimated. This means that S_{met} is underestimated as well, which however is acceptable as such a high S_{met} is unacceptable even in the underestimated case. Therefore its precise knowledge is of minor importance.

The initial recombination behavior of the investigated layers was found to be significantly different. p_{eff} for the SiC_x-based *PassDop* layer was by a factor of approx. 5 lower than that of SiN_x. However, p_{eff} for the SiN_x layers improved significantly during an annealing step. To further investigate this, Micro-PL measurements were performed for a SiN_x sample as shown in Figure 7.20. While before the annealing inner structure of the spot can hardly be seen due to the high contrast, after the annealing an inner ring structure can be observed indicating that either the inside improved or (unlikely) the outside of the spot degraded significantly. The ring structures themselves were caused by improperly ablated SiN_x layers as can be observed from the microscopy picture (Figure 7.21a). In the Micro-PL measurements these are expected to be optical effects resulting in a variation of the signal. The line scans (see Figure 7.21b) showed that it was mostly the inner parts of the spot that showed an improved PL signal and therefore could be responsible for the reduced recombination. The line scans also showed clearly that the change in signal is not due to a change in the before-mentioned optical properties, but a real increase in the PL signal, as the curves shapes before and after annealing matched quite well. This leads to the question what effect caused these massive differences in the behavior. The investigated annealing temperature of 425 °C would not be high enough to allow for a massive effusion of nitrogen, thus a reduction of nitrogen in the LBSF can be excluded. As the FGA does not provide atomic hydrogen a saturation of dangling bonds or crystal defects by hydrogen was unlikely by this source at these temperatures. Hydrogen from the molten layer would not be expected to be available at large amounts after the laser process due to the high temperature (up to 2000 °C), which would exclude this hydrogen source as well. However, it could be possible that hydrogen from the (mainly untouched) passivation layer is mobilized at the given temperatures and migrates to the LBSF reducing recombination at defects. This would be an effect that should be present for both SiC_x and SiN_x in relatively similar ways as both contain high amounts of hydrogen. Such an effect could already be present at relatively low temperatures like 300 °C as shown in Figure 7.19. Unfortunately, proving this would be hard, as in effusion experiments mainly hydrogen originating from the (unlasered) areas would dominate the results and after the effusion, the lifetime would be expected to be low due to the missing passivation effect. It could be possible to use a method like the discussed »3D-SIMS«, but on request it turned out that most likely the sensitivity would be too low. One way to increase the sensitivity would be to use Deuterium-based precursors, but such a change would be too expensive to be feasible.

However, as can be observed in Figure 7.19, it seemed like a certain thermal budget was necessary to reduce the recombination to the optimum. Here, it should be mentioned that two samples (at 425 and 450 °C) did not fit into the trend. Checking the sample history revealed that they were in the same spot during the *PassDop* deposition and only these two samples used this spot. Thus inhomogeneities during the *PassDop* proces could be responsible for the diverting behavior. The lifetime that was measured for these two samples before the laser process indicated that it was significantly lower than that determined for the samples surrounding them, which supports this possiblity.

The second possible effect might be partly coupled to hydrogen and could explain the observed trend in Figure 7.19 as well. Due to the locally high temperatures during the laser process an influence on the surrounding passivation layer is expected even if the passivation layer seems untouched, both by heat migration as well as remaining laser fluence of the Gaussian-shaped fluence profile. This could lead to an increased defect density in the passivation layer while at the same time hydrogen can effuse if the thermal budget was high enough, thus being visible in the reduced lifetime. Due to relaxation processes and mobilized hydrogen, these defect could be healed out during the annealing step. For this, low temperatures could be sufficient (e.g. see [143]). Figure 7.21b indicated that such an effect might be present as a slight gradient towards the middle in the PL signal level in the passivated areas was observed. After the annealing step, these areas showed an improved PL signal indicating the healing process. However, it has to be considered that this could be at least partially influenced by the PL signal within the laser spot, due to carrier migration and optical smearing. Also, the main effect seemed to be present within the laser spot and not the edge, thus healing of the passivation at the edge did not seem to be the dominant effect.

As a third effect, (both intrinsic and non-intrinsic) crystal defects have to be considered. As the laser process melts the silicon and the recrystallization phase is very short, vacancies, dislocations, impurity defects etc. would be expected in the LBSF. A temperature step could lead to relaxation processes here, even if performed at moderate temperatures in the range of 400 to 500 °C. This could explain the trend that was found in Figure 7.19 where higher temperatures seemed to have a positive influence, while the hydrogen effusion process (both within the LBSF and the passivation) would limit the usable upper temperatures. This effect would be expected to be the best candidate explaining the found differences between SiC *PassDop* and SiN *PassDop* directly after the laser process as nitrogen-related impurities could lead to a higher density of such crystal defects. The thermal treatment could lead

to a relaxation of crystal defects and thus reduce recombination, possibly combined for mobilized hydrogen passivating crystal defects.

The fourth effect that was considered was the formation of a surface SiO_2 that passivated the LBSF and therefore reduce recombination. This was excluded by putting the wafers into a solution of 1 % HF for a couple of minutes which should remove any SiO_2 present at the surface. Excluding this was important, as this effect would not expected to hold when applying a metal layer to the surface and therefore vanish in the solar cell process.

This all means that while the initial recombination in the *PassDop* LBSF was found to be very high, especially for the SiN_x-based process, it can be reduced significantly by simply performing a FGA anneal in the range of 400 to 450 °C. This leads to a very low p_{eff} of around 5×10^{-3} cm^3/s. Under the assumption of having 50 µm contacts as used as input in the simulations, this would result in an S_{met} of around 250 cm/s and a $J_{0\mathrm{b,met}}$ of below 600 fA/cm^2. Thus, assuming a $J_{0\mathrm{b,met}}$ of 600 fA/cm^2 seemed like a sensible choice for simulations, as performed in Chapter 8.2. At the L_{p} (400 µm) that is used in the solar cell, an $S_{\mathrm{eff}} < 10$ cm/s can be achieved after FGA using the SiN *PassDop* layer. Therefore the total J_0 contribution of the rear side is in the range of 10 to 15 fA/cm^2 emphasizing the excellent recombination performance.

7.3 Summary

In this chapter, the properties of the *PassDop* LBSF were investigated. The main results were that the impurities driven into the LBSF during the laser process can have a significant influence on the measurements and the electrical performance of the LBSF. The doping profile characterization for laser doped samples is necessarily straight forward and many effects have to be considered. The recombination at the LBSF can be very high directly after the laser process. It was shown that this can be significantly improved during a dedicated annealing step.

Profile Characterization

The first part was dedicated to the laser doping process itself, thus determining the doping profile. Here, two types of samples were used. The first type of samples exposed a (series of) single laser spot(s) that were characterized by microscopic methods. The second type used a structure of overlapping laser spots, which form 20 mm × 20 mm areas which can be characterized by macroscopic means.

Measurements on single laser spots is the ultimate goal, but due to the microscopic nature hard to perform. The first method that was investigated was »3D« SIMS. This method uses a small sputter spot which scans the surface and thus can reveal localized inhomogeneities in the doping profiles. Using this method it could be shown that for SiC *PassDop* close to the edge of the laser spot a similar surface doping concentration than in the middle is expected, however with a lower profile depth. Due to the finite spot size the lateral resolution was limited and nothing could be said about the »very« edge of the laser spot. As an alternative Micro-Raman was investigated to characterize the electrical doping properties as the *Raman* signal can be correlated to the doping concentration [197]. In case of *n*-type (like for the *PassDop* LBSF) the sensitivity however is low, which is why approaches were investigated to work around this limit. In the first method, the *PassDop* LBSF was exposed to a BBr_3 furnace diffusion making use of the »blocking« effect [198] and the LBSF was characterized by *Raman* for *p*-type doping (for which the sensitivity is much better). Here it could be shown that the amount of boron diffused into the LBSF is significantly hindered by the presence of both phosphorus and nitrogen. Thus it was not possible to distinguish between phosphorus and nitrogen and to determine the localized dopant distribution. The second method was to perform the *PassDop* laser process on a highly doped *p*-type background, looking for a compensation of the *p*-type doping.

This method looked more promising, but due to the lack of more reference samples it was not possible to determine the localized dopant distribution as well. However, using this method, it was possible to show that at the edge of the spot there were areas where the *PassDop* layer seems to be damaged, but not properly ablated, while in this area no significant laser doping seemed to have happened. Thus an indication for local inhomogeneities in the doping concentration was observed. While uncritical in terms of contact formation (due to the non-ablated remnants), recombination could be higher in these areas.

On the structures for macroscopic measurements, mainly 4pp, SIMS and ECV were investigated. The results determined by the two profiling methods diverted significantly and such that the typical explanations like inactive dopants cannot be responsible for the observed differences. 4pp and (integrated) SIMS matched quite well and 4pp was verified independently by measuring the inductive conductivity of the sample. Using XRD, it was shown that for both SiC_x and SiN_x a high amount of the respective impurity was incorporated into the LBSF, e.g. in the form of the corresponding crystalline structures SiC and Si_3N_4. For both impurities it was shown that a strong correlation between the differences observed between ECV and SIMS and the concentration of the impurity was present. While the exact mechanism could not be determined, some causes could be excluded like traps or doping of the c-Si using carbon/nitrogen.

By a comparison of the *fPassDop* Gen2 and Gen3 layers, it was shown that the amount of nitrogen (much higher for Gen2) has a significant influence on the laser doping process, visible in SEM pictures as well as EDX mappings. The high amount of nitrogen can lead to voids [169], contact hindering [168] as well as a lower doping efficiency. In addition, it was shown using XRD that in case of nitrogen polycrystalline silicon can be determined, which can be seen as a candidate for increased recombination.

Not only carbon and nitrogen, but also fluorine, magnesium and oxygen were investigated as possible impurities in the *PassDop* LBSF, the former two originating from the optional MgF_2 optical layer. Magnesium and oxygen could be detected, but only oxygen at a relatively high concentration of above $1 \times 10^{18}\,\mathrm{cm}^{-3}$. In case of fluorine no trace of a relevant concentration was found by using SIMS. These measurements showed as well that SIMS measurements have to be carefully interpreted as material modifications resulted in a detection of impurities (e.g. fluorine) even if there was no such source available during the laser doping process. for these samples, nitrogen and carbon were tracked again, but this time as a background element

(e.g. nitrogen for SiC *PassDop*). Nitrogen as a background element (from the ambient) was incorporated only at low concentrations and can therefore be seen uncritical. The concentration of carbon on the other hand increased to around $1 \times 10^{18}\,\mathrm{cm}^{-3}$ during the laser doping.

Recombination

To characterize the recombination at the LBSF, two models were compared, the Fischer model and the p_{LPA} model. While it was found that both yield similar results for S_{met} (within the respective uncertainties), the p_{LPA} model was found to be superior due to defining two parameters that characterize the LBSF recombination but do not (p_{eff}) or only weakly (p_{LPA}) depend on the LBSF diameter d_{cont}.

Using the p_{LPA} model, it was found that the recombination between the SiC and the SiN *PassDop* layers differs significantly directly after the laser process, the SiN *PassDop* layers showing significantly higher recombination initially. However, annealing steps at temperatures $> 300\,^{\circ}\mathrm{C}$ significantly reduced the LBSF recombination leading to a better performance for SiN *PassDop* if annealed at 425 °C. The effect could not be identified exactly, but it was likely that stress release and mobilized hydrogen played a major role in the improved recombination.

After applying the annealing to SiN *PassDop*, S_{met} in the range of 250 cm/s could be determined for $1\,\Omega\,\mathrm{cm}$ *n*-type base material. This would mean a local J_0 contribution of $\approx 600\,\mathrm{fA/cm^2}$ and a total J_0 of the rear of around 10 to $15\,\mathrm{fA/cm^2}$.

8 *PassDop* PERL Solar Cells

In the previous two chapters, multiple PassDop layers were developed and the PassDop Local Back Surface Field (LBSF) was characterized. The purpose of these layers was to act as a rear side passivation in a n-type Passivated Emitter and Rear Locally Diffused (PERL) silicon solar cell. Thus it is essential to implement the layers into a full solar cell structure. This is to both verify predictions made on test samples as well as to find issues that the test samples might not be sensitive to. All of the different PassDop approaches presented in section 6 were tested on compatible solar cell structures to verify their performance, find bottlenecks and for characterization at the device level. In addition to the device characterization, simulations were performed to compare the performance prediction with the measurements and to performace a loss analysis for the cells as described in Chapter 3. While all of the cell concepts are based on the same rear side approach, the determined results differ significantly. These differences become apparent in the loss analysis and, if possible, solutions are discussed.

8.1 *fPassDop* for n-Type PERL Solar Cells with Screen Printed Front Side Contacts

The most commonly used technique for creating metal contacts on silicon solar cells is the screen printing technique. It makes use of a mask (=screen) through which a paste based on Ag (or in case of boron emitters Ag + Al) is printed onto the wafer followed by a drying step. Usually the printed paste has a low conductivity and—if printed directly onto the Anti-Reflective Coating (ARC)—no contact to the emitter. Therefore a thermal treatment is necessary for reorganisation of the paste resulting in conductive metal fingers. The paste usually contains glass particles as well that remove the ARC during the thermal treatment allowing a contact to the emitter. This thermal treatment is done commonly using a firing step at a peak temperature from 700 to 800 °C for 1 to 3 s. Therefore, for a rear side being compatible with

such metal pastes firing stability is required which led to the development of the *fPassDop* layers. While metal pastes exist for low-temperature contacting approaches, these pastes are usually more expensive and less tested.

8.1.1 Single Layer: Question of Feasibility

Motivation

As mentioned in section 6.3.1, a single layer simplifies the *PassDop* process and therefore reduces costs. However, the results showed that compromises have to be made when trying to implement such a single layer based on a-SiN_x:P. Despite the questionable feasibility, the layer was brought onto *n*-type silicon solar cells and compared to a double layer system (*fPassDop* »Gen1«) to verify the results found on test samples. These results were presented in [179].

Cell Process

For these cells, 1 Ω cm shiny-etched Floatzone (FZ), 200 µm thick *n*-type silicon material of 100 mm diameter was used. With a mask created by thermal oxidation, texturization in KOH and BBr_3 emitter diffusion were performed in a tube furnace at 890 °C within the active cell area creating a shallow diffused boron emitter with a R_{Sheet} of 90 Ω/sq on inverted pyramids. The active cell area was defined to be 20 mm × 20 mm. The emitter was passivated by a stack of Al_2O_3 (Atomic Layer Deposition (ALD)) and SiN_x (Plasma-Enhanced Chemical Vapor Deposition (PECVD)). After the front side passivation, the rear side was passivated with the *fPassDop* layer followed by the *PassDop* laser process. The laser fluence was set to 9.1 J cm^{-2}. A rear side contact spacing of 400 µm was chosen. After the laser process, a firing step in a Fast Firing Oven (FFO) was performed at 810 °C set temperature (around 700 °C wafer temperature). While there was no metal present on the cells yet, this was required to simulate the effect of such a thermal treatment when used in combination with screen printing pastes as well as to activate the passivation on the front and the rear. The front side was opened using photolithography, the metallization was performed by Physical Vapour Deposition (PVD) of a seed layer consisting of titanium, palladium and silver, followed by electroplating to thicken the contacts. The rear side was metallized by PVD aluminum.

The two *PassDop* layers are described in detail in Section 6.3. The depositions were performed at a set temperature of 475 °C. For the single layer, a SiN_x:P

layer with a refractive of ≈ 2.1 and a thickness of ≈ 130 nm was deposited. In case of *fPassDop* Gen1 the same SiN_x:P layer was used at a lower thickness of ≈ 40 nm as a *Passivation* layer, but combined with a *Doping* layer with 130 nm thickness and $n \approx 2.5$.

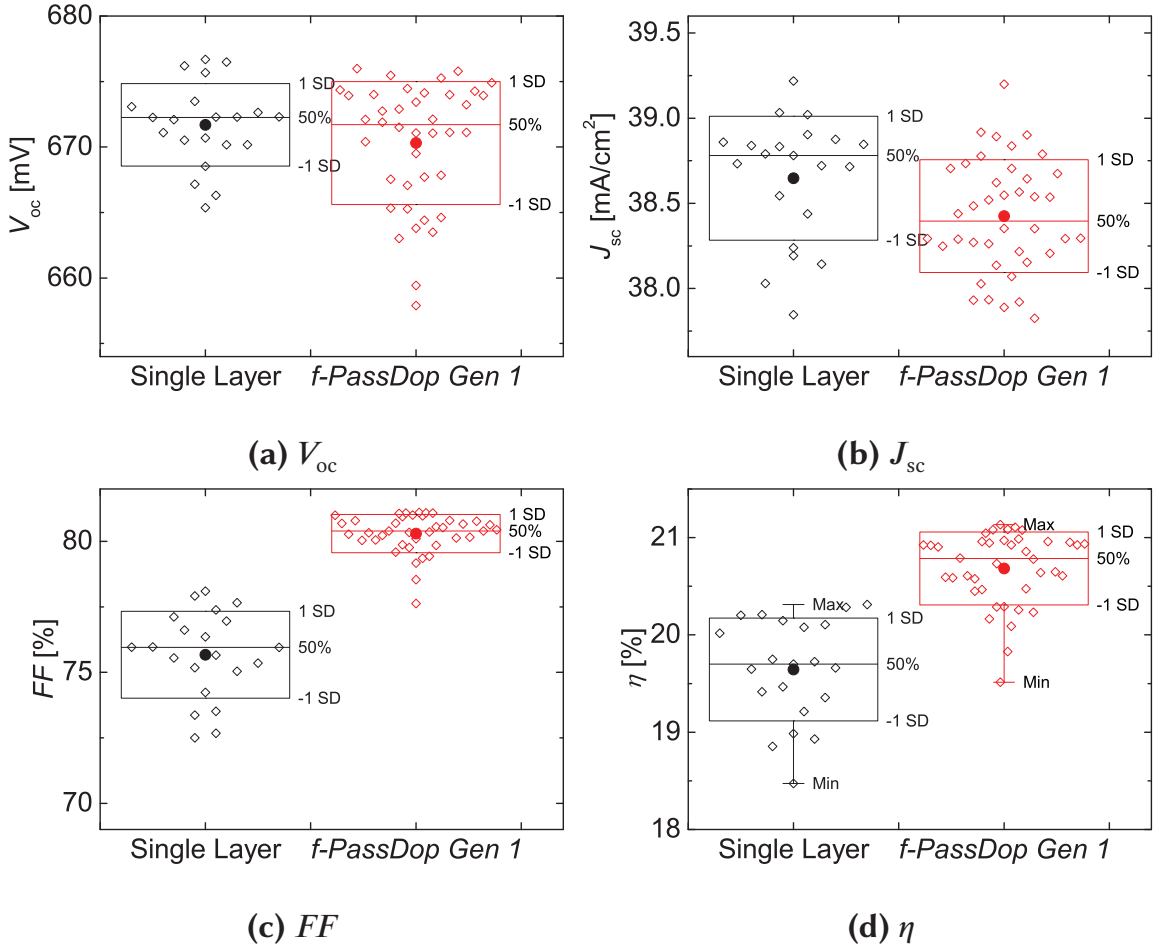

Figure 8.1: Results of the *internal JV* measurement for the small area (20 mm × 20 mm) *fPassDop* cells comparing a single layer to the *fPassDop* Gen1 stack.

Results

Figure 8.1 shows the results of the *JV* measurement for η for both the single layer *fPassDop* as well as the double layer (*fPassDop* »Gen1«). V_{oc} was determined similar for both the single layer and *fPassDop* Gen1, with the mean around 670 mV, but the scattering being slightly higher for Gen1. For J_{sc} a slightly higher mean was determined for the single layer but both showed a high deviation. As can be observed in Figure 8.1c, the most significant difference was determined in the fill factor, where the mean was determined at 75.6 % for the single layer and 80.3 % for the stack. Here, the deviation was much higher for the single layer with a standard deviation of 1.6 $\%_{abs}$

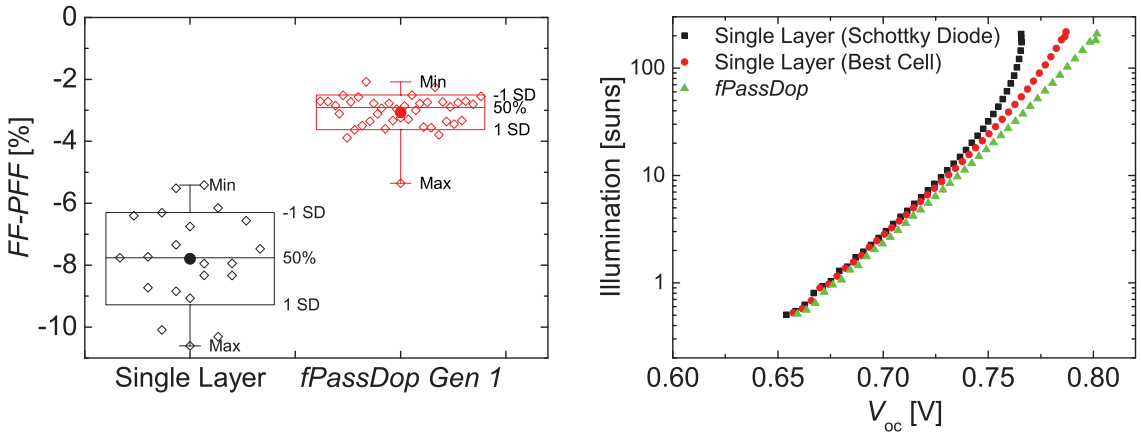

(a) ΔFF **(b)** High-Injection *Suns-*V_{oc}

Figure 8.2: Series resistance of the small area *fPassDop* cells and *Suns-*V_{oc} measurements for some of these cells illustrating the *Schottky* diode effect.

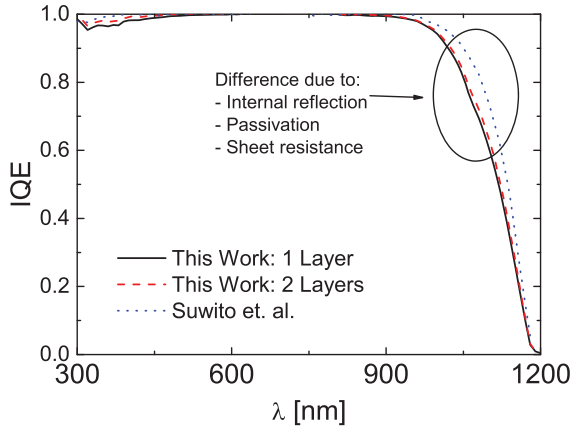

Figure 8.3: *SR* results for the small area *fPassDop* cells in a comparison to the original SiC_x-based *PassDop* cell.

while Gen1 was at 0.7 $\%_{abs}$. The differences in *FF* reflected into the device efficiency where the single layer reached a maximum of 20.3 %, while where the Gen1 stack reached efficiencies up to 21.1 %.

The *PFF* (not shown) was very similar for all cells, both with the single layer and with *fPassDop* Gen1, with the mean around 83.5 %. Figure 8.2a shows the series resistance in the form of the difference $\Delta FF = FF - PFF$ which showed a similar trend to the *FF*. Here, the mean values for the single layer were around −8 % and for Gen1 around −3 %. Figure 8.2b shows a *Suns-*V_{oc} measurement at high injection for three layers: i) a single layer *fPassDop* cell with a low *FF* ii) a single layer *fPassDop* cell with a medium to high *FF* iii) a *fPassDop* Gen1 cell. The measurement was performed to detect the presence of a Schottky diode (in the form of a reversion point [214]) at the rear due to inadequate surface doping. For the first measured cell, a reversion point was detected at around 200 suns, for the second, one could surmise a similar

Table 8.1: JV results for the best small *fPassDop* cell. The asteriks marks internal measurements. All others were determined in a calibrated measurement by Fraunhofer ISE *CalLab*.

	V_{oc} [mV]	J_{sc} [mA/cm^2]	*FF* %	*PFF* %	η %
Single Layer	672	39.0	77.7	83.3*	20.3
fPassDop Gen1	675	38.9	80.9	83.7*	21.3

trend, but without a reversion point within the measured range. For the double layer, no such effect was present, instead the cell behaved as expected for a single-diode. Figure 8.3 shows the Internal Quantum Efficiency (IQE) of the best cells for the single layer and Gen1 in comparison to the IQE for a reference SiC *PassDop* cell [19]. The graph shows that the IQE is reduced in the infrared, which can be attributed to suboptimal light trapping.

Table 8.1 shows calibrated JV data for the best single layer cell as well as the best *fPassDop* Gen1 cell. Therefore, the best cell for the single layer was verified at an efficiency of 20.3 %, while the double layer reached an efficiency of 21.3 %, thus being slightly higher than the internal measurement shown above.

Discussion

The results show that the implementation of the *fPassDop* layer at the device level was successful. At around 670 mV the V_{oc} can be considered relatively high, however it was at least partly limited by the front side structure which did not feature a low recombination emitter. For the rear, a similar influence would be expected as the *Passivation* layer was similar in composition. Due to the reduced thickness of the *Passivation* layer from 130 nm (single layer) to 40 nm (Gen1 stack) an influence could be present and was observed for other stacks. It was however not observed for these exact processes at the lifetime level. Still this as well as differences in the LBSF recombination have to be considered to be responsible for the differences and deviation observed in V_{oc}.

The differences in J_{sc} are not due to the rear side, as reflectivity measurements showed that inhomogeneties in the ARC thickness were responsible. In case of a J_{sc} loss at the rear, it would be expected to be visible in the External Quantum Efficiency (EQE) and especially IQE. As Figure 8.3 shows the IQE of the two measured cells were nearly identical at the rear, but also

showed that improvements in light trapping should be a goal, if compared to the original SiC based layer, e.g. by an additional optical layer.

The most interesting part within the cell results was definitely the *FF*. As the differences in the determined *PFF* were rather low for all of the cells, the deviation in the *FF* showed in ΔFF as well, which is proportional to the series resistance [75]. Here, it seemed that the single layer with its relatively low doping of approx. $R_{\mathrm{Sheet}} = 120\,\Omega/\mathrm{sq}$ was right at the edge of what can be contacted by aluminum. In addition, the high-injection *Suns-*V_{oc} measurements showed that these differences in ΔFF correlated to some degree to the building of a *Schottky* diode leading to a reversion point as shown in Figure 8.2b. For the double layer due to the higher doping efficiency, no such effect was present and therefore all except one cell had $\Delta FF < 4\,\%$ which would translate into a total $R_{\mathrm{S}} < 0.8\,\mathrm{m\Omega\,cm^2}$ (see Section 3.2.2). Hence, it can be concluded that a single layer is questionable as an implementation for the *fPassDop* process. The results suggest that it might be possible when investing a high amount of time into optimizing the process, but a second doping layer (be it a-SiN$_x$:P or a-Si:P) allows for a higher spectrum of variation and therefore it is more straight forward in its realization.

8.1.2 Double Layer Stacks: Influence of the Doping Layer Choice

Motivation

In the previous section it was shown that a double layer gives a significant advantage in terms of contact ability over the single layer. However, as it was shown in Section 7.1.3, even the double layer stacks Gen1 and Gen2 that featured an a-SiN$_x$:P *Doping* layer are at the edge of contact ability. Slight variations in the process can result in a decrease in the donor concentration at the surface of the LBSF (see section 7.1.3) or to improper ablation, leading to a high R_{S} and therefore a low *FF* as the safety margin is not large. Therefore, while a successful implementation was shown using the Gen2 stack [179] subsequent solar cell batches suffered from a large variation in *FF*. The Gen3 stack—on test samples—suggested that these problems can be solved, but the actual prove at the device level was pending. Thus, the goal of this experiment is to fabricate solar cells featuring the *fPassDop* Gen2 and Gen3 layers and compare their performance at the device level.

In contrast to the previous section, large area *n*-type solar cells with screen printed front contacts were chosen as a test vehicle. Most of the results in this section were published in [154].

Cell Process

As material, 1 Ω cm shiny-etched FZ, 250 µm thick *n*-type silicon material of 150 mm diameter was used. Before processing, the material was cut to a size of 125 mm × 125 mm pseudo-square defining the cell area of 148.6 cm^2. To prevent texturization and diffusion on the rear, thermal SiO_2 was used as a mask. With the rear side masked, texturization and BBr_3 tube furnace diffusion were performed to create a shallow diffused, highly doped emitter on random pyramids. The surface concentration of this emitter was in the range of 8×10^{19} cm^{-3}, the R_{Sheet} was 70 Ω/sq. The measured profile is shown in Figure 8.10. With the mask removed, the rear and front were passivated by the *fPassDop* process and a stack of Al_2O_3 (ALD) and SiN_x (PECVD), respectively. The front side contacts were created by a two-step printing of an Al-Ag paste to define the contact fingers followed a printing step of a non-firing-through Ag paste for the bus bars. For contact and passivation activation, a firing step in an in-line FFO at a set temperature of 770 °C (approx. 700 °C wafer temperature) was performed. After the front side metallization, the rear was coated by a PVD MgF_2 layer to enhance internal reflectivity followed by the *PassDop* laser process at a fluence of 11 J/cm^2. The rear side contact spacing was set to 400 µm. Finally the rear side was metallized by PVD of aluminum.

The *fPassDop* Gen2 and Gen3 layers are described in detail in Section 6.3.2. Both have the structure of a *Passivation* layer applied directly to the silicon surface and a *Doping* layer on top (see Figure 6.14 on page 103). The main difference between the two is that Gen2 uses SiN_x:P for both layers, while for Gen3 an a-Si:P *Doping* layer was used together with the necessary *Passivation* layer adaptions as shown in Section 6.3.2.

Results

Figure 8.4 shows the results for V_{oc}, J_{sc}, FF and η for both Gen2 and Gen3. For both variants V_{oc} was determined at above 670 mV with the mean at 671 mV for Gen2 and 673 mV for Gen3. J_{sc} was determined at a mean of 39.6 mA/cm^2 for Gen2 and 39.2 mA/cm^2 for Gen3 with the latter showing a large spread of the values.

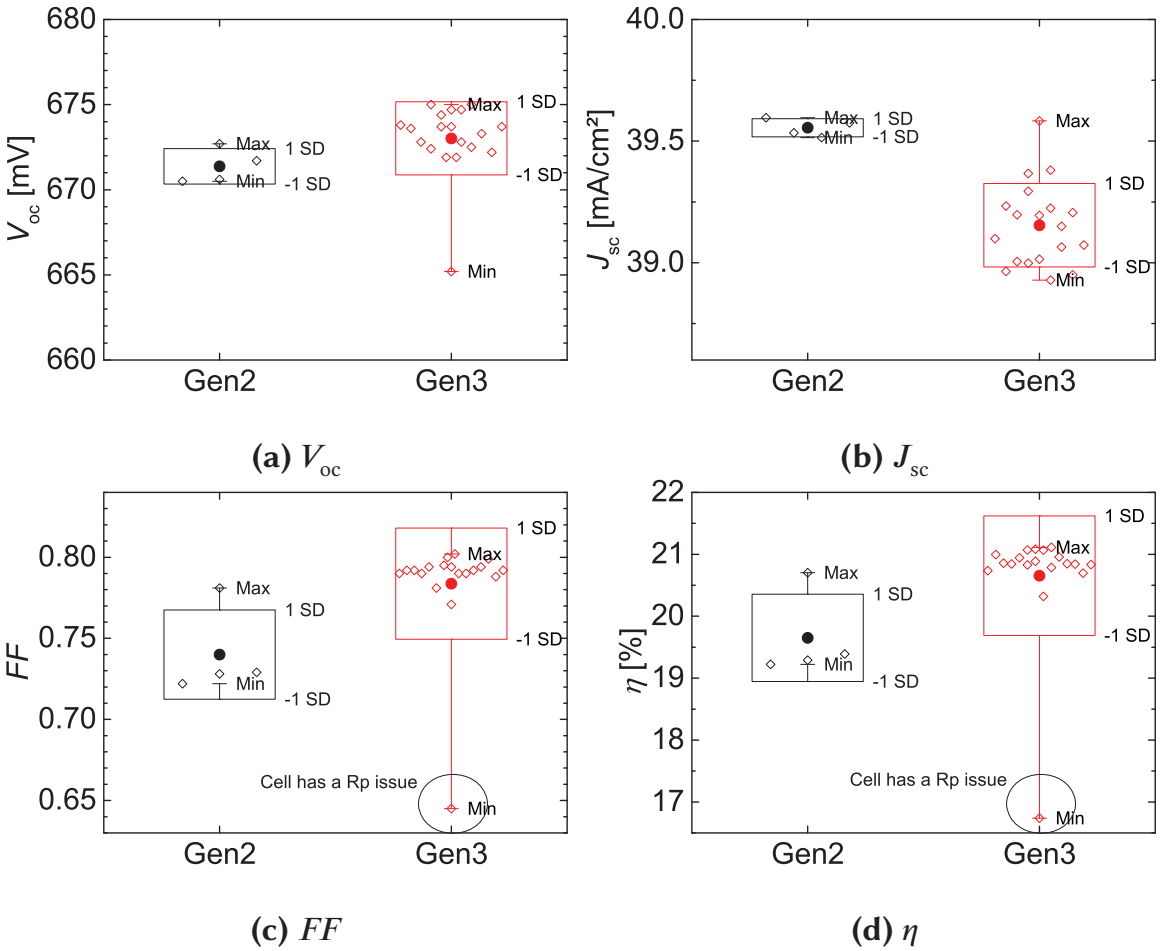

Figure 8.4: Results of the *JV* measurement for the large area *fPassDop* cells with screen printed front contacts at one sun illumination.

The biggest influence of the respective *PassDop* stacks was determined in *FF*. For Gen2, only one cell had an acceptable *FF* of 78.2 %, while the rest was in the range of 72 %. For Gen3, the mean was at 78.4 % with only three cells below the mean for one of which a R_P problem was detected. Except for this cell, the *PFF* (not shown) determined by *Suns-V_{oc}* was similar for both Gen2 and Gen3. Figure 8.5a shows the series resistance in the form of ΔFF. This indicated a similar trend for R_S as described for *FF*. Figure 8.5b shows that there was a clear correlation of ΔFF (thus R_S) and η. Figure 8.6 shows the reflection, EQE and IQE for the best cells of Gen2 and Gen3. The measured reflection was about 0.7 % higher for a wavelength range from 500 to 1000 nm. At higher wavelengths, the determined reflection increased stronger for Gen2 than for Gen3. Similar effects can be observed in the EQE, which was determined to be lower for Gen3 than for Gen2 at wavelengths above 400 nm. The calculated IQE for both cells was identical up to 1000 nm, above which a stronger decrease was determined for Gen3.

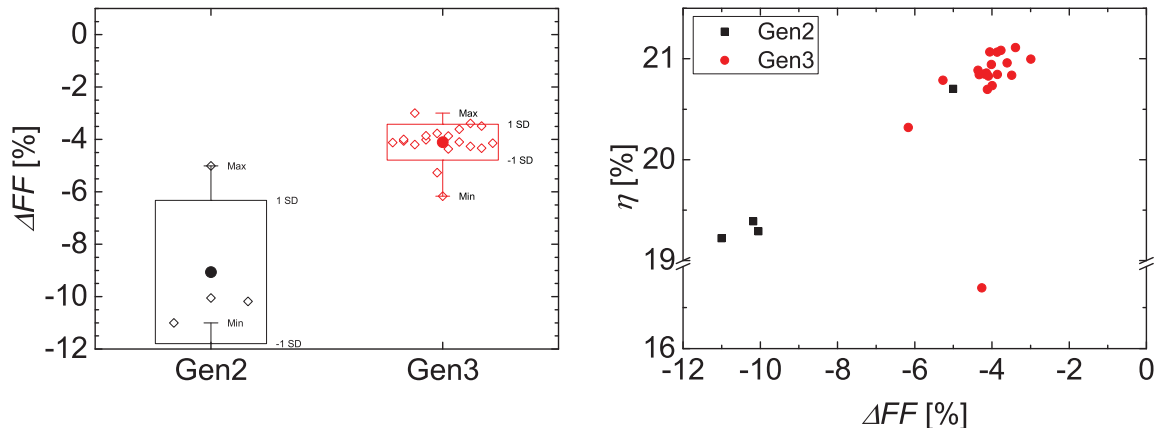

(a) ΔFF **(b)** η in dependence on ΔFF

Figure 8.5: ΔFF for the large area *fPassDop* cells with screen printed contacts at one sun illumination and correlation between η and ΔFF.

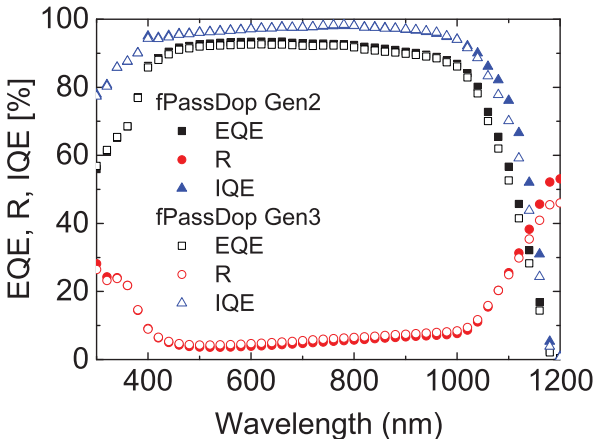

Figure 8.6: EQE, reflection and IQE for the »Gen2« and »Gen3« *fPassDop* cells in comparison.

Discussion

As outlined in the motivation, the main focus of the experiment was on a more stable FF, which was not satisfactory within previous batches. This effect was again clearly visible in the present experiment, where the scattering of FF for the Gen2 cells was high (see Figure 8.4c). As the results show the Gen3 stack indeed provided a clear improvement here. The representation of the series resistance in the form of ΔFF in Figure 8.5a and 8.5b clearly showed that it was the bottleneck in the respective cell performance. To ensure that the front side was not limiting the cell performance due to a high series resistance contribution, Transfer-Length Measurement (TLM) was performed and a reasonable specific contact resistivity of 5 $m\Omega\,cm^2$ was determined for the front side for both Gen2 and Gen3. Similarly, no significant variation in the grid resistance could be determined. Therefore, it was clear that a high R_S contribution was causing the FF losses determined for

some of the cells. This means that with respect to the doping efficiency the significant improvements achieved for *fPassDop* Gen3 can be confirmed to have a significant influence at the device level as well. Especially as not only the best cell had a significantly higher FF, but even the mean FF was higher than for the best Gen2 cell. It should be mentioned that there was one Gen3 cell which had a very low FF. For this cell a low PFF was determined as well and especially a low R_P, of which the origin remained unknown. With respect to the series resistance, this cell was within the same range as the rest of the cells ($\Delta FF = -4.3\,\%$).

While the focus in the experiment was on FF for *fPassDop* Gen3 to be fully successful the cells have to be on par with Gen2 with respect to the other parameters as well. In section 6.3.2 it was shown that the firing stability does not have to be sacrificed for an improved doping efficiency and this showed in the determined V_{oc} as well. Not only was the V_{oc} of Gen2 (mean: 671 mV) matched, but even slightly exceeded (mean: 673 mV). Especially it should be pointed out that the cells featuring the highest V_{oc} of 675 mV at the same time had FF of 80 %. This can be seen as a direct confirmation that the good performance that was determined for *fPassDop* Gen3 on test samples (see Section 6.3.2) translated well to the device level.

A slight drawback for Gen3 could be determined with respect to J_{sc}. Most of the differences determined in J_{sc} as well as the large scattering shown in Figure 8.4b can be attributed to the front side grid. During the processing (the Gen2 cells were first) an alignment problem emerged and thus the first and second printing steps (both Ag-Al for the fingers) were not properly aligned leading to a higher metallization fraction, which is visible in the increased reflection for the Gen3 cells (see Figure 8.6) accounting for approx 0.2 to 0.4 mA/cm^2. However, there was also a contribution in the infrared visible in the lower escape reflection as well as the IQE in the range of 1000 to 1200 nm. Here, the measured Gen2 cell indicated better light trapping with a gain in the range of 0.1 to 0.2 mA/cm^2. The differences in the refractive index of the *Doping* layer (higher for Gen3) should not be responsible as the MgF_2 *Optical* layer should prevent a significant decrease caused by this. As for Gen3 a 100 nm a-Si:P layer was used as a *Doping* layer, it might be possible that Free-Carrier Absorption (FCA) was responsible for this decrease. If this was the case, it might be possible to prevent such a decrease by adding a small portion of nitrogen to the layer, but this will have to be investigated separately.

Overall the improvements in the *fPassDop* layer translated well into the device efficiency with a significant increase in the process stability. While the

maximum efficiency of the Gen2 cells at 20.7 % was not far behind the series resistance limited the cell performance. For Gen3 most of the cells were measured close to 21 % with a couple of cells exceeding this limit slightly. While the calibrated measurement of the best cell lowered this efficiency slightly to 20.9 % this still means that these large area (148 cm^2) *fPassDop* Gen3 cells achieved a similar performance as the small area (4 cm^2 with PVD contacts) discussed in the previous section. This alone is already a good achievement. In comparison to the results presented in [179] (V_{oc} = 668 mV, J_{sc} = 38.4 mA/cm^2, FF = 78.2 %, η = 20.1 %), even for the Gen2 layer, an improved performance was achieved. The improvements in V_{oc} were mainly achieved by a the new generation of Ag-Al screen printing pastes, the floating Bus Bar (BB) and the improvements in the *fPassDop* layer (Gen2 to Gen3). For the improvement in J_{sc} two contributions have to be considered. The two-step printing resulted in a smaller finger width on the front and thus less shading, the addition of an optical layer on the rear resulted in enhanced light trapping. Finally the improved contact resistance both on the front (due to the new screen printing pastes) and the rear (due to the improved *fPassDop* stack) as well as an optimized grid led to the gain in the FF. All of this put together a gain in the efficiency of almost 1 % was achieved with only low variation.

Thus, it can be concluded, that the *fPassDop* Gen3 layer at the device level was a great success. The decoupling of the passivation and doping properties allowed for a broader process window resulting in a more stable cell output. The improved doping efficiency resulted in an improved series resistance allowing for higher FF without sacrificing V_{oc}.

Loss Analysis – Motivation

The results determined for *fPassDop* Gen3 both on test samples as well as at the device level suggest that most of the limiting factors at the rear were removed or at least reduced to an acceptable level. To further investigate this and to determine if the balancing of the front and rear with respect to resistive and recombinative losses was good, a Free Energy Loss Analysis (FELA) was performed. The goal for this analysis is mainly to determine if with the given front side structure a significant improvement can still be achieved or if it is now the front that needs significant adaptions. Before the loss analysis, a brief comparison of the simulation to the measured cell will be performed to verify the model.

For the interpretation of the loss analysis graphs, the remarks from Section 3.3.2 should be kept in mind.

Loss Analysis – Parameters

The J_0 contributions for the front (50 fA/cm^2) and rear (20 fA/cm^2) side passivated surface are based on values determined for the respective layers, in case of the front side for a symmetrical J_{0e} lifetime structure. $J_{0e,met}$ (1400 fA/cm^2) was calculated using *EDNA* [215], assuming recombination at the surface limited by the thermal velocity of the carriers. $J_{0b,met}$ is based on values determined in Section 7.2 for the low temperature layer, which should be a good estimate. Based on these results, two values for $J_{0b,met}$ were assumed: 1) before annealing (4500 fA/cm^2), which would correspond to the cells as measured above 2) a reduced $J_{0b,met}$ of 1000 fA/cm^2 conservatively estimated from the measured $J_{0b,met}$ after annealing in Section 7.2. Such a reduction might be achieved if the laser process would be performed before firing. This was the only variation between the two simulations.

The shading was calculated by determining the finger width in the properly aligned regions, for the simulation an effective value was determined to include the effect of the bus bar within the unit cell. This resulted in an overall shading of 5.7 % or an effective finger width of 45.6 µm. The misalignment observed for some of the Gen3 cells was not taken into account. For the emitter, a collection efficiency of 99 % was assumed. The front side transmission was determined by a scanning reflectivity measurement, thus no ARC absorption is included within the simulation. The rear side optics were calculated using a ray tracer [77].

The contact resistivities on the front and rear were set to 5 and 2 mΩ cm^2 respectively. While the former was determined by TLM, the latter is an assumption, but could not be determined precisely. The grid resistivity was simulated analytically [78] and provided to the simulation as an external series resistance.

Table 8.2: *JV* results for the best *fPassDop* Gen3 cell in comparison to the *Quokka* simulation. The first simulation was performed with a $J_{0b,met}$ of 4500 fA/cm^2, the second simulation with a lower $J_{0b,met}$ of 1000 fA/cm^2.

	V_{oc} [mV]	J_{sc} [mA/cm^2]	*FF* %	*PFF* %	η %
Measured	675.0	39.0	80.2	83.2	21.1
Sim. – High $J_{0b,met}$	675.6	39.8	79.6	84.3	21.5
Sim. - Low $J_{0b,met}$	680.6	39.9	79.7	84.4	21.8

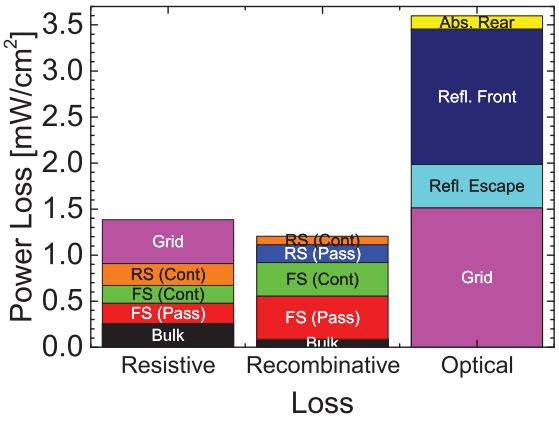

Figure 8.7: FELA in mW/cm^2 for the *fPassDop* Gen3 cell structure, if simulated with the lower $J_{0b,met}$ of 1000 fA/cm^2.

Loss Analysis – Results

A comparison of the results for the cell measurement and the simulation can be found in Table 8.2. The simulation resulted in a V_{oc} of 675.6 mV, a J_{sc} of 39.8 mA/cm^2 and a *FF* of 79.6 %, while the *PFF* was simulated to be 84.3 % for the higher $J_{0b,met}$ of 4500 fA/cm^2. With the lower $J_{0b,met}$ of 1000 fA/cm^2 V_{oc} increased to 680.6 mV while the other parameters increased only marginally. In comparison to the measured *fPassDop* Gen3 cell, V_{oc} was reproduced well, while J_{sc} and *PFF* were predicted to be higher than in the measurement. In contrast, the simulated *FF* was lower than the measured one.

Figure 8.7 shows the results of the FELA [79] for the simulated *fPassDop* Gen3 cell with the lower $J_{0b,met}$ of 1000 fA/cm^2. Overall, the optical losses were dominating, with a higher power loss than both resistive and recombination losses combined. Within the optical losses, the grid and the reflection on the front were the highest contributions with each approx. 1.5 mW/cm^2. In case of the resistive losses, the grid was the biggest contribution, while the rest of the contributions were evenly split. The recombination losses with the lower $J_{0b,met}$ were biased towards the front. The rear contact recombination loss very low at around 0.1 mW/cm^2 (with the higher $J_{0b,met}$ around 0.3 mW/cm^2), the higher contributions originated from the front, both the passivated as well as the contacted areas.

Loss Analysis – Preface

Before starting with the loss analysis, the simulation was compared to the measured cell data for validation. Here, not only the *JV* data was taken into account, but also the measured and simulated EQE and IQE (both not

shown). If the measured spot (4 cm^2) was chosen such that alignment issues do not have to be considered, the spectral match between simulation and experiment was good, although the comparison showed that the used values for the pathlength enhancement Z were possibly chosen too conservatively. Thus, while the difference in the simulated and measured J_{sc} is quite large, the simulation does actually represent well the J_{sc} could have had, if taking technological issues aside.

Similar statements can be made regarding the *PFF*, which in the simulation was $\approx$ 1 % higher. Here, Dark Lock-In Thermography (DLIT) and dark JV measurements showed that at the edge minor shunting led to this decrease, which was not taken into account for the device simulation, as the focus was on the balancing of the front and rear. This difference in *PFF* means that while the differences in the simulated *FF* is relatively low, the series resistance (represented by the difference of the two) at $\Delta FF = 4.7\,\%$ is over-estimated in the simulation, as in the measurement a difference of 3 % was determined. Here, the contributions with the highest uncertainties are the rear contact resistance, for which no reliable values could be determined and the grid resistance, for which not all of the input parameters could be verified. The difference in ΔFF of 1.7 % would correspond to a series resistance loss equivalent to 0.3 mW/cm^2, which is more than the contact resistance contribution from the rear meaning that this contribution alone cannot be responsible for the observed difference. As the emitter and base contributions were well known, it was mainly the grid resistive contribution that was over-estimated.

The differences in V_{oc} in case of the simulation with the higher $J_{0b,met}$ of 4500 fA/cm^2 were negligible as the actual cell was measured with only 0.6 mV below the simulated value. However, this value did correspond to a $J_{0b,met}$ in the unannealed state, as determined for SiN *PassDop* in Section 7.2. While the firing step for the cells was performed before the laser process, an annealing step followed at 350 °C after the evaporation of aluminum to activate the rear side metallization. This should have some effect on $J_{0b,met}$ and therefore the $J_{0b,met}$ would be expected to be lower. Thus, the rear contact recombination in the simulation was over-estimated, which is why the simulation with the lower $J_{0b,met}$ was performed in addition. The lower $J_{0b,met}$ should represent a value that is closer to the optimum which might be achieved (e.g. by performing the laser process before annealing), the real $J_{0b,met}$ for the given cell would be expected to be in between the two. The lower $J_{0b,met}$ led to a higher V_{oc} as shown in Table 8.2 and that would have to be compensated by other contributions. Here one candidate is the front side contacted area.

For this contribution the simulated value using *EDNA* might under-estimate the recombination as additional recombination might be caused by Al spikes forming during the firing step [216–218].

Loss Analysis – Discussion

The main focus for the loss analysis was on the balancing of the loss contributions. Especially the question raised if with the current cell layout it would be possible to achieve a significant gain in the cell efficiency. Here, from the results shown in Figure 8.7 it becomes clear that this is not the case. Even if considering that the resistive loss in the grid was over-estimated, the front side has the significantly higher contributions in all three categories.

This was especially the case for the recombinative losses. Even though the simulation with a $J_{0b,met}$ of 1000 fA/cm^2 might slightly under-estimate the recombination at the rear, this was likely the case for the emitter contact as well. This means that approx. 2/3 of the recombination losses can be attributed to the emitter contact and passivation. While certainly some improvements can be made for the *fPassDop* layers, e.g. by reducing the $J_{0b,pass}$ to around 5 fA/cm^2, the gain in V_{oc} would be negligible (in this range) as the relation of V_{oc} and J_0 is of logarithmic nature. Even the reduction in $J_{0b,met}$ (weighted from 55 to 12 fA/cm^2) »only« resulted in a gain of 5 mV. For comparison, the total (yet under-estimated) J_{0e} for the front was in the range of 100 fA/cm^2. Thus to achieve a higher efficiency, it would be key to reduce the recombination on the front, which could be done by using a drive-in step after the diffusion of the boron emitter.

However, a deep diffused emitter can be problematic to be contacted by the Ag-Al screen printing pastes due to the reduced surface concentration. Thus it is currently not known if it is feasible. A way to work around this would be a selective emitter, but that could potentially increase complexity in the process significantly.

The other strongly limiting factor is the front side grid. While some sacrifice will always have to be made here due to the balancing of shading and grid resistivity, it was clear that even with the optimized grid the combined loss was too high. Here, significant progress at printing small finger widths would be required to reduce the amount of shading and possibly allow for smaller finger distances on the front.

8.2 *PassDop* for n-Type PERL Solar Cells with Low-Temperature Front Side Contacts

8.2.1 Small-Area Cells with Evaporated Contacts

Motivation

Two approaches aiming for low temperature metallization were pursued in Chapter 6, SiC *PassDop* and SiN *PassDop*. The former is based on the original *PassDop* layer presented by Suwito *et al.* and therefore it was already tested on cells. The SiN *PassDop* Gen1 layer was a new development and such a proof at the device level was still pending.

Thus, the first goal of this experiment is to test the new SiN *PassDop* layer, the second to approve the development that was done for the SiC *PassDop* layer. In addition, for these small area cells, less compromises have to be made in the design of the front side due to the smaller finger length. This should allow for efficiencies up to 24 % [95], thus providing a vehicle to really test the performance of the *PassDop* layers at the device level.

Cell Process

As the development of the two layers was not done in parallel, the solar cells for the two investigated *PassDop* layers were fabricated in separate batches with slightly different properties.

In case of the SiC *PassDop* layer, the cells were fabricated on 150 mm shiny-etched, 1.7 Ω cm Cz *n*-type c-Si wafers with a thickness of 250 µm. With the rear side masked by thermal oxide, texturization by KOH and BBr_3 tube furnace diffusion were performed in the 20 mm × 20 mm active cell area. After a subsequent drive-in step the final 140 Ω/sq deep diffused emitter was formed. With the thermal oxide mask removed, the front was passivated by a stack of 10 nm Al_2O_3 and 65 nm SiN_x followed by thermal activation at 425 °C for 25 min in a Forming Gas Anneal (FGA). With the front passivation activated, the SiC *PassDop* Gen2 layer was deposited on the rear. The metallization of the rear was performed by applying the *PassDop* laser process at a laser fluence of 9 J/cm^2 followed by PVD of aluminum. The front side was opened using lithography and metallized by PVD of titanium, palladium and silver. The contacts were activated in a FGA at 350 °C for 15 min. The front contacts were thickened using electroplating. After initial measurements (denoted as »Single Layer Anti-Reflective Coating (SARC)«), an additional ARC layer of

MgF_2 was deposited by PVD on the front (denoted as »Double Layer Anti-Reflective Coating (DARC)«), although it should be noted that the initial ARC thickness was not optimized for the additional MgF_2 layer.

For the SiN *PassDop* layer, the cell process was similar, but with small changes. These cells were processed on 100 mm shiny-etched, 1 Ω cm FZ *n*-type c-Si with thickness of 200 µm. The emitter formation was done as described above for the SiC *PassDop* cells. The active cell area was 20 cm × 20 cm as well. In case of the SiN *PassDop* cell, the rear was passivated by SiN *PassDop* Gen1 (single layer a-SiN_x:P) first followed by the passivation of the front by 10 nm Al_2O_3 and 65 nm SiN_x. The passivation was activated at 425 °C for 25 min in a FGA step. The rest of the cell process was as described above for the SiC *PassDop* cells.

Table 8.3: Results of the certified *JV* measurement for the best small area cells with the SiC *PassDop* Gen2 or SiN *PassDop* Gen1 rear side. Excluding *PFF*, the results were achieved by calibrated measurements by Fraunhofer ISE CalLab. All cells had an active cell area of 4 cm^2.

PassDop Layer	ARC	V_{oc} [mV]	J_{sc} [mA/cm^2]	*FF* [%]	*PFF* [%]	η [%]
SiC *PassDop* Gen2	SARC	698.9	41.3	80.5	84.6	23.2
SiC *PassDop* Gen2	DARC	698.7	41.7	80.5	84.6	23.5
SiN *PassDop* Gen1/MgF_2	SARC	694.2	40.4	81.0	84.0	22.7
SiN *PassDop* Gen1/MgF_2	DARC	694.9	40.7	80.8	84.0	22.8

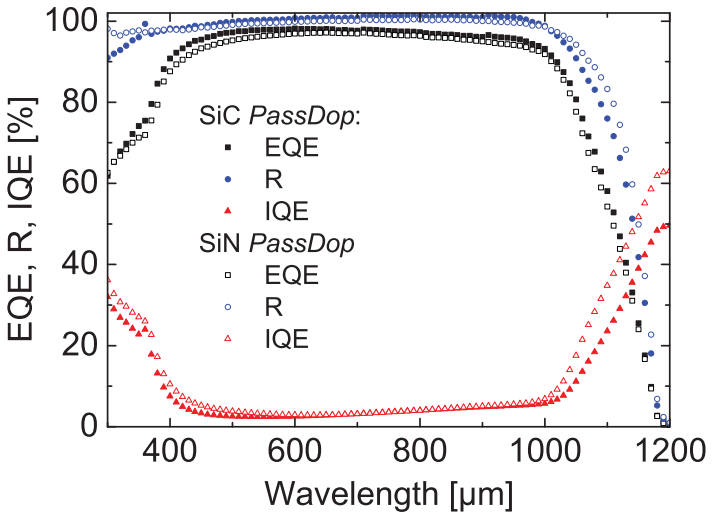

Figure 8.8: EQE, IQE and reflexion measurement for the SiC_x- and SiN_x-based *PassDop* cells. These measurements were performed without the additional MgF_2 ARC layer.

Results

Table 8.3 shows the determined J-V results for the best high-efficiency small-area *PassDop* cells.

For SiC *PassDop*, a high V_{oc} of almost 700 mV was reached. J_{sc} for this well was measured at 41.3 mA/cm^2 before (SARC) and 41.7 mA/cm^2 after applying the additional MgF_2 layer (DARC) on the front. With a ***FF*** of 80.5 %, this resulted in an efficiency of 23.2 %. The ***PFF*** was at 84.6 %. With DARC, the efficiency climbed to 23.5 %.

For SiN *PassDop*, a high V_{oc} was measured as well at 694 mV. J_{sc} was measured at 40.4 mA/cm^2 with SARC and at 40.7 mA/cm^2 with DARC. ***FF*** was determined at 81.0 % but decreased slightly to 80.8 % after applying MgF_2 on the front. This resulted in an efficiency of 22.7 % with SARC and 22.8 % with DARC. For this cell, a ***PFF*** of 84.0 % was determined.

Fig 8.8 shows the external and internal Quantom Efficiency (QE) as well as the reflection for the two cells. The EQE for both cells was similar, but with the SiN *PassDop* cell reaching a slightly lower spectral responce over the complete wavelength range. In accordance the reflection was equal or higher for SiN *PassDop* as well. A significantly higher reflection was determined in the infrared for the SiN *PassDop* cell with a reflectance of above 60 % at 1200 nm. The IQE was close to 1 for both SiC and SiN *PassDop* over a broad range of wavelengths. Here, the higher determined infrared reflectance for SiN *PassDop* resulted in a higher IQE than SiC *PassDop* at wavelengths above 1000 nm.

Discussion

As outlined in the motivation, the focus on the batch was on testing the SiN *PassDop* Gen1 layer at the device level. The results show that this test was successful. The high V_{oc} of over 690 mV approves the excellent passivation quality of the layer, the high ***FF*** of 81.0 % the good doping efficiency.

The second goal was to approve the development that was done for the SiC *PassDop* Gen2 layer. This was very successful as well. Especially the improvements on the front (better adapted SiN_x ARC thickness) led to a very high J_{sc} of 41.3 mA/cm^2). On the rear the improvements in the SiC *PassDop* Gen2 layer allowed for a pitch of 400 µm. This allowed for a high ***FF*** of 80.5 % while retaining a V_{oc} close to 700 mV.

The third goal was to compare the two *PassDop* layers. Due to the fact that the two layers were tested in separate batches and especially on separate

materials, this comparison is hindered, but still possible. First, the results obtained on test samples should be recalled (see Section 6.2.1 and 6.2.2). With regard to the passivation, the performance of both layers was very good, with SiC *PassDop* Gen2 reaching an S_{pass} below 1 cm/s and SiN *PassDop* Gen1 approx. 2 cm/s. The higher influence on recombination would be expected from the LBSF, for which (see Section 7.2) significant differences in $J_{0b,met}$ were observed, especially directly after the laser. Here SiC *PassDop* Gen2 achieved a $J_{0b,met}$ after laser of around 1400 fA/cm^2 while for SiN *PassDop* Gen1 10 000 fA/cm^2 was determined. While a dedicated anneal at 425 °C would result in a reduced $J_{0b,met}$ for the SiN *PassDop* Gen1 layer, such an anneal was not performed. Instead the only annealing after the laser process was performed at 350 °C for 15 min to activate the rear side metallization. In terms of doping efficiency, differences were obtained, but the influence would be expected to be low.

The outlined differences would mean that the biggest difference in performances of the SiN *PassDop* cell and the SiC *PassDop* cell would be expected in the V_{oc} and that this difference would be due to the higher LBSF recombination. If taking the values determined directly after the laser process, the difference in V_{oc} between the two cells would be expected to be in the range of 7 to 8 mV. Instead a difference of 4 to 5 mV was determined, the lower difference being a consequence of the annealing at 350 °C.

For both J_{sc} and FF, there were no significant differences expected that were caused by the use of the respective *PassDop* layer. Still a significant difference was determined in J_{sc}. Here, most of the difference can be attributed to reduced shading of the metal contacts leading to an improvement in J_{sc} of 0.8 to 1.0 mA/cm^2. This can be observed in the EQE, which was almost constantly higher for the SiC *PassDop* cell. In addition, the used material resulted in a higher J_{sc} as well. The higher base resistivity of 1.7 Ω cm of the SiC *PassDop* cell (the SiN *PassDop* cell had 1.0 Ω cm) led to an increase of approx. 0.1 mA/cm^2 due to the higher diffusion length according to simulations used *Quokka* and the higher thickness of 250 µm to 0.2 to 0.3 mA/cm^2 improvement. The only effect that can be attributed to the rear can be best observed in the IQE as well as the reflection of the two cells. Here the SiN *PassDop* cell shows a significant higher IQE at wavelengths above 1000 nm suggesting improved light trapping (see Figure 8.8). This can be attributed to the used MgF_2 optical layer in case of SiN *PassDop* Gen1. MgF_2 has a refractive index of 1.38, while for SiC *PassDop* Gen2, a SiC_x:P layer was used that had a refractive index of 1.8. The improved light trapping resulted in a J_{sc} increase of 0.1 to 0.2 mA/cm^2 for the SiN *PassDop* cell in comparison to the

SiC *PassDop* cell.

Regarding the series resistance in the representation of ΔFF, differences were determined for the two cells was well. The SiC *PassDop* cell had a ΔFF of 4.1 %, while the SiN *PassDop* cell had 3 %. Most of this can be explained by the higher base resistivitiy of the SiC *PassDop* cell (1.7 Ω cm) which led to an increase in the spreading resistance as well as a slightly higher grid resistivity. An influence of the rear in form of a higher contact resistivity for SiC *PassDop* Gen2 compared to SiN *PassDop* Gen1 cannot be fully excluded as the contact resistivity could not be determined. It is however highly unlikely given the high surface concentration of 3 to 4×10^{19} cm^{-3} for the LBSF.

To conclude, most of the differences that were determined for the SiN *PassDop* and SiC *PassDop* cells can be attributed to the slight differences that were made in the device processing. The performance for both SiC *PassDop* Gen2 and SiN *PassDop* Gen1 would be expected to be much closer when being processed within the same batch. In that case the differences in $J_{0b,pass}$ and $J_{0b,met}$ would be visible mostly in a small difference in V_{oc} of approx. 4–5 mV which would separate them by approx. 0.1 to 0.2 $\%_{abs}$ in the cell efficiency. This difference should decrease further when applying a dedicated annealing step *after* the laser process, which could possibly even result in an advantage for SiN *PassDop* Gen1 as determined in Section 7.2.

Cell Simulation and Loss Analysis – Motivation

The results showed that the SiN *PassDop* layer was successfully transferred to the device level. However, within the interpretation of the results there was an uncertainty regarding the LBSF recombination and therefore $J_{0b,met}$. While directly after the laser process this would be expected to be around 10 000 fA/cm^2, an annealing after the laser process can reduce this significantly as was shown in Section 7.2. At the time of the cell process, this was not known and an annealing at 350 °C was performed rather than 425 °C, thus possibly further away from the optimum. Therefore the exact $J_{0b,met}$ was unknown.

For the cell simulations performed for this structure, there are therefore three goals:

1. Determine the range for $J_{0b,met}$ that would be expected in the actual cell
2. Simulate the optimum V_{oc} and cell efficiency based on the results that were achieved for $J_{0b,met}$ in Section 7.2

3. Simulate the maximum cell efficiency that could realistically be reached using an optimized solar cell front featuring a selective emitter and adapted metallization fractions

For the interpretation of the loss analysis graphs, the remarks from Section 3.3.2 should be kept in mind.

Table 8.4: JV results for the best SiN-based *PassDop* cell in comparison to the simulation. For the simulation a variation of the rear side $J_{0b,met}$ was performed. As a technological outlook, the simulation with an optimized cell structure was performed as well. This featured a selective emitter, adapted pitch on the front and rear and a double layer ARC as well as designated area (bus bar out of cell area).

	$J_{0b,met}$ [fA/cm^2]	V_{oc} [mV]	J_{sc} [mA/cm^2]	FF [%]	PFF [%]	η [%]
Measured		694.2	40.4	81.0	84.0	22.7
Simulated	10000	683.6	40.7	80.6	84.2	22.5
Simulated	5000	689.0	40.8	80.9	84.5	22.7
Simulated	2000	695.2	40.8	81.1	84.7	23.0
Simulated	1000	698.7	40.8	81.2	84.8	23.2
Simulated	600	700.0	40.8	81.2	84.8	23.3
Simulated – Optimized Cell	600	705.3	42.0	83.2	84.9	24.7

Cell Simulation and Loss Analysis - Parameters

All simulations were performed for a temperature of 298.15 K. As the performance of the two layers is expected to be relatively similar, the loss analysis was only performed for the SiN *PassDop* Cell. $J_{0e,pass}$ (15 fA/cm^2) and $J_{0b,pass}$ (5 fA/cm^2) were determined on symmetrical lifetime structures.
$J_{0e,met}$ (1800 fA/cm^2) was calculated using *EDNA* [215], assuming that recombination is limited by the thermal velocity of the charge carriers to the surface. For $J_{0b,met}$, the values in section 7.2 were used as a reference. Based on this, the simulation was done in a broad range from worst ($J_{0b,met}$ = 10 000 fA/cm^2) to best ($J_{0b,met}$ = 600 fA/cm^2) case. Apart from the variation in $J_{0b,met}$, for this series of simulations all other parameters were kept constant. Shockley-Read-Hall (SRH) recombination was assumed to be insignificant.

The shading was calculated by determining the finger width. For the simulation an effective finger width of 11.6 µm was determined to include the

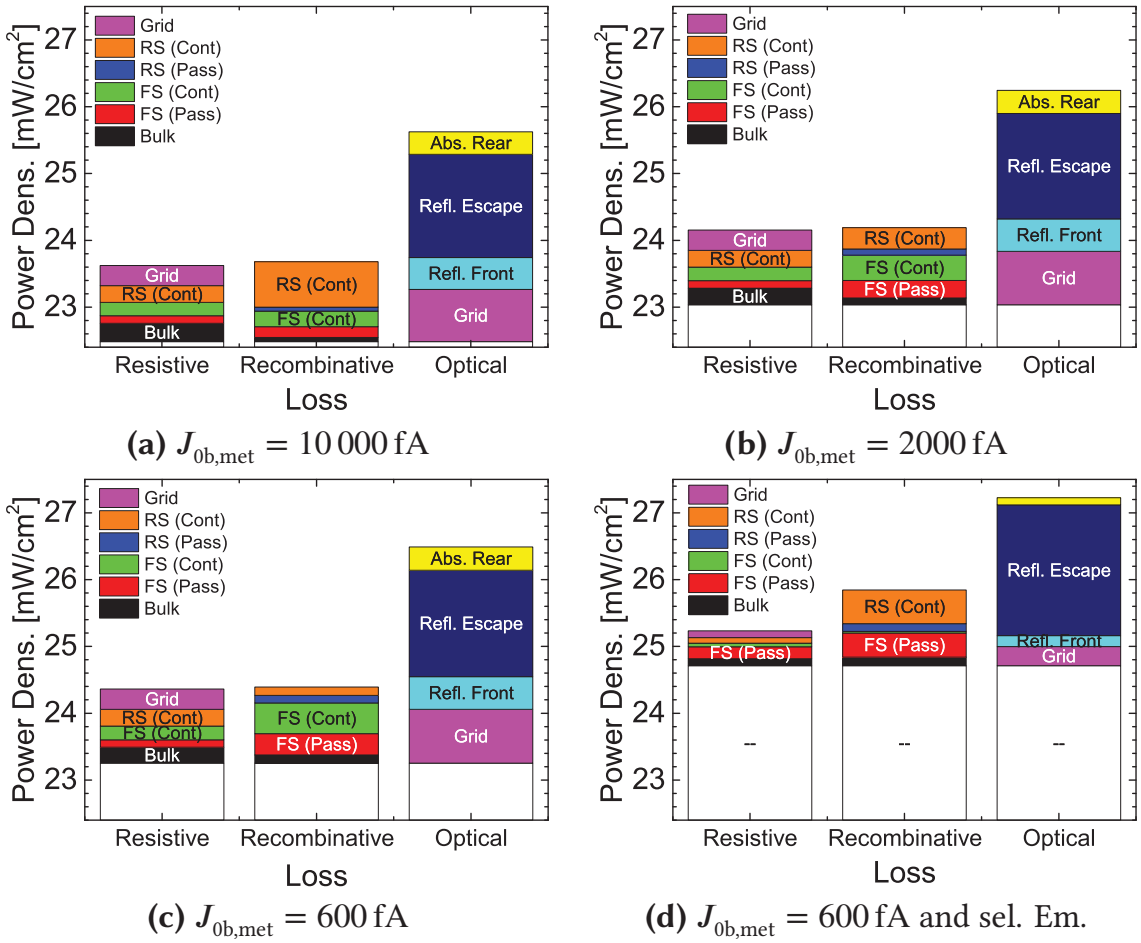

Figure 8.9: FELA for the small area *PassDop* cells with varying $J_{0b,met}$. For comparison, the loss contributions were added on top of the simulated cell efficiency. For the interpretation, the remarks outlined in Section 3.3.2 should be considered.

shading of the bus bar within the unit cell. For the emitter, a collection efficiency of 100 % was assumed. The front side transmission was determined by a reflectivity measurement, thus no ARC absorption is included within the simulation. The rear side optics were calculated using a ray tracer provided by [77].

The specific contact resistivity for the front (1 mΩ cm^2) were determined from TLM samples. The specific contact resistivity for the rear was assumed as 2 mΩ cm^2. Measured values were not available. The grid resistivity was simulated analytically [78] and provided to the simulation as an external series resistance of 0.2 Ω cm^2.

For the best case $J_{0b,met}$, an additional simulation was performed with simulating an optimized cell structure. This cell structure is based on the current record cell achieving 25.15 % efficiency processed at Fraunhofer ISE. It features an adapted front side with a selective emitter and outlying bus bars.

Both the front and rear side pitches were adapted to give the optimum cell efficiency. To account for the selective emitter, the specific contact resistivity for the front contact was set to 0.2 mΩ cm^2 (selective emitter), the $J_{0e,met}$ to 200 fA/cm^2. The simulated grid resistivity reduced to 0.062 Ω cm^2.

Cell Simulation and Loss Analysis - Results

The JV results for the simulation in comparison to the best SiN-based *PassDop* cell can be found in Table 8.4. The biggest influence of $J_{0b,met}$ was found in the cell voltage which ranged from 684 mV ($J_{0b,met}$ = 10 000 fA/cm^2) to 700 mV ($J_{0b,met}$ = 600 fA/cm^2). An additional small gain was observed in both J_{sc} as well as FF due to the reduced recombination. This led to a range in the cell efficiency from 22.5 % for the highest $J_{0b,met}$ to 23.3 % for the lowest simulated $J_{0b,met}$.

For the optimized cell structure, all of the JV results improved. V_{oc} increased to 705 mV, J_{sc} to 42.0 mA/cm^2 and FF to 83.2 %. This led to an estimated cell efficiency of 24.7 %.

Figure 8.9 shows the loss analysis for the simulations with a $J_{0b,met}$ of 10000, 2000 and 600 fA/cm^2 as well as for the optimized cell structure. The graphs 8.9a to 8.9c visualize the constant reduction of the »RS (Cont.)« (rear side contact) recombination contribution, which is quantified by $J_{0b,met}$. At the same time the other recombinative loss paths increase and especially the recombination loss at the front (passivated and contacted areas) is higher than at the rear for a $J_{0b,met}$ of 600 fA/cm^2. Figure 8.9d shows the loss analysis for the optimized cell structure. Here, the contribution of the rear contact recombination becomes large again, but most contributions are significantly reduced. Together with the front side passivation, the rear contact recombination is now the larges loss contribution. Thus further optimization would focus on reducing these contributions.

Cell Simulation and Loss Analysis - Discussion

The first goal of the simulation was to estimate the actual $J_{0b,met}$ that was likely present in the measured cells. From the simulation results shown in Table 8.4 it can be obtained, that the influence of $J_{0b,met}$ on V_{oc} is large, despite the low metallization fraction. The large influence of $J_{0b,met}$ on V_{oc} and therefore η is also visualized in the loss analysis in Figure 8.9. Especially at 10 000 fA/cm^2 almost 0.5 mW/cm^2 can be attributed to the recombinative loss at the rear contact (even more if considering the synergy effects). The best match was achieved for a $J_{0b,met}$ of 2000 fA/cm^2. This is in accordance

with the results determined in Section 7.2, where an effect of the anneal on the lifetime and therefore on $J_{0b,met}$ was already determined at 350 °C, the temperature at which the cells were annealed. The cell results therefore suggest that with this anneal, the optimum $J_{0b,met}$ could not be achieved. To achieve a V_{oc} close to that of the SiC *PassDop* cell, a $J_{0b,met}$ of around 1000 fA/cm^2 would be required. This is actually very close to the $J_{0b,met}$ that was determined for SiC *PassDop* Gen2 in Section 7.2.

The second important influence of $J_{0b,met}$ was visible in the simulated *PFF*. This is a result of the rear contact recombination limiting the injection dependent minority carrier lifetime. This results in a reduction of Δn at the pseudo-Maximum Power Point (mpp) and hence a reduction of V_{mpp}. As the series resistance of the solar cell was nearly constant ($\Delta FF \approx 3.6\,\%$) throughout the $J_{0b,met}$ variation, *PFF* and therefore *FF* increased by 0.6 $\%_{abs}$

These simulation results make clear that the rear contact recombination is an important parameter that should be kept low. With the annealing experiments in Section 7.2 it was found, that with a dedicated anneal after the laser process, a $J_{0b,met}$ of around 600 fA/cm^2 can be achieved. Therefore the simulation with 600 fA/cm^2 can be used as a prediction of what the rear side would be able to achieve within this cell structure. However, before getting into this the simulation results should be compared to that of the actual cell measurement and possibly divergences caused by uncertainties in the simulation parameters should be discussed. With the front side contact opening created by photolithography, all J_0 contributions except for $J_{0b,met}$ are well known. Thus with the matching of V_{oc} for $J_{0b,met} = 2000$ fA/cm^2 this set of J_0 parameters describes the cell well. In the following, only this simulation will be discussed.

From Table 8.4 it can be extracted that there is a difference in *PFF*. This difference in *PFF* could be taken into account by adding a J_{02} of the boron emitter. As it is not critical for the interpretation of the cell results it was not further pursued, but one should keep in mind that the actual *PFF* is approx. 0.5 $\%_{abs}$ lower than that of the simulation. *FF* in the simulation was actually lower than expected. Thus the series resistance (determined in the form of the difference between *PFF* and *FF*) in the cell was over-estimated. Here the same arguments as for the *fPassDop* cells in Section 8.1.2 applies and likely this effect can be attributed to an over-estimated contact resistivity at the rear. The last parameter to be compared is J_{sc}. Here the simulation predicted a higher J_{sc} by approx. 0.4 mA/cm^2. A comparison of the simulated to the measured EQE (not shown) revealed that this can be attributed to uncertainties in the light trapping.

All of this put together this means that by using a dedicated anneal at 425 °C after the laser process, V_{oc} could be improved to 700 mV. At the same time, ***PFF*** would be expected to improve to 84.3 % resulting in a ***FF*** of approx. 81.3 % Therefore the cell efficiency would increase to 23.0 %.

If such a cell would be fabricated, the front side and the optics would limit the device efficiency. Thus another simulation was performed to see if a significantly higher efficiency could be achieved with SiN *PassDop* given an optimized front side. The selective emitter of this structure results in a significant reduction of both the resistive and recombination losses at the front side contacts as can be observed in Figure 8.9. The outlying bus bar means that the effective finger lengths will be reduced. Together with a better aspect ratio of the contact fingers, this would result in a significant reduction of the grid shading while being able to reduce the grid resistivity as well. On the rear, the pitch could be reduced from 400 to 250 µm resulting in a significant improvement in ***FF***. Due to this change, the rear contact recombination is again one of the largest contributions. While a higher V_{oc} of around 710 mV could be achieved with a contact spacing of 400 µm, the increase in ***FF*** is worth sacrificing approx. 5 mV in V_{oc}.

All of this put together, SiN *PassDop* Gen1 should be able to reach efficiencies up to 24.7 % if given an appropriate front side design. While it will be demanding to achieve this level of cell efficiency, this shows the high efficiency potential of the *PassDop* approach.

8.2.2 Large-Area *nPassDop* Cells with evaporated Front Contacts

Motivation

To evaluate the potential of the *PassDop* process, the small area cells (active cell area: 20 mm × 20 mm) were a good test vehicle. However, for an industrial implementation of such a cell concept a process on larger area is a required. The final process aims for Laser Contact Opening in combination with Ni- and Cu-plated (NiCu-plated) contacts on the front. To prevent taking all of these steps at once the purpose of this experiment is to create a reference implementation for the large area process. Similar to the small area cells presented previously, this reference implementation will feature photolithography contact opening and evaporated seed layers. The final cell

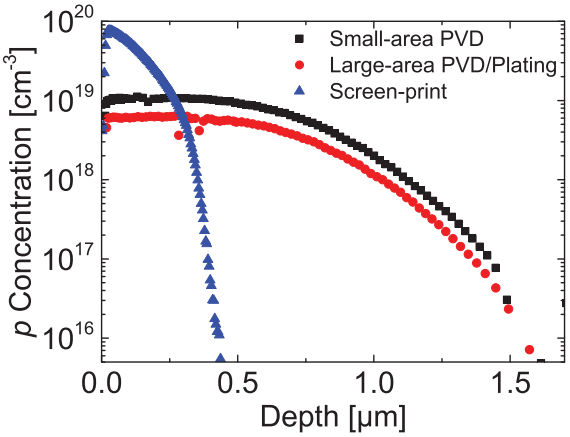

Figure 8.10: Comparison of the emitter profiles that were used throughout this work. Black squares: the emitter used for small area reference cells; Red circles: the emitter used for the large area *PassDop* cells with low temperature metallization; blue triangles: emitter used for screen-printed contacts. All profiles were determined by the Electrochemical Capacitance-Voltage Profiling (ECV) technique.

Table 8.5: Comparison of the J_{0e} for the emitters used within this work. The profiles can be extracted from Figure 8.10. $J_{0e,pass}$ was determined from symmetrically textured and diffused/implanted lifetime samples, $J_{0e,met}$ was calculated using *EDNA* at 300 K for planar surfaces. To take the textured surface into a factor of 1.7 was applied. Finally as all measurements and the simulations were performed at 298.15 K the $J_{0e,met}$ was recalculated to this temperature by taking the reduced $n_{i,eff}$ into account.

Emitter	Usual Metallization	R_{Sheet} [Ω/sq]	$J_{0e,pass}$ [fA/cm^2]	$J_{0e,met}$ [fA/cm^2]
Small Area	PVD	140	15	1800
Large Area	PVD/Plating	100	30	1100
Large Area	Screen-print	70	60	1400

concept including NiCu-plated contacts will be presented in the next section.

Front Side Design

The main two reasons that a change in the front side design might be required are the finger length and the contact opening. To allow for a process that can be replicated on a ps pulsed laser to create the front side contact opening, the opening of the front side was set to 20 µm. The finger length is mainly determined by the number of bus bars with fewer bus bars resulting in a higher finger length (2 cm for the small area cells, 3.125 cm for the large area cells). A higher finger length requires a higher finger cross-section to account

Table 8.6: Potential V_{oc} calculation for the emitters. The values taken from Table 8.5 were weighted with their respective area. For the small area cells, the contact area was 1.1 % and for the large area cells 2.6 %. Both were determined from the lithography masks. Note that the shallow emitter was used for screen printed contacts and in case of screen printed contacts (as used in Section 8.1.2) a higher contact fraction of 4.1 % on the front would have to be assumed. As this comparison aims for plated contacts the lower contact fraction of 2.6 % was used for the shallow emitter as well. From J_{0e} a V_{oc} was calculated using Equation (3.2). For this calculation a $J_{0b,pass}$ of 3 fA/cm^2 and a $J_{0b,met}$ of 600 fA/cm^2 were taken into account resulting in a total J_{0b} of 20 fA/cm^2, including the 1 Ω cm base. The metallization fracton on the rear was 1.23 %.

Emitter	Weigthed $J_{0e,pass}$ [fA/cm^2]	Weighted $J_{0e,met}$ [fA/cm^2]	Total J_{0e} [fA/cm^2]	Total J_0 [fA/cm^2]	V_{oc} [mV]
Small Area (deep)	15	20	35	55	702.5
Large Area (deep)	29	29	58	79	693.5
Large Area (shallow)	58	36	95	115	683.7

for the higher current flowing through it. To prevent increased shading this results in an increased finger spacing and thus in a reduction of the emitter sheet resistance. Thus, for a large area cell, the compromises to be made can have a strong influence on the cell performance.

Usually emitter formation is done by a shallow diffusion resulting in a doping profile like shown in Figure 8.10 (blue triangles). Such an emitter featuring a high surface concentration is commonly required when creating the contacts by screen-printing (paste development might change this in the future). For NiCu-plating, such a high surface concentration is not required and therefore leads to more flexibility in the emitter design. It was shown that even a lowly doped boron emitter as used for the small area cells (Figure 8.10, black squares) can be contacted by Ni [219]. However, the higher width of the contact opening of 20 µm for the large area cells will lead to a higher contact spacing to reduce shading and therefore a higher emitter doping is desirable as shown in Figure 8.10 (red circles). Table 8.5 gives an overview over the relevant properties of the three discussed emitters. The emitter for the small area cells allows for an excellent surface passivation, but the low surface concentration results in a high $J_{0e,met}$ contribution. The high R_{Sheet} would require a relatively low contact spacing around 1000 µm. The emitter originally used for the screen printed cells would allow for a higher contact spacing, but the $J_{0e,pass}$ is 4 times higher due to the high surface concentration.

The new emitter represents an excellent compromise. $J_{0e,pass}$ at 30 fA/cm^2 is only 2 times higher and the increase in $J_{0e,pass}$ can be partially compensated by a lower $J_{0e,met}$. Table 8.6 gives the area-weighted J_{0e} contributions for the three emitters as well as the total J_0 and the calculated V_{oc} if implemented into a *PassDop* cell. For the small area cells with a contact spacing of 800 µm on the front (total contacted area including bus bar of 1.1 %), the total J_{0e} was 35 fA/cm^2 and thus is an optimum V_{oc} of 702.5 mV. The new deep diffused emitter for the large area cells would result in an increase of the total J_{0e} to approx. 60 fA/cm^2 and thus still allow for a high V_{oc} of above 690 mV given a contact spacing of 1300 µm. If instead the shallow emitter were used, the total J_{0e} would be close to 100 fA/cm^2 and thus result in a further decrease in V_{oc} of about 10 mV.

All of this put together, the initial cell design on 125 mm × 125 mm wafers was set to 2 bus bars. The width of the bus bars was set to 1 mm. The contact spacing was found to be close to optimum at 1300 µm for contact opening of 20 µm and a plated finger width of 35 µm.

Cell Process

The cells were processed on shiny-etched FZ 1 Ω cm *n*-type Si material at a wafer size of 125 mm × 125 mm (pseudo-square). As the the active cell area covers the complete wafer, less structuring was required compared to the small area cells. With the rear side masked by thermal SiO_2, the front side was textured in KOH to form random pyramids. For emitter formation, boron was implanted on the front and activated by thermal oxidation at 1050 °C. The emitter profile is shown in Figure 8.10 (red circles). After etching the SiO_2, the rear side was passivated by SiN *PassDop* Gen1. The front was passivated by Al_2O_3 (10 nm) and SiN_x (65 nm). Before metallization, the passivation on the front and rear were activated by a FGA at 425 °C for 25 min. The front side metallization was done in a lift-off process of PVD titanium, palladium and silver. In contrast to the values listed in Table 8.6, for this batch the bus bar was not contacted resulting in a lower contact fraction of 1.6 %.

Before the *PassDop* laser process, a layer of MgF_2 (100 nm) was evaporated on the rear to enhance light trapping. The rear side metallization was done using the *PassDop* laser process followed by PVD of aluminum. The metallization on the front and rear were activated by FGA at 350 °C for 15 min. Finally, the front side metallization was thickened by electroplating of silver.

After initial characterization, the edge of the best cell was cutted using a chip

saw to reduce the series resistance close to the edge. This was done in two steps, first only the straight wafer edges were cut and in a second step the rond edges as well. After cutting, an additional ARC of MgF_2 (100 nm) was evaporated on the front.

Table 8.7: Results of JV measurement for the large-area n-type *PassDop* cell with evaporated contacts by Fraunhofer ISE CalLab. The asteriks marks internal measurements. After the initial measurement, the cell edge was cutted using a chip saw. First only the straight cell edges and afterwards the round edges as well. Finally, MgF_2 was evaporated on the front to reduce the front side surface reflection.

PassDop Layer	State	Cell Area [cm^2]	ARC	V_{oc} [mV]	J_{sc} [mA/cm^2]	*FF* [%]	*PFF* [%]	η [%]
SiN *PassDop* Gen1/MgF_2	Plated	148.6	SARC	689.2	40.0	78.4	82.5*	21.6*
SiN *PassDop* Gen1/MgF_2	Cut	145.2	SARC	687.2	40.3	78.9	82.6*	21.86
SiN *PassDop* Gen1/MgF_2	Cut II	143.2	SARC	686.1	40.4	79.2	82.4*	21.95
SiN *PassDop* Gen1/MgF_2	MgF_2	143.2	DARC	686.6	40.6	79.3		22.12

Results

The JV results for the best cell from the batch are summarized in Table 8.7. After plating the cell featured a high V_{oc} close to 690 mV. J_{sc} was measured at 40.0 mA/cm^2. *PFF* and *FF* were determined at 82.5 % and 78.4 %, respectively. This resulted a cell efficiency of 21.6 %.

In this state the local R_S was determined as shown in Figure 8.11 ([220]). It was found that close to the wafer edge the series resistance was increased by a factor of 2 to 3 compared to the area in between the bus bars.

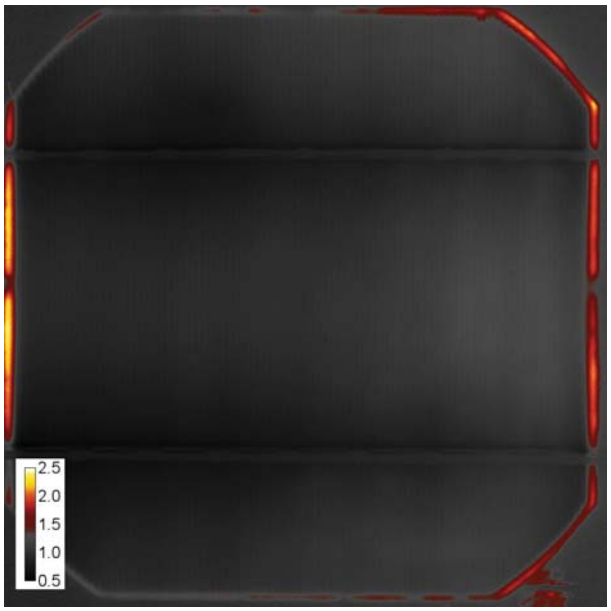

Figure 8.11: R_S image of the cell in the inital state after plating [220]. The values in the legend are given in $\Omega\,\mathrm{cm}^2$.

To reduce this series resistance influence and hence to improve *FF*, the wafer was cutted in two steps. The JV results after these cutting steps are shown in Table 8.7 as well. V_{oc} decreased slightly to 686 – 687 while with each cutting step J_{sc} and *FF* improved. A significant influence on *PFF* (internal measurement using *Suns-V_{oc}*) was not observed. Thus, the cutting of the wafer led to an improvement in the device efficiency to almost 22 %.

Finally, the cell received a second layer of ARC before the final measurement. This led to an improvement in J_{sc} to 40.6 % and therefore to a cell efficiency of 22.1 %.

Discussion

As outlined in the paragraph about the front side design, more compromises compared to the small area cells were necessary. However, the results show

that the compromises were well chosen with V_{oc} reaching close to 690 mV. In fact the highest V_{oc} determined within the batch was 692 mV, although this particular cell had a series resistance problem. Therefore, the large area cells reached a V_{oc} that was at the same level as that determined for the small area cells. This is mainly accomplished by the new emitter used for the large area cells. Since the $J_{0e,met}$ for this new emitter is lower than for the lowly doped emitter used on small area, a high V_{oc} can be kept despite the increase in the contact fraction from 1.1 % to 1.6 %. Thus the total J_{0e} increased from approx. 35 to 50 fA/cm^2. Assuming a contribution J_{0b} from the rear and base of 40 fA/cm^2 (for reasonable $J_{0b,met} = 2000$ fA/cm^2 as discussed in the previous section for the small area cells) the V_{oc} would only decrease from 695 mV to 691 mV, which is in good agreement to the determined results.

While J_{sc} was reasonably high at above 40.4 mA/cm^2 (after edge cutting), it has to be considered that the limitation by the bus bar is stronger. At 1 mm width, each bus bar leads to additional shading of 0.8 % and thus the bus bar shading at 1.6 % is more than three times larger than on the small area cells (0.5 %). Here, significant improvements could be made by reducing the bus bar width, which however might not be compatible with bus bar soldering. Nevertheless, the difference to the small area cells (40.6 mA/cm^2) was small. This can be explained by the J_{sc} losses that were discussed for these cells in the previous section.

The good compromise that was found with the selected emitter and the grid design did not only show in an excellent V_{oc} and J_{sc}, but also in *FF*. At 78.6 %, this was already reasonably high directly after plating. Here the first limitation was found in *PFF*, which after plating was determined at 82.5 %. While some wafers in the batch reached a *PFF* up to 83.6 %, the mean value was still below 83 %. In comparison to the small area cells, this means a loss of 1 to 2 % in *PFF*. DLIT measurements showed that the wafer edge had a significant contribution here, leading to a higher J_{02} and therefore a lower *PFF*.

The second influence on *FF* was the series resistance. After plating $\Delta FF = 4.1$ % was determined and thus significantly higher than for the small area cells (around 3 %). As Figure 8.11 shows, in this state, there was a high contribution from the wafer edge. The first reason for this was that the distance between the wafer edge and the grid was relatively high at 1.5 to 2 mm. And, as no redundance line was present, this would be expected to lead to a high series resistance contribution at the edges orthogonal to the finger direction. However, it were the edges parallel to the finger direction that gave the highest contribution. One effect that had to be considered is that on the left side

in Figure 8.11, there was one finger that was not metallized. On the right side in the Figure, as well as on two of the round edges, the maximum spacing of the grid to the wafer edge of around 2 mm was reached leading to a higher series resistance contribution. Both of these losses are caused by the limit of photolithography at the wafer edge. During the spin-on coating of the resist a wall builds up at the edge. During illumination and development of the resist, it might not be possible to reliably remove the resist at the edge. Thus the grid spacing at the edge had to be increased. As the wafers had no dedicated alignment symbols, alignment had to be done with respect to the wafer edge and thus much lower precision. In some cases—as with the wafer shown in Figure 8.11—this could lead to some fingers not or not completely being metallized during the seed layer evaporation.

To reduce the influence of the high series resistance onto the cell performance, the wafer edge was cutted off in two steps. This allowed ΔFF to decrease to around −3.2 %, which is in range of the small area cells and which once again emphasizes the good compromise that was made with the emitter and grid design. With the lower series resistance, FF increased to 79.2 % and was now clearly limited by PFF. While a side effect of the wafer cutting should have been the edge isolation and thus a possible improvement in PFF, this was not observed.

Thus, PFF and hence edge recombination was the strongest limitation for the cell performance and future work should focus on improvements here. Despite the losses, an excellent cell efficiency was achieved with close to 22 % before and 22.1 % after applying the additional MgF_2 ARC.

Cell Simulation

The limitation of the SiN *PassDop* small area cells already revealed the potential of the approach and discussed the influence of several *PassDop* parameters (e.g. $J_{0b,met}$) on the cell performance. The main difference between the small area cells and the large area cells were the front side design and edge recombination. The influences of grid and emitter were already widely discussed previously and cell simulations would only confirm these while not revealing new information. Taking the edge recombination into account is not straight forward, especially as the origin and nature of the observed effect is not known.

Thus, no further cell simulations and loss analysis are shown here.

8.2.3 Large-Area *nPassDop* Cells featuring NiCu-plated Contacts

Motivation

The cells with evaporated contacts discussed in the previous section were a good test vehicle to analyze the cell performance of the newly developed cell process on large area. However, the final cell structure would feature Laser Contact Opening (LCO) and nickel and copper plated contacts instead of Photolithographically defined Contact Opening (PLO) and evaporated contacts. Thus, the focus in this section is to test and investigate the influence of these processes.

The first selection (»Batch I«) of cells directly compares the combinations:

1. PLO and evaporated contacts (TiPdAg)
2. PLO and NiCu plated contacts
3. LCO and NiCu plated contacts.

The main questions investigated within this experiment are:

1. Does LCO result in a reduction in V_{oc} due to laser damage?
2. Is the contact resistivity of nickel on a boron emitter comparable to titanium?
3. Can copper be used as a replacement of silver without significant losses?

Cell Process

The main cell process was similar to the one described in the previous section, but with the respective opening and metallization steps being replaced. In contrast to the cells discussed in the previous section, the bus bars were fully contacted for all cells. Thus, the contact fraction increased from 1.6 % to 2.6 %.

For Batch I, the rear side reflector (MgF_2) was omitted. In principle LCO would not suffer from the same issues regarding edge spacing that were discussed in the previous section. To ensure comparability of all cells, the PLO grid was replicated identically using LCO, thus the edge spacing is identical for all cells in Batch I.

For Batch II, MgF_2 on the rear was included again to improve light trapping. The edge spacing of the grid was reduced to approx. 100 µm as PLO was no

longer used. In addition, the grid for these cells featured a redundance line. For this batch the main goal was to improve the plating homogeneity and edge spacing, thus a lower series resistance.

Results

Table 8.8: Results of the JV measurements for the large-area n-type *PassDop* cells with nickel plated contacts in comparison to evaporated contacts. All measurements were performed internally with a calibrated reference cell. The *PassDop* layer (here abbreviated with »SiN« was SiN *PassDop* Gen1

PassDop Layer	B.	Contact	Area [cm^2]	V_{oc} [mV]	J_{sc} [mA/cm^2]	*FF* [%]	*PFF* [%]	η [%]
SiN	I	PLO/TiPdAg	148.6	674.1	38.7	78.6	82.8	20.5
SiN	I	PLO/NiCu	148.6	672.3	38.4	68.6	82.8	17.7
SiN	I	LCO/NiCu	148.6	675.8	38.5	78.0	82.9	20.3
SiN/MgF_2	II	LCO/NiCu	148.6	668.2	39.2	80.1	83.0	21.0

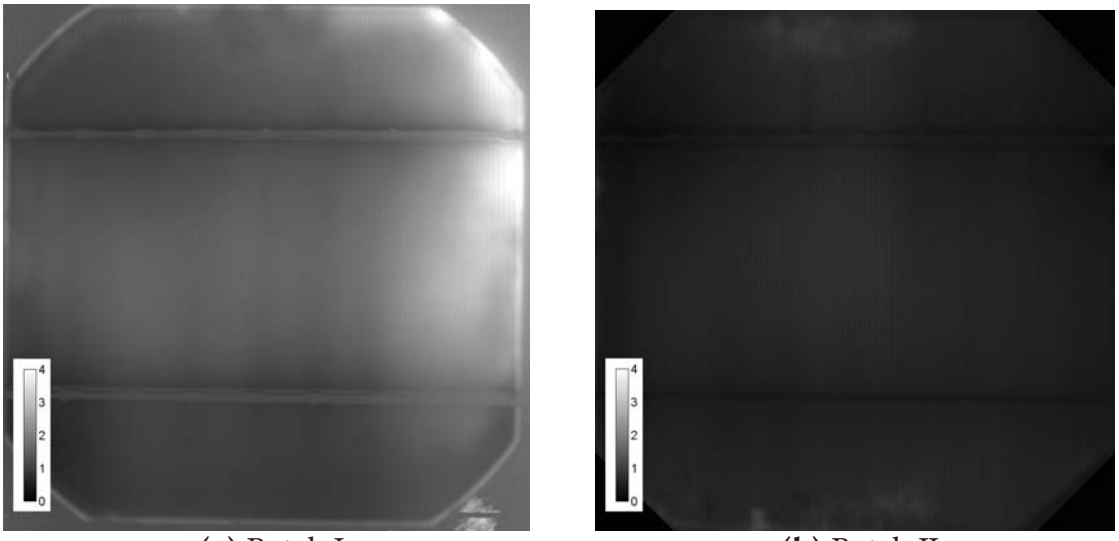

(a) Batch I **(b)** Batch II

Figure 8.12: R_S image of the LCO/NiCu cells from Batch I and II. For the best cells from either batch, no R_S-Imaging was available. Instead the measurements were performed on cells showing similar performance. The R_S-Imaging illustrates the improvements in R_S homogeneity and level that were made for Batch II. The values in the legend are given in $\Omega\,cm^2$. The scale was selected identical for both cells.

Table 8.8 shows the JV results determined for the cells using the respective contact technologies.
In Batch I, a reasonable V_{oc} in the range of 670 to 675 mV was determined. J_{sc} was relatively low with values below 39 mA/cm^2. Both PLO/TiPdAg as

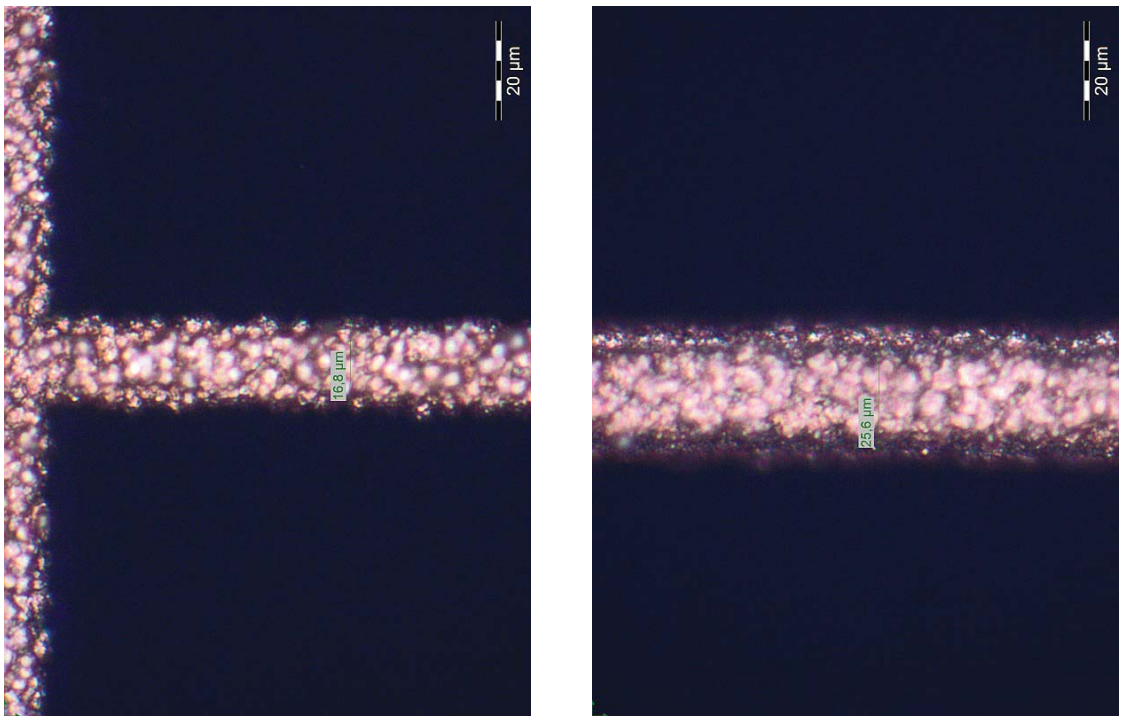

(a) Distance to BB: 0 cm **(b)** Distance to BB: 3 cm

Figure 8.13: Light microscope image of a NiCu plated finger for Batch I close to the bus bar and 3 cm away.

well as LCO/NiCu showed a reasonable fill factor above 78 %. However, the combination of PLO/NiCu showed a much lower fill factor of only 69 %. For this cell, finger adhesion was found to be low. *PFF* was determined similar for all cells (close to 83 %). The efficiency for PLO/TiPdAg and LCO/NiCu was 20.5 % and 20.3 %, respectively. The PLO/NiCu cell was limited by the low *FF* resulting in an efficiency of 17.7 %.

For PLO/TiPdAg and LCO/NiCu, TLM measurements were performed to analyze the contact ability. For the former, a specific contact resistivity of 0.3 to 0.4 $\mathrm{m\Omega\,cm^2}$ was determined, for the latter we determined 0.4 $\mathrm{m\Omega\,cm^2}$. Measurements of the grid resistance were performed to analyze the finger conductivity. 60 mΩ was measured for PLO/TiPdAg and 40 to 45 mΩ for LCO/NiCu.

In Batch II, V_{oc} decreased to below 670 mV, while J_{sc} (39.2 $\mathrm{mA/cm^2}$) and *FF* (80.1 %) improved significantly. This led to an increase in the cell efficiency to 21.0 %.

Figure 8.12 shows the R_{S}-Imaging for an exemplary cell with LCO/NiCu from Batch I and Batch II. The cell from Batch I showed a hot spot in the at one of the edges, where the finger adhesion was not optimal. The cell from Batch II showed a generally lower R_{S} and a low contribution from the wafer edge.

However, the local R_S showed that the cell from Batch II suffered from at least 16 finger interruptions, most of them close to the bus bars.

Figure 8.13 shows microscopy images of the front grid of the LCO/NiCu cell from Batch I. Close to the bus bar a finger width of 17 µm was determined while 3 cm away the finger width was 26 µm.

Discussion

For Batch I, there were three main questions: 1. Does LCO result in additional recombination in comparison to PLO? 2. Can nickel achieve a similar specific contact resistivity? 3. Does a copper grid result in a similar grid resistance? For the second and third the answers were directly given by the results. The specific contact resistivity for nickel was identical to that of titanium and therefore the front contact resistivity at the given contact fraction (2.6 % will not be a limiting factor in the cell performance. The grid resistance for the copper grid was actually determined to be lower than for silver, despite not resulting in a higher shading.

For the first question, V_{oc} is the best indicator. Here, only insignificant differences were found within the scattering determined for the whole batch (PLO: 670.3 to 676.3 mV LCO: 670.2 to 675.6 mV). Thus it can be concluded that at least at the current V_{oc} level, no additional recombination by laser damage was found to influence the cell performance.

So while in principle all of the cells from Batch I should show the same performance differences were observed. These differences were mostly visible in FF. Figure 8.12a shows a hot spot in the R_S-Imaging and this hot spot was a consequence of a low finger adhesion in this area leading to a high local resistance. Generally, Ni-plating on LCO was found to work significantly better, with low finger adhesion increasing the local resistance only occasionally. On PLO, Ni-plating resulted in low finger adhesion over a large area and therefore the significant decrease in FF.

The last influence on the series resistance was found in inhomogeneous plating. As Figure 8.13 shows, the fingers close to the bus bars were showed reduced width from 26 (close to the middle) 17 µm (at the bus bar). This either results in an additional finger width and shading in the middle of the wafer or in an increased series resistance at the connection of bus bar and finger. For TiPdAg, this was not visible. The phenomenom is caused by the large contacted area of the bus bars. In the plating process, each part of the surface has to be seen as being part of a net of resistances in a parallel circuit. In the electroplating process, a deposition of metal (here, nickel or

copper) will happen wherever there is a current of charge carriers exposed at the surface. Thus, the strongest amount of metal will be deposited where the parallel resistance is the lowest, which is the case for the bus bar. The bus bar will draw carriers away from the fingers initially, which further decreases the resistance in this area leading to an amplification of the effect. For TiPdAg contacts, during the silver plating, this is not visible, as the seed layer is deposited by PVD and a subsequent lift-off. The seed layer allows for a sufficiently good initial distribution of carriers and currents at the surface and therefore for an improved homogeneity of the fingers.

For plating of nickel, a seed layer is not available. Instead, this issue was reduced to a minimum by inducing a lower current into the silicon by the external circuit for Batch II. This led to a reduced deposition rate allowing for a more homogeneous growth of the metal. Thus, for cells from Batch II, such a reduction of the finger width close to the bus bar was not observed with the fingers having a homogeneous width over the complete wafer (38 µm finger width at the bus bars, 39 µm in the middle of the wafer and 40 µm close to the wafer edge). Together with the reduced spacing at the wafer edge, this accounts for a significant improvement in the fill factor of 80.1 %, out-performing even the 22 % cell from the previous section. As shown in the R_S image (Figure 8.12b) this was despite the presence of several finger interruptions, leading to the conclusion that the fill factor potential of the given cell layout is even higher.

As is visible from the results, both V_{oc} and J_{sc} were rather low. This was especially the case in comparison to the cell results discussed in the previous section, where a V_{oc} of 687 mV and a J_{sc} of 40.4 mA/cm^2 was determined. For J_{sc} an effect of increased shading was excluded. Some effect was expected on V_{oc} as the contacted area increased due to the fully contacted bus bar. However, if $J_{0e,pass}$ and $J_{0e,met}$ remain similar, this decrease in V_{oc} should not be above 5 mV. Instead the observed effects were caused by high recombination in the emitter and/or bulk. Especially for Batch II, reference samples showed that the bulk lifetime degraded during the process, limiting V_{oc}. While recombination has the strongest influence on V_{oc}, a high level of recombination in the emitter or bulk can result in a decreased J_{sc} (and the respective value at mpp) as well, which was the case for both batches. With the solar cell batch from the previous section it was shown that the process can achieve much reduced recombination and thus, this problem should be solvable.

Nevertheless it was possible to achieve a small increase in J_{sc} from Batch I to Batch II. Most of this was attributed to the improved light trapping by the

applied MgF_2 reflector on the rear with an expected improvement of approx. 0.5 mA/cm^2 in J_{sc}. The rest was caused by slightly improved shading due to the optimized plating homogeneity.

To conclude, it was found that LCO/NiCu can be used as a suitable replacement for PLO/TiPdAg. PLO/NiCu was not found to be a feasible solution due to low adhesion of the contacts. The cell performance was limited by bulk recombination caused by the cell process, but this should be solvable as indicated in the previous section. Apart from the small decrease in V_{oc} due to the fully contacted bus bars, no reason was found why the cells should not be able to achieve the same level of performance in the range of 22 %. Or even exceed the performance as the laser process allows to overcome the limitations discussed regarding PLO in the previous section. Thus, improving the bulk quality and reducing bottlenecks in the process should allow these scalable technologies to show their full potential in the future.

8.3 Summary

The *PassDop* layers that were described in the previous chapters were successfully transferred into solar cell devices. Multiple approaches were investigated. For new layers, commonly small-area cells to evaluate the potential were fabricated first. This step was especially important for the *fPassDop* layers, for which a completely new device had to be developed as screen-printing on boron emitter was not broadly investigated within the photovoltaic community before. Thus, to test the *fPassDop* layers, small area cells with evaporated contacts on the front were used. The focus was on testing a single layer versus a double layer stack. The single layer was not found to provide a good balance between doping and passivation properties and therefore the fill factor of the fabricated cells suffered badly due to a high series resistance. This was further analyzed using High-Injection *Suns-V_{oc}* measurements which showed that a Schottky barrier had formed on some of these cells. In contrast the double layer *fPassDop* cells already showed the potential of the approach reaching fill factors of 80 % or even above. The concept was then transferred to larger areas, where the focus was on the Gen2 (SiN_x:P(N-rich)/SiN_x:P(Si-rich)) and Gen3 (SiN_x:P(N-rich)/a-Si:P) versions of the *fPassDop* layer that were described in Chapter 6. The concept was then transferred to larger areas, where the focus was on the Gen2 (SiN_x:P(N-rich)/SiN_x:P(Si-rich)) and Gen3 (SiN_x:P(N-rich)/a-Si:P) versions of the *fPassDop* layer that were described in Chapter 6. Here it was shown that

the latest iteration featuring an a-Si:P doping layer resulted in a very stable process with ΔFF being in the range of −4 % for almost all of the fabricated Gen3 cells. This allowed for a very stable efficiency output within the batch resulting in a mean efficiency of 20.9 %. Improvements in the screen-printing on the front allowed for a high V_{oc} of 675 mV and a J_{sc} of 39.0 mA/cm^2. A loss analysis of the cell performance was performed showing that the rear side contribution to the cell's loss mechanisms was relatively low and that the focus should be on reducing recombination on the front.

The second route that was pursued at the device level was an approach for low-temperature metallization, i.e. plated contacts. Small area cells with the SiC *PassDop* Gen2 and SiN *PassDop* Gen1 layers were presented that could show the potential of the *PassDop* approach especially in the case of SiC_x, for which the cells reached an efficiency of 23.5 %. The single layer SiN *PassDop* Gen1 at 22.8 % was not far behind and the difference was mostly attributed to differences in the cell processing (resulting in differences in J_{sc}) and only a small portion to the layer performance due to a higher $J_{0b,met}$. A significant difference in $J_{0b,pass}$ was not expected as both showed an excellent performance in Chapter 6. This was a very good result for SiN *PassDop* Gen1 given the novel nature of the SiN_x:P approach and its simple structure of a single layer. A loss analysis of the cell using *Quokka* was performed showing especially the influence of $J_{0b,met}$ on the recombination properties. With the optimized $J_{0b,met}$ of approx. 600 fA/cm^2 (as determined in section 7.2) the contribution of the rear side to J_0 was found to be low when keeping the metallization fraction constant.

After successful implementation of this single layer *PassDop* system based on SiN_x, a transfer to large areas was presented. In a first step, a cell layout was defined still with evaporated front side seed layers (and subsequent silver plating). As no base process existed for this kind of cell, a new process sequence had to be developed and tested. The emitter formation was now based on implantation and high-temperature annealing, the front side doping was adapted to a wider finger pitch on the front. A H-pattern grid was defined with industrial-feasible properties. With evaporated contacts, a high voltage of approx. 690 mV was kept for these first low-temperature *PassDop* cells, with the best V_{oc} reaching 692 mV and therefore very close to that of the best small-area cell (694 mV). Despite the grid adaptions that had to be made due to the bigger cell area a high J_{sc} of 40.6 mA/cm^2 could be kept as well with the FF being determined at 79.3 %. Overall this resulted in a cell efficiency of 22.1 %, which at the time was a record efficiency at Fraunhofer Institute for Solar Energy Systems (Fraunhofer ISE) for large area c-Si based

solar cells. The cell performance was thoroughly analyzed showing that the *PFF* of 82.4 % is currently the strongest limitation that should be handled for future batches.

In the last step, the migration towards a solar concept with plated NiCu front contacts was made, thus removing the necessity for a PVD seed layer and lithographic structuring of the ARC. To investigate the potential and implications of these technologies, a comparison of LCO and PLO was performed as well as a comparison of TiPdAg with NiCu metallization.
For the laser process, no significant influence of possible laser damage was found on the cell performance, as a similar V_{oc} was achieved for both LCO and PLO. For the metallization, ρ_c for Ni and Ti were both found to be approx. 0.4 mΩ cm^2 and therefore only having a minor influence on the series resistance and cell performance. The copper grid was found to have similar grid resistivities as the reference silver grid, thus no significant impact on *FF* was found. Remaining differences in *FF* were found to be caused by inhomogeneities in the plating process.
After this comparison was performed, the grid was slightly optimized for LCO + NiCu metallization and the optimized cell showed a good plating homogeneity as well as a high *FF* of 80.1 %. As process degradation limited the cell performance, V_{oc} was found to be low at 668 mV, but the good *FF* still allowed for a good starting efficiency of 21.0 % and thus even with the given limitations being in the range of typical Passivated Emitter and Rear Cell (PERC) *p*-type solar cells. Once the process degradation will be removed, it should be possible to once again achieve a V_{oc} in the range of 680 to 690 mV and therefore efficiencies of 22 % or above, as shown previously.

9 Summary

The main objective of this work was to develop and characterize *PassDop* layers for high-efficiency *n*-type silicon solar cells. This means that these layers, deposited by Plasma-Enhanced Chemical Vapor Deposition (PECVD), have to both act as an excellent surface passivation as well as contain dopants to act as a doping source during the *PassDop* laser doping process. As an alternative to the original *PassDop* approach based on SiC_x:P (SiC *PassDop*), *PassDop* layers based on SiN_x:P were presented. Based on SiN_x:P variants for low temperature metallization like plating (SiN *PassDop*) and screen printed contacts (firing-stable *fPassDop*) were developed. These new layers have the advantage of being deposited only by the use of microwave plasma excitation which would allow for a transfer to in-line deposition tools. The effect of the new layers on the Local Back Surface Field (LBSF) formation and its doping and recombination properties was studied in detail. By applying the new layers to *n*-type silicon solar cells their viability at the device level was shown and analyzed.

In summary, the main results of this work are:

1. SiN_x:P can be used as an alternative to SiC_x:P for fully functional *PassDop* layers.
    a) A single SiN_x:P layer is only feasible if firing stability is not a requirement
    b) a-Si:P can be used as an excellent *Doping* layer in SiN_x:P/a-Si:P stacks
    c) SiN *PassDop* Gen2 (up to 450 °C): $S_{pass} \approx 2$ cm/s (1 Ω cm *n*-type) and $R_{Sheet} \approx 25$ Ω/sq.
    d) *fPassDop* Gen3: $S_{pass} \approx$ 6–8 cm/s (1 Ω cm *n*-type) after firing (700–850 °C) and $R_{Sheet} \approx 20$ Ω/sq.
2. The nitrogen content in the *PassDop* layer or stack was found to be of utter importance. A high nitrogen content can lead to
    a) reduced doping efficiency (thermal stability of the layers).
    b) improper ablation.
    c) reduced contact ability (SiN_x remnants at the surface).

3. Every element present in the *PassDop* layer can be present in the LBSF after laser doping.
4. Annealing at 425 °C is indispensable to reduce recombination at the LBSF for SiN *PassDop*. $J_{0b,met} \approx 600\,fA/cm^2$ (after annealing).
5. Realization of *fPassDop* cells with screen printed contacts with an efficiency of up to 20.9 % on large area.
6. Achieving an excellent solar cell efficiency of 23.5 % on small area with evaporated contacts.
7. Proof of concept of large area *PassDop* cells with low temperature metallization achieving 22.1 % efficiency with PVD contacts and 21 % with Ni- and Cu-plated contacts.

In the following, more details on the results are given:
The basis for the *PassDop* development was already build by Suwito and Jäger [19, 182]. In a first step, this original SiC *PassDop* layer was further developed with the main goal on improving the thermal stability of the stack. This was achieved by the introduction of a stoichiometric *Capping* layer in the stack to prevent or retard outdiffusion of hydrogen during thermal treatment. With this *Capping* layer SiC *PassDop* Gen2 was found to be stable at higher temperatures achieving a S_{pass} of 1 cm/s after annealing at 400 °C for one hour. Due to adjustments in the thickness of the *Passivation* layer in the stack R_{Sheet} was reduced to 13 Ω/sq.

Based on SiN_x:P an alternative was developed, with the focus on low-temperature metallization like nickel plating. It was shown that a single layer (SiN *PassDop* Gen1) is feasible for this approach resulting in a R_{Sheet} of approx. 33 Ω/sq and a S_{pass} of approx. 2 cm/s. The SiN_x surface passivation did not require a dedicated activation anneal but can slightly improve when annealing at 425 °C as commonly used for the activation of Al_2O_3. After the single layer was established, SiN_x:P/a-Si:P stacks were investigated. For this SiN *PassDop* Gen2, it was observed that such a stack improves the doping efficiency (R_{Sheet} of approx. 25 Ω/sq) and is less prone to process fluctuation.

The third approach that was developed had the focus on solar cells with screen printed (front) contacts. Therefore the surface passivation had to be stable after a firing step. Both SiC *PassDop* and SiN *PassDop* were not suitable for such a process. Therefore a modified SiN_x:P layer, *fPassDop*, was developed that provided a good surface passivation after firing. For *fPassDop*, it was found that a single layer is not easily realizable as either the surface passivation or the doping efficiency have to be sacrificed. Instead double layer stacks were pursued as alternatives. For these stacks the combination of a N-rich SiN_x:P *Passivation* layer and an a-Si:P *Doping* layer were found to deliver

the best performance. With this *fPassDop* Gen3 stack a S_{pass} of 6–8 cm/s can be achieved after firing at peak temperatures of 700–850 °C. At the same time this *fPassDop* stack achieves a R_{Sheet} of 25 Ω/sq. The other two variants that were investigated (Si-rich SiN_x:P + N-rich SiN_x:P and N-rich SiN_x:P + Si-rich SiN_x:P) either did not provide a suitable surface passivation after firing or were not fully compatible with the laser doping process. By using a-Si:P as a *Doping* layer in a two-layer stack, a decoupling of the surface passivation and doping efficiency was achieved for both SiN *PassDop* as well as *fPassDop*.

While SiN_x can be doped with phosphorus, the material properties were found to have a significant influence on the laser doping process. In case of SiN_x, especially the thermal stability was found to be problematic. Due to this thermal stability (increasing with N-content) of the SiN_x layers laser doping from SiN_x:P was found to work best for Si-rich layers ($n \geq 2.45$). N-rich layers ($n \leq 2.2$) were found to be only compatible with the laser doping process when used in combination with a-Si:P. If the laser fluence is too low, their thermal stability led to remnants of the layer at the surface preventing contact formation. Such an effect was already observed by Hameiri *et al.* [168]. In addition, the thermal stability of the SiN_x:P layers can lead to a burst-off of parts of the layers before the layer/stack is completely molten, thus reducing the doping efficiency. This was investigated in Chapter 6, where it was shown that for laser doping from SiN_x:P the first approx. 30 nm were very important. If this part of the layer was undoped, the phosphorus dose in the LBSF decreased by a factor of 3.8 compared to a fully doped SiN_x:P layer. a-Si:P as a *Doping* layer was able to cushion this effect, but even in that case a decreased phosphorus dose (factor of 1.7) was observed.

One implication of using composite layers like SiN_x:P or SiC_x:P for a laser doping process is the presence of (possibly unwanted) impurities that can be incorporated into the LBSF. For both nitrogen and carbon (originating from the respective *PassDop* layers) very high concentrations above 1×10^{20} cm^{-3} were observed by Secondary Ion Mass Spectrometry (SIMS) in the LBSF after the laser doping process. Both were found to significantly influence the results determined by Electrochemical Capacitance-Voltage Profiling (ECV) meaning that this technique cannot be used to reliably determine the doping profile. In addition, the crystalline forms β-SiC and β-Si_3N_4 were observed by X-Ray Diffraction in the respective LBSF after laser doping. While for the presence of carbon in the LBSF, no negative influence was observed (apart from the influence on ECV), for nitrogen, the nitrogen dose available during the laser process was found to be important. In addition to the thermal stability (see above), the presence of nitrogen during the laser doping process can lead to the formation of voids [169], which was observed for N-rich stacks

(*fPassDop* Gen2). Nitrogen can also be seen as a candidate for crystal defects in the LBSF. Signs of such defects were determined using X-Ray Diffraction (XRD), where polycrystalline structures were detected. It should also be considered that Si_3N_4 crystals in the LBSF could lead to regions in the LBSF with low conductivity as proposed by Hameiri *et al.* [168].

In addition to the macroscopic methods to determine the doping profile like SIMS, microscopic methods were investigated as well. For SIMS a method (»3D« SIMS) with a very small spot size was used scanning the surface and thus resulting in information about the doping distribution. With this method, it was shown that the surface concentration over the LBSF is mostly uniform and it was the depth of the doping profile that varied. However, for a laser doping process the edge region where no ablation occurs is the most interesting area and this method was not able to deliver reliable information here due to the spot size and the overlapping, scanning nature of the method. Alternatively, microscopic *Raman* measurements were investigated as the width of the Si *Raman* peak can be correlated to the concentration of free carriers. However, for *n*-type doping, the sensitivity is much lower than for *p*-type [197]. Therefore two methods using compensated *p*-type doping were investigated. In the first method, the *PassDop* LBSF was exposed to a BBr_3 furnace diffusion making use of the »blocking« effect [198]. Here it was shown that the amount of boron diffused into the LBSF is significantly hindered by the presence of both phosphorus and nitrogen. However, it was not possible to distinguish between blocking by phosphorus and nitrogen and thus to determine the localized dopant distribution. The second method was to perform the *PassDop* laser process on a highly doped *p*-type background, looking for a compensation of the *p*-type doping. This method looked more promising, but due to the lack of more reference samples it was not possible to determine the localized dopant distribution as well. However, using this method, it was possible to shown that at the edge of the spot there are areas where the *PassDop* layer seems to be damaged, but not properly ablated, while in this area no significant laser doping seemed to have happened. Thus an indication for a mismatch of the area where the surface passivation was damaged and the area where (significant) laser doping occurred was found.

The last property of the LBSF that was investigated is the recombination at the LBSF. Here two models were compared, the Fischer model [56] and the pLPA model [58]. While it was found that both yield similar results for S_{met}, the p_{LPA} model was thought to be superior due to defining two parameters that characterize the LBSF recombination but do not (p_{eff}) or only weakly (p_{LPA}) depend on the LBSF diameter d_{cont}. Using the p_{LPA} model, it was found that the recombination between the SiC and the SiN *PassDop* layers differs

significantly directly after the laser process, the SiN *PassDop* layers showing significantly higher recombination initially. However, annealing of the LBSF at temperatures > 300 °C significantly reduced the LBSF recombination leading to a better performance for SiN *PassDop*. The effect could not be identified exactly, but it was likely that stress release and mobilized hydrogen played a major role in the improved recombination. The best performance was observed if annealed at 425 °C. After applying the anneal an S_{met} in the range of 250 cm/s (1 Ω cm *n*-type) was determined. This would mean a local contribution of approx. 600 fA/cm^2 and a total J_0 for the rear of around 10–15 fA/cm^2.

Finally the *PassDop* layers that were developed were transferred into solar cell devices. For *fPassDop*, it was shown once more at the device level that a single layer is not feasible, as no realiable contact formation was observed. Using *fPassDop* Gen3, solar cells with Ag-Al screen printed front contacts were fabricated achieving an efficiency of 20.9 % on an area of 148.6 cm^2. The use of a-Si:P as a *Doping* layer allowed for a low variation in the series resistance and therefore a high mean *FF* of 78.4 %. A loss analysis was performed for this cell structure and revealed that the front side was limiting the cell performance strongly (both in recombination and optics). Thus improvements in paste develop and adjustments in the front side emitter and grid design would be required to significantly improve the cell efficiency for this approach.

The second route that was pursued at the device level was an approach for low-temperature metallization. Small area cells with the SiC *PassDop* Gen2 and SiN *PassDop* Gen1 layers were presented that could show the potential of the *PassDop* approach especially in the case of SiC$_x$, for which the cells reached an efficiency of 23.5 % with a V_{oc} of 699 mV. The single layer SiN *PassDop* Gen1 at 22.8 % and a V_{oc} of 694 mV was not far behind and the difference was mostly attributed to differences in the cell processing, resulting in differences in J_{sc} and only a small portion to the layer performance due to a higher $J_{\mathrm{0b,met}}$, the cells were fabricated before the effects of the anneal were investigated. This was a very good result for SiN *PassDop* Gen1 given the novel nature of the SiN$_x$ approach and its simple structure of a single layer. A loss analysis of the cell using *Quokka* was performed analyzing especially the influence of $J_{\mathrm{0b,met}}$ on the recombination properties. With the optimized $J_{\mathrm{0b,met}}$ of approx. 600 fA/cm^2 (as determined in Section 7.2) the contribution of the rear side to J_0 was found to be low and a V_{oc} in the range of 700 mV would be the result.

After successful implementation of this single layer *PassDop* system based on SiN_x, a transfer to large areas was presented. In a first step, a cell layout was defined still with evaporated front side seed layers (and subsequent silver plating). As no base process existed for this kind of cell, a new process sequence had to be developed and tested. With evaporated contacts, a high voltage of approx. 690 mV was kept for these first low-temperature *PassDop* cells, with the best V_{oc} reaching 692 mV and therefore very close to that of the best small-area cell (694 mV) featuring the same SiN *PassDop* Gen1 rear side. Despite the grid adaptions that had to be made due to the bigger cell area a high J_{sc} of 40.6 mA/cm^2 could be kept as well with the *FF* being determined at 79.3 %. Overall this resulted in a cell efficiency of 22.1 %, which at the time was a record efficiency at Fraunhofer Institute for Solar Energy Systems (Fraunhofer ISE) for large area c-Si based solar cells.

Finally solar cells with contacts structured by Laser Contact Opening (LCO) and plated by nickel and copper were presented as a proof of concept. To investigate the potential and implications of these technologies, a comparison of LCO and Photolithographically defined Contact Opening (PLO) was performed as well as a comparison of TiPdAg with NiCu metallization. For the metallization, ρ_c for both Ni and Ti was found to be approx. 0.4 mΩ cm^2 and therefore only having a minor influence on the series resistance and cell performance. The copper grid was found to have similar grid resistivities as the reference silver grid, thus no significant impact on *FF* was found.
While the cell efficiency for this batch was limited by bulk degradation during the fabrication of the cells (resulting in a significant loss in V_{oc} and J_{sc}) a high *FF* of 80.1 % and a good plating homogeneity indicated the potential of the approach. The good *FF* allowed for a good starting cell efficiency of 21.0 % for the (large area) NiCu-plated *PassDop* cells and thus even with the degraded bulk in the range of typical PERC *p*-type solar cells. Once the process degradation will be removed, it should be possible to once again achieve a V_{oc} in the range of 680 to 690 mV and therefore efficiencies of 22 % or above, as shown previously.

10 Deutsche Zusammenfassung

Das Hauptziel dieser Arbeit war es *PassDop* Schichten für hocheffiziente *n*-Typ Silizium Solarzellen zu entwickeln und charakterisieren. Wichtig ist hierbei, dass diese Schichten – abgeschieden mit der PECVD Technik – sowohl eine gute Oberflächenpassivierung als auch eine gute Dotiereffizienz wärend des Laserdotierprozesses bieten. Als eine Alternative zu dem originalen *PassDop* Ansatz auf Basis von SiC_x:P (SiC *PassDop*) wurde ein Ansatz basierend auf SiN_x:P vorgestellt. Dabei wurden sowohl Varianten für Niedertemperaturmetallisierung wie Plating (SiN *PassDop*) als auch für siebgedruckte Kontakte (feuerstabiles *fPassDop*) entwickelt. Diese neuen Schichten haben den Vorteil nur die Mikrowellenquelle zur Erzeugung des Plasmas zu nutzen und daher mit nicht-stationären Abscheide Methoden besser kompatibel zu sein. Der Effekt der neuen Schichten auf die Formierung der lokalen Hochdotierung (LBSF) wurde detailliert untersucht. Mit den neuen Schichten wurden *n*-Typ Silizium Solarzellen hergestellt um ihre Eignung für Solarzellen zu testen und analysieren.

Kurz zusammengefasst sind die wesentlichen Ergebnisse dieser Arbeit:

1. SiN_x:P kann als Alternative zu SiC_x:P für voll funktionale *PassDop* Schichten verwendet werden
    a) Eine Einzelschicht wurde nur als machbar bestimmt, wenn keine feuerstabile Passivierung benötigt wird
    b) a-Si:P kann als exzellente Dotierschicht verwendet werden, z.B. in SiN_x:P/a-Si:P Schichtstapeln
    c) SiN *PassDop* Gen2 (stabil bis 450 °C): S_{pass} von 2 cm/s (1 Ω cm *n*-Typ) und R_{Sheet} von 25 Ω/sq.
    d) *fPassDop* Gen3: S_{pass} von 6–8 cm/s (1 Ω cm *n*-Typ) nach Feuern (700–850 °C) und R_{Sheet} von 20 Ω/sq.
2. Der Stickstoff in den Schichten hat einen signifikanten Einfluss auf den Laserdotierprozess. Mehr Stickstoff bedeutet:
    a) Reduzierte Dotiereffizienz auf Grund der thermischen Stabilität der Schichten.
    b) Unvollständige Ablatierung.

   c) Rückstände auf der Oberfläche können negativen Einfluss auf die Kontakteigenschaften haben.

3. Jedes Element das in den Schichten oder während des Laserprozesses verfügbar ist kann in das LBSF eingebaut werden.
4. Thermische Behandlung bei 425 °C ist essenziell für geringe Rekombination ams LBSF. $J_{0b,met}$ nach Tempern: ca. 600 fA/cm^2.
5. Herstellung von *fPassDop* Solarzellen mit Siebdruckkontakten mit einer Effizienz von bis zu 20.9 % auf großer Fläche.
6. Erreichen von einer exzellenten Zelleffizienz von 23.5 % auf kleiner Fläche mit aufgedampften Kontakten.
7. Erreichen von 22.1 % Zelleffizienz mit aufgedampften Kontakten und 21 % mit galvanisch aufgebrachten Kontakten auf großer Fläche.

Im Folgenden sind die Resultate detaillierter ausgeführt:
Die Basis für die *PassDop* Entwicklung wurde bereits von Suwito und Jäger aufgestellt [19, 182]. In einem ersten Schritt wurde der ursprüngliche SiC *PassDop* Schichtstapel weiterentwickelt. Das Ziel dieser Entwicklung war eine verbesserte Temperaturstabilität. Dies wurde erreicht indem eine stöchiometrische *Capping* Schicht eingeführt wurde deren Funktion es ist die Ausdiffusion von Wasserstoff zu verhindern oder verlangsamen, wenn der Schichtstapel getempert wird. Mit dieser *Capping* Schicht konnte für SiC *PassDop* Gen2 ein S_{pass} von 1 cm/s nach einer Temperaturbehandlung von einer Stunde bei 400 °C bestimmt werden. Durch Anpassungen in der Schichtdicke der Passivierschicht wurde zudem R_{Sheet} auf 13 Ω/sq reduziert.

Basierend auf SiN_x:P wurde eine Alternative zu SiC_x:P entwickelt. Der Fokus dieser Entwicklung war auf einer Niedertemperaturmetallisierung wie Nickelgalvanik. Es konnte gezeigt werden, das eine Einzelschicht (SiN *PassDop* Gen1) in diesem Fall möglich ist und in einem R_{Sheet} von ca. 33 Ω/sq sowie einem S_{pass} von ca. 2 cm/s resultiert. Diese Passivierung benötigt keinen Temperschritt zur Aktivierung aber ist bei 425 °C stabil, wie es üblicherweise für Al_2O_3 verwendet wird. Nachdem der Prozess für die Einzelschicht etabliert war wurden Schichtstapel basierend auf SiN_x:P als Passivierschicht und a-Si:P als Dotierschicht untersucht. Für diese zweite Generation von SiN *PassDop* wurde festgestellt, dass die Verwendung von a-Si:P als Dotierschicht zu einer Verbesserung der Dotiereffizienz führt und weniger anfällig gegenüber Prozessfluktuationen ist.

Der dritte Ansatz der verfolgt wurde hatte den Fokus auf siebgedruckten Kontakten (auf der Vorderseite). Daher war eine Oberflächenpassivierung Voraussetzung die einen Feuerschritt übersteht. Das war weder für SiC *PassDop* noch für SiN *PassDop* der Fall. Daher wurde eine modifizierte SiN_x:P

Schicht, *fPassDop*, entwickelt, die nach einem Feuerschritt eine gute Oberflächenpassivierung bereitstellt. Für *fPassDop* zeigte sich, dass eine Einzelschicht nicht einfach realisierbar ist, da entweder Kompromisse bei der Oberflächenpassivierung oder bei der Dotiereffizienz eingegangen werden müssten. Stattdessen wurden Schichtstapel aus zwei Schichten als Alternative detaillierter untersucht. Bei diesen Schichtstapeln wurde die Kombination von stickstoffreichem SiN_x:P mit a-Si:P als beste Variante befunden. Mit diesem *fPassDop* Gen3 Stapel konnte ein S_{pass} von 6–8 cm/s nach Feuern bei einer Temperatur von 700–850 °C erreicht werden. Gleichzeitig bewirkt die a-Si:P Schicht ein niedriges R_{Sheet} von 25 Ω/sq. Die anderen beiden untersuchten Varianten (Si-reiches SiN_x:P + N-reiches SiN_x:P sowie N-reiches SiN_x:P + Si-reiches SiN_x:P) konnten entweder keine entsprechende Oberflächenpassivierung bewirken oder waren nicht voll kompatibel mit dem Laserdotierprozess. Durch die Verwendung von a-Si:P als Dotierschicht konnte sowohl für SiN *PassDop* als auch für *fPassDop* eine weitgehende Entkopplung der Oberflächenpassivierung von der Dotiereffizienz erreicht werden.

Zwar kann SiN_x mit Phosphor dotiert werden, allerdings wurde festgestellt, dass die Materialeigenschaften signifikanten Einfluss auf den Laserdotierprozess haben. Insbesondere die thermische Stabilität war problematisch, welche mit steigendem N Inhalt stärker wurde. Auf Grund dieser thermischen Stabilität der SiN_x Schichten funktionierte der Laserdotierprozess am Besten mit Si-reichen Schichten ($n \geq 2.45$). N-reiche Schichten ($n \leq 2.2$) konnten nur dann sehr gute Ergebnisse erzielen, wenn sie in Kombination mit a-Si:P verwendet wurden. War die Laserfluenz niedrig, so führte der Laserprozess zu Überresten der Schicht an der Oberfläche, welche die Kontaktfläche potentiell verringerten. Solch ein Effekt wurde auch schon von Hameiri *et al.* diskutiert [168]. Zudem kann die thermische Stabilität der SiN_x:P Schichten dazu führen, dass Teile der Schichten nicht aufgeschmolzen werden, sondern unter dem Druck der Schmelze abplatzen. Diese Teile können folglich nicht mehr zum Laserdotierprozess beitragen. Dies wurde in Kapitel 6 untersucht. Es konnte gezeigt werden, dass für Laserdotieren aus SiN_x:P Schichten die ersten ≈ 30 nm sehr wichtig sind. Waren diese nicht dotiert, so war eine Verringerung der Phosphordosis im LBSF um einen Faktor von 3.8 im Vergleich zu einer voll dotierten Schicht die Folge. Mit a-Si:P als Dotierschicht war dieser Effekt weniger stark ausgeprägt, allerdings wurde auch in diesem Fall eine Verringerung der Dosis um einen Faktor 1.7 festgestellt.

Eine Konsequenz von zusammengesetzten Schichten wie SiN_x:P oder SiC_x:P in einem Laserdotierprozess ist, dass Elemente und Verunreinigungen, die sich in der Schicht befinden ins LBSF eingebracht werden können. Sowohl für Stickstoff als auch für Kohlenstoff (aus den jeweiligen Schichten) wurden

sehr hohe Konzentrationen (über $1 \times 10^{20}\,\mathrm{cm}^{-3}$) mit SIMS im LBSF nach dem Laserprozess gemessen. Für beide wurde ein signifikanter Einfluss auf die ECV Messung festgestellt, was bedeutet, dass diese Methode nicht geeignet ist um das Dotierprfil für Laserdotieren aus diesen Schichten zuverlässig zu bestimmen. Weiterhin wurde mittels XRD ermittelt, dass die jeweiligen LBSF auch die kristallinen Formen β-SiC und β-Si_3N_4 enthalten. Während für Kohlenstoff – abgesehen von dem Einfluss auf die ECV Messung – kein negativer Einfluss festgestellt wurde, war Stickstoff im LBSF wesentlich kritischer. Hier spielte die Menge an Stickstoff die während dem Laserdotierprozess verfügbar war eine wichtige Rolle. Zusätzlich zur oben angemerkten thermischen Stabilität führte das dazu, dass Hohlräume am Rande des LBSF entstehen können [169], wie es auch für stickstoffreiche Schichtstapel (*fPassDop* Gen2) beobachtet wurde. Auch kann Stickstoff als ein Kandidat für Kristalldefekte gesehen werden. Ein Hinweis auf solche wurde mittels XRD gefunden, wo polykristalline Strukturen im LBSF detektiert wurde. Durch die Si_3N_4 Kristalle, die ebenfalls mittels XRD detektiert wurden könnten zudem Bereiche im LBSF vorhanden sein, die eine niedriegere Leitfähigkeit aufweisen, ein Effekt der bereits von Hameiri *et al.* vorgeschlagen wurde [168].

Nicht nur makroskopische (wie SIMS), sondern auch mikroskopische Methoden zur Bestimmung des Dotierprofils wurden untersucht. Eine Variante von SIMS, hier genannt »3D« SIMS, mit kleinem Messdurchmesser wurde verwendet um in einem Rasterverfahren die Oberfläche abzutasten und somit Informationen über die Verteilung des Dotierstoffs zu erlangen. Mittels dieser Methode konnte gezeigt werden, dass die Oberflächenkonzentration über das LBSF größtenteils konstant ist und, dass hauptsächlich die Tiefe der Profile lokal variiert. Allerdings konnte mit dieser Methode keine Information über Fehlstellen in der Dotierung oder die Randbereiche gewonnen werden, da die Größe der einzelnen Messbereiche sowie deren Überlapp diese Information verschmieren. Als Alternative wurden mikroskopische *Raman* Messungen durchgeführt. Bei dieser Messmethode kann für Silizium die Breite des *Raman* peaks mit der Konzentrationen freier Ladungsträger korreliert werden. Allerdings ist für *n* Dotierung die Sensitivität deutlich geringer als für *p*-Typ [197], weshalb die Methode bei den gegebenen Konzentrationen nicht direkt angewendet werden kann. Stattdessen wurden zwei Methoden getestet bei denen eine kompensierte *p*-Typ Dotierung untersucht wurde. Bei der ersten Methode wurde das *PassDop* LBSF nach dem Laserprozess einer Bordiffusion ausgesetzt. Das Ziel war es zu untersuchen, ob es durch den Phosphor des LBSF zu einem Blockiereffekt kommt, der die Bordiffusion verlangsamt oder stoppt [198]. Hier konnte gezeigt werden, dass das für das *PassDop* LBSF definitiv der Fall war, wobei allerdings Referenzproben für

Phosphor und Stickstoff zeigten, dass beide Elemente die Bordiffusion signifikant hemmen. Es war nicht möglich für die SiN_x:P Schichten zwischen den Blockiereffekten der beiden Elementen zu unterscheiden und daher kann die Methode nicht verwendet werden um ein lokales Phosphorprofil zu extrahieren. Die zweite Methode wendete den *PassDop* Laserprozess auf eine Bordotierung an, welche zuvor mittels Bortiefdiffusion erzeugt wurde. Wieder war es das Ziel eine Kompensation der Bordotierung zu bestimmen. Diese Methode brachte vielversprechende Resultate hervor, allerdings war es auf Grund fehlender Referenzproben und -messungen auch hier nicht möglich die lokalisierte Phosphor zu extrahieren. Allerdings konnten durch diese Methode einige Bereiche am Rande der Laserpunkte aufgedeckt werden, bei welchen die Passivierschicht beschädigt, aber nicht vollständig ablatiert wurde. Nach diesen Messungen scheint in diesen Bereichen keine signifikante Laserdotierung erfolgt zu sein, was zu der Erkenntnis führte, dass der (in Bezug auf die Oberflächenpassivierung) geschädigte Bereich und der dotierte Bereich nicht übereinstimmen.

Die letzte Eigenschaft des LBSF, die untersucht wurde ist die Rekombination an demselben. Hier wurden zwei Modelle verglichen, das Modell nach der Theorie von Fischer [56] und das pLPA Modell [58]. Beide Modelle ergaben ähnliche Resultate für S_{met}, allerdings hatte das p_{LPA} Modell den Vorteil, dass es zwei Parameter definiert, die die LBSF Rekombination charakterisieren, aber nicht (p_{eff}) oder nur schwach (p_{LPA}) vom Durchmesser der Laserpunkte d_{cont} abhängen. Durch Anwendung des p_{LPA} Modells auf SiC und SiN *PassDop* Proben konnte gezeigt werden, dass die Rekombination für SiN *PassDop* am LBSF direkt nach dem Laserprozess signifikant höher ist ($J_{0\mathrm{b,met}}$ im Bereich von 10 000 fA/cm^2). Allerdings profitiert SiN *PassDop* stark davon, wenn die Proben bei Temperaturen $>$ 300 °C getempert werden, was zu einer signifikanten Verringerung der Rekombination am LBSF führte. Der genaue Effekt konnte nicht bestimmt werden, aber es wurde vermutet, dass der Abbau von Spannungen im Kristall sowie Diffusion von Wasserstoff eine wichtige Rolle spielen. Der Effekt war am stärksten, wenn bei einer Temperatur von 425 °C getempert wurde. Nach diesem Temperschritt wurde ein S_{met} im Bereich von 250 cm/s (1 Ω cm *n*-Typ) bestimmt. Das würde einen lokalen Beitrag von $J_{0\mathrm{b,met}}$ von ca. 600 fA/cm^2 und einen Beitrag für die komplette Rückseite von 10–15 fA/cm^2 bedeuten.

Abschließend wurden die entwickelten *PassDop* Schichten auf der Rückseite von *n*-Typ Solarzellen getestet. Für *fPassDop* wurde auch auf dieser Ebene noch ein Test mit einer Einzelschicht durchgeführt, allerdings wurde gezeigt, dass es nicht zu einer zuverlässigen Kontaktausbildung kommt. Bei

den Schichtstapeln konnten mit *fPassDop* Gen3 Solarzellen hergestellt werden, welche siebgedruckte Ag-Al Kontakte auf der Vorderseite verwendeten und eine Zelleffizienz von 20.9 % auf einer Fläche von 148.6 cm^2 erreichten. Die Verwendung von a-Si:P als Dotierschicht erlaubte hier eine Kontaktausbildung mit geringer Variation, was in einem mittleren Füllfaktor von 78.4 % resultierte. Für diese Zellen wurde eine Verlustanalyse durchgeführt, deren Ergebnis es war, dass die Vorderseite die Zellperformance sowohl in Bezug auf die Optik als auch Rekombination weitgehend limitiert. Für eine signifikante Verbesserung wären daher weiterentwickelte Pasten, sowie ein angepasstes Grid und ein angepasster Emitter notwendig, sollte dieser Ansatz weiterverfolgt werden.

Die zweite Route, die verfolgt wurde hatte den Fokus auf Niedertemperaturmetallisierung wie galvanisch aufgebrachter Kontakte. Hier wurden sowohl für SiC *PassDop* Gen2 als auch SiN *PassDop* Gen1 Solarzellen auf kleiner Fläche hergestellt um das Potential des *PassDop* Ansatzes auszutesten. Insbesondere für SiC *PassDop* konnten hier exzellente Ergebnisse erzielt werden, mit einem erreichten Wirkungsgrad von 23.5 % bei einem V_{oc} von 699 mV. Die Einzelschicht SiN *PassDop* Gen1 war mit 22.8 % Wirkungsgrad sowie einem V_{oc} von 694 mV nicht weit zurück. Hierbei konnte gezeigt werden, dass die Unterschiede hauptsächlich auf Unterschiede in der Zellprozessierung, die sich auf die Kurzschlussstromdichte auswirkten, zurückzuführen waren. Allerdings kam ein geringer Unterschied von etwa 0.1 % im Wirkungsgrad im Falle von SiN *PassDop* Gen1 durch eine höhere Rekombination am LBSF zustande. Dies war darauf zurückzuführen, dass die Zellen fertiggestellt wurden bevor der Einfluss des Temperschritts auf die Rekombination am LBSF bekannt war. Vor dem Hintergrund, dass es sich bei SiN *PassDop* um einen neuen Ansatz handelte und, dass die Struktur mit einer einzelnen Schicht wesentlich einfacher ist als bei SiC *PassDop*, sind diese Ergebnisse sehr gut. Auch für diese Zellstruktur wurden Simulationen sowie eine Verlustanalyse durchgeführt. Hier stand insbesondere der Einfluss der LBSF Rekombination in Form von $J_{0b,met}$ im Vordergrund. Mit einem optimierten $J_{0b,met}$ von etwa 600 fA/cm^2 (wie zuvor in Kapitel 7 bestimmt) wäre der Beitrag der Rückseite sehr klein gewesen und V_{oc} im Bereich von 700 mV.

Nachdem SiN *PassDop* erfolgreich in Solarzellen getestet wurde wurde ein Transfer auf große Flächen angestrebt. Zunächst wurde eine Zellstruktur definiert, welche weiterhin aufgedampfte Saatschichten verwendete. Zwar konnte auf dem vorhandenen Zellprozess aufgebaut werden, allerdings mussten die Prozessequenz sowie einige Prozesse angepasst und getestet werden. Mit dieser neuen Zellstruktur wurden hohe Offenklemmspannungen im Be-

reich von 690 mV erzielt, wobei die Solarzelle mit der besten Offenklemmspannung von 692 mV sehr nahe an den zuvor hergestellten Solarzellen auf kleiner Fläche war (V_{oc} von 694 mV). Trotz der notwendigen Anpassungen im Grid konnte zudem eine hohe Kurzschlussstromdichte von 40.6 mA/cm^2 sowie ein hoher Füllfaktor von 79.3 % erreicht werden. Das führte zu einem Zellwirkungsgrad von 22.1 %, was zu dem Zeitpunkt ein Rekord am Fraunhofer ISE für großflächige, kristalline Siliziumsolarzellen war.

Abschließend wurden ähnliche Solarzellen hergestellt, wobei die Vorderseitenöffnung hier mittels Laser durchgeführt wurde. Die Metallisierung der Vorderseite erfolgte durch Galvanik von Nickel und Kupfer. Um das Potential sowie die Implikationen dieser Technologie im Vergleich zu den bisher verwendeten Technologien abschätzen zu können wurde ein Vergleichstest auf Solarzellen durchgeführt. Hier konnte gezeigt werden, dass der Kontaktübergangswiderstand für Nickel und Titan auf Boremitter bei jeweils 0.4 mΩ cm^2 liegt. Das Kupfergrid zeigte ähnliche Leitfähigkeit wie ein entsprechendes Silbergrid und auch bei der Laseröffnung konnte keine erhöhte Rekombination gegenüber photolithographisch geöffneten Kontakten festgestellt werden. Wenngleich der Wirkungsgrad der Solarzellen in diesem Fall durch eine Degradation des Siliziums im Prozess limitiert wurde, was sich in einem signifikanten Verlust in V_{oc} und J_{sc} wiederspiegelte, deuteten ein hoher Füllfaktor von 80.1 % und eine gute Homogenität der geplateten Kontakte das Potential dieses Ansatzes an. Der gute Füllfaktor führte dazu, dass die initiale Effizienz dieser neuen Solarzellenstruktur mit galvanischen Ni-/Cu-Kontakten immerhin noch bei 21.0 % lag und damit auf einem Level zu typischen PERC *p*-Typ Solarzellen. Sobald diese Degradation im Prozess entfernt wurde sollte es möglich sein mit diesen Solarzellen ein V_{oc} im Bereich von 680 bis 690 mV zu erreichen, was zu Wirkungsgraden von 22 % und höher führen wird.

11 Outlook

While significant progress in the development of *PassDop* layers and *PassDop* cells was made, it is an ongoing process. Therefore there are some aspects with respect to *PassDop* layers and cells that should be implemented in the future or possibly even were at the time of this writing. Most of these aspects were inspired by this work.

In chapter 6 it was shown that a-Si:P can be used as an excellent *Doping* layer in combination with SiN_x:P *Passivation* layers. However using such a layer can have a negative side effect as well due to the conductivity of a-Si:P. This was observed on Ni-plated solar cells where the conductivity of the a-Si:P led to shunts at the wafer edge, as this layer is deposited both on the rear and on the edge. This was solved by adding a touch of nitrogen to the layer (thus a very Si-rich SiN_x:P layer). Enough to reduce the conductivity to a minimum, but not too much to reduce the doping efficiency.

For *fPassDop*, the use of the a-Si:P *Doping* layer led to such a significant improvement in the doping efficiency that experiments with contacting the LBSF using screen printing became feasible. It was shown that with silver pastes a specific contact resistivity in the range of $1\,\Omega\,cm^2$ can be achieved [154]. While it was not yet possible to demonstrate this at the device level, it would be interesting to show that *fPassDop* cells can be fabricated making the use of screen printed contacts both on the front and on the rear.

In chapter 7 it was shown that annealing of the LBSF results in significantly reduced recombination at the LBSF. At the device level, it was not possible at the time to show this, but the cell simulations shown in chapter 8 indicated that in such a case a significant improvement in V_{oc} could be achieved, especially in combination with a selective emitter. To prove this and to further evaluate the potential of the SiN *PassDop* Gen2 approach, such solar cells are currently in the making, featuring a selective emitter and improved front side optics.

In chapter 8, solar cells were presented that featured LCO and NiCu plated contacts. Due to bulk degradation, these solar cells were not able to achieve

the same performance as the reference batch. The source of this bulk degradation was found and prevented, which allowed for a significantly improved performance allowing LCO/NiCu to close this gap and leading to a new record cell efficiency of 22.2 % (calibrated measurement by Fraunhofer ISE CalLab) for large area silicon solar cells at Fraunhofer ISE.

The ultimative objective is not to fabricate »only« solar cells, but solar cell modules. Therefore the rear side has to be compatible with module technology and all of the layers have to show good adhesion after soldering. Here, some approaches are being investigated to contact the rear side aluminum [221] yielding promising results. However, due to low adhesion, the MgF_2 layer should not be used when fabricating modules. As an alternative, SiO_2 would be desirable and with this layer the adhesion was found to be good. However, it was shown by Suwito [143] that SiO_2 is not compatible with the laser doping process due to its thermal stability and elasticity. As a workaround, experiments are ongoing to determine if the remnants of the SiO_2 can be removed using lowly concentrated HF without removing the complete layer. While there are promising results it is not clear if a stable process can be found. Still, good *FF* above 80 % were already observed when using SiO_2 as an *Optical* layer on the rear. Solar cells for module tests featuring this approach are currently in the making.

Glossary

Notion	Description
4pp	4-point probes
AC	Alternating Current
accumulation	Surface state in which the majority carriers are »accumulated« at the surface resulting in a depletion of the minority carriers
ALD	Atomic Layer Deposition
AM1.5	Solar spectrum with air mass 1.5, thus an incident angle of 48°
ARC	Anti-Reflective Coating
BB	Bus Bar
BSF	Back-Surface-Field
CalLab	Institution at Fraunhofer ISE for calibrated *JV* and *SR* measurements
COCOS	Corona Oxide Characterization Of Semiconductor
CV	Capacitance-Voltage measurement, e.g. of a *pn*-junction
CVD	Chemical Vapour Deposition
CW	Continuous Wave
Cz	Czochralski-grown material
dangling bonds	Unsaturized bonds that can be responsible for increased recombination
DARC	Double Layer Anti-Reflective Coating
DLIT	Dark Lock-In Thermography
ECV	Electrochemical Capacitance-Voltage Profiling
EDNA	Freeware 1D emitter model for silicon solar cells

Notion	Description
EDX	Energy-Dispersive X-Ray spectroscopy
EQE	External Quantum Efficiency
FCA	Free-Carrier Absorption
FELA	Free Energy Loss Analysis
FFO	Fast Firing Oven
FGA	Forming Gas Anneal
Fraunhofer ISE	Fraunhofer Institute for Solar Energy Systems
FT-IR	Fourier-Transformed Infrared Spectroscopy
FZ	Floatzone
Hall	Hall Measurement
HF	Hydrofluoric Acid
HIT	Hetero junction solar cell featuring an thin intrinsic passivation layer
HNO_3	Nitric Acid
IBC	Interdigitated Back-Contact
inversion	Surface state in which the majority carriers are »depleted« from the surface resulting in a doping inversion
IQE	Internal Quantum Efficiency
JV	Current-Voltage measurement of the solar cell
LBSF	Local Back Surface Field
LCO	Laser Contact Opening
LEXT	Laser Excitation Microscope
LFC	Laser Fired Contacts
LID	Light Induced Degradation
LPA	Locally Processed Area
Micro-PL	Microscopic Photoluminescence
Micro-Raman	Microscopic *Raman*
modPL	modulated Photoluminescence
mpp	Maximum Power Point
MW	Microwave
nPERT	*n*-type PERT
NREL	National Renewable Energy Laboratory
OC	Open Circuit

Notion	Description
PECVD	Plasma-Enhanced Chemical Vapor Deposition
PERC	Passivated Emitter and Rear Cell
PERL	Passivated Emitter and Rear Locally Diffused
PERT	Passivated Emitter and Rear Totally Diffused
PL	Photoluminescence
PLO	Photolithographically defined Contact Opening
pLPA	Model describing the recombination at a "Locally Processed Area"
pn	Interfacing areas with opposite doping
PV Lighthouse	See https://pvlighthouse.com.au/
PVD	Physical Vapour Deposition
QE	Quantom Efficiency
QSSPC	Quasi-Steady-State Photoconductance
Quokka	3D solar device simulator based on the conductive boundary approach
Raman	Raman Spectroscopy
RCA	Standard cleaning sequence as defined by the Radio Corporation of America
RF	Radio Frequency
R_S-Imaging	R_S imaging based on multiple images taken by photoluminescence
SARC	Single Layer Anti-Reflective Coating
Schottky	A Schottky diode describes the interface of a semiconductor and a metal with non-matching work function resulting in a depletion of the majority carriers and therefore in a diode behavior.
SEM	Scanning Electron Microscope
Sentaurus Device	Semiconductor simulation program [222]
SIMS	Secondary Ion Mass Spectrometry
SR	Spectral Response measurement to determine the External Quantum Efficiency (EQE)
SRH	Shockley-Read-Hall
SRP	Spreading Resistance Profiling

Notion	Description
Suns-V_{oc}	SunsVoc measurement
TLM	Transfer-Length Measurement
TOPCon	Tunnel Oxide Passivated Contact, a concept for full area selective contacts
XRD	X-Ray Diffraction

Symbols

Symbol	Unit	Description
A	cm^2	Area of the measurement spot
α_0		Implicit parameter for the surface recombination model
A_{LPA}	cm^2	Area of Locally Processed Area (LPA)
A_{pass}	cm^2	Area of the passivated surface
B_{low}	$cm^{-3}\,s^{-1}$	Coefficient for the radiative recombination for low dopant concentrations
B_{rad}	$cm^{-3}\,s^{-1}$	Coefficient for the radiative recombination
B_{rel}	$cm^{-3}\,s^{-1}$	Rel coefficient of the radiative recombination to account for coulomb screening
C	F	Capacitance
C_n		Coefficient for the Auger recombination
C_p		Coefficient for the Auger recombination
D	cm^2/s	Diffusivty
δ	cm^{-3}	Difference of the electron (ECV) and phosphorous concentration (SIMS)
d_{cont}	µm	Diameter of the laser spot
ΔG	$cm^{-3}\,s^{-1}$	Excess generation rate
ΔFF		Difference of FF-$PFF \propto R_S$
D_{it}	$cm^{-2}\,eV^{-1}$	Surface defect density
Δn	cm^{-3}	Excess carrier density
Δp	cm^{-3}	Excess carrier density
$\Delta\sigma$	$\Omega^{-1}\,cm^{-1}$	Excess conductivity
E_c	eV	Energy of the conductance band
E_t	eV	Energy level of a trap/defect
E_f	eV	Fermi energy
E_{fc}	eV	Quasi Fermi energy for the conductance band

Symbol	Unit	Description
E_{fv}	eV	Quasi Fermi energy for the valence band
E_g	eV	Width of the bandgap
E_λ	eV	Photon energy
ϵ_r		Relative permittivity
η		Efficiency
E_v	eV	Energy of the valence band
FF		Fill factor of the solar cell
FF_0		The theoretical maximum of FF as determined by Green *et al.*
f_{met}	%	Fraction of the contacted area
$f_{met,FS}$	%	Fraction of the contacted area on the front
$f_{met,RS}$	%	Fraction of the contacted area on the rear
G_0	$cm^{-3}\ s^{-1}$	Generation rate at thermal equilibrium
g_{eeh}		Auger coulomb enhancement factor
g_{ehh}		Auger coulomb enhancement factor
J_{02}	$A\ cm^{-2}$	Reverse/dark saturation current density of the second diode with n=2
J_{sc}	$A\ cm^{-2}$	Short-circuit current density
J	$A\ cm^{-2}$	Terminal current density of the device
J_0	$fA\ cm^{-2}$	Saturation current density
J_{0b}	$fA\ cm^{-2}$	Base saturation current density
$J_{0b,met}$	fA/cm^2	Saturation current density contribution of the emitter contacts
$J_{0b,pass}$	fA/cm^2	Saturation current density contribution of the passivated rear side surface
J_{0e}	$fA\ cm^{-2}$	Emitter saturation current density
$J_{0e,met}$	fA/cm^2	Saturation current density contribution of the rear side contacts
$J_{0e,pass}$	fA/cm^2	Saturation current desity contribution of the passivated emitter
J_{0s}	$fA\ cm^{-2}$	Surface saturation current density
j_{eff}	$A\ cm^{-2}$	Effective recombination current for the rear side
J_{gen}	mA/cm^2	The generated photo-current excluding metal shading

Symbol	Unit	Description
J_{inc}	A cm^{-2}	Incident illumination current density
j_{LPA}	A cm^{-2}	Recombination current at the LPA
J_{mpp}	A cm^{-2}	Current Density at MPP
j_{pass}	A cm^{-2}	Recombination current at the passivated surface
k		Extinction coefficient
k		Segregation coefficient
L	cm	(Minority Carrier) Diffusion length
L_n	m	Diffusion length for electrons
L_p	m	Diffusion length for holes
n		Ideality factor to account for injection dependent effects
n	cm^{-3}	Electron concentration
n		Refractive index
n_0	cm^{-3}	Electron concentration at thermal Equilibrium
n_1	cm^{-3}	electron concentration of the Shockley-Read-Hall (SRH) model
N_c	cm^{-3}	Conduction band state density
N_D	cm^{-3}	Donor concentration
N_{ECV}	cm^{-3}	Electron concentration determined by ECV
n_{eff}	cm^{-3}	Effective carrier concentration
$n_{i,eff}$	cm^{-3}	Intrinsic carrier concentration
N_{LPA}	cm^{-2}	Density of the LPA
n_{LPA}	cm^{-3}	Average excess carrier density at the LPA
n_{pass}	cm^{-3}	Average excess carrier density at passivated surface
N_{peak}	cm^{-3}	Maximum concentration of a doping profile
n_s	cm^{-2}	Surface recombination density for electrons
N_{SIMS}	cm^{-3}	Phosphorous concentration determined by SIMS
N_t	cm^{-3}	Defect density
v_{th}	cm/s	Thermal velocity for charge carriers
N_v	cm^{-3}	Valence band state density

Symbol	Unit	Description
ω_0	µm	Minimum width of the gaussian laser beam
P	W cm^{-2}	Terminal output power density of the device
p	Pa	Pressure during the deposition
p	cm^{-3}	Hole concentration
p_0	cm^{-3}	Hole concentration at thermal Equilibrium
p_1	cm^{-3}	hole concentration of the SRH model
p_d	µm	Laser pulse distance
p_eff	cm^3/s	Recombination parameter for the "Laser Processed Area" Model for the complete processed area
PFF		Pseudo fill factor of the solar cell
ϕ	J/cm^2	Laser fluence
P_inc	W cm^{-2}	Incident illumination power density
p_LPA	cm^3/s	Point recombination for the "Laser Processed Area" Model
P_mpp	W cm^{-2}	Terminal output power density of the device at maximum power point
p_s	cm^{-2}	Surface recombination density for holes
Q_f	cm^{-2}	Fixed charge density
R_0	cm^{-3} s^{-1}	Recombination rate at thermal equilibrium
R_Auger	cm^{-3} s^{-1}	Auger recombination rate
ρ_b	Ω cm	Base resistivity
ρ_c	Ω cm^2	Specific contact resistivity
r_cont	µm	Radius of the laser spot
R_diff	A^{-1} cm^{-1}	Diffusion resistance
r_diff	s cm^{-2}	Normalized diffusion resistance
R_eeh	cm^{-3} s^{-1}	Auger recombination rate for the electron-electron-hole process
R_ehh	cm^{-3} s^{-1}	Auger recombination rate for the electron-hole-hole process
R_P	Ω	Parallel resistance
R_rad	cm^{-3} s^{-1}	Radiative recombination rate
R_S	Ω	Series resistance
R_s	cm^{-2} s^{-1}	Surface recombination rate

Symbol	Unit	Description
R_{Sheet}	Ω	Sheet resistance
R_{spr}	m^{-1}	Spreading resistance
R_{SRH}	$\mathrm{cm}^{-3}\,\mathrm{s}^{-1}$	SRH recombination rate
S	$\mathrm{cm\,s}^{-1}$	Surface recombination velocity
σ	%	Overlap of the laser spots
S_1	$\mathrm{cm\,s}^{-1}$	Surface recombination velocity of the first surface
S_2	$\mathrm{cm\,s}^{-1}$	Surface recombination velocity of the second surface
S_{cont}	$\mathrm{cm\,s}^{-1}$	Contact recombination velocity
S_{eff}	$\mathrm{cm\,s}^{-1}$	Effective surface recombination velocity
σ	$\Omega^{-1}\,\mathrm{cm}^{-1}$	Conductivity
σ_{n}	cm^2	Cross-section for electrons
σ_{p}	cm^2	Cross-section for holes
S_{met}	$\mathrm{cm\,s}^{-1}$	Recombination velocity at the contact interface
$S_{\mathrm{met,max}}$	$\mathrm{cm\,s}^{-1}$	Recombination velocity at the contact interface
$S_{\mathrm{met,min}}$	$\mathrm{cm\,s}^{-1}$	Recombination velocity at the contact interface
S_{n}	$\mathrm{cm\,s}^{-1}$	Electron surface recombination velocity
S_{p}	$\mathrm{cm\,s}^{-1}$	Hole surface recombination velocity
S_{pass}	$\mathrm{cm\,s}^{-1}$	Recombination velocity at the passivated surface
sp_{eff}	cm^3/s	Uncertainty of p_{eff}
sp_{LPA}	cm^3/s	Uncertainty of p_{LPA}
sr_{cont}	µm	Uncertainty of r_{cont}
sr_{diff}	$\mathrm{s\,cm}^{-2}$	Uncertainty of r_{diff}
sS_{met}	$\mathrm{cm\,s}^{-1}$	Uncertainty of Smet
T	K	Temperature
t	s	Time
τ	s	Minority carrier lifetime
τ_{b}	s	Bulk lifetime
τ_{eff}	s	Effective minority carrier lifetime

Symbol	Unit	Description
τ_{intr}	s	Minority carrier lifetime including Auger and radiative recombination
τ_{n0}	s	Electron lifetime in SRH trap
τ_{p0}	s	Hole lifetime in SRH trap
τ_s	s	Surface lifetime
τ_{SRH}	s	Effective SRH lifetime
T_{dep}	℃	Set deposition temperature
T_{max}	℃	Maximum process temperature
R	$cm^{-3}\,s^{-1}$	Excess recombination rate
V	V	Terminal voltage of the device
V_{fb}	V	Flat-Band voltage
V_{mpp}	V	Voltage at MPP
V_{oc}	V	Open-circuit voltage
v_{oc}		Normalized voltage V_{oc}/U_T
W	cm	Wafer thickness
ξ		Quotient of the electron (ECV) and phosphorous concentration (SIMS)
x_{scr}	m	Depth of the edge of the space charge region
Z		Pathlength enhancement. Effective optical "thickness"
z_F	µm	Depth factor for a Gaussian profile

Constants

Symbol	Value	Description
e	$2.718\ldots$	Base of the natural logarithm
ϵ_0	$8.85 \times 10^{-12}\,\mathrm{A\,s\,V^{-1}\,m^{-1}}$	Vacuum Permittivity
$\epsilon_{\mathrm{r,Si}}$	11.68	Relative permittivity of silicon
k_B	$8.617 \times 10^{-5}\,\mathrm{eV\,K^{-1}}$	Boltzmann constant
$N_{0,\mathrm{eeh}}$	$3.3 \times 10^{17}\,\mathrm{cm^{-3}}$	
$N_{0,\mathrm{ehh}}$	$7.0 \times 10^{17}\,\mathrm{cm^{-3}}$	
q	$1.6 \times 10^{-19}\,\mathrm{C}$	Elementary charge
U_T	25.7 mV@298 K	Thermal Voltage

List of Publications

Journal Publications

- P. Repo, J. Benick, V. Vähänissi, J. Schön, G. v. Gastrow, B. Steinhauser, M. C. Schubert, M. Hermle and H. Savin. n-type black silicon solar cells. *Energy Procedia*, 38: 866-871, 2013.
- B. Steinhauser, M. bin Mansoor, U. Jäger, J. Benick and M. Hermle. Firing-stable PassDop passivation for screen printed n-type PERL solar cells based on a-SiN_x:P. *Solar Energy Materials & Solar Cells*, 126: 96-100, 2014.
- B. Steinhauser, U. Jäger, J. Benick and M. Hermle. PassDop rear side passivation based on Al2O3/a-SiC_x:B stack for p-type PERL solar cells. *Solar Energy Materials & Solar Cells*, 131: 129-133, 2014.
- J. Bartsch, M. Kamp, D. Hartleb, C. Wittich, A. Mondon, B. Steinhauser, F. Feldmann, A. Richter, J. Benick and M. Glatthaar. 21.8% efficient n-type solar cells with industrially feasible plated metallization. *Energy Procedia*, 55: 400-409, 2014.
- T. Rachow, N. Milenkovic, B. Steinhauser, J. Benick, S. Janz, M. Hermle and S. Reber. Solar cells with epitaxial or gas phase diffused emitters above 21% efficiency. *Energy Procedia*, 77:540-545, 2015.
- B. Steinhauser, U. Jäger, J. Benick, E. Chong, J. Lam, R. Steeman, H. Rostan, J. Nekarda, M. Hermle, R. Preu and S.W. Glunz. The influence of nitrogen on laser doping from phosphorous doped a-SiN_x layers. *Solar Energy Materials & Solar Cells*, 157: 295-304, 2016.
- B. Steinhauser, M. Kamp, A.A. Brand, U. Jäger, J. Bartsch, J. Benick and M. Hermle. High-efficiency n-type silicon solar cells: Advances in PassDop technology and NiCu plating on boron emitter. *IEEE Journal of Photovoltaics*, 6(2): 419-425, 2016.

Diploma Thesis

- B. Steinhauser. *Entwicklung von a-SixC1-x Schichtsystemen für die Solarzellenvorderseite.* Diplomarbeit, Universität Freiburg, 2010.

In Conference Proceedings

- B. Steinhauser, D. Suwito, S. Janz and M. Hermle. Stacks of a-SiC_x layers on planar and textured surfaces for the solar cell front side on both n^+ and p^+ emitters. In *25th EU PVSEC 2010*, pages 2250-2254, 2010.
- U. Jäger, A. Wolf, B. Steinhauser, J. Benick, J. Nekarda and R. Preu. Laser doping for high-efficiency silicon solar cells. In *Proc. SPIE 8473*, pages 847309-847312, 2012.
- B. Steinhauser, M. bin Mansoor, U. Jäger, J. Benick and M. Hermle. PassDop based on firing stable a-SiN_x:P as a concept for the industrial implementation of n-type PERL silicon solar cells. In *28th EU PVSEC 2013*, pages 722-726, 2013.
- T. Rachow, N. Milenkovic, F. Heinz, M. Breitwieser, B. Steinhauser, S. Janz and S. Reber. Potential and limitations of epitaxial emitters. In *28th EU PVSEC 2013*, 2013.
- J. Benick, B. Steinhauser, R. Müller, J. Bartsch, M. Kamp, A. Mondon, A. Richter, M. Hermle and S.W. Glunz. High efficiency n-type PERT and PERL solar cells. In *40th IEEE Photovoltaic Specialists Conference 2014*, pages 3637-3640, 2014.
- A. Mondon, J. Bartsch, M. Kamp, A.A. Brand, B. Steinhauser, N. Bay, J. Horzel, M. Glatthaar and S.W. Glunz. Plated nickel-copper contacts on c-Si. From microelectronic processing to cost effective silicon solar cell production. In *29th EU PVSEC 2014*, pages 1286-1291, 2014.
- U. Jäger, B. Steinhauser, J. Benick, E. Chong, J. Lam, R. Steeman, H. Rostan, J. Nekarda and M. Hermle. Industrial n-type PERL cells with screen printed front side electrodes approaching 21% efficiency. In *29th EU PVSEC 2014*, pages 390-393, 2014.

Oral Presentations

- B. Steinhauser, M. bin Mansoor, U. Jäger, J. Benick and M. Hermle. Firing stable PassDop layer based on doped amorphous SiN_x. *3rd nPV Workshop.* Chambéry, France, 2013.

- B. Steinhauser, M. bin Mansoor, U. Jäger, J. Benick and M. Hermle. PassDop based on firing stable a-SiN$_x$:P as a concept for the industrial implementation of n-type PERL silicon solar cells. *28th EU PVSEC 2013*. Paris, France, 2013.
- B. Steinhauser, U. Jäger, J. Benick and M. Hermle. PassDop rear side passivation based on Al2O3/a-SiC$_x$:B stack for p-type PERL solar cells. *4th International Conference on Crystalline Silicon Photovoltaics*, 's-Hertogenbosch, Netherlands, 2014.
- B. Steinhauser, M. Kamp, A.A. Brand, J. Bartsch, H. Nagel, J. Benick and M. Hermle. NiCu plating for n-type solar cells – avoiding Voc losses due to screen printing. *5th nPV Workshop*. Konstanz, Germany, 2015.

Poster Presentations

- B. Steinhauser, D. Suwito, S. Janz and M. Hermle. Stacks of a-SiC$_x$ layers on planar and textured surfaces for the solar cell front side on both n$^+$ and p$^+$ emitters. *25th EU PVSEC 2010*. Valencia, Spain, 2010.
- B. Steinhauser, M. Rüdiger, U. Jäger, J. Benick and M. Hermle. Optimization of local BSF formation for n-type silicon solar cells allowing wide base resistivity variation. *2nd International Conference on Crystalline Silicon Photovoltaics*. Leuven, Belgium, 2012.

Bibliography

[1] D. M. Chapin, C. S. Fuller, and G. L. Pearson. A new silicon p-n junction photocell for converting solar radiation into electrical power. *Journal of Applied Physics*, 25(5):676, 1954. ISSN 00218979. doi:10.1063/1.1721711.

[2] M. A. Green, K. Emery, Y. Hishikawa, W. Warta, and E. D. Dunlop. Solar cell efficiency tables (version 46). *Progress in Photovoltaics: Research and Applications*, 23(7):805–812, 2015. ISSN 10627995. doi:10.1002/pip.2637.

[3] D. Macdonald and L. J. Geerligs. Recombination activity of interstitial iron and other transition metal point defects in p- and n-type crystalline silicon. *Applied Physics Letters*, 85(18):4061–4063, 2004. ISSN 00036951. doi:10.1063/1.1812833].

[4] H. Fischer and W. Pschunder. Investigation of photon and thermal induced changes in silicon solar cells. In *10th IEEE Photovoltaic Specialists Conference Palo Alto*, pages 404–411, 1973.

[5] S. W. Glunz, S. Rein, J. Y. Lee, and W. Warta. Minority carrier lifetime degradation in boron-doped czochralski silicon. *Journal of Applied Physics*, 90(5):2397, 2001. ISSN 00218979. doi:10.1063/1.1389076.

[6] S. Wilking, S. Ebert, A. Herguth, and G. Hahn. Influence of hydrogen effusion from hydrogenated silicon nitride layers on the regeneration of boron-oxygen related defects in crystalline silicon. *Journal of Applied Physics*, 114(19):194512, 2013. ISSN 00218979. doi:10.1063/1.4833243.

[7] M. Taguchi, K. Kawamoto, S. Tsuge, T. Baba, H. Sakata, M. Morizane, K. Uchihashi, N. Nakamura, S. Kiyama, and O. Oota. Hittm cells?high-efficiency crystalline si cells with novel structure. *Progress in Photovoltaics: Research and Applications*, 8(5):503–513, 2000. ISSN 1099-159X. doi:10.1002/1099-159X(200009/10)8:5.

[8] K. Masuko, M. Shigematsu, T. Hashiguchi, D. Fujishima, M. Kai, N. Yoshimura, T. Yamaguchi, Y. Ichihashi, T. Mishima, N. Matsubara, T. Yamanishi, T. Takahama, M. Taguchi, E. Maruyama, and S. Okamoto. Achievement of more than 25 % conversion efficiency with crystalline silicon heterojunction solar cell. *IEEE Journal of Photovoltaics*, 4(6):1433–1435, Nov 2014. ISSN 2156-3381. doi:10.1109/JPHOTOV.2014.2352151.

[9] D. D. Smith, P. J. Cousins, A. Masad, S. Westerberg, M. Defensor, R. Ilaw, T. Dennis, R. Daquin, N. Bergstrom, A. Leygo, X. Zhu, B. Meyers, B. Bourne, M. Shields, and D. Rose. Sunpower's maxeon gen iii solar cell: High efficiency and energy yield. In *39th IEEE Photovoltaic Specialists Conference Tampa*, pages 908–913, 2013. doi:10.1109/pvsc.2013.6744291.

[10] F. Feldmann, M. Bivour, C. Reichel, H. Steinkemper, M. Hermle, and S. W. Glunz. Tunnel oxide passivated contacts as an alternative to partial rear contacts. *Solar Energy Materials and Solar Cells*, 131:46–50, 2014. ISSN 0927-0248. doi:10.1016/j.solmat.2014.06.015.

[11] A. Richter, J. Benick, A. Kalio, J. Seiffe, M. Hörteis, M. Hermle, and S. W. Glunz. Towards industrial n-type pert silicon solar cells: rear passivation and metallization scheme: Rear passivation and metallization scheme. *Energy Procedia*, 8:479–486, 2011. doi:10.1016/j.egypro.2011.06.169.

[12] E. Lohmüller, S. Werner, J. Schön, M. Thanasa, S. Mack, W. Wolke, A. Wolf, F. Clement, and D. Biro. Depletion of boron-doped surfaces protected with barrier layers during pocl3-diffusion. In *28th European Photovoltaic Solar Energy Conference*, pages 1043–1047, 2013.

[13] A. Lanterne, S. Gall, Y. Veschetti, R. Cabal, M. Coig, F. Miléši, and A. Tauzin. High efficiency fully implanted and co-annealed bifacial n-type solar cells. *Energy Procedia*, 38:283–288, 2013. doi:10.1016/j.egypro.2013.07.279.

[14] S. Goda. Cell mass production and array field demonstration of n-type bifacial 'earthon'. Presentation at the nPV workshop 2014, 's-Hertogenbosch, Nederlands, 2014.

[15] S. H. Yu, C. J. Huang, P. T. Hsieh, H. C. Chang, W. C. Mo, Z. W. Peng, C. W. Lai, and C. C. Li. 20.63 % npert cells and 20% pr gain bifacial module. In *2014 IEEE 40th Photovoltaic Specialist Conference (PVSC)*, pages 2134–2137, June 2014. doi:10.1109/PVSC.2014.6925347.

[16] T. Dullweber and J. Schmidt. Industrial silicon solar cells applying the passivated emitter and rear cell (perc) concept – a review. *IEEE Journal of Photovoltaics*, PP(99):1–16, 2016. ISSN 2156-3381. doi:10.1109/JPHOTOV.2016.2571627.

[17] J. M. Fairfield and G. H. Schwuttke. Silicon diodes made by laser irradiation. *Solid-State Electronics*, 11(12):1175–1176, 1968. ISSN 0038-1101. doi:10.1016/0038-1101(68)90008-7.

[18] E. Schneiderlöchner, R. Preu, R. Lüdemann, S. W. Glunz, and G. Willeke. Laser-fired contacts (lfc). In *17th European Photovoltaic Solar Energy Conference*, pages 1303–1306, 2001.

[19] D. Suwito, U. Jäger, J. Benick, S. Janz, M. Hermle, and S. W. Glunz. Industrially Feasible Rear Passivation and Contacting Scheme for High-Efficiency n-Type Solar Cells Yielding a V_{OC} of 700 mV. *IEEE Transactions on Electron Devices*, 57(8):2032–2036, 2010. doi:10.1109/TED.2010.2051194.

[20] M. A. Green. *High efficiency silicon solar cells.* Materials Science Surveys. Trans Tech Publications, Kensington, 1987. ISBN 0-87849-537-1.

[21] W. Shockley. The theory of p-n junctions in semiconductors and p-n junction transistors. *Bell System Technical Journal*, 28(3):435–489, 1949. doi:10.1002/j.1538-7305.1949.tb03645.x.

[22] H. Schlangenotto, H. Maeder, and W. Gerlach. Temperature dependence of the radiative recombination coefficient in silicon. *physica status solidi (a)*, 21(1):357–367, 1974. ISSN 18626300. doi:10.1002/pssa.2210210140.

[23] P. P. Altermatt, F. Geelhaar, T. Trupke, X. Dai, A. Neisser, and E. Daub. Injection dependence of spontaneous radiative recombination in crystalline silicon: Experimental verification and theoretical analysis: Experimental verification and theoretical analysis. *Applied Physics Letters*, 88(26):261901, 2006. ISSN 00036951. doi:10.1063/1.2218041.

[24] A. R. Beattie and P. T. Landsberg. Auger effect in semiconductors. *Proceedings of the Royal Society A: Mathematical, Physical and Engineering Sciences*, 249(1256):16–29, 1959. ISSN 1364-5021. doi:10.1098/rspa.1959.0003.

[25] Pierre Auger, P. Ehrenfest, R. Maze, J. Daudin, and Robley A. Fréon. Extensive cosmic-ray showers. *Rev. Mod. Phys.*, 11:288–291, Jul 1939. doi:10.1103/RevModPhys.11.288.

[26] J. Dziewior and W. Schmid. Auger coefficients for highly doped and highly excited silicon. *Applied Physics Letters*, 31(5):346–348, 1977. ISSN 00036951. doi:10.1063/1.89694.

[27] A. Hangleiter and R. Häcker. Enhancement of band-to-band auger recombination by electron-hole correlations. *Phys. Rev. Lett.*, 65:215–218, Jul 1990. doi:10.1103/PhysRevLett.65.215.

[28] A. Haug. Carrier density dependence of auger recombination. *Solid-State Electronics*, 21(11-12):1281–1284, 1978. ISSN 0038-1101. doi:10.1016/0038-1101(78)90193-4.

[29] P. P. Altermatt, J. Schmidt, G. Heiser, and A. G. Aberle. Assessment and parameterisation of coulomb-enhanced auger recombination coefficients in lowly injected crystalline silicon. *Journal of Applied Physics*, 82(10):4938–4944, 1997. ISSN 00218979. doi:10.1063/1.366360.

[30] J. Schmidt, M. Kerr, and P. P. Altermatt. Coulomb-enhanced auger recombination in crystalline silicon at intermediate and high injection densities. *Journal of Applied Physics*, 88(3):1494–1497, 2000. ISSN 00218979. doi:10.1063/1.373878.

[31] R. A. Sinton and R. M. Swanson. Recombination in highly injected silicon. *IEEE Transactions on Electron Devices*, 34(6):1380–1389, Jun 1987. ISSN 0018-9383. doi:10.1109/T-ED.1987.23095.

[32] S. W. Glunz, D. Biro, S. Rein, and W. Warta. Field-effect passivation of the sio2si interface. *Journal of Applied Physics*, 86(1):683–691, 1999. ISSN 00218979. doi:10.1063/1.370784.

[33] M. J. Kerr and A. Cuevas. General parameterization of auger recombination in crystalline silicon. *Journal of Applied Physics*, 91(4):2473, 2002. ISSN 00218979. doi:10.1063/1.1432476.

[34] A. Richter, S. W. Glunz, F. Werner, J. Schmidt, and A. Cuevas. Improved quantitative description of auger recombination in crystalline silicon. *Physical Review B*, 86(16):1–14, 2012. ISSN 0163-1829. doi:10.1103/PhysRevB.86.165202.

[35] T. Trupke, M. A. Green, P. Würfel, P. P. Altermatt, A. Wang, J. Zhao, and R. Corkish. Temperature dependence of the radiative recombination coefficient of intrinsic crystalline silicon. *Journal of Applied Physics*, 94(8):4930, 2003. ISSN 00218979. doi:10.1063/1.1610231.

[36] J. Schmidt and A. G. Aberle. Carrier recombination at silicon–silicon nitride interfaces fabricated by plasma-enhanced chemical vapor deposition. *Journal of Applied Physics*, 85(7):3626–3633, 1999. ISSN 00218979. doi:10.1063/1.369725.

[37] J. A. Hornbeck and J. R. Haynes. Trapping of minority carriers in silicon. i. p-type silicon. *Physical Review*, 97(2):311–321, 1955. ISSN 0031-899X. doi:10.1103/physrev.97.311.

[38] J. R. Haynes and J. A. Hornbeck. Trapping of minority carriers in silicon. ii. n-type silicon. *Physical Review*, 100(2):606–615, 1955. ISSN 0031-899X. doi:10.1103/physrev.100.606.

[39] W. Shockley and W. T. Read. Statistics of the recombination of holes and electrons. *Physical Review*, 87:835–42, 1952. doi:10.1103/physrev.87.835.

[40] R. N. Hall. Electron-hole recombination in germanium. *Physical Review*, 87(2):387, 1952. doi:10.1103/PhysRev.87.387.

[41] D. J. Fitzgerald and A. S. Grove. Surface recombination in semiconductors. *Surface Science*, 9(2):347–369, 1968. ISSN 0039-6028. doi:10.1016/0039-6028(68)90182-9.

[42] A. S. Grove and D. J. Fitzgerald. Surface effects on p-n junctions: Characteristics of surface space-charge regions under non-equilibrium conditions. *Solid-State Electronics*, 9(8):783–806, 1966. ISSN 0038-1101. doi:10.1016/0038-1101(66)90118-3.

[43] J. B. Gunn. On carrier accumulation, and the properties of certain semiconductor junctions†. *Journal of Electronics and Control*, 4(1):17–50, 1958. ISSN 0368-1947. doi:10.1080/00207215808953823.

[44] R. B. M. Girisch, R. P. Mertens, and R. F. De Keersmaecker. Determination of si-sio2 interface recombination parameters using a gate-controlled point-junction diode under illumination. *IEEE Transactions on Electron Devices*, 35(2):203–222, Feb 1988. ISSN 0018-9383. doi:10.1109/16.2441.

[45] A. G. Aberle, S. W. Glunz, and W. Warta. Impact of illumination level and oxide parameters on shockley–read–hall recombination at the si-sio2 interface. *Journal of Applied Physics*, 71(9):4422, 1992. ISSN 00218979. doi:10.1063/1.350782.

[46] Keith R. McIntosh and Lachlan E. Black. On effective surface recombination parameters. *Journal of Applied Physics*, 116(1):014503, 2014. doi:10.1063/1.4886595.

[47] S. Steingrube, P. P. Altermatt, J. Schmidt, and R. Brendel. Modelling c-si/sin x interface recombination by surface damage. *physica status solidi (RRL) - Rapid Research Letters*, 4(3-4):91–93, 2010. ISSN 18626254. doi:10.1002/pssr.201004023.

[48] A. B. Sproul. Dimensionless solution of the equation describing the effect of surface recombination on carrier decay in semiconductors. *Journal of Applied Physics*, 76:2851–4, 1994. doi:10.1063/1.357521.

[49] M. Rauer. *Alloying from screen-printed aluminum pastes for silicon solar cell applications*. Dissertation, Universität Konstanz, Konstanz, 2015. URL `http://nbn-resolving.de/urn:nbn:de:bsz:352-0-297302`.

[50] M. Rauer. Untersuchung und Optimierung von PECVD-Schichten zur Oberflächenpassivierung von n-Typ Silicium-Solarzellen. Master's thesis, Albert-Ludwigs-Universität Freiburg im Breisgau, 2009.

[51] S. Sterk. *Simulation und Technologie von hocheffizienten Einsonnen- und Konzentratorsolarzellen aus monokristallinem Silicium*. Dissertation, Freiburg, Universität, Freiburg, 1995.

[52] P. Saint-Cast, M. Rüdiger, A. Wolf, M. Hofmann, J. Rentsch, and R. Preu. Advanced analytical model for the effective recombination velocity of locally contacted surfaces. *Journal of Applied Physics*, 108 (1):013705, 2010. ISSN 00218979. doi:10.1063/1.3437126.

[53] H. Plagwitz and R. Brendel. Analytical model for the diode saturation current of point-contacted solar cells. *Progress in Photovoltaics: Research and Applications*, 14(1):1–12, 2006. ISSN 1099-159X. doi:10.1002/pip.637.

[54] J. Müller, K. Bothe, S. Gatz, H. Plagwitz, G. Schubert, and R. Brendel. Contact formation and recombination at screen-printed local aluminum-alloyed silicon solar cell base contacts. *IEEE Transactions on Electron Devices*, 58(10):3239–3245, 2011. ISSN 0018-9383. doi:10.1109/TED.2011.2161089.

[55] D. Kray and K. R. McIntosh. Analysis of ultrathin high-efficiency silicon solar cells. *physica status solidi (a)*, 206(7):1647–1654, 2009. ISSN 18626300. doi:10.1002/pssa.200824500.

[56] B. Fischer. *Loss analysis of crystalline silicon solar cells using photoconductance and quantum efficiency measurements*. PhD thesis, Universität Konstanz, 2003.

[57] R. H. Cox and H. Strack. Ohmic contacts for gaas devices. *Solid-State Electronics*, 10(12):1213–1218, 1967. ISSN 0038-1101. doi:10.1016/0038-1101(67)90063-9.

[58] P. Saint-Cast, J. Nekarda, M. Hofmann, S. Kuehnhold, and R. Preu. Recombination on locally processed wafer surfaces. *Energy Procedia*, 27: 259–266, 2012. doi:10.1016/j.egypro.2012.07.061.

[59] P. Saint-Cast. *Passivation of Si surfaces by PECVD aluminium oxide*. Dissertation, Konstanz, Universität, Konstanz, 2012.

[60] P. Würfel. *Physics of Solar Cells - From principles to new concepts*. Wiley-VCH, Weinheim, 2005. ISBN 3-527-40428-7.

[61] A. Cuevas. The recombination parameter j0. *Energy Procedia*, 55:53–62, 2014. doi:10.1016/j.egypro.2014.08.073.

[62] S. W. Glunz. *Ladungsträgerrekombination in Silicium und Siliciumsolarzellen*. Dissertation, Freiburg, Universität, Freiburg, 1995.

[63] K. R. McIntosh. *Lumps, humps and bumps: Three detrimental effects in the current-voltage curve of silicon solar cells*. Dissertation, University of New South Wales, Sydney and Australia, 2001.

[64] D. E. Kane and R. M. Swanson. Measurement of the emitter saturation current by a contactless photoconductivity decay method (silicon solar cells). In *18th IEEE Photovoltaic Specialists Conference Las Vegas*, pages 578–583, 1985.

[65] C. Reichel, F. Granek, J. Benick, O. Schultz-Wittmann, and S. W. Glunz. Comparison of emitter saturation current densities determined by injection-dependent lifetime spectroscopy in high and low injection regimes. *Progress in Photovoltaics: Research and Applications*, 20(1): 21–30, 2012. ISSN 1099-159X. doi:10.1002/pip.942.

[66] J. P. McKelvey. *Solid State and Semiconductor Physics*. Materials Science Surveys. Harper & Row, 1966. ISBN 0-89874-396-6.

[67] M. P. Godlewski, C. R. Baraona, and H. W. Brandhorst, Jr. Low-high junction theory applied to solar cells. In *10th IEEE Photovoltaic Specialists Conference Palo Alto*, pages 40–49, 1973.

[68] R. A. Sinton and A. Cuevas. Contactless determination of current–voltage characteristics and minority-carrier lifetimes in semiconductors from quasi-steady-state photoconductance data. *Applied Physics Letters*, 69(17):2510–2512, 1996. ISSN 00036951. doi:10.1063/1.117723.

[69] J. A. Giesecke, B. Michl, F. Schindler, M. C. Schubert, and W. Warta. Minority carrier lifetime of silicon solar cells from quasi-steady-state photoluminescence. *Solar Energy Materials and Solar Cells*, 95(7): 1979–1982, 2011. ISSN 0927-0248. doi:10.1016/j.solmat.2011.02.023.

[70] H. Nagel, C. Berge, and A. G. Aberle. Generalized analysis of quasi-steady-state and quasi-transient measurements of carrier lifetimes in semiconductors. *Journal of Applied Physics*, 86:6218–21, 1999. doi:10.1063/1.371633.

[71] A. Goetzberger, J. Knobloch, and B. Voss. *Crystalline silicon solar cells*. John Wiley & Sons Ltd, Chichester, UK, 1998. ISBN 0-471-97144-8.

[72] W. Shockley and H. J. Queisser. Detailed balance limit of efficiency of p-n junction solar cells. *Journal of Applied Physics*, 32(3):510–519, 1961. ISSN 00218979. doi:10.1063/1.1736034.

[73] A. Richter, M. Hermle, and S. W. Glunz. Reassessment of the limiting efficiency for crystalline silicon solar cells. *IEEE Journal of Photovoltaics*, 3(4):1184–1191, Oct 2013. ISSN 2156-3381. doi:10.1109/JPHOTOV.2013.2270351.

[74] R. A. Sinton and A. Cuevas. A quasi-steady-state open-circuit voltage method for solar cell characterization. In *16th European Photovoltaic Solar Energy Conference*, pages 1152–1155, 2000.

[75] D. Pysch, A. Mette, and S. W. Glunz. A review and comparison of different methods to determine the series resistance of solar cells. *Solar Energy Materials and Solar Cells*, 91(18):1698–1706, 2007. ISSN 0927-0248. doi:10.1016/j.solmat.2007.05.026.

[76] A. Fell. A free and fast three-dimensional/two-dimensional solar cell simulator featuring conductive boundary and quasi-neutrality approximations. *IEEE Transactions on Electron Devices*, 60(2):733–738, 2013. ISSN 0018-9383. doi:10.1109/TED.2012.2231415.

[77] Wafer ray tracer on pv lighthouse. `https://www.pvlighthouse.com.au/calculators/wafer%20ray%20tracer/wafer%20ray%20tracer.html`, 2015. Used Version: 1.6.7.

[78] T. Fellmeth. *Entwicklung einer MWT (Metal Wrap Through) Silizium Solarzelle zur Anwendung in niederkonzentrierenden PV-Systemen*. Diplomarbeit, Konstanz, Universität, Freiburg im Breisgau, Juli 2009.

[79] R. Brendel, S. Dreissigacker, N.-P. Harder, and P. P. Altermatt. Theory of analyzing free energy losses in solar cells. *Applied Physics Letters*, 93(17):173503, 2008. ISSN 00036951. doi:10.1063/1.3006053.

[80] R. M. Swanson. Point-contact solar cells: modeling and experiment. *Solar Cells*, 17(1):85–118, 1986. doi:10.1016/0379-6787(86)90061-x.

[81] Rolf Brendel, Thorsten Dullweber, Robby Peibst, Christopher Kranz, Agnes Merkle, and Daniel Walter. Breakdown of the efficiency gap to 29% based on experimental input data and modeling. *Progress in Photovoltaics: Research and Applications*, pages n/a–n/a, 2015. ISSN 10627995. doi:10.1002/pip.2696.

[82] M. Lieberman and A. Lichtenberg. *Principles of Plasma Discharges and Materials Processing*. Wiley Interscience, 1994.

[83] S. Janz. *Amorphous silicon carbide for photovoltaic applications*. Dissertation, Konstanz, Universität, Freiburg im Breisgau, 2006.

[84] M. Liehr and M. Dieguez-Campo. Microwave pecvd for large area coating. *Surface and Coatings Technology*, 200(1-4):21–25, 2005. doi:10.1016/j.surfcoat.2005.02.061.

[85] H. F. W. Dekkers, S. de Wolf, G. Agostinelli, F. Duerinckx, and G. Beaucarne. Requirements of pecvd sinx:h layers for bulk passivation of mc-si. *Solar Energy Materials and Solar Cells*, 90(18-19):3244–3250, 2006. ISSN 0927-0248. doi:10.1016/j.solmat.2006.06.024.

[86] S. Behle. *Leistungsmodulierte großvolumige mikrowellenangeregte Plasmen: Eine experimentelle und theoretische Untersuchung*. Dissertation, Wuppertal, Universität, Wuppertal, 1999.

[87] T. Lauinger, J. Schmidt, A. G. Aberle, and R. Hezel. Record low surface recombination velocities on 1 ohm cm p-silicon using remote plasma silicon nitride passivation. *Applied Physics Letters*, 68(9):1232–1234, 1996. ISSN 00036951. doi:10.1063/1.115936.

[88] P. Kae-Nune, J. Perrin, J. Guillon, and J. Jolly. Mass spectrometry detection of radicals in sih4-ch4-h2 glow discharge plasmas. *Plasma Sources Science and Technology*, 4(2):250, 1995. ISSN 0963-0252.

[89] R. K. Janev and D. Reiter. Collision processes of chy and chy+ hydrocarbons with plasma electrons and protons. *Physics of Plasmas*, 9(9): 4071–4081, 2002. doi:10.1063/1.1500735.

[90] R. K. Janev and D. Reiter. Collision processes of hydride species in hydrogen plasmas: Iii. the silane family. *Contributions to Plasma Physics*, 43(7):401–417, 2003. ISSN 0863-1042. doi:10.1002/ctpp.200310055.

[91] S. J. B. Corrigan. Dissociation of molecular hydrogen by electron impact. *The Journal of Chemical Physics*, 43(12):4381–4386, 1965. doi:10.1063/1.1696701.

[92] Y. Itikawa. Cross sections for electron collisions with nitrogen molecules. *Journal of Physical and Chemical Reference Data*, 35(1): 31–53, 2006. doi:10.1063/1.1937426.

[93] T. Karabacak, Y. P. Zhao, G. C. Wang, and T. M. Lu. Growth front roughening in silicon nitride films by plasma-enhanced chemical vapor deposition. *Phys. Rev. B*, 66:075329, Aug 2002. doi:10.1103/PhysRevB.66.075329.

[94] J. Zhao, A. Wang, and M. A. Green. 24.5% efficiency silicon PERT cells on MCZ substrates and 24.7% efficiency PERL cells on FZ substrates. *Progress in Photovoltaics: Research and Applications*, 7(6): 471–474, 1999. doi:10.1002/(SICI)1099-159X(199911/12)7:6<471::AID-PIP298>3.0.CO;2-7.

[95] J. Benick, B. Hoex, M. C. M. van de Sanden, W. M. M. Kessels, O. Schultz, and S. W. Glunz. High efficiency n-type Si solar cells on Al2O3-passivated boron emitters. *Applied Physics Letters*, 92: 253504/1–3, 2008. doi:10.1063/1.2945287.

[96] S. Rein. *Lifetime spectroscopy: A method of defect characterization in silicon for photovoltaic applications*, volume 85 of *Springer Series in Materials Science*. Springer, Berlin and New York, 1st edition, 2005. ISBN 3-540-27922-9.

[97] W. D. Eades and R. M. Swanson. Calculation of surface generation and recombination velocities at the si-sio2 interface. *Journal of Applied Physics*, 58(11):4267–4276, 1985. ISSN 00218979. doi:10.1063/1.335562.

[98] T. Inada, T. Ohkubo, S. Sawada, T. Hara, and M. Nakajima. Chemical vapor deposition of silicon nitride. *Journal of the Electrochemical Society*, 125(9):1525–1529, 1978. doi:10.1149/1.2131709.

[99] G. Bilger, T. Voss, T. Schlenker, and A. Strohm. High-temperature diffusion barriers from si-rich silicon-nitride. *Surface and Interface Analysis*, 38(12-13):1687–1691, 2006. ISSN 1096-9918. doi:10.1002/sia.2396.

[100] R. Hezel and R. Schörner. Plasma si nitride—a promising dielectric to achieve high-quality silicon mis/il solar cells. *Journal of Applied Physics*, 52(4):3076–3079, 1981. doi:10.1063/1.329058.

[101] R. Hezel and K. Jaeger. Low-temperature surface passivation of silicon for solar cells. *Journal of The Electrochemical Society*, 136(2):518–523, 1989. doi:10.1149/1.2096673.

[102] C. Leguijt, P. Lölgen, J. A. Eikelboom, A. S. H. van der Heide, R. A. Steeman, W. C. Sinke, P. M. Sarro, L. A. Verhoef, P.-P. Michiels, Z. Chen, and A. Rohatgi. Stable surface passivation of silicon by low-temperature processing. In *12th European Photovoltaic Solar Energy Conference*, pages 720–723, 1994.

[103] A. G. Aberle, T. Lauinger, J. Schmidt, and R. Hezel. Injection-level dependent surface recombination velocities at the silicon-plasma silicon nitride interface. *Applied Physics Letters*, 66(21):2828–2830, 1995. ISSN 00036951. doi:10.1063/1.113443.

[104] T. Lauinger, J. Moschner, A. G. Aberle, and R. Hezel. Optimization and characterization of remote plasma-enhanced chemical vapor deposition silicon nitride for the passivation of p-type crystalline silicon surfaces. *Journal of Vacuum Science & Technology A: Vacuum, Surfaces, and Films*, 16(2):530–543, 1998. ISSN 07342101. doi:10.1116/1.581095.

[105] W. Wolke, J. Catoir, G. Emanuel, J. Liu, M. Ruske, and R. Preu. Surface passivation for solar cells by large scale inline sputtering of silicon nitride. In *20th European Photovoltaic Solar Energy Conference*, pages 733–736, 2005.

[106] W. Wolke. *Kathodenzerstäubung zur Beschichtung von kristallinen Silizium-Solarzellen.* Dissertation, Freiburg, Universität, Freiburg, 2005.

[107] S. Dauwe, L. Mittelstädt, A. Metz, and R. Hezel. Experimental evidence of parasitic shunting in silicon nitride rear surface passivated solar cells. *Progress in Photovoltaics: Research and Applications*, 10(4): 271–278, 2002. ISSN 1099-159X. doi:10.1002/pip.420.

[108] A. W. Weeber, H. C. Rieffe, I. G. Romijn, W. C. Sinke, and W. J. Soppe. The fundamental properties of sin/sub x/:h that determine its passivating qualities. In *31st IEEE Photovoltaic Specialists Conference Lake Buena Vista: Conference Record*, pages 1043–1046, 2005. doi:10.1109/pvsc.2005.1488312.

[109] S. Dauwe. *Low-temperature surface passivation of crystalline silicon and its application to the rear side of solar cells.* Dissertation, Hannover, Universität, Hannover, 2004.

[110] K. J. Weber and H. Jin. Improved silicon surface passivation achieved by negatively charged silicon nitride films. *Applied Physics Letters*, 94 (6):063509, 2009. doi:10.1063/1.3077157.

[111] M. Hofmann, E. Schneiderlöchner, W. Wolke, and R. Preu. Silicon nitride-silicon oxide stacks for solar cell rear side passivation. In *19th European Photovoltaic Solar Energy Conference*, volume 1, pages 1037–1040, 2004.

[112] S. Gatz, T. Dullweber, V. Mertens, F. Einsele, and R. Brendel. Firing stability of SiNy/SiNx stacks for the surface passivation of crystalline silicon solar cells. *Solar Energy Materials and Solar Cells*, 96(0):180–185, 2012. ISSN 0927-0248. doi:10.1016/j.solmat.2011.09.051.

[113] S. Gatz, H. Plagwitz, P. P. Altermatt, B. Terheiden, and R. Brendel. Thermal stability of amorphous silicon/silicon nitride stacks for passivating crystalline silicon solar cells. *Applied Physics Letters*, 93(17):173502, 2008. ISSN 00036951. doi:10.1063/1.3009571.

[114] B. Hoex, S. B. S. Heil, E. Langereis, M. C. M. van de Sanden, and W. M. M. Kessels. Ultralow surface recombination of c-si substrates passivated by plasma-assisted atomic layer deposited al[sub 2]o[sub 3]. *Applied Physics Letters*, 89(4):042112, 2006. ISSN 00036951. doi:10.1063/1.2240736.

[115] C. Leguijt, P. Lölgen, J. A. Eikelboom, A. W. Weeber, F. M. Schuurmans, W. C. Sinke, P. F. A. Alkemade, P. M. Sarro, C. H. M. Marée, and L. A. Verhoef. Low temperature surface passivation for silicon solar cells. *Solar Energy Materials and Solar Cells*, 40(4):297–345, 1996. ISSN 0927-0248. doi:10.1016/0927-0248(95)00155-7.

[116] S. Dauwe, J. Schmidt, and R. Hezel. Very low surface recombination velocities on p- und n-type silicon wafers passivated with hydrogenated amorphous silicon films. In *29th IEEE Photovoltaic Specialists Conference New Orleans*, pages 1246–1249, 2002.

[117] B. E. Deal, P. J. Fleming, and P. L. Castro. Electrical properties of vapor-deposited silicon nitride and silicon oxide films on silicon. *Journal of the Electrochemical Society*, 115(3):300–307, 1968. doi:10.1149/1.2411146.

[118] Shang-Yuan Ren and W. Y. Ching. Electronic structures of β- and α-silicon nitride. *Phys. Rev. B*, 23:5454–5463, May 1981. doi:10.1103/PhysRevB.23.5454.

[119] J. Robertson. The electronic properties of silicon nitride. *Philosophical Magazine Part B*, 44(2):215–237, 1981. doi:10.1080/01418638108222558.

[120] J. Robertson. Electronic structure of silicon nitride. *Philosophical Magazine Part B*, 63(1):47–77, 1991. ISSN 1364-2812. doi:10.1080/01418639108224430.

[121] H. Mäckel and R. Lüdemann. Detailed study of the composition of hydrogenated sinx layers for high-quality silicon surface passivation. *Journal of Applied Physics*, 92(5):2602, 2002. ISSN 00218979. doi:10.1063/1.1495529.

[122] J. Robertson. Defects and hydrogen in amorphous silicon nitride. *Philosophical Magazine Part B*, 69(2):307–326, 1994. doi:10.1080/01418639408240111.

[123] E. Bustarret, M. Bensouda, M. C. Habrard, and J. C. Bruyere. Configurational statistics in a-sixnyhz alloys: A quantitative bonding analysis. *Physical Review B*, 38(12):8171, 1988. ISSN 0163-1829. doi:10.1103/PhysRevB.38.8171.

[124] A. Cuevas, F. Chen, J. Tan, H. Mackel, S. Winderbaum, and K. Roth. Ftir analysis of microwave-excited pecvd silicon nitride layers. In *2006 IEEE 4th World Conference on Photovoltaic Energy Conference*, volume 1, pages 1148–1151, May 2006. doi:10.1109/WCPEC.2006.279365.

[125] N. Ahmed, C. B. Singh, S. Bhattacharya, S. Dhara, and P. B. Bhargav. Raman and ftir studies on pecvd grown ammonia-free amorphous silicon nitride thin films for solar cell applications. *Conference Papers in Energy*, 2013(1-2):1–4, 2013. ISSN 2314-4009. doi:10.1155/2013/837676.

[126] T. Kuzuba, K. Kijima, and Y. Bando. Raman-active modes of alpha silicon nitride. *The Journal of Chemical Physics*, 69(1):40, 1978. ISSN 00219606. doi:10.1063/1.436368.

[127] A. G. Aberle. *Crystalline silicon solar cells: Advanced surface passivation and analysis*. Centre for Photovoltaic Engineering, University of New South Wales, Sydney, 1999. ISBN 0733406459 9780733406454.

[128] L. Zhong and F. Shimura. Investigation of charge trapping centers in silicon nitride films with a laser-microwave photoconductive method. *Applied Physics Letters*, 62(6):615–617, 1993. ISSN 00036951. doi:10.1063/1.108873.

[129] D. T. Krick, P. M. Lenahan, and J. Kanicki. Electrically active point defects in amorphous silicon nitride: An illumination and charge injection study. *Journal of Applied Physics*, 64(7):3558–3563, 1988. ISSN 00218979. doi:10.1063/1.341499.

[130] S. Dauwe, J. Schmidt, A. Metz, and R. Hezel. Fixed charge density in silicon nitride films on crystalline silicon surfaces under illumination. In *Photovoltaic Specialists Conference, 2002. Conference Record of the Twenty-Ninth IEEE*, pages 162–165, May 2002. doi:10.1109/PVSC.2002.1190481.

[131] S. Janz, S. Reber, and S. W. Glunz. Amorphous sic: Applications for silicon solar cells. In *21st European Photovoltaic Solar Energy Conference*, pages 660–663, 2006.

[132] K. Schillinger. *Crystalline Silicon Carbide Intermediate Layers for Silicon Thin-Film Solar Cells*. Dissertation, Freiburg, Universität, Freiburg, 2014.

[133] I. Martín, M. Vetter, A. Orpella, C. Voz, J. Puigdollers, and R. Alcubilla. Characterization of p-type c-si surface passivation by n-doped a-sicx: H films. In *17th European Photovoltaic Solar Energy Conference*, pages 2954–2958, 2001.

[134] I. Martín, M. Vetter, A. Orpella, C. Voz, J. Puigdollers, and R. Alcubilla. Surface passivation of n-type crystalline si by plasma-enhanced-chemical-vapor-deposited amorphous sicx:h and amorphous sicxny:h films. *Applied Physics Letters*, 81(23):4461–4463, 2002. doi:10.1063/1.1527230.

[135] S. W. Glunz, S. Janz, M. Hofmann, T. Roth, and G. Willeke. Surface passivation of silicon solar cells using amorphous silicon carbide layers. In *4th World Conference on Photovoltaic Energy Conversion Hawaii*, pages 1016–1019, 2006. doi:10.1109/wcpec.2006.279291.

[136] S. Janz, S. Riepe, M. Hofmann, S. Reber, and S. W. Glunz. Phosphorus-doped sic as an excellent p-type si surface passivation layer. *Applied Physics Letters*, 88(13):133516, 2006. ISSN 00036951. doi:10.1063/1.2191954.

[137] S. Riegel, B. Raabe, R. Petres, S. Dixit, L. Zhou, and G. Hahn. Towards higher efficiencies for crystalline silicon solar cells using sic layers. In *23rd European Photovoltaic Solar Energy Conference*, pages 1604–1607, 2008.

[138] R. Ferre, I. Martín, P. Ortega, M. Vetter, I. Torres, and R. Alcubilla. N-type emitter surface passivation in c-si solar cells by means of antireflective amorphous silicon carbide layers. *Journal of Applied Physics*, 100(7):073703, 2006. ISSN 00218979. doi:10.1063/1.2354323.

[139] M. Vetter, R. Ferre, I. Martin, P. Ortega, R. Alcubilla, R. Petres, J. Libal, and R. Kopecek. Investigation of the surface passivation of p+-type si emitters by pecvd silicon carbide films. In *4th World Conference on Photovoltaic Energy Conversion Hawaii*, pages 1271–1274, 2006. doi:10.1109/wcpec.2006.279645.

[140] B. Steinhauser, D. Suwito, S. Janz, and M. Hermle. Stacks of a-sicx layers on planar and textured surfaces for the solar cell front side on both n+ and p+-emitters. In *25th European Photovoltaic Solar Energy Conference*, pages 2250–2254, 2010.

[141] B. Steinhauser. *Entwicklung von a-SixC1-x Schichtsystemen für die Solarzellenvorderseite*. Diplomarbeit, Freiburg, Universität, Freiburg and Germany, 2010.

[142] D. Suwito, T. Roth, D. Pysch, L. Korte, A. Richter, S. Janz, and S. W. Glunz. Detailed study on the passivation mechanism of a-sixc1-x for the solar cell rear side. In *23rd European Photovoltaic Solar Energy Conference*, pages 1023–1028, 2008.

[143] D. Suwito. *Intrinsic and doped amorphous silicon carbide for the surface passivation of silicon solar cells*. Dissertation, Universität Konstanz, 2011.

[144] D. Suwito, S. Janz, C. Schetter, S. W. Glunz, and K. Roth. Process transfer of a-sixc1-x passivation layers from a laboratorytype to an industrial in-line pecvd reactor. In *33rd IEEE Photovoltaic Specialists Conference San Diego*, pages 1–4, 2008. doi:10.1109/pvsc.2008.4922797.

[145] D. Pysch. *Assembly and analysis of alternative emitter systems for high efficient silicon solar cells*. Dissertation, Konstanz, Universität, Konstanz, 2011.

[146] J. Temmler, M. Bivour, H. Steinkemper, and M. Hermle. Boron doped a-sic:h front layers for silicon heterojunction cells. In *40th IEEE Photovoltaic Specialists Conference (PVSC) 2014*, pages 481–483, 2014. doi:10.4229/EUPVSEC20142014-2BO.4.5.

[147] A. Moldovan, F. Feldmann, G. Krugel, M. Zimmer, J. Rentsch, M. Hermle, A. Roth-Fölsch, K. Kaufmann, and C. Hagendorf. Simple cleaning and conditioning of silicon surfaces with uv/ozone sources. *Energy Procedia*, 55:834–844, 2014. doi:10.1016/j.egypro.2014.08.067.

[148] F. Feldmann, M. Simon, M. Bivour, C. Reichel, M. Hermle, and S. W. Glunz. Efficient carrier-selective p- and n-contacts for si solar cells. *Solar Energy Materials and Solar Cells*, 131(0):100–104, 2014. ISSN 0927-0248. doi:10.1016/j.solmat.2014.05.039.

[149] H. Steinkemper, F. Feldmann, M. Bivour, and M. Hermle. Numerical simulation of carrier-selective electron contacts featuring tunnel oxides. *IEEE Journal of Photovoltaics*, 5(5):1348–1356, 2015. ISSN 2156-3381. doi:10.1109/JPHOTOV.2015.2455346.

[150] N. I. Klyui, V. G. Litovchenko, A. N. Lukyanov, and A. N. Klyui. Optical properties of diamond-like carbon films subjected to ultraviolet irradiation. *Semiconductor Physics, Quantum Electronics & Optoelectronics*, 11(4):396–399, 2008.

[151] M. Lattemann, E. Nold, S. Ulrich, H. Leiste, and H. Holleck. Investigation and characterisation of silicon nitride and silicon carbide thin films. *Surface and Coatings Technology*, 174–175:365–369, 2003. ISSN 0257-8972. doi:10.1016/S0257-8972(03)00695-9. Proceedings of the Eight International Conference on Plasma Surface Engineering.

[152] K. B. Sundaram and J. Alizadeh. Deposition and optical studies of silicon carbide nitride thin films. *Thin Solid Films*, 370(1-2):151–154, 2000. ISSN 0040-6090. doi:10.1016/S0040-6090(00)00956-1.

[153] R. Ferre, I. Martín, M. Vetter, D. Baetzner, J. Tan, A. Cuevas, and R. Alcubilla. Surface and emitter passivation of crystalline silicon by amorphous silicon carbide: Evolution with annealing. In *21st European Photovoltaic Solar Energy Conference*, pages 919–922, 2006.

[154] B. Steinhauser, U. Jäger, J. Benick, E. Chong, R. Steeman, H. Rostan, J. Nekarda, M. Hermle, R. Preu, and S. W. Glunz. The influence of nitrogen on laser doping from phosphorous doped a-sinx layers. *Solar Energy Materials and Solar Cells*, 157:295–304, 2016. doi:10.1016/j.solmat.2016.05.047.

[155] F. Harper and M. Cohen. Properties of si diodes prepared by alloying al into n-type si with heat pulses from a nd:yag laser. *IEEE Journal of Quantum Electronics*, 5(6):335–336, 1969. ISSN 0018-9197. doi:10.1109/jqe.1969.1081969.

[156] Y. Matsuoka. Laser-induced damage to semiconductors. *Journal of Physics D: Applied Physics*, 9(2):215–224, 1976. ISSN 0022-3727. doi:10.1088/0022-3727/9/2/012.

[157] Y. Matsuoka and A. Usami. Normal laser damage of silicon solar cells without phase change. *Applied Physics Letters*, 25(10):574, 1974. ISSN 00036951. doi:10.1063/1.1655316.

[158] P. M. Mooney and J. C. Bourgoin. Laser annealing of defects in vpe and cz grown gallium arsenide with a pulsed nd:yag laser. In *Laser and electron-beam solid interactions and materials processing*, volume 1, pages 255–260, 1982.

[159] P. M. Mooney, R. T. Young, J. Karins, Y. H. Lee, and J. W. Corbett. Defects in laser damaged silicon observed by dlts. *Physica Status Solidi (a)*, 48(1):K31–K34, 1978. ISSN 00318965. doi:10.1002/pssa.2210480144.

[160] L. C. Kimerling and J. L. Benton. Defects in laser-processed semiconductors. In C. White, editor, *Laser and Electron Beam Processing of Materials*, pages 385–396. Academic Pr, New York, 1980. ISBN 0127468501. doi:10.1016/b978-0-12-746850-1.50059-1.

[161] V. K. Arora and A. L. Dawar. Laser-induced damage studies in silicon and silicon-based photodetectors. *Applied Optics*, 35(36):7061–7065, 1996. doi:10.1364/ao.35.007061.

[162] R. Stuck, E. Fogarassy, J. J. Grob, and P. Siffert. Solubility limit of impurities in silicon after laser induced melting. *Applied Physics*, 23(1): 15–19, 1980. ISSN 0340-3793. doi:10.1007/BF00899564.

[163] R. Wood and G. Giles. Macroscopic theory of pulsed-laser annealing. i. thermal transport and melting. *Physical Review B*, 23(6):2923–2942, 1981. ISSN 0163-1829. doi:10.1103/physrevb.23.2923.

[164] R. Wood, J. Kirkpatrick, and G. Giles. Macroscopic theory of pulsed-laser annealing. ii. dopant diffusion and segregation. *Physical Review B*, 23(10):5555–5569, 1981. ISSN 0163-1829. doi:10.1103/physrevb.23.5555.

[165] R. Wood. Macroscopic theory of pulsed-laser annealing. iii. nonequilibrium segregation effects. *Physical Review B*, 25(4):2786–2811, 1982. ISSN 0163-1829. doi:10.1103/physrevb.25.2786.

[166] E. Fogarassy, R. Stuck, M. Toulemonde, D. Salles, and P. Siffert. A model for laser induced diffusion. *Journal of Applied Physics*, 54(9):5059–5063, 1983. ISSN 00218979. doi:10.1063/1.332778.

[167] K. Hoh, H. Koyama, K. Uda, and Y. Miura. Incorporation of oxygen into silicon during pulsed-laser irradiation. *Japanese Journal of Applied Physics*, 19(7):L375, 1980. ISSN 0021-4922. doi:10.1143/JJAP.19.L375.

[168] Z. Hameiri, T. Puzzer, L. Mai, A. B. Sproul, and S. R. Wenham. Laser induced defects in laser doped solar cells. *Progress in Photovoltaics: Research and Applications*, 19(4):391–405, 2011. ISSN 1099-159X. doi:10.1002/pip.1043.

[169] C. Geisler, S. Kluska, S. Hopman, J. Giesecke, and M. Glatthaar. Passivation-induced cavity defects in laser-doped selective emitter si solar cells—formation model and recombination analysis. *IEEE Journal of Photovoltaics*, 5(3):792–798, 2015. ISSN 2156-3381. doi:10.1109/JPHOTOV.2015.2407152.

[170] R. T. Young, R. F. Wood, W. H. Christie, and G. E. Jellison Jr. Substrate heating and emitter dopant effects in laser-annealed solar cells. *Applied Physics Letters*, 39(4):313, 1981. ISSN 00036951. doi:10.1063/1.92704.

[171] R. T. Young, R. F. Wood, and W. H. Christie. Laser processing for high-efficiency si solar cells. *Journal of Applied Physics*, 53(2):1178, 1982. ISSN 00218979. doi:10.1063/1.330568.

[172] E. Fogarassy, R. Stuck, J. J. Grob, and P. Siffert. Silicon solar cells realized by laser induced diffusion of vacuum-deposited dopants. *Journal of Applied Physics*, 52(2):1076–1082, 1981. ISSN 00218979. doi:10.1063/1.328806.

[173] A. W. Blakers, A. Wang, A. M. Milne, J. Zhao, and M. A. Green. 22.8% efficient silicon solar cell. *Applied Physics Letters*, 55(13):1363–1365, 1989. ISSN 00036951. doi:10.1063/1.101596.

[174] G. Agostinelli, P. Choulat, H. F. W. Dekkers, S. de Wolf, and G. Beaucarne. Screen printed large area crystalline silicon solar cells on thin substrates. In *20th European Photovoltaic Solar Energy Conference*, pages 647–650, 2005.

[175] G. Agostinelli, J. Szlufcick, P. Choulat, and G. Beaucarne. Local contact structures for industrial perc-type solar cells. In *20th European Photovoltaic Solar Energy Conference*, pages 942–945, 2005.

[176] S. R. Wenham and M. A. Green. Self aligning method for forming a selective emitter and metallization in a solar cell, August 6 2002. US Patent 6,429,037.

[177] B. Paviet-Salomon, S. Gall, R. Monna, S. Manuel, A. Slaoui, L. Vandroux, R. Hida, and S. Dechenaux. Laser doping using phosphorus-doped silicon nitrides. *Energy Procedia*, 8(0):700–705, 2011. ISSN 1876-6102. doi:10.1016/j.egypro.2011.06.204. Proceedings of the SiliconPV 2011 Conference (1st International Conference on Crystalline Silicon Photovoltaics).

[178] B. Paviet-Salomon, S. Gall, and A. Slaoui. Investigation of charges carrier density in phosphorus and boron doped SiNx:H layers for crystalline silicon solar cells. *Materials Science and Engineering: B*, 178(9): 580–585, 2013. ISSN 0921-5107. doi:10.1016/j.mseb.2012.11.009. Advanced materials and characterization techniques for solar cells.

[179] B. Steinhauser, M. bin Mansoor, U. Jäger, J. Benick, and M. Hermle. Firing-stable PassDop passivation for screen printed n-type PERL solar cells based on a-SiNx:P. *Solar Energy Materials and Solar Cells*, 126: 96–100, 2014. doi:10.1016/j.solmat.2014.03.047.

[180] P. Ortega, I. Martín, G. Lopez, M. Colina, A. Orpella, C. Voz, and R. Alcubilla. P-type c-si solar cells based on rear side laser processing of al2o3/sicx stacks. *Solar Energy Materials and Solar Cells*, 106:80–83, 2012. ISSN 0927-0248. doi:10.1016/j.solmat.2012.05.012.

[181] B. Steinhauser, U. Jäger, J. Benick, and M. Hermle. PassDop rear side passivation based on Al2O3/a-SiCx: B stacks for p-type PERL solar cells. *Solar Energy Materials and Solar Cells*, 131:129–133, 2014. ISSN 0927-0248. doi:10.1016/j.solmat.2014.05.001.

[182] U. Jäger, D. Suwito, J. Benick, S. Janz, and R. Preu. A laser based process for the formation of a local back surface field for n-type silicon solar cells. *Thin Solid Films*, 519(11):3827–30, 2011. doi:10.1016/j.tsf.2011.01.237.

[183] U. Jäger. *Selektive Laserdiffusion für hocheffiziente Solarzellen aus kristallinem Silicium*. Dissertation, Albert-Ludwigs-Universität Freiburg im Breisgau, 2012.

[184] M.T. Künle. *Silicon carbide single and multilayer thin films for photovoltaic applications*. Dissertation, Tübingen, Universität, Tübingen and Germany, 2011.

[185] B. Legradic, B. Strahm, D. Lachenal, D. Bätzner, W. Frammelsberger, J. Meixenberger, P. Papet, G. Wahli, Jun Zhao, D. Decker, and E. Vetter. High efficiency si-heterojunction technology - it's ready for mass production. In *Photovoltaic Specialist Conference (PVSC), 2015 IEEE 42nd*, pages 1–3, June 2015. doi:10.1109/PVSC.2015.7355747.

[186] R. A. Street. *Hydrogenated Amorphous Silicon*. Cambridge University Press, Cambridge, 1991. doi:10.1017/cbo9780511525247.

[187] M. Wilson, J. Lagowski, A. Savtchouk, L. Jastrzebski, and J. D'Amico. COCOS (corona oxide characterization of semiconductor) metrology: Physical principles and applications. In *ASTM Conference on Gate Dielectric Oxide Integrity*, 1999.

[188] S. M. Sze. *Physics of semiconductor devices*. John Wiley & Sons, Inc., 2 edition, 1981. ISBN 0-471-09837-X.

[189] O. N. Carlson. The N-Si (Nitrogen-Silicon) system. *Bulletin of Alloy Phase Diagrams*, 11(6):569–573, 1990. ISSN 0197-0216. doi:10.1007/BF02841719.

[190] M. bin Mansoor. Development of an industrially feasible rear side passivation concept for n-type solar cells. Master's thesis, Albert-Ludwigs-Universität Freiburg im Breisgau, 2013.

[191] P. Saint-Cast, M. Hofmann, T. Dimitrova, D. Wagenmann, J. Rentsch, and R. Preu. Firing stable passivation with a-si/sinx stack layers for crystalline silicon solar cells. In *24th European Photovoltaic Solar Energy Conference*, pages 1649–1653, 2009. doi:10.4229/24thEUPVSEC2009-2CV.2.64.

[192] M. S. Wenclawiak. Erstellung eines modells zur bestimmung der dotiereffizienz bei laserdiffusion. Master's thesis, University of Freiburg, 20013.

[193] D. B. M. Klaassen. A unified mobility model for device simulation: I. model equations and concentration dependence. *Solid-State Electronics*, 35(7):953–959, 1992. ISSN 0038-1101. doi:10.1016/0038-1101(92)90325-7.

[194] D. B. M. Klaassen. A unified mobility model for device simulation: Ii. temperature dependence of carrier mobility and lifetime. *Solid-State Electronics*, 35(7):961–967, 1992. ISSN 0038-1101. doi:10.1016/0038-1101(92)90326-8.

[195] C. V. Raman and K. S. Krishnan. A new type of secondary radiation. *Nature*, 121:501–502, Mar 1928. doi:10.1038/121501c0.

[196] Gr. Landsberg and L. Mandelstam. Über die lichtzerstreuung in kristallen. *Zeitschrift für Physik*, 50:769–780, 1928. doi:10.1007/BF01339412.

[197] M. Becker, U. Gösele, A. Hofmann, and S. Christiansen. Highly p-doped regions in silicon solar cells quantitatively analyzed by small angle beveling and micro-raman spectroscopy. *Journal of Applied Physics*, 106(7):074515, 2009. ISSN 00218979. doi:10.1063/1.3236571.

[198] R. Müller, J. Schrof, C. Reichel, J. Benick, and M. Hermle. Back-junction back-contact n-type silicon solar cell with diffused boron emitter locally blocked by implanted phosphorus. *Applied Physics Letters*, 105 (10):103503, 2014. ISSN 0003-6951. doi:10.1063/1.4895538.

[199] V. N. Doshi, T. Niuya, and M. Yang. Silicon nitride dopant diffusion barrier in integrated circuits, August 21 2001. URL `https://www.google.com/patents/US6277720`. US Patent 6,277,720.

[200] W. Kaiser and C. D. Thurmond. Nitrogen in silicon. *Journal of Applied Physics*, 30(3):427–431, 1959. doi:10.1063/1.1735180.

[201] L. C. Kimerling. Influence of deep traps on the measurement of free-carrier distributions in semiconductors by junction capacitance techniques. *Journal of Applied Physics*, 45:1839–1845, 1974. doi:10.1063/1.1663500.

[202] P. Blood. Capacitance-voltage profiling and the characterisation of iii-v semiconductors using electrolyte barriers. *Semiconductor Science and Technology*, 1(1):7–27, 1986. doi:10.1088/0268-1242/1/1/002.

[203] P. K. Ghosh and M. E. Azimi. Numerical calculation of effective permittivity of lossless dielectric mixtures using boundary integral method. *IEEE Transactions on Dielectrics and Electrical Insulation*, 1 (6):975–981, 1994. doi:10.1109/94.368637.

[204] R. T. Young, R. F. Wood, and W. H. Christie. Laser processing for high-efficiency si solar cells. *Journal of Applied Physics*, 53(2):1178, 1982. ISSN 00218979. doi:10.1063/1.330568.

[205] K. H. Yang. An etch for delineation of defects in silicon. *Journal of The Electrochemical Society*, 131(5):1140–1145, 1984. doi:10.1149/1.2115767.

[206] R. C. Newmann. Carbon in crystalline silicon. In *MRS Proceedings*, volume 59, pages 403–417, 1986. doi:10.1557/PROC-59-403.

[207] B. Reedy, 2016. Email correspondence.

[208] H. Kojima, S. G. Whiteway, and C. R. Masson. Melting points of inorganic fluorides. *Canadian Journal of Chemistry*, 46(18):2968–2971, 1968. doi:10.1139/v68-494.

[209] S.-P. Jeng, T.-P. Ma, R. Canteri, M. Anderle, and G. W. Rubloff. Anomalous diffusion of fluorine in silicon. *Appl. Phys. Lett.*, 61(11):1310–1312, 1992. doi:10.1063/1.107575.

[210] R. R. Robinson. *Simulation of Fluorine Diffusion Behavior and Boron-Fluorine Co-Interaction in Silicon.* PhD thesis, University of Florida, 2006.

[211] H. Francois-Saint-Cyr, E. Anoshkina, F. Stevie, L. Chow, K. Richardson, and D. Zhou. Secondary ion mass spectrometry characterization of the diffusion properties of 17 elements implanted into silicon. *J. Vac. Sci. Technol. B*, 19(5):1769–1774, 2001. doi:10.1116/1.1396638.

[212] J. W. Chen and A. G. Milnes. Energy levels in silicon. *Annual Review of Materials Science*, 10(1):157–228, 1980. doi:10.1146/annurev.ms.10.080180.001105.

[213] V. M. Arutyunyan, A. P. Akhoyan, Z. N. Adamyan, and R. S. Barsegyan. Laser-induced implantation and diffusion of magnesium into silicon. *Technical Physics*, 46(2):198–201, 2001. ISSN 1090-6525. doi:10.1134/1.1349276.

[214] S. W. Glunz, J. Nekarda, H. Mäckel, and A. Cuevas. Analyzing back contacts of silicon solar cells by suns-voc-measurements at high illumination densities. In *22nd European Photovoltaic Solar Energy Conference*, pages 849–853, 2007.

[215] K. R. McIntosh and P. P. Altermatt. A freeware 1d emitter model for silicon solar cells. In *35th IEEE Photovoltaic Specialists Conference Honolulu*, pages 1–6, 2010. doi:10.1109/pvsc.2010.5616124.

[216] F. D. Heinz, M. Breitwieser, P. Gundel, M. König, M. Hörteis, W. Warta, and M. C. Schubert. Microscopic origin of the aluminium assisted spiking effects in n-type silicon solar cells. *Solar Energy Materials and Solar Cells*, 131:105–109, 2014. ISSN 0927-0248. doi:10.1016/j.solmat.2014.05.036.

[217] E. Lohmüller. *Transfer of the Metal Wrap Through Solar Cell Concept to n-Type Silicon.* Dissertation, Freiburg, Universität, Freiburg, 2015.

[218] N. Wöhrle, E. Lohmüller, J. Greulich, S. Werner, and S. Mack. Towards understanding the characteristics of ag–al spiking on boron-doped silicon for solar cells. *Solar Energy Materials and Solar Cells*, 146:72–79, 2016. ISSN 0927-0248. doi:10.1016/j.solmat.2015.11.032.

[219] J. Bartsch, M. Kamp, D. Hartleb, C. Wittich, A. Mondon, B. Steinhauser, F. Feldmann, A. Richter, J. Benick, M. Glatthaar, M. Hermle, and S. W. Glunz. 21.8% efficient n-type solar cells with industrially feasible plated metallization. *Energy Procedia*, 55:400–409, 2014. doi:10.1016/j.egypro.2014.08.116.

[220] M. Glatthaar, J. Haunschild, M. Kasemann, J. Giesecke, W. Warta, and S. Rein. Spatially resolved determination of dark saturation current and series resistance of silicon solar cells. *physica status solidi (RRL) - Rapid Research Letters*, 4(1-2):13–15, 2010. ISSN 18626254. doi:10.1002/pssr.200903290.

[221] H. Nagel, M. Kamp, D. Eberlein, A. Kraft, J. Bartsch, M. Glatthaar, and S. W. Glunz. Enabling solderability of pvd al rear contacts on high-efficiency crystalline silicon solar cells by wet chemical treatment. In *32nd European Photovoltaic Solar Energy Conference*, pages 48–52, 2016. doi:10.4229/EUPVSEC20162016-1BO.12.3.

[222] Synopsys tcad. `http://www.synopsys.com`, 2013.

Danksagung

An dieser Stelle möchte ich mich bei allen bedanken, die zum Gelingen dieser Arbeit beigetragen haben. Mein besonderer Dank gilt dabei

Prof. Dr. Gerhard Willeke für die Betreuung der Arbeit.

Prof. Dr. Elke Scheer für die Übernahme des Co-Referats.

Prof. Dr. Eva Weig, für die Teilnahme an der Prüfung als Zweitprüferin.

Prof. Dr. Peter Nielaba, der sich bereit erklärt hat den Prüfungsvorsitz zu übernehmen.

Prof. Dr. Stefan W. Glunz für Aufnahme in seinen Bereich und angenehme und exzellente wissenschaftliche Arbeitsumgebung in diesem.

Dr. Martin Hermle für die Aufnahme in seine Abteilung und das in mich gesetzte Vertrauen, sowie vielfache Unterstützung rund um die Themen Simulation und Charakterisierung.

Dr. Jan Benick für die Betreuung der Arbeit, die Aufnahme in sein Team und die vielen Diskussionen zu den Ergebnissen und Fragestellungen dieser Arbeit sowie die weitreichende Unterstützung am ISE und auch privat.

Dr. Ulrich Jäger für eine Vielzahl von *PassDop* Laserprozessen sowie viele interessante Diskussionen zu den relevanten Ergebnissen und dem Zusammenspiel der Schichten mit dem Laserprozess.

Muhammad bin Mansoor für die sehr gute und engagierte Arbeit bei der Entwicklung des *fPassDop* Prozesses im Rahmen seiner Masterarbeit.

Christian Schetter und Harald Steidl für die exzellente technische Betreuung, u.a. der PECVD Anlagen.

dem Reinraumteam Nadine Brändlin, Antonio Leimenstoll, Andreas Lösel, Felix Schätzle, Sonja Seitz, Harald Steidl und Karin Zimmermann für die Vielzahl an Prozessen sowohl für Testproben als auch im Rahmen der Herstellung der Solarzellen.

Rupprecht Ackermann, Nicole Hoffmann, Norbert Kohn und Daniel Trogus für die vielen Beschichtungen mit ARC-SiN_x.

Andreas A. Brand, Simon Gutscher und Dr. Elmar Lohmüller für die vielen Laserablations- und *PassDop* Laserprozesse.

Dr. Elmar Lohmüller und Vanessa Krumm für die Unterstützung bei der Herstellung von Solarzellen mit Siebdruckkontakten sowie deren Charakterisierung.

Dr. Jonas Bartsch, Gisela Cimiotti, Dr. Mathias Kamp, Dr. Sven Kluska und Gabriele Mikolasch für die Unterstützung bei der Herstellung von Solarzellen mit NiCu Kontakten.

Elisabeth Schäffer für eine Vielzahl an Messungen an meinen Solarzellen.

Dr. Bernhard Michl, Stephen T. Haag und Dr. Milan Padilla für die Unterstützung bei der fortgeschrittenen Charakterisierung der Solarzellen.

Dr. Pierre Saint-Cast, u.a. für die Diskussionen zu den Modellen zur Beschreibung der lokalen Rekombination sowie die Übernahme der Leitung der *pPass-Dop* Entwicklung, was mich an dieser Stelle sehr entlastet hat.

Charlotte Weiss für XRD Messungen sowie Diskussion der Ergebnisse.

Dr. Friedemann Heinz und Andreas Büchler für Mikro-Raman und Mikro-PL Messungen.

Dr. Benjamin G. Lee und Bob Reedy für SIMS Messungen sowie Unterstützung bei der Interpretation der Ergebnisse.

Andreas Büchler, Dr. Andrew Mondon und Jutta Zielonka für Scanning Electron Microscope (SEM) und Energy-Dispersive X-Ray spectroscopy (EDX) Messungen.

Dr. Andreas Fell für die Bereitstellung von *Quokka*, welches mir mit einer Vielzahl an Simulationen ermöglichte meine Solarzellen besser zu analysieren.

Dr. Keith McIntosh für den Aufbau der PV Lighthouse Plattform, welche den Zugriff auf und die Anwendung von Standardmethoden rund um das Thema Siliciumsolarzellen beschleunigte.

Christian Harmel für die Hilfe bei der Erstellung des Titelbilds sowie bei der Unterstützung mit diversen Laserprozessen.

meinen HiWis Konstantin Abrarov, Michael Fechtig, Aile Ge-Ernst, Wajhi Jafri, Kai Mühlbach, Clara Siber und Tobias Unmüssig, die mir bei einer Vielzahl von Prozessen Arbeit abgenommen haben.

meinen ehemaligen und aktuellen Bürokollegen Nadine Brändlin, Dr. Lena Breitenstein, Dr. Frank Feldmann, Dr. Philipp Löper, Dr. Christian Reichel, Dr. Armin Richter, Dr. Henning Nagel, Elisabeth Schäffer, Sonja Seitz, Dr. Manuel Schnabel und Karin Zimmermann, sowie meine aktuellen und ehemaligen Kollegen aus den Bereichen SEC, MST und PTQ, u.a. für die angenehme Atmosphäre sowie viele interessante Gespräche und Diskussionen.

meinen Kollegen und Freunden Dr. Jan Benick, Dr. Frank Feldmann, Rita M. da Silva Freitas, Vanessa Isenberg, Dr. Stefan Janz, Saskia Pospischil-Kühnhold, Dr. Bernhard Michl, Dr. Nena Milenkovic, Dr. Ralph Müller, Dr. Regina Pavlovic, Dr. Maximilian Pospischil, Annika Raugewitz, Heiko Steinkemper, Charlotte Weiss, Mathias Weis für die vielen Freizeitaktivitäten und damit viel Ausgleich zur Arbeit.

meiner Familie für die fortwährende Unterstützung während und nach dem Studium, was diese Arbeit schlussendlich erst ermöglicht hat.

zuletzt auch all denjenigen, die ich hier vergessen oder nicht explizit erwähnt habe, die aber dennoch ihren Beitrag zu der Arbeit geleistet haben.

Passivated emitter and rear locally diffused silicon solar cells have proven to offer a high efficiency potential, but there were doubts about the industrial feasibility due to the complex structuring being required for device fabrication. The PassDop concept introduced an approach that allowed reducing the number of process steps significantly by using doped passivation layers in combination with a laser process.

The first topic of this work is focused on the development and characterization of the multifunctional layers that form a central part of this concept. Here new layers based on a-SiNx:P are introduced. It is shown that layers for both low temperature device fabrication as well as firing stable layers (for screen printed contacts) are viable.

The next part aims for an improved understanding of the properties and implications of the local laser processing. The laser spots are analyzed with focus on doping profiles, impurities as well as minority carrier recombination.

Finally the transfer of the concept to the device level is described demonstrating that with this industrially feasible approach high efficiency solar cells can be fabricated achieving efficiencies up to 23.5%.

Universität Konstanz

ISBN 978-3-8396-1207-1

9 783839 612071